NiMH battery forensics: Instrumentation, modelling and prognostics for identifying failure

A thesis submitted

for the degree of

Doctor of Philosophy

in Engineering

by

Petrus Jozef Martinus Leijen

The University of Waikato
Te Whare Wānanga o Waikato

August 2016

The University of Waikato

Abstract

Battery forensics is a growing research field that is becoming increasingly important with the introduction of hybrid-electric and electric vehicles. The need to correctly diagnose battery condition and predict signs of early failure is well recognised. Many presently used techniques are only applicable to laboratory situations where sensitive measurement is required or where complicated mathematical approaches are needed to assess battery condition. Advanced techniques are explored, such as extended Kalman filtering, to identify the challenges associated with analysis of multi-cell battery modules. Energy-recycling hardware is developed that is capable of efficiently cycling energy to and from cells connected in a series configuration. Switching a supercapacitor-bank-based energy store between series and parallel configurations, coupled with a bidirectional switch-mode power-supply, ensures that maximum energy is retained during the analysis cycle. Extended Kalman filtering (EKF) applied to three different battery models was used to quantify the internal component values of the battery equivalent circuits. The bulk-surface model was determined to be the most appropriate for the Toyota Prius battery modules as the EKF predicted component values converge to stable values, and the recovered voltage trace has a low error. However, the computational complexity when considering 12 series-connected NiMH cells, with their individual component variation with state-of-charge and state-of-health, make the EKF approach unviable. The data harvested during the energy recycling is used to calculate a new *effective capacitance* measure which relates directly to battery state-of-health. Not only is there a direct relationship between effective capacitance and state-of-health, but the (Q, V) coordinate of maximum effective capacitance on the charge–voltage plane, captured during battery discharge, is able to distinguish clearly between ordinary ageing and catastrophic cell failures.

Original contributions

This work was completed while working part-time in industry. Having a close working relationship with a company gives this research industrial focus and forced practical applications for the research. For this thesis, I need to state which components of the research originated with me. In general, unless otherwise stated, all numerical calculations and all graphic presentations are my own work. Here is a list of my main contributions:

- identification of battery failure modes within Prius battery pack (Chap. 1)
- development of "quick check" procedure with commercial diagnostic equipment to identify different failures and when further investigation is required (Chap. 1)
- development of unique energy cycling technique and confirmation of supercapacitor variation within a batch of capacitors (Chap. 3)
- development of hardware and confirmation through simulation that intelligent switching of a supercapacitor bank improves energy conversion efficiency by up to a factor of two compared with other control techniques (Chap. 4)
- investigation of the suitability of various battery parameter measurement techniques for three battery models, with the final realization that extended Kalman filtering applied to the bulk-surface battery model was suitable for recovering the required parameters. However, the component values vary with environmental factors meaning that EKF can ultimately only be applied in laboratory conditions (Chap. 5)
- I acknowledge the contribution that Alistair Steyn-Ross has made to this chapter where we have developed and proved a relationship between a new grouped *effective capacitance* and state-of-health (Chap. 6)

Peer-reviewed conference papers

- Leijen, P. & Kularatna, N. Developing a monitoring system for Toyota Prius battery-packs for longer term performance issues, IEEE International Symposium on Industrial Electronics (ISIE), 2013, 1-6
- Leijen, P. & Scott, J. Failure analysis of some Toyota Prius battery packs and potential for recovery, SAE Technical Paper 2013-01-2561, 2013
- Leijen, P. Real world battery diagnostics model based and a Prius case study, IEEE International Symposium on Industrial Electronics (ISIE), 2014, 1-6

Book chapter

- Leijen, P., "HV Battery", Chapter 6: Hybrid Diagnostics (EMS1-4) AECS Ltd, 2012

Acknowledgements

I wish to acknowledge with considerable gratitude the contributions and help received from a host of colleagues:

Dr Nihal Kularatna, Dr Alistair Steyn-Ross for their support, supervision and helpful insight and addition to my work during the course of this research.

I thank AECS Ltd for providing valuable assistance with the interpretation of the large amount of test data and the use of their test equipment. I would also like to specially thank Herbert Leijen for his help in analysing the large amounts of data throughout the project and providing a business perspective.

Dan Simon and Dean Freeman whom I've been in email contact with regarding some issues faced in perfecting the extended Kalman filtering mathematics. Towards the latter stages I'd also like to mention Anna Kutschireiter, who after meeting Alistair at a conference in Prague, has looked at my EKF work and provided some opinions regarding the approach that I've taken.

Matthew Seabright as an undergraduate student working with Alistair on an unrelated project has given me a well needed reintroduction to LTSpice used for some simulation work.

I'd also like to thank the rest of my family for helping me through the tough stages from Cunie's (my mother) input regarding how her brother (my uncle) completed his PhD. My brother Tom who has given some technical hardware design input and has always listened and given advice as to how he interacted with his supervisory team when in a similar situation to me.

I would also like to thank Toyota New Zealand, Hyde Automotive and Mudgeway Partsworld for providing the battery packs used during the experiments. I also acknowledge the New Zealand Ministry of Business Innovation and Enterprise for funding support.

To you all—thank you

Contents

List of Figures

List of Tables

Acronyms and Abbreviations

AC	alternating current
BMS	battery management system
CCM	continuous conduction mode
DC	direct current
DCM	discontinuous conduction mode
DTC	diagnostic trouble code
ECU	electronic control unit
ESR	equivalent series resistance
EV	electric vehicle
HEV	hybrid electric vehicle
HV	high voltage
ICE	internal combustion engine
IGBT	insulted gate bipolar transistor
MG	motor generator
MH	metal-hydride
NiMH	Nickel metal-hydride
OBD	onboard diagnostics
OCV	open circuit voltage
RC	resistor capacitor
RMS	root-mean square
SC	supercapacitor
SEPIC	single-ended primary-inductor converter
SMPS	switch-mode power-supply
SOC	state-of-charge
SOH	state-of-health

Chapter 1

Performance issues with series-connected battery packs: A Toyota Prius case study

1.1 A brief history

Toyota Prius hybrid electric vehicles (HEV) were introduced into the market in 1998. Since then, the HEVs have aged, and are now exhibiting a range of high-voltage (HV) battery-related faults. AECS Ltd has been training elite-level Toyota technicians in New Zealand since 2008 with battery technology and related issues being a major focus. From these training seminars it has become apparent that there is little knowledge on how to test and/or rebuild these battery packs to enable the vehicle to function as new. Developing an improved understanding of HEV battery pack technology and failure modes has been a major research focus at the University of Waikato and has become the topic of this PhD thesis.

Good battery-pack health is critical to the performance of any HEV or EV [1]. Previous studies have shown that the NiMH battery packs found in the Toyota Prius HEV frequently fail [2]. A prototype battery analyser produced during this study required careful and painstaking disassembly of the battery pack to access the individual battery modules; this was a slow and costly process. This experience helped to motivate the present project: to develop a timely and cost-effective method to quantify battery condition by making use of the existing vehicle wiring harness.

1.2 Contents overview

This thesis is a comprehensive report of work undertaken to find a suitable method for measuring state-of-charge (SOC) and state-of-health (SOH) of Toyota Prius battery packs. An extensive literature search investigating methods for testing battery packs including advanced modelling techniques was performed: a summary of the literature survey forms the first part of this thesis.

Starting from the initial proof of concept (presented at the Oct. 2013 SAE Powertrains, Fuels and Lubricants Conference, Korea 2013), the design and modelling of a battery measurement tool, and the development of a new battery parameter, *effective capacitance* (C_{eff}), as a measure of battery state-of-health is described. A comprehensive set of results is presented to validate this new measure.

The thesis proceeds as follows.

Chapter 1 introduces the original problem of HV battery failure and describes the on-board measurements performed by the Toyota Prius Battery Management System (BMS). Information was extracted from the Toyota workshop manuals to highlight how rudimentary the on-board fault detection is. The Toyota repair advice, once battery failure has occurred, is to replace the entire battery at the cost of several thousands of dollars. The chapter shows the effect of reduced battery performance on the vehicle and highlights the importance of battery testing and matching. A preliminary diagnostic procedure, (presented at IEEE International Symposium on Industrial Electronics 2014), is presented to allow the diagnostician to determine whether or not battery module failure has actually occurred, or if some other mechanism has caused the BMS to deem the battery faulty.

In **Chapter 2** the terms relevant to the NiMH battery are defined and various mathematical and analytical relationships from the literature are introduced. Several of these relationships are critically assessed in later chapters. Three commonly used battery models are described and the mathematics required to simulate them is presented. The range of methods reported in the literature for measuring SOC and SOH were surveyed.

Chapter 3 discusses the philosophy behind the charger/analyser hardware, introduces the bidirectional switch-mode power-supply (SMPS) and how energy will be cycled through the battery blocks during the analysis. The variation in supercapacitor capacitance and ESR within a batch of capacitors was examined, and how these parameters change with temperature. The data presented in this chapter will be used in Chapter 4 when energy losses within the energy cycling tool are investigated.

Chapter 4 investigates techniques used to minimise energy lost during the analysis process. MATLAB and LTSpice models are compared under different conditions. Only first-order component effects are included in energy balance equations. The simulations demonstrate that appropriate series/parallel switching of the supercapacitor bank provides ≈50% improvement

in energy conversion efficiency with respect to a standard fixed duty-cycle switched buck circuit.

The focus returns to battery models in **Chapter 5** where the models introduced in Chapter 2 and various methods for extracting and estimating model parameters are investigated. Real battery data are used for both parameter estimation and a comparative assessment of the three battery models. Relationships between the most appropriate model (the bulk-surface model in this case) and state-of-charge are shown along with parameter variations during a standard drive showing that extended Kalman filtering is only useful when the battery is subjected to a regularly repeating current pulse of constant shape.

From Chapter 5 it will have become clear that the standard model-based measurement techniques reported in the literature have many shortcomings, and a new method is needed to quantify battery health. **Chapter 6** introduces the concept of *effective capacitance*, (C_{eff}). The peak value of effective capacitance and its location on the charge–voltage plane indicates ageing and distinguishes among various failure methods.

In **Chapter 7** the thesis is concluded and further work is highlighted.

1.3 Background information

The most difficult issue in developing electric vehicles (EV) and hybrid electric vehicles (HEV) is to achieve optimally performing large-capacity battery packs with suitable battery management systems (BMS). Over the past two decades there has been considerable research and development of battery packs, drive trains and optimizations applicable to these areas [3].

The Toyota Prius HEV has been present in the market for the last decade. The Toyota Prius has an auxiliary conventional 12 V lead acid battery but the focus of this research project is on the 7.2 V NiMH battery modules within the high-voltage battery pack. The HV battery pack consists of 228 NiMH cells organized into modules of six series-connected cells. The Toyota Prius system contains a number of technically advanced systems that make diagnostics both interesting and challenging. The battery management electronic control unit (ECU) of the Toyota Prius measures various battery-related parameters including temperature, voltage and current. When one of these parameters falls outside a predetermined range of acceptable values, a diagnostic trouble code (DTC) is logged.

The quality of the battery pack determines the fuel efficiency of the vehicle. Swings in battery voltage indicate to the BMS when to start and stop charging the batteries through

either regenerative braking or a generator driven by the internal combustion engine (ICE). Battery quality can be defined as its capacity or state-of-health [4]. Capacity is a measure of the "size" of the battery in amp-hours (Ah), and indicates how much energy is able to be stored in the cell. There are many different methods for measuring state-of-health (SOH) and state-of-charge (SOC) as outlined in [4–9]. State-of-charge is a measure of how "full" the battery is expressed as a percentage of its capacity. The easiest method of measuring battery capacity is "coulomb counting", a simple integral of current over time [2], $Q = \int I dt$. Battery SOH defined in [2] to include failure modes such as short-circuited cells, cell reversal or open-circuit cells as well as ordinary capacity fade effects, is more difficult to assess. Ref [10] details a method for measuring SOH, including other failure modes, and capacity of Prius battery packs. Section 2.2.3 defines SOH as used in this thesis.

A major concern to Prius owners is the lifetime of the battery pack. Toyota claims that the battery pack should last 160,000 km or ten years. However, as per the experience of service companies such as AECS Ltd, it is not uncommon for Prius battery packs to fail prematurely. This chapter describes the characteristics of a reduced-capacity battery module, and the effects of a module with very poor SOH on the performance of the battery pack as a whole. This thesis investigates a range of battery models and equivalent circuits to describe the behaviour of modules under different conditions, and proposes a monitoring system for early detection and prevention of battery failure, based on a supercapacitor bank charge-transfer subsystem.

1.4 Toyota Prius system

The battery pack of the NHW11 Toyota Prius consists of 38 NiMH modules (Figure 1.1) each of which contains six NiMH cells connected in series [11]. Later Prius models, such as the Prius C, contain fewer battery modules; for example, one vehicle used during this research contained only 28 battery modules. Toyota have designed their system to operate in a split-battery fashion, i.e., the apparent "ground" (chassis) of the HV battery pack occurs in the middle of the pack. Each *pair* of battery modules will be referred to as a *battery block* in this thesis. This means that an NHW11 Prius has 19 battery blocks corresponding to the 38 individual modules.

Figure 1.1 does not show how the inverter/converter assembly links the battery management ECU, the battery pack and the auxiliary power source (12 V battery). All control units, lights, radio, etc in the Prius are powered from the auxiliary 12 V lead-acid battery. Powering the

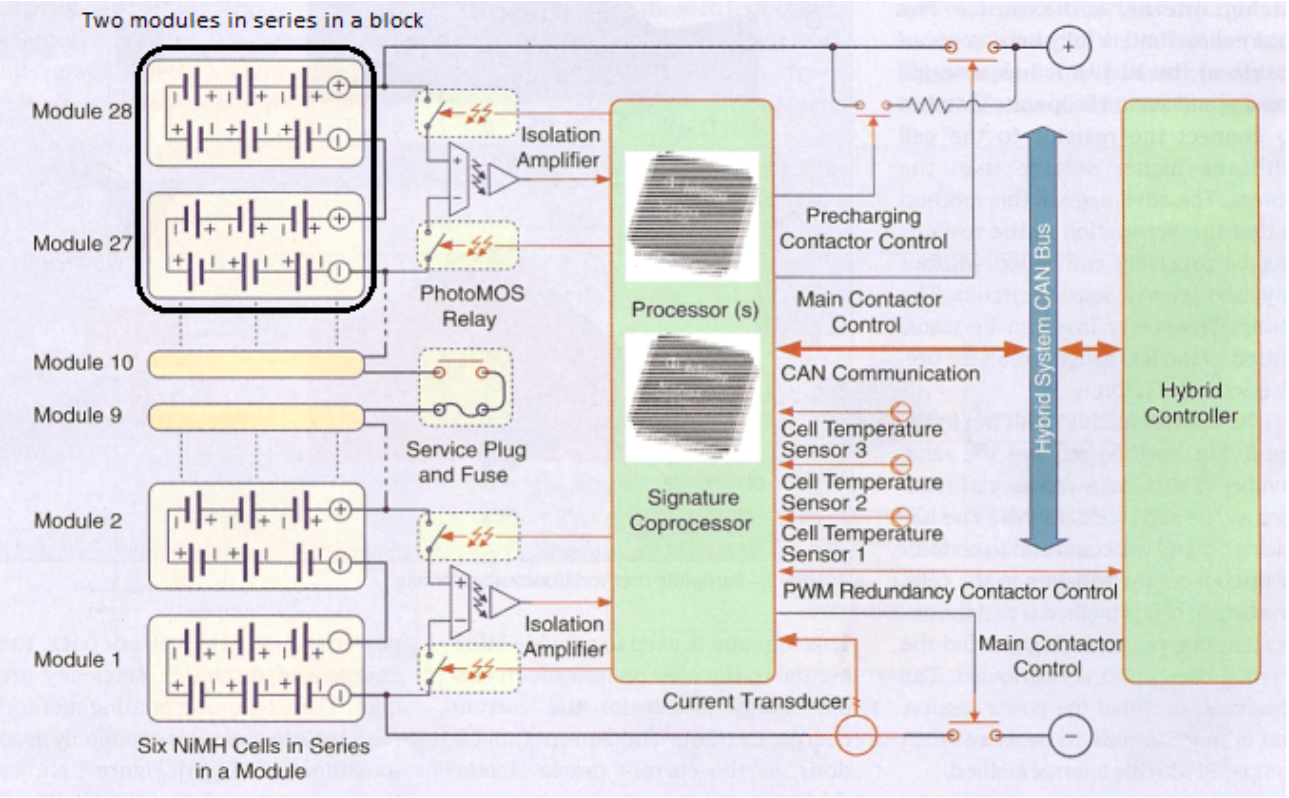

Figure 1.1: A typical battery management system for HEV-2009 Toyota Prius [12]

control units with 12 V is similar to a conventional vehicle. However, the 12 V battery is charged through a step-down transformer from the high-voltage battery pack, effectively creating a high-impedance connection between the centre of the HV battery pack and vehicle chassis. The inverter converts the HV battery voltage to a pseudo three-phase sinusoidal waveform using six duty-cycle and frequency controlled switches, insulated gate bipolar transistors (IGBTs). The frequency and duty-cycle of these IGBTs is dependent on the power and speed requirements for the three-phase electric motors, ultimately a calculation including factors such as battery SOC and requested torque from the drivers accelerator pedal. The "three-phase" voltage is used to drive the motor-generator (MG) set and is the main source of propulsion, see Figure 1.2.

Previously, components such as the hydraulic power steering pump, air-conditioning compressor and the alternator were belt-driven off the ICE. These components have been removed from the ICE and replaced by electronic alternatives allowing these components to work without the engine running. The hydraulic power-steering has been replaced by electronic power-steering. Similarly the air-conditioning compressor has been changed from a belt-driven compressor to an electric compressor requiring special non-conductive lubrication. The alternator has been replaced by a DC-DC converter. Later versions of Prius (second generation onwards) are also fitted with a boost voltage regulator that is capable of stepping the battery voltage up from 200 V to as high as 650 V during ordinary vehicle operation.

1.5 Toyota Prius battery management system - onboard diagnostics (OBD)

The Toyota Prius battery management system (BMS) provides the diagnostic specialist with diagnostic trouble codes (DTC) and datastream information. The battery management system of the Prius (Figure 1.1) monitors battery status by taking several measurements:

- differential voltage across each pair of modules (battery block)
- total current through the pack
- temperatures sampled at four points across the pack

Datastream mode is a method of reading internal parameters from the on-board management systems though serial, CAN-bus[1] or K-line[2] communication. Due to prioritisation delays and overheads in serial communication the data will always be delayed and the sampling speed will be low. However, in cases where high-voltages need to be recorded, such as battery block voltages, datastream recording may be the only way to safely access these diagnostic parameters.

The battery management system combines this information to determine state-of-charge [12]. Methods for determining state-of-charge are covered in Chapter 2. Two lines of datastream

[1]CAN-bus is a differential signalling communication system developed by Bosch specifically for communication between multiple ECUs or ECUs and diagnostic equipment

[2]Single-wire two-way communication scheme between diagnostic tool and automotive ECU

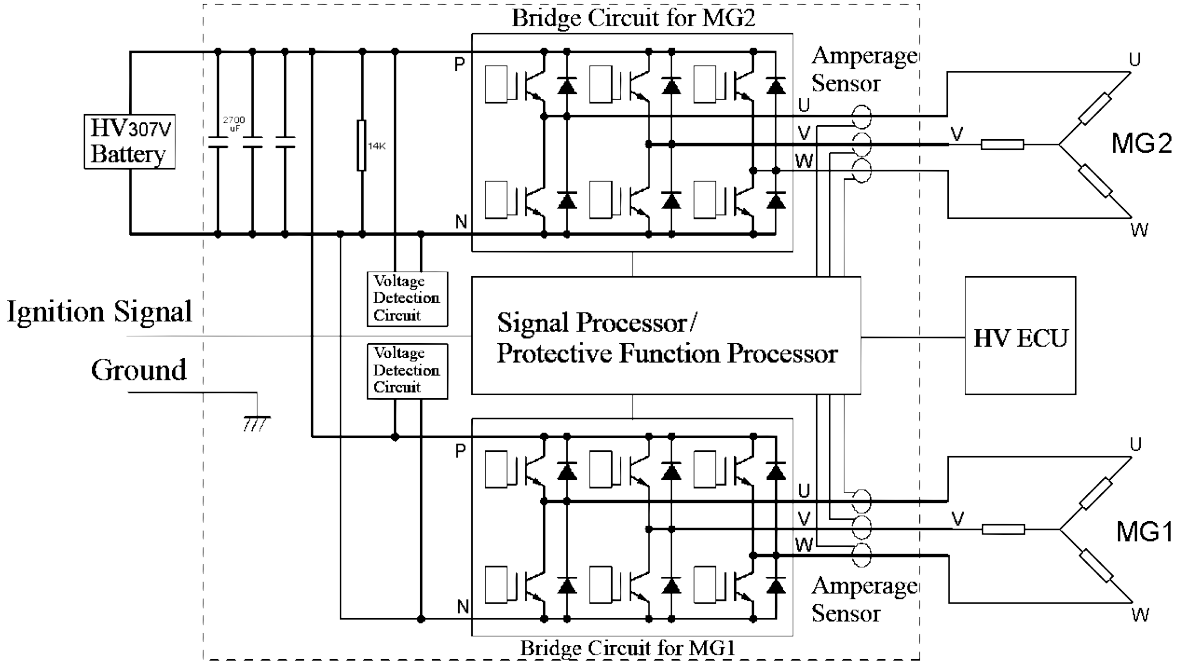

Figure 1.2: Prius inverter showing six switches per motor-generator (MG1 and MG2) [13]

information of particular relevance for battery health determination are “maximum voltage battery code” and “minimum voltage battery code”, which can be measured using commercially available diagnostic equipment. Maximum and minimum voltage battery code datalines return the index numbers (1 to 19) of the battery block with the highest and lowest voltage at that point in time.

1.6 Toyota Prius BMS battery-related fault codes

The Toyota Prius battery management system monitors battery temperature and battery voltage with the sensors shown in Figure 1.1. If any of the voltages or temperatures of the battery blocks fall outside predetermined nominal ranges for a prolonged period of time (to reduce the risk of a false-positive event triggered sensor noise) the BMS will log the malfunction and store a DTC. The vehicle will then enter a reduced power “turtle” mode when battery-related fault codes are set. Turtle mode is equivalent to limp-home mode in a conventional vehicle. This means that the current drawn from the battery, and charging current, are limited, resulting in poor fuel economy and a vehicle that is almost undrivable.

Two of the most common battery-related DTCs are “Leak Detected” and “Battery Block Malfunction”. The “leak” refers to an insulation issue i.e., a current leak.

The Battery Block Malfunction code (DTC number P3011 to P3029) can be triggered by cells that have poor state-of-health. The battery management ECU looks at the voltage differences between individual battery blocks during charge and discharge. A voltage difference of less than 0.3 V is acceptable (Fig. 1.3(a)) according to Toyota repair advice [14]. This measurement technique is an indirect method for comparing battery-block equivalent series resistances or impedance. A cell with higher AC or DC impedance, and therefore higher voltage difference, is deemed to be of lesser SOH (as clarified in Section 2.2.3). This method also gives an indication of relative SOC between battery blocks. The voltage of the block with lower SOC will collapse before that of a cell with higher SOC.

Another method of diagnosing the battery block malfunction DTC, suggested by Toyota, is to look at the swing between the maximum and the minimum block voltages, as shown in Figure 1.3(b). The maximum allowable voltage swing is 2 V.

This fault code is generated when a significant mismatch of battery modules is detected within the battery pack. Replacing the complete battery pack assembly is one possible fix to

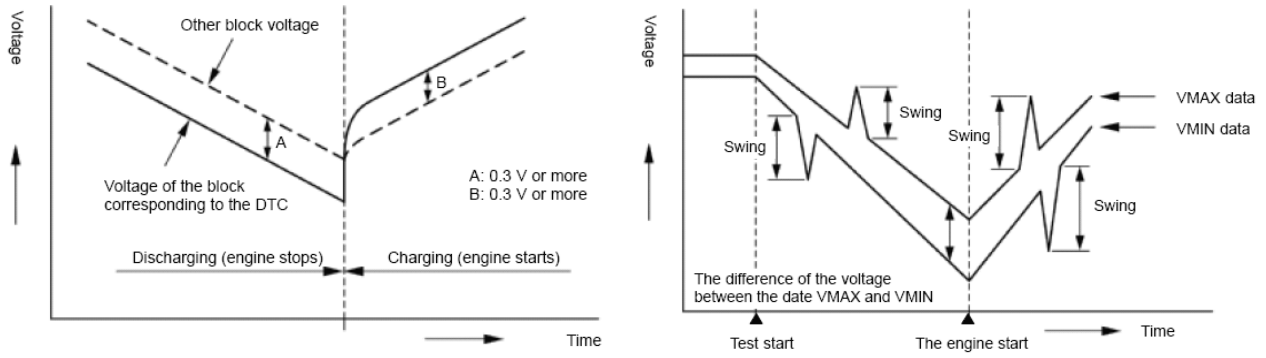

(a) (b)

Figure 1.3: (a) Voltage difference while discharging and charging, (b) voltage swing while discharging and charging [14]

this problem. However the replacement cost, of the order of several thousand dollars, can be prohibitive particularly for a car used for several years. In addition to this single faulty module condition, there is also large range of battery configurations and battery SOH distributions which will not generate a fault code. The next sections discuss the implications of such battery arrangements and outline a proposed monitoring system to identify these particular situations.

1.7 Problem description

When a large number of series-connected cells are exposed to high charge and discharge rates under slightly varying conditions, some cells can degrade unevenly. Figure 1.4 shows the uneven fashion in which four different battery packs have deteriorated. The four battery packs selected have been known to have been in service for different durations. These battery packs were analyzed in the lab to find the capacity distribution and steady state voltages of the individual battery modules. Known broken and poor state-of-health cells were then substituted into a good battery pack and road-tested in a Toyota Prius (Model: NHW11, Engine Type: 1FX, Year: 2001), to investigate the failure modes of the battery packs.

As HEVs age, battery degradation limits vehicle performance. Large state-of-health mismatches across a battery pack can lead to failure of the entire pack [2]. Accurately and efficiently diagnosing battery failure will become a necessity for automotive repair workshops specialising in HEV or EV repairs.

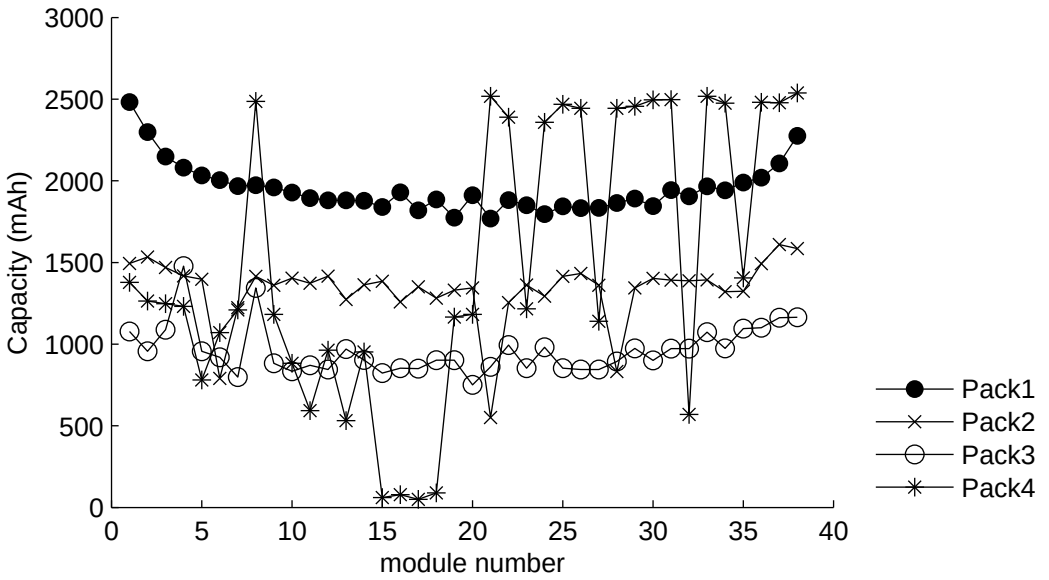

Figure 1.4: Capacity distribution across four tested packs

1.8 Battery capacity and the issue of the weakest link

Figure 1.4 shows the measured capacities per battery module, as determined using a coulomb-counting algorithm between end-of-discharge and end-of-charge points. Both Packs 2 and 3 have aged in a similar fashion: the modules near the ends of the packs have higher capacities than the modules in the middle, but are otherwise uniform. The "bathtub" curve appears to be due to the temperature differences, measured to be as high as 15°C, throughout the pack during normal operation. The outer modules are able to dissipate heat through the outer casing of the battery pack, hence remaining cooler. Whereas the inner modules cannot dissipate heat as effectively. Raising the temperature of a battery accelerates the undesirable side reactions within the battery modules responsible for SOH reduction.

It was determined that Pack 1 was of good health because the pack performed the same as the original Prius battery pack. Module #38 (module ID 01M) from Pack 1 was replaced with module #38 (module ID 41D) from Pack 2. The battery characteristics are summarized in Table 1.1. Module 41D was chosen to have approximately half the capacity of the average value for the pack but with a similar steady state voltage.

Table 1.1: Modules replaced within battery pack

Module ID	Capacity	Steady Voltage
01M	2482.2 mAh	7.81 V
41D	1164.4 mAh	7.55 V

With battery pack-1 in the vehicle it was able to drive 2.6 km in EV mode (EV mode is where the vehicle is driven at 25 $\mathrm{km\,h^{-1}}$ using battery power only). EV mode terminates when the vehicle cannot drive any further without the ICE starting. The state-of-charge at the start and at the end of the tests was measured using a diagnostic scantool. When one module was replaced with a module of approximately half its capacity (as shown in Table 1.1), the vehicle was only able to travel 1.3 km in EV mode. No fault code was triggered with this module arrangement even though the fuel efficiency of the vehicle was halved. This test confirmed that the battery pack was only as good as its weakest module and that matching state-of-health (of each module) and balancing state-of-charge throughout the battery pack is vital to the performance and fuel efficiency of the vehicle.

1.9 Case studies: Failures from the field

Researchers at AECS Ltd have recorded measurements from many vehicles which have failed in the field. The data presented below contain datastream information recorded using the LAUNCH range of diagnostic equipment. The datastream lines that were recorded during an ordinary drive cycle were battery current, maximum voltage battery code and minimum voltage battery code. A histogram-type plot is presented where the 19 different battery block number occurrences (y-axis) are plotted against battery current (x-axis). Figures 1.5 to 1.7 show a centralised peak in the -15 to 15 A range. This is the most common current draw i.e., vehicle cruising which means that most data is collected in this current range. Three "failed" battery packs were investigated.

1.9.1 Capacity mismatch in a series-connected battery pack

Figure 1.5(a) shows data obtained from Pack1 from figure 1.4, a moderately balanced battery pack. The general ageing characteristics of a Toyota Prius battery pack indicate that the capacity of the centre battery modules have faded more than those at the periphery. This can be caused by temperature variations throughout the pack [2]. Blocks with index number 1, 18 and 19 are most frequently identified as having the highest voltage. These blocks are located at either end of the battery pack.

Figure 1.5(b) shows the minimum voltage battery code plotted against current for the same driving cycle. The figure shows that blocks 8, 10 and 15 dominate the low voltage histogram.

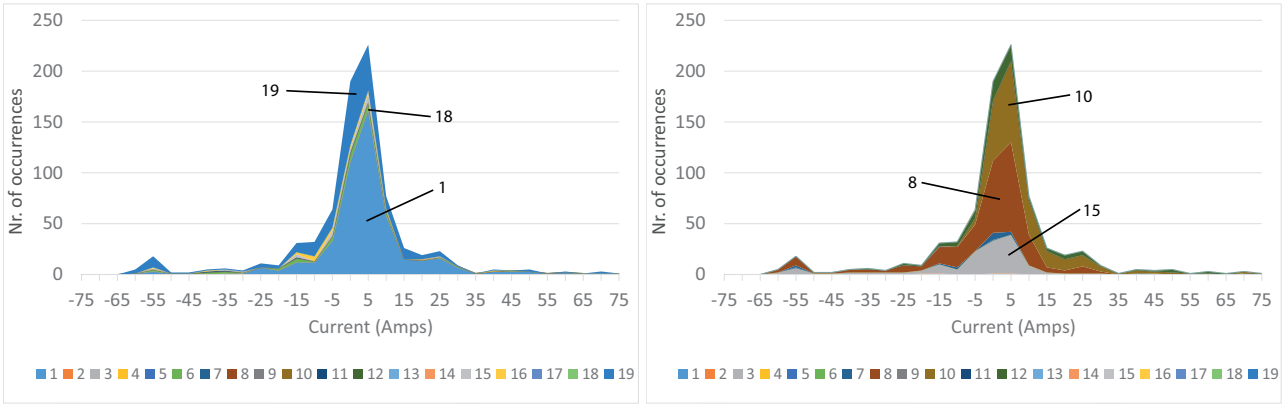

(a) (b)

Figure 1.5: Histogram plot of (a) maximum voltage battery code and (b) minimum voltage battery code vs battery current for a moderately balanced battery pack. Note the sign convention: negative battery current indicates charging

So, it can be concluded that the capacities of the blocks in the centre of the battery pack are *lower* than those on the outsides of the pack. The interesting observation is that the same blocks (8, 10 and 15) have the lowest voltage during charge and discharge, negative and positive current respectively, and the same blocks (1, 18 and 19) have the highest voltage during charge and discharge.

1.9.2 Corrosion on sensor wiring

When diagnosing large series-connected battery packs we must consider the complete system. For example, when a HEV presents with a battery-related fault code the possibility of control unit failure, sensor failure and wiring damage must also be considered. As mentioned previously there are voltage sensing wires connected across each pair of battery modules. The data in figure 1.6(a) and 1.6(b) are the same measurements as described in Section 1.9.1 but now one of the sensing wires (on block 19) is severely corroded causing a 1 V drop from the battery terminals to the BMS.

Figure 1.6(a) shows that blocks 1 and 18 have the highest voltage throughout a driving cycle. Again the same blocks retain the highest voltage during charge and discharge. But the minimum voltage battery histogram (Figure 1.6(b)) shows that block 19 always measures the lowest terminal voltage during both charge and discharge. This situation generated a diagnostic trouble code “block 19 becoming weak” for which the Toyota repair advice is to replace battery pack after a number of tests [14]. This is poor advice because the DTC is being falsely triggered as a result of a corrupted measurement arising from the corroded voltage-sensing wire.

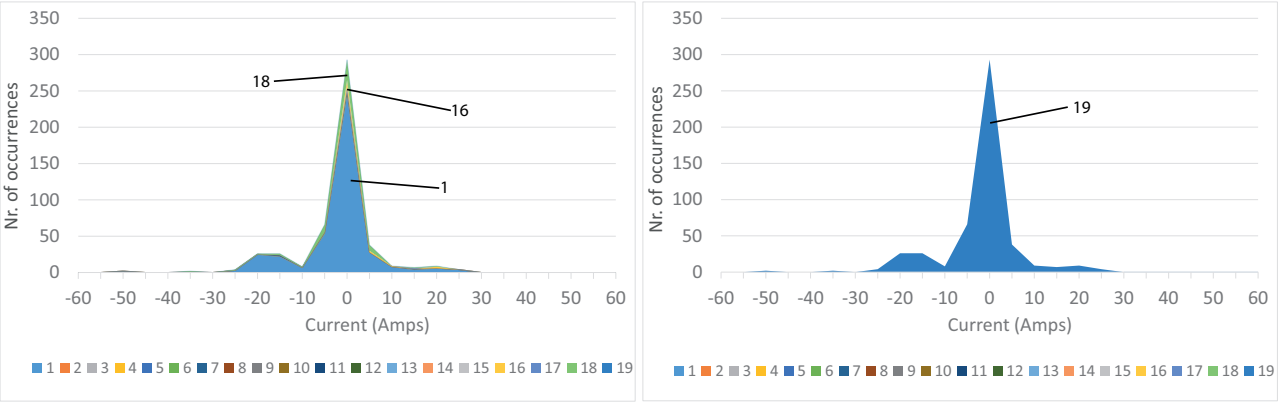

(a) (b)

Figure 1.6: Histogram plot of (a) maximum voltage battery code and (b) minimum voltage battery code vs battery current for a pack in which the voltage-sensing wire to block 19 is corroded

1.9.3 Module failure

The third set of data was extracted from a battery pack that contains one failed battery block. Figure 1.7(a) shows that block 1 has the maximum voltage during discharge which confirms that battery modules towards the ends of the battery packs tend to have higher SOH than the battery blocks in the centre of the battery pack. This graph shows that block 4 shows the maximum voltage during charging. Significantly, block 4 does not show the maximum voltage during discharge (positive current).

The minimum voltage block number presented in Figure 1.7(b) must also be examined. During charging, the blocks in the centre of the battery pack have the minimum, voltage again confirming the bathtub-shaped capacity distribution. However during discharge battery block 4 has the minimum voltage. From this information it can be concluded that the voltage of a failed block will overshoot the other block voltages during charge, and undershoot the other

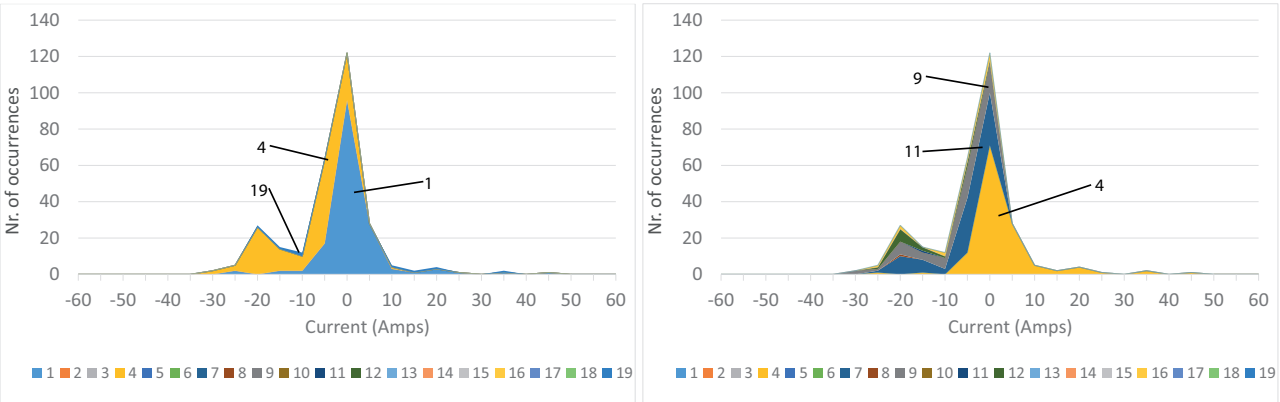

(a) (b)

Figure 1.7: Histogram plot of (a) maximum voltage battery code and (b) minimum voltage battery code vs battery current for a pack in which block 4 has failed

block voltages during discharge. Plotting the scantool data in such a fashion leads to fast and accurate battery diagnostics.

1.10 Chapter summary

The chapter described the battery state-of-health problem faced with large series-connected battery packs and the effect a single reduced-capacity module can have on pack performance. The chapter shows how module capacity can vary between different battery packs analysed. A simple check is introduced which shows how battery failure can be diagnosed using existing diagnostic equipment and smart presentation of simple datastream recordings.

Chapter 2 explains battery related terminology, introduces commonly used battery models and describes battery health and state-of-charge measurement techniques found in the literature.

Chapter 2

NiMH battery models and equivalent circuits

2.1 Desired outcomes

This chapter provides an overview on NiMH (nickel metal-hydride) battery terms and some important electro-chemical aspects related to batteries. The following sections discuss relationships between environmental and usage data and battery parameters found in the literature. In the latter sections the simple, Thévenin and bulk-surface battery equivalent circuits are introduced including a description of the mathematics required to simulate each circuit. A brief analysis of each equivalent circuit is given outlining the pros and cons of each approach.

2.2 NiMH battery terms and definitions

2.2.1 Voltage

The battery voltage, sometimes referred to as electromotive force (EMF), depends on the half-cell voltages of the chemicals used in the battery. Voltage is easily measured at the battery terminals and changes under different conditions such as state-of-charge, temperature and discharge/charge current. NiMH chemistry is rechargeable which means that energy can be taken from the cell during discharge and restored to the cell during charging. The chemical reactions that occur within a NiMH cell are as follows [15], where the discharge reaction is read left to right:

At the positive electrode:

$$\mathrm{NiO(OH)} + \mathrm{H_2O} + e^- \rightleftharpoons \mathrm{Ni(OH)_2} + \mathrm{OH^-} \tag{2.1}$$

$$2\mathrm{OH}^- \rightleftharpoons \frac{1}{2}\mathrm{O}_2 + \mathrm{H}_2\mathrm{O} + 2e^- \tag{2.2}$$

At the negative electrode:

$$\frac{1}{p}\mathrm{MH}_p + \mathrm{OH}^- \rightleftharpoons \mathrm{H}_2\mathrm{O} + \frac{1}{p}\mathrm{M} + e^- \tag{2.3}$$

$$\frac{1}{2}\mathrm{O}_2 + \mathrm{H}_2\mathrm{O} + 2e^- \rightleftharpoons 2\mathrm{OH}^- \tag{2.4}$$

In equations (2.3) and (2.4) p is the reaction order of atomic hydrogen in the negative electrode [15]. The reaction order is dependent on the type of metal-hydride (MH) used, and is assumed to correspond to the stoichiometric coefficients. For example, if the common $\mathrm{LaNi_5H_6}$ metal-hydride is used then $p = 6$.

The cell operating voltage produced by the chemical potential between these two reactions is 1.2 V [16], with [17] quoting the open circuit voltage (OCV) to be 1.3 V. The 1.2–1.3 V range represents is the average voltage for a single cell in its normal operating region. A Prius battery module has an average voltage of 7.8 V in its normal operating region at, 40–50% SOC, (see Figure 2.1), which is achieved with six series-connected cells.

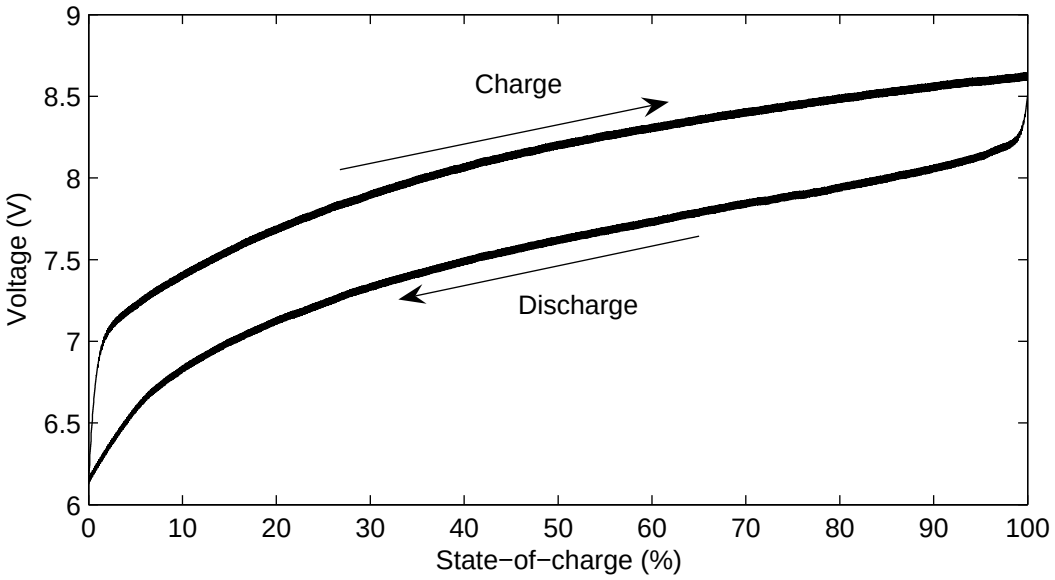

Figure 2.1: Toyota Prius battery module curves under 4 Amp constant current charge and discharge at 15°C

2.2.2 State-of-charge

State-of-charge (SOC) is a measure of the charge remaining in the cell expressed as a fraction of that stored in the fully-charged state. There are three generic methods of measuring state-of-charge: coulomb counting, voltage method or chemical methods [17–19]. SOC is usually calculated by coulomb counting i.e., by evaluating the integral with-respect-to time of the current flowing from the battery pack,

$$\mathrm{SOC}(t) = \frac{Q(t)}{Q_{\max}} 100\% \tag{2.5}$$

where $\mathrm{SOC}(t)$ is state-of-charge at time t and,

$$Q(t) = Q(t_0) + \int_{t_0}^{t} i \; dt \tag{2.6}$$

where i is current flowing from the cell and $Q(t_0)$ is the charge at time t_0. Coulomb counting is the easiest to implement in hardware; however, it is costly to obtain accurate results [5]. Large cumulative errors can occur due to slight sensor errors, therefore it is recommended to use other SOC estimation techniques to adjust for induced errors. An on-line state-of-charge measurement system requires an accurate estimate of the initial SOC ($\mathrm{SOC}(t_0)$) of the cell but this can be difficult to obtain [6, 20]. In most systems, the accuracy of the SOC measurement is improved by using multiple SOC approximation approaches [20].

Voltage methods require an accurate mapping of battery terminal voltage to state-of-charge taking into account variations due to temperature etc. Various advanced improvements of accurately calculating SOC can be applied to the three techniques mentioned above [4,7,15,21]. Such advanced methods include impedance measurement, Kalman filtering, neural networks and fuzzy logic. These alternative approaches are described in Section 2.5.

2.2.3 State-of-health

Battery state-of-health (SOH) is defined to be the capacity of the cell at full charge as a percentage of the standard (rated) capacity of the cell [4]. For example, if a cell is rated at 1000 mAh and from full charge the cell only delivers 500 mAh then the cell is said to be at 50% SOH. Rechargeable chemistries have a limited cycle-life meaning that battery performance degrades over time. Degradation can be caused by factors such as impurities within the electrolyte,

manufacturing defects, etc. The cell cycle-life can be significantly shortened if the cell is not maintained properly or is abused. In [22, 23] this relationship is presented as,

$$\text{SOH} = \frac{Q_{\text{max}}}{Q_{\text{rated}}} 100\% \tag{2.7}$$

where Q_{max} and Q_{rated} represent the maximum charge extracted from the battery and the rated capacity respectively.

For the purposes of this project state-of-health estimation is divided into two categories: functional and failed cells. Both need to be considered when assessing series arrangements of cells. Functional cells show the expected signs of *ordinary ageing*, such as capacity fade, which occurs when the amount of active material within the cell reduces, and resistive film growth resulting from unwanted side reactions at the surface of the electrodes. Battery state-of-health can be related to the impedance of the cell [8, 9, 24, 25]. A cell with higher DC impedance is deemed to be of lesser state-of-health. The DC impedance of the cell is the equivalent resistive-film or mass-transport series resistance of the cell, and is assessed by applying DC charge-and-discharge pulses to the cell and measuring the voltage deflections away from the open circuit voltage [8]. Capacity fade and resistive film growth eventually become too great and the module will reach "end-of-life", usually taken to mean a reduction in SOH beyond 80% of rated capacity.

The assumption of battery SOH being related to impedance is accurate for single-cell systems; however, the Toyota Prius (and other hybrid vehicles) use modules of six NiMH cells in series [12]. As a result, module SOH must also take into account the various *failure modes*, such as cell reversal and short circuits, that can occur in individual cells. When a module shows other failure modes, re-use is no longer possible so these failures are classed as *catastrophic*. Detecting and distinguishing between failure modes can be technically challenging.

2.3 Electro-chemical processes

2.3.1 Internal impedance

Internal impedance or equivalent series resistance (ESR) is measured by comparing the voltage and current responses of the cell to an applied sinusoidal current or voltage around some DC bias point [26],

$$Z(f) = \frac{V_{\max}}{I_{\max}} e^{j\phi} \tag{2.8}$$

A complex impedance indicates that there is a capacitive or inductive component to the impedance. A complex impedance is expected due to the terminal connections and parallel plates within the cell. Cell impedance is commonly presented as a Nyquist diagram, plotting the real and imaginary components as a function of frequency. This is covered in more detail in Section 2.5.1.

ESR and open-circuit voltage can be used for state-of-charge estimation [27]. Various studies [1, 9, 19, 25, 26, 28–30] have quoted different relationships between cell internal resistance and other, indirect measures such as SOC. There is little agreement in the literature whether internal impedance measurement of the Toyota Prius battery modules will be a good indicator of state-of-health. Internal impedance measurement results are presented in Chapter 5.

2.3.2 Diffusion and polarisation

Both diffusion and polarisation chemical processes occur within a cell, contributing to the non-linear electrical behaviour shown in Figure 2.2 [29,31]. To represent these processes, resistances and capacitances (RC pairs), which need not be constant, can be added to a battery equivalent circuit. This nonlinear behaviour is caused by the electrolyte and the porous electrode material [17, 32]. Three major diffusive mechanisms have been identified: free electrolyte, porous electrode and electrode material, see Figure 2.3.

Figure 2.3 shows the three contributing factors to the nonlinear voltage response measured at the battery terminals [33]. The *first* diffusion effect is caused by differences in concentration throughout the free electrolyte material. The free electrolyte, not trapped in the porous electrode, can be either a gel mat or a liquid electrolyte as seen in older lead-acid batteries. Chemical diffusion within a fluid in a uniform micro-fluidic channel was investigated by Miyamoto [34]. Miyamoto uses Fick's second law of diffusion,

$$\frac{\partial C(x,t)}{\partial t} = D \frac{\partial^2 C(x,t)}{\partial x^2} \tag{2.9}$$

where $C(x,t)$ describes the spatiotemporal concentration of ions [mol·m^{-3}] and D is the diffusion coefficient [m$^2 \cdot$ s^{-1}]. This law assumes that the solute is diffusing down the concentration

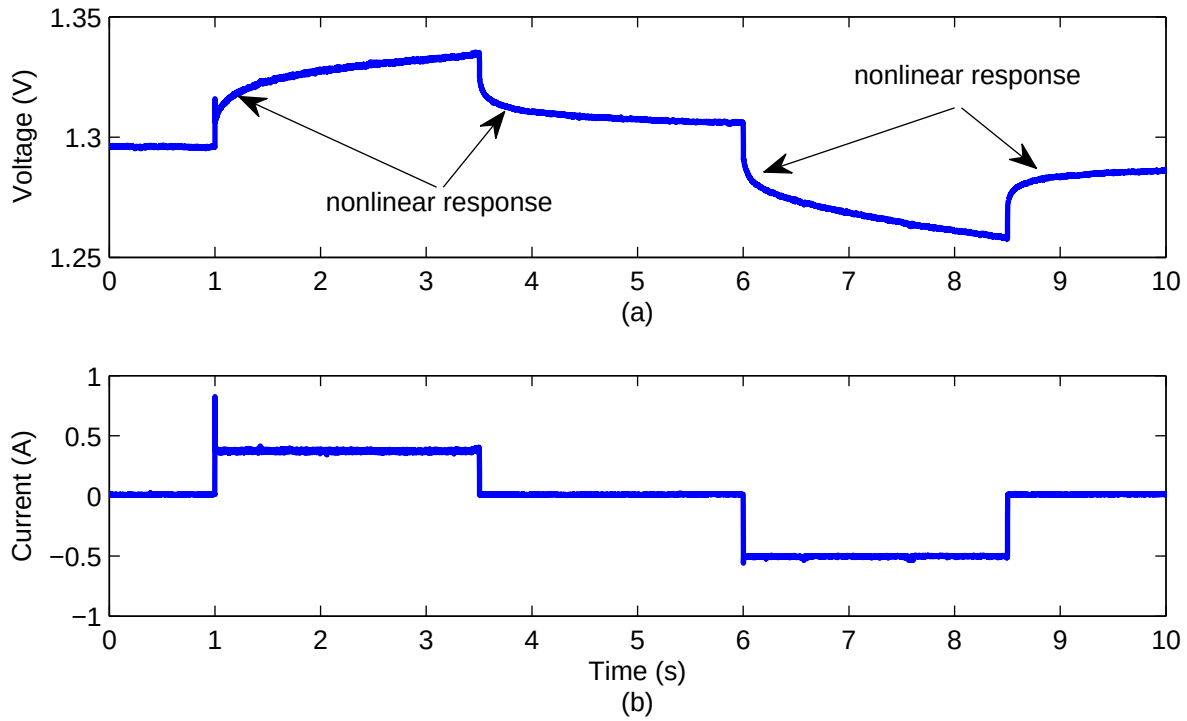

Figure 2.2: Nonlinear voltage response to square current pulse for single AA size NiMH cell (a) voltage, (b) current

gradient in one dimension. This matches Miyamoto's experiments as he was investigating diffusion of a solute along a tube. Fick's higher-order diffusion formulas [35] are more suited to

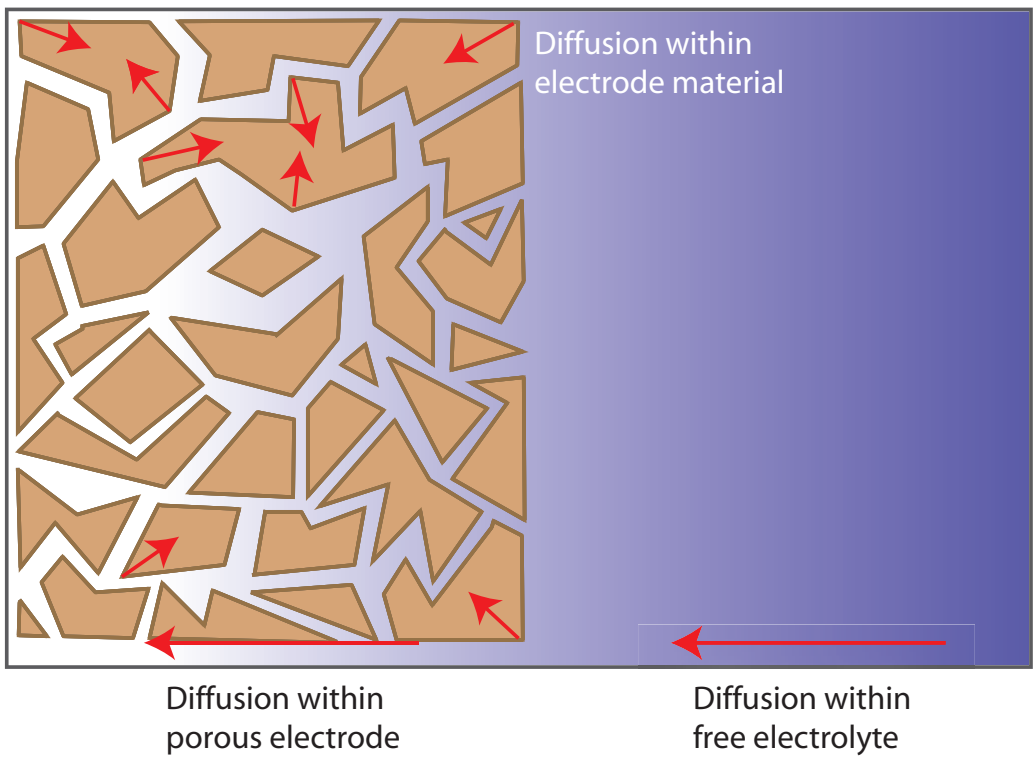

Figure 2.3: Cross-section of a porous electrode in electrolyte showing the three diffusion effects commonly seen within a battery. Diffusion occurs within free electrolyte, within the porous electrode and within the electrode material. Concentration is indicated by colour: darker blue represents higher concentration

the battery chemistry model as non-uniform cross-sections (Q) are being dealt with. One such higher-order model is,

$$\frac{\partial C(x,t)}{\partial t} = D\left(\frac{\partial^2 C(x,t)}{dx^2} + \frac{1}{Q}\frac{\partial Q}{\partial x}\frac{\partial C(x,t)}{\partial x}\right) \tag{2.10}$$

The *second* diffusion effect is the migration of the active electrolyte within the porous electrode. As the electrode grows, depending on the chemistry of the cell, the migration of active material from the electrode/electrolyte boundary is impeded, increasing the time-constant of the diffusion processes within the cell. The effective diffusion coefficient (D_e) for a porous material is described by [36],

$$D_e = \frac{D\epsilon_t\delta}{\tau} \tag{2.11}$$

where D is the diffusion coefficient in a free medium, ϵ_t is the porosity, δ is the constrictivity and τ is the tortuosity of the electrode. *Porosity* is the ratio of the volume of the voids (empty space) to total volume. *Constrictivity* is the ratio of particle diameter to pore diameter and describes the slowing down of diffusion due to increased viscosity in narrow pores. *Tortuosity*, mathematically, is the ratio of the length of the curve to the distance between the ends of the curve in 2-D. For an electrode, tortousity indicates the amount of exposed surface area. Both porosity and constricivity increase as the electrode material grows.

The *third* effect is diffusion within the electrode material determined by electron migration speeds. Good conductors such as gold or graphite electrodes will have a shorter diffusion time-constant. Equations (2.9) to (2.11) can be used to describe the diffusion of the active material within the free electrolyte (Eq. (2.9)) and within the porous electrode (Eq. (2.10)). Ohm's law, which is similar to Fick's first law [37], can now be applied to describe the diffusion within the electrode material. Comparing Ohm's law for current I,

$$I = \frac{V}{R} \tag{2.12}$$

with Fick's law for diffusive flow,

$$JA = D\frac{A}{L}C \tag{2.13}$$

where J is diffusion flux [$\mathrm{mol}\cdot\mathrm{m}^{-2}\cdot\mathrm{s}^{-1}$] and A is cross sectional area [m^2].

For Ohm's law current is measured in $\mathrm{C} \cdot \mathrm{s}^{-1}$, while diffusion flow is measured in $\mathrm{mol} \cdot \mathrm{s}^{-1}$. The driving force for Ohm's law is potential difference V [volts], and for Fick's law the driving force is the concentration C [$\mathrm{mol} \cdot \mathrm{m}^{-3}$]. The conductance of electricity is R^{-1} and of diffusing chemicals is DL^{-1} so, the "resistance" for diffusing chemicals is DL^{-1} which means that if the separation between the two plates (L) within a battery increases then the diffusion time-constant also increases [37]. Rewriting Ohm's law gives,

$$J = \sigma E \tag{2.14}$$

which relates the current density J to the electric field strength E by the conductivity of the material σ, confirming that materials or electrolyte with higher conductivity will have a shorter diffusion time-constant.

Figure 2.4 illustrates the charge separation that occurs at the boundary between electrolyte and electrode. The negatively-charged electrode attracts the positive ions suspended in the electrolyte and the positively-charged ends of the electrolyte material, resulting in a region of separated charges. This causes the cell to behave as a double-layer capacitor as a similar

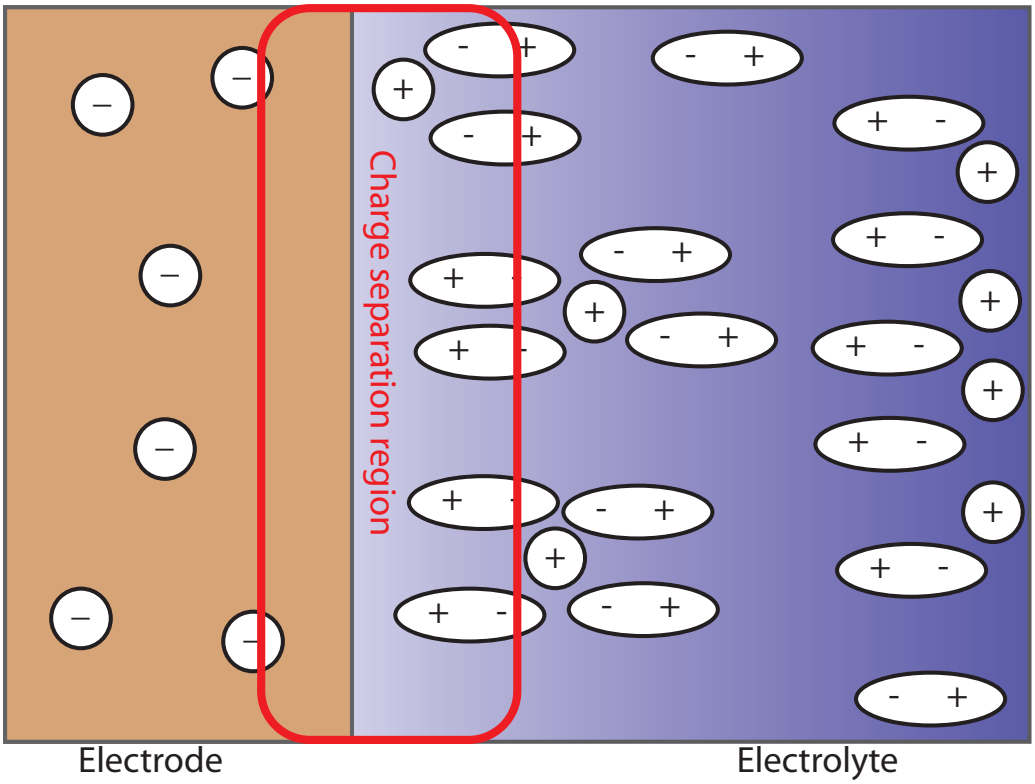

Figure 2.4: Charge separation region at the electrode/electrolyte boundary showing a negatively-charged electrode with positive ions suspended in a bipolar electrolyte with a higher concentration of positive ions further away from the electrolyte due to diffusion within the free electrolyte

interface is present on the other electrode surface [33]. The time-constant of this layered capacitance is shorter than that of diffusion because the electrons (or holes depending on which electrode is examined) are readily available at the battery cell terminals, and only obey Ohm's law. The time-constant resulting from this double-layer is referred to as the *polarisation* time-constant in this thesis.

When all of the active material has been removed from the electrolyte by reduction and oxidation (redox) reactions, the new charge separation region becomes the entire electrolyte, as seen in Figure 2.5. The voltage response from this effect is only seen at the start of discharge when the cell is fully charged, and also at the start of charging when the cell is fully discharged. The near instantaneous voltage drop, at the start of discharging, and voltage rise, at the start of charging, as seen in Figure 2.9, is due to this effect. Modelling this section of the battery characteristics is difficult as little information is available about battery behaviour at, and around, these points.

In the literature these nonlinear diffusion and polarisation effects are modelled in different ways. Most common is the addition of parallel resistor-capacitor (RC) pairs to the battery model as seen in [29], where the time-constants of the RC pairs are matched to the diffusion and polarisation time-constants; see Section 2.4 for further details.

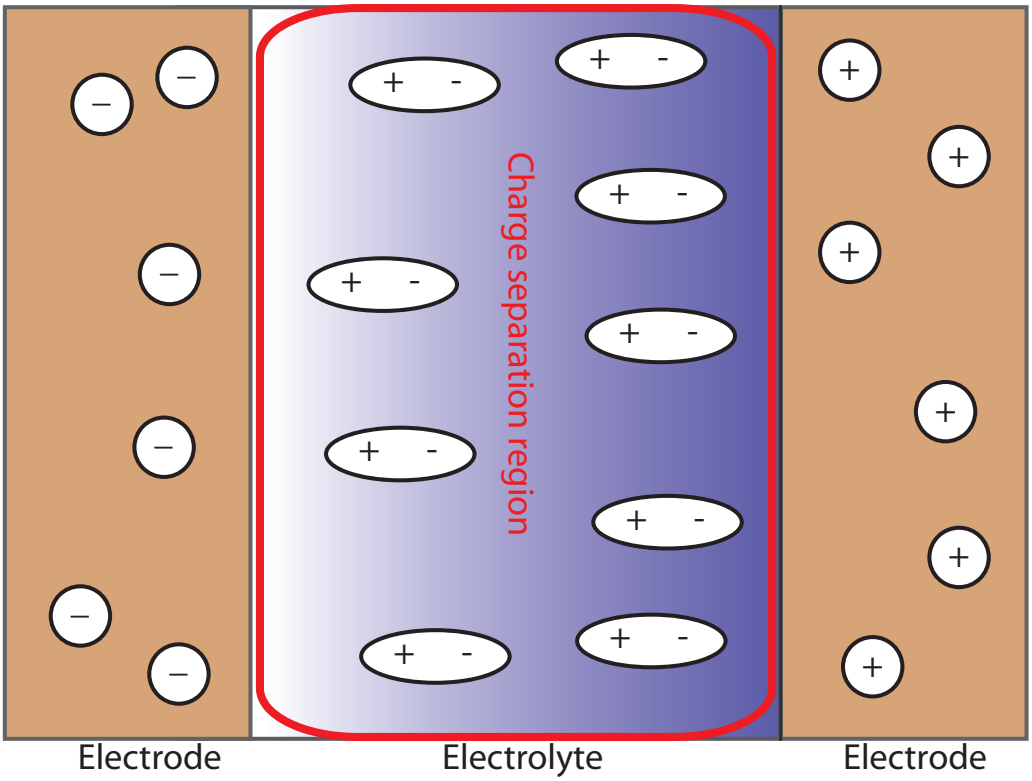

Figure 2.5: Charge separation region in a fully charged cell where no active material is left in the electrolyte

2.3.3 Warburg impedance

The Warburg impedance (Z_{W}) is added to a battery model to simulate the effects of diffusion within the battery electrolyte [33,38–40]. Greenleaf [38] writes the Warburg impedance voltage response (v_{W}) as an infinite summation of RC time constants,

$$v_{\mathrm{W}}(t) = \sum_{n=1}^{\infty} iR_{\mathrm{T}n}\left(1 - e^{-\frac{t}{R_{\mathrm{T}n}C_{\mathrm{T}n}}}\right) \tag{2.15}$$

where i represents the terminal current and $R_{\mathrm{T}n}C_{\mathrm{T}n}$ represents the n^{th} Thévenin resistor-capacitor combination. Greenleaf states that the infinite summation is impractical for battery modelling and simulation. Using impedance spectroscopy (see Section 2.5.1) one finds that addition of carefully selected RC pairs to the battery model simulates the low frequency impedance better. On a Nyquist plot, the locus of $\mathrm{Re}(Z_{\mathrm{W}})$ vs $\mathrm{Im}(Z_{\mathrm{W}})$, the real and imaginary parts of Warburg impedance, moves away from the origin at a 45° phase angle as excitation frequency decreases. This is confirmed in [33,38,39]. Jossen [33] likens a 45° phase-angle to a semi-infinite diffusion layer, corresponding to a planar electrode with infinite electrolyte reservoir.

An investigation by Karden [39] relates the Nyquist plot of battery impedance to charging current and present a dynamic impedance plot of the battery at different charging and discharging currents. Karden suggests that low frequency Warburg impedance effects reduce as the charging current increases, thus the summation of an infinite number of RC time constants can be replaced by only one or two RC pairs when DC bias current is flowing into the cell.

2.3.4 Temperature effects

Figure 2.6 shows simulation results for temperature variations within a NiMH cell during the charging process [17]. Cell temperature remains constant until the 100% state-of-charge point is reached. The temperature increase beyond this point has been attributed to the oxygen recombination reactions which occur during overcharge.

Detection of this temperature increase can be used as a charge-termination method [41]. Pascoe [42] presents thermal accumulation as one possible SOH indicator, however he concludes that this method has only low to medium reliability as the rise in temperature is small compared to the variation in SOH.

Battery voltage and capacity also vary with temperature. Kutluay [43] presents interesting data relating temperature with effective capacity of a sealed lead-acid battery. The data show

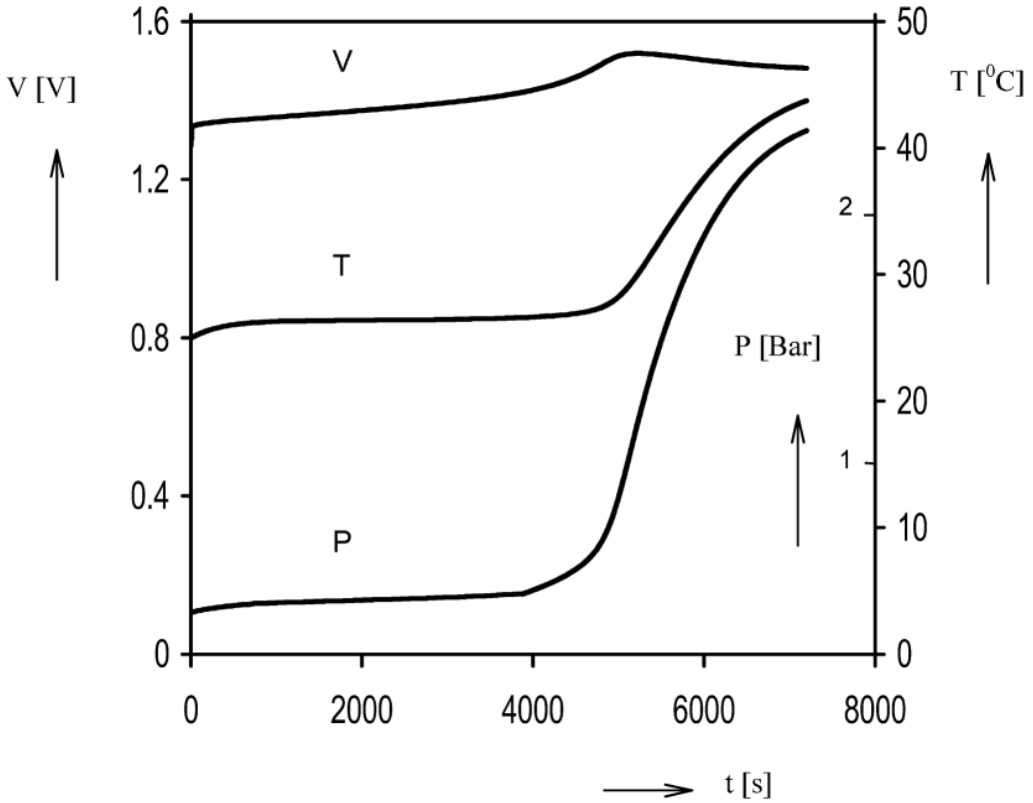

Figure 2.6: Simulation results from Ledovskikh et al. showing battery voltage, temperature and internal gas pressure during battery operation [17]

that a battery at 40°C is capable of delivering 104% of the energy that the same battery was capable of delivering at 20°C. Conversely, the battery at 5°C was capable of only delivering 88% of the energy. This relationship suggests that batteries at higher temperatures are capable of delivering more energy. A similar relationship between temperature and capacity is also presented in [44]. The researchers in [30] however present a set of data which suggests that the apparent capacity of a NiMH cell seems to peak at approximately 20°C and reduces at higher temperatures. Renhart et al [45] presents a normalisation function for battery useful capacity as a function of temperature showing that battery capacity drops to 50% when the temperature approaches −15°C, probably due to freezing of the electrolyte.

Hu et al. [11] investigated battery voltage variation with temperature by plotting discharge curves for a NiMH battery at different temperatures. Ledovskikh et al. [17] plot the variations in electrochemical potentials at the electrodes for two different temperatures which is difficult to achieve. There are significant variations in the relationships, between voltage and temperature, presented in the literature. A measurement of Toyota Prius battery module open-circuit voltage (OCV) variation with temperature is presented in Figure 2.7. The battery module was heated to 28°C and left to cool naturally, while the OCV was sampled. The MATLAB curve fitting toolbox was used to find a suitable relationship between temperature and OCV. The linear fit,

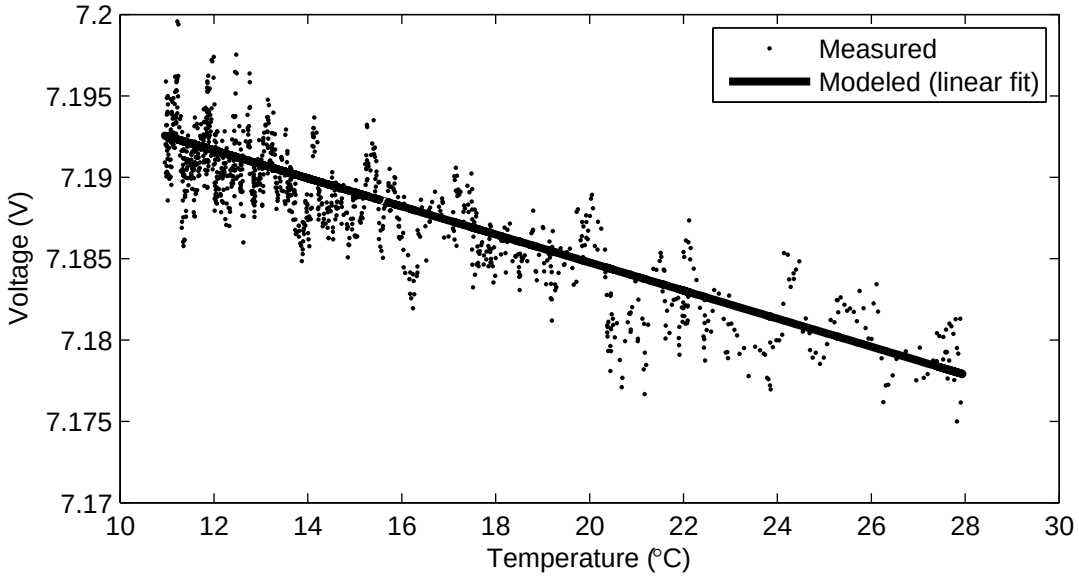

Figure 2.7: Measured Toyota Prius battery module open circuit voltage vs temperature with linear fit

$$v(T) = -0.86 \times 10^{-3} T + 7.2 \tag{2.16}$$

where T is temperature, is superimposed on the data in Figure 2.7. The relationship shows that there is a variation in OCV of 0.9 mV per degree. However, the RMS residual error of 2.1 mV suggests that measurement errors will tend to swamp the underlying temperature trend.

Naturally the internal impedance varies with temperature as well; the reader is pointed to [25] for further details.

2.4 Battery equivalent circuits and model descriptions

Accurate battery equivalent circuits and models are required to predict battery parameters such as SOC and SOH based on externally measurable quantities such as terminal voltage, current and temperature [1]. Various battery equivalents exist such as the Simple, Takacs, Thévenin and Bulk-Surface models [19,20,31]. These vary in complexity and relevance to different chemistries and cell construction. The following sections cover battery equivalent circuits and models found to be appropriate for this thesis.

2.4.1 Simple battery equivalent circuit

The simple battery circuit used by the ADVISOR battery library [1] consists of a voltage source (v_o) and a resistor (R_T) (see Figure 2.8), where v_o and R_T are defined as,

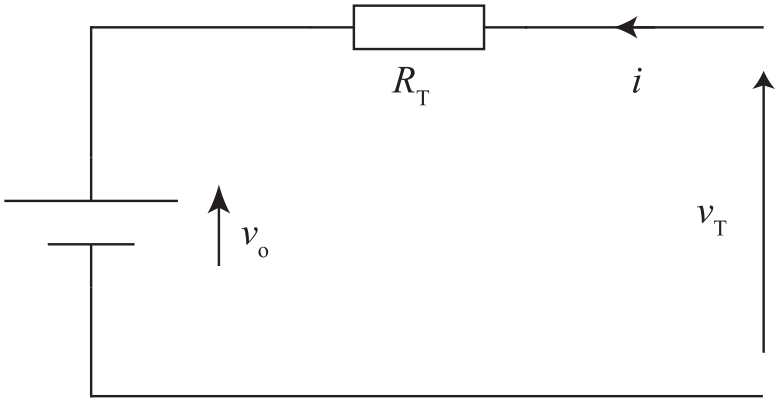

Figure 2.8: Simple battery equivalent circuit

$$v_o = f(\text{SOC}, T, \text{charge/discharge}) \tag{2.17}$$

$$R_T = \Delta v / i = f(\text{SOC}, T, \text{charge/discharge}) \tag{2.18}$$

The $f(\cdot)$ notation describes a function of the parameters included within the parenthesis, where SOC is state-of-charge, T is battery temperature and charge/discharge indicates the direction of the current. A similar equivalent circuit is also constructed in [46] where the authors utilise the single-state simplicity of the model to reduce computation times in their optimisation routines.

Representing the battery as a voltage source and series resistor means that this model is unable to accurately describe nonlinearities, such as the effects caused by diffusion and polarisation time-constants. A discussion on nonlinear effects with measurements will be presented in Chapter 5.

More complex battery equivalent circuits exist such as the two-capacitor bulk-surface model used in [1] and [31]. The models described are used for lead acid, Li-ion and NiMH cells. In [6], [47] and [48] more appropriate models are described. The equivalent circuit in [6] and [47] consists of a voltage source, four resistances and two capacitors and is used to find a relationship between OCV and SOC.

2.4.2 Takacs hysteresis model

The investigation in [6] led to a piecewise-linear relationship between OCV and SOC for a single NiMH cell,

$$\mathrm{SOC} = \begin{cases} a_1 v_\mathrm{T} + b_1 & 0 \leq \mathrm{SOC} < 0.1 \\ a_2 v_\mathrm{T} + b_2 & 0.1 \leq \mathrm{SOC} < 0.8 \\ a_3 v_\mathrm{T} + b_3 & 0.8 \leq \mathrm{SOC} \leq 1 \end{cases} \tag{2.19}$$

Shahriari [22] presents a linear relationship between OCV and SOC. Various researchers [6, 47, 48] suggest that finding a suitable model for a multi-cell pack, such as the Prius battery module, is difficult because of slight variations between the internal parameters of each cell. In [49] however a model is suggested for a multi-cell pack such as the batteries found in the Toyota HEV battery packs. The piecewise-linear relationship shown in Eq. (2.19) can be applied to a multi-cell module by adjusting the a_n and b_n coefficients.

The relationship between OCV and SOC is different during charge and discharges. This history dependence is referred to as the *hysteresis effect* [20,48], and requires an expansion of the relationships in Eq. (2.19) into the Takacs hysteresis model [20]. The mathematical description of hysteresis curves is a well known problem in many fields of engineering. Windarko et al [20] finds that the hysteresis curves for NiMH cells are similar to those found in magnetism. The hyperbolic tangents shown in Eq. (2.20) describe the ascending and descending branches of a hysteresis model [50],

$$\begin{aligned} f_+ &= \tanh(x - a_0) + b_1 \\ f_- &= \tanh(x + a_0) - b_1 \end{aligned} \tag{2.20}$$

Windarko et al [20] adds a polynomial function to these formulas to account for differences between the model and measured data.

State-of-charge was plotted against voltage for a Toyota Prius battery module, see Figure 2.9. These curves vary from those presented by Windarko [20], because he only tests a single cell whereas Fig. 2.9 shows the charge–discharge curves for six series-connected cells. Minor hysteresis loops are discussed in [50] and apply to the Toyota Prius battery model because during an ordinary operating cycle the battery pack SOC only cycles between 48% and 62%.

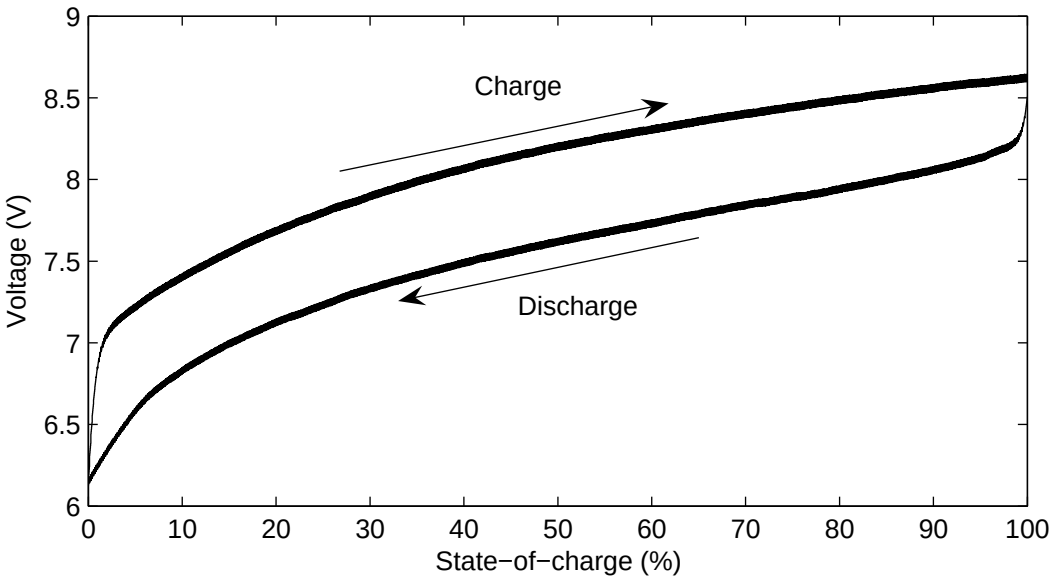

Figure 2.9: Toyota Prius battery module hysteresis curves under 4 Amp constant current charge and discharge at 15°C, repeat of figure 2.1 for completeness

2.4.3 Thévenin battery equivalent circuit (diffusion-polarisation model)

Most battery modelling papers discuss small signal behaviour. The most common battery equivalent circuit suggested in the literature [5–7,18,19,26,28,29,47–49,51–54] is the equivalent circuit shown in Figure 2.10. In [52] this equivalent circuit is also referred to as the diffusion-polarisation (DP) model.

The battery equivalent circuit shown in [6] can be simplified by ignoring self-discharge, giving the equivalent circuit shown in Figure 2.10. Self-discharge is modelled by a resistance R_S parrallel to v_o. The self-discharge rate of NiMH cells is very low; Guoliang [6] states that self-discharge only becomes relevant after leaving the cell idle for more than a week. Here, R_T is the DC internal resistance, R_D, C_D, R_P and C_P are electrochemical diffusion and concentration polarisation resistances and capacitances respectively [6, 18, 26, 28, 47, 52]. Schweighofer [47] quotes values in Table 2.1 for a single NiMH cell, and he has found that these parameters remain constant with different applied discharge pulses.

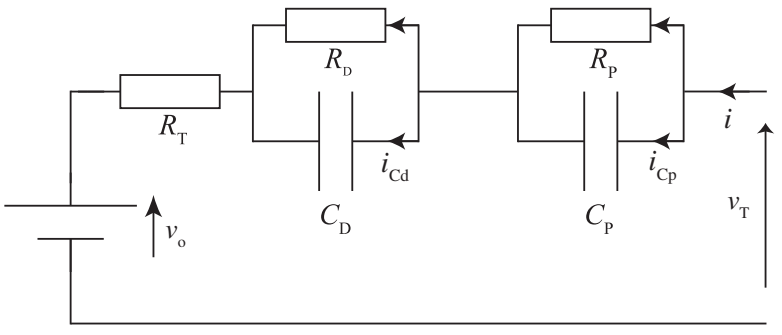

Figure 2.10: Thévenin battery equivalent circuit

Table 2.1: Thévenin equivalent circuit parameters of NiMH cell as suggested in [47]

Parameter	Value
R_{T}	1 mΩ
R_{D}	0.35 mΩ
C_{D}	171 F
R_{P}	1.6 mΩ
C_{P}	16 kF

Serrao et al [49] states that these circuit parameters vary with SOC, SOH and temperature. These relationships, in particular the relationship with respect to SOH, will be investigated in later chapters.

A series of fundamental equations can be made to describe the behaviour of the battery circuit in Figure 2.10. Here the assumption is that all currents and voltages are time-dependent, except v_{o}. We are also going to define v_{D}, v_{P} and v_{R} as the voltages across C_{D}, C_{P} and R_{T} respectively. Applying Ohm's law and writing expressions for capacitive displacement currents ($i = C\frac{dv}{dt}$), we obtain,

$$v_{\mathrm{R}} = iR_{\mathrm{T}} \tag{2.21}$$

$$v_{\mathrm{D}} = (i - i_{\mathrm{Cd}})R_{\mathrm{D}} \qquad \text{and} \qquad i_{\mathrm{Cd}} = C_{\mathrm{D}}\frac{dv_{\mathrm{D}}}{dt} \tag{2.22}$$

similarly,

$$v_{\mathrm{P}} = (i - i_{\mathrm{Cp}})R_{\mathrm{P}} \qquad \text{and} \qquad i_{\mathrm{Cp}} = C_{\mathrm{P}}\frac{dv_{\mathrm{P}}}{dt} \tag{2.23}$$

Equations (2.22) and (2.23) can be rearranged to form differential equations describing the battery circuit,

$$\frac{dv_{\mathrm{D}}}{dt} = \frac{1}{C_{\mathrm{D}}}i_{\mathrm{Cd}} = \frac{1}{C_{\mathrm{D}}}\left(i - \frac{v_{\mathrm{D}}}{R_{\mathrm{D}}}\right) \tag{2.24}$$

$$\frac{dv_{\mathrm{P}}}{dt} = \frac{1}{C_{\mathrm{P}}}i_{\mathrm{Cp}} = \frac{1}{C_{\mathrm{P}}}\left(i - \frac{v_{\mathrm{P}}}{R_{\mathrm{P}}}\right) \tag{2.25}$$

We can now formulate a state-variable equation,

$$\frac{d}{dt}\begin{bmatrix} v_{\mathrm{D}} \\ \\ v_{\mathrm{P}} \end{bmatrix} = \begin{bmatrix} \frac{-1}{C_{\mathrm{D}}R_{\mathrm{D}}} & 0 \\ \\ 0 & \frac{-1}{C_{\mathrm{P}}R_{\mathrm{P}}} \end{bmatrix}\begin{bmatrix} v_{\mathrm{D}} \\ \\ v_{\mathrm{P}} \end{bmatrix} + \begin{bmatrix} \frac{1}{C_{\mathrm{D}}} \\ \\ \frac{1}{C_{\mathrm{P}}} \end{bmatrix} i \tag{2.26}$$

The sum the individual voltages gives the terminal voltage,

$$v_{\mathrm{T}} = v_{\mathrm{o}} + v_{\mathrm{R}} + v_{\mathrm{D}} + v_{\mathrm{P}} \tag{2.27}$$

Realistically v_{o} also changes with time and can be modelled by a relationship such as the Takacs model for OCV vs SOC. Some researchers replaced this fixed voltage source with a capacitor (C_{o}) [44, 55–57]. The v_{o} term in Eq. (2.27) can then be replaced with $\frac{i}{C_{\mathrm{o}}}t$ i.e., the voltage across the capacitor C_{o}. Although this creates a more realistic relationship between v_{T} and i it still does not account for the sharp drop-off in voltage seen in Figure 2.9 as the battery nears the 5% and 95% SOC endpoints.

2.4.4 Bulk-surface equivalent circuit

Bhangu [31] investigates the bulk-surface capacitor equivalent circuit of Figure 2.11. The battery equivalent circuit now consists of two series *RC* pairs as opposed to the two parallel *RC* pairs of Fig. 2.10. In Bhangu's model, the two capacitors represent a bulk-capacitance and a surface-capacitance, with the former being taken as a predictor of battery state-of-health. An extended Kalman filter is applied to the data in [31] to continuously adjust the circuit parameters by comparison against actual measurements, resulting in an online SOH diagnostic tool.

Bhangu presents a set of equations describing the circuit in Fig. 2.11 [31]. These equations are presented below; state-variable equations are constructed for implementation in MATLAB simulation software. Bhangu also presents an initial set of values for his circuit, these values are listed in Table 2.2. To correctly describe this circuit we need to build equations for the two

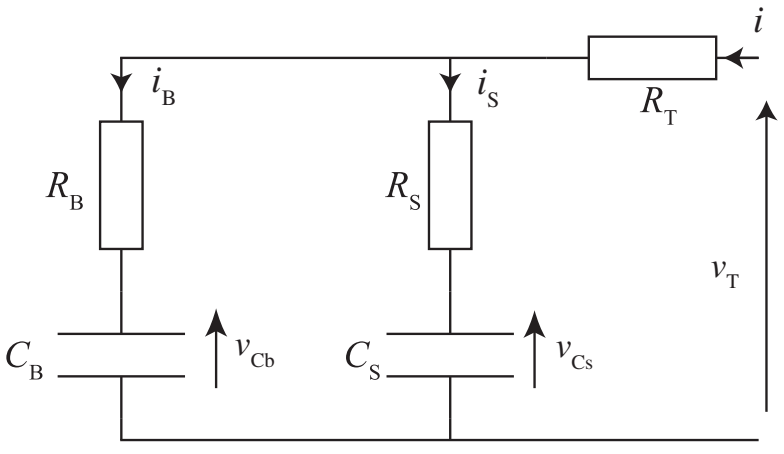

Figure 2.11: Bulk-surface equivalent circuit [31].

Table 2.2: Bulk-surface equivalent circuit parameters for a lead-acid cell suggested in [31]

Parameter	Value
R_{T}	2.745 mΩ
R_{B}	3.75 mΩ
C_{B}	88372.83 F
R_{S}	3.75 mΩ
C_{S}	82.11 F

parallel RC pairs respectively. The loop equations through the C_{B} and C_{S} capacitances are given by,

$$v_{\mathrm{T}} = iR_{\mathrm{T}} + i_{\mathrm{B}}R_{\mathrm{B}} + v_{\mathrm{Cb}}, \tag{2.28}$$

$$v_{\mathrm{T}} = iR_{\mathrm{T}} + i_{\mathrm{S}}R_{\mathrm{S}} + v_{\mathrm{Cs}} \tag{2.29}$$

with capacitive displacement currents

$$i_{\mathrm{B}} = C_{\mathrm{B}}\frac{dv_{\mathrm{Cb}}}{dt} \qquad \text{and} \qquad i_{\mathrm{S}} = C_{\mathrm{S}}\frac{dv_{\mathrm{Cs}}}{dt} \tag{2.30}$$

which sum to give the terminal current,

$$i = i_{\mathrm{B}} + i_{\mathrm{S}} \tag{2.31}$$

Eliminating i_{B} and i_{S} from Eqs. (2.28) and (2.29), we obtain,

$$\frac{dv_{\mathrm{Cb}}}{dt} = -\frac{v_{\mathrm{Cb}}}{C_{\mathrm{B}}(R_{\mathrm{B}}+R_{\mathrm{S}})} + \frac{v_{\mathrm{Cs}}}{C_{\mathrm{B}}(R_{\mathrm{B}}+R_{\mathrm{S}})} + \frac{iR_{\mathrm{S}}}{C_{\mathrm{B}}(R_{\mathrm{B}}+R_{\mathrm{S}})}, \tag{2.32}$$

and

$$\frac{dv_{\mathrm{Cs}}}{dt} = -\frac{v_{\mathrm{Cs}}}{C_{\mathrm{S}}(R_{\mathrm{B}}+R_{\mathrm{S}})} + \frac{v_{\mathrm{Cb}}}{C_{\mathrm{S}}(R_{\mathrm{B}}+R_{\mathrm{S}})} + \frac{iR_{\mathrm{B}}}{C_{\mathrm{S}}(R_{\mathrm{B}}+R_{\mathrm{S}})}. \tag{2.33}$$

leading to the state-variable equation,

$$\frac{d}{dt}\begin{bmatrix} v_{\mathrm{Cb}} \\ v_{\mathrm{Cs}} \end{bmatrix} = \begin{bmatrix} \frac{-1}{C_{\mathrm{B}}(R_{\mathrm{B}}+R_{\mathrm{S}})} & \frac{1}{C_{\mathrm{B}}(R_{\mathrm{B}}+R_{\mathrm{S}})} \\ \frac{1}{C_{\mathrm{S}}(R_{\mathrm{B}}+R_{\mathrm{S}})} & \frac{-1}{C_{\mathrm{S}}(R_{\mathrm{B}}+R_{\mathrm{S}})} \end{bmatrix} \begin{bmatrix} v_{\mathrm{Cb}} \\ v_{\mathrm{Cs}} \end{bmatrix} + \begin{bmatrix} \frac{R_{\mathrm{S}}}{C_{\mathrm{B}}(R_{\mathrm{B}}+R_{\mathrm{S}})} \\ \frac{R_{\mathrm{B}}}{C_{\mathrm{S}}(R_{\mathrm{B}}+R_{\mathrm{S}})} \end{bmatrix} i \tag{2.34}$$

From Eqs. (2.28) and (2.29) we can write the terminal voltage as,

$$v_{\mathrm{T}} = \begin{bmatrix} \frac{R_{\mathrm{S}}}{R_{\mathrm{B}}+R_{\mathrm{S}}} & \frac{R_{\mathrm{B}}}{R_{\mathrm{B}}+R_{\mathrm{S}}} \end{bmatrix} \begin{bmatrix} v_{\mathrm{Cb}} \\ \\ v_{\mathrm{Cs}} \end{bmatrix} + \begin{bmatrix} R_{\mathrm{T}} + \frac{R_{\mathrm{B}}R_{\mathrm{S}}}{R_{\mathrm{B}}+R_{\mathrm{S}}} \end{bmatrix} i \tag{2.35}$$

2.4.5 Energy throughput model

The energy throughput model is based on the assumption that a battery can handle a certain amount of terminal power over time before it reaches end-of-life [58]. State-of-charge is described in [58] by the following equation,

$$x_2(t) = x_{2,0} - \frac{1}{2NQ_0(0)} \int_0^t |P_{\mathrm{i}}(\tau)| d\tau \tag{2.36}$$

where $0 \leq x_2(t) \leq 1$ represents SOH, $x_{2,0} = 1$, the initial SOH, Q_0 is initial energy capacity, N is number of cycles before end-of-life and P_i is the power measured at the battery terminal. The following Arrhenius relationship describes SOH loss ΔQ_0 with-respect-to energy throughput,

$$\Delta Q_0 = B(c)\exp\left(\frac{-E_a(c)}{RT}\right) A(c)^z \tag{2.37}$$

where R is the gas constant, T is the absolute temperature, E_a is the activation energy in joules, $A(c)$ is the total throughput (in ampere-hour) as a function of c, $B(c)$ is a pre-exponential factor (also a function of c) where c is the c-rate of the battery and z is some exponential constant. Equation (2.37) was fitted to measured data in [58–60] to evaluate the constants. Equation (2.38) is derived in [58] by algebraically rearranging equations (2.36) and (2.37) and using $c = P_{\mathrm{i}}/Q_0$ as a linear transformation,

$$\frac{dx_2}{dt} = -\frac{|P_{\mathrm{i}}(t)|}{2N(|P_{\mathrm{i}}(t)|)Q_0(0)} \tag{2.38}$$

This equation shows that the time-derivative of x_2, capacity fading, is directly related to battery power $P_{\mathrm{i}}(t)$, where $P_i(t) = V_{\mathrm{oc}}I_{\mathrm{b}}(t)$. To optimise the battery lifetime we want to minimise Eq. (2.38) i.e., the rate-of-change in SOH is minimal. Unfortunately historic battery data (current and voltage) are not stored by the Toyota BMS so this method of tracking SOH would require continuous monitoring of battery terminal power and is therefore not suitable as an off-line diagnostic.

2.5 Measurement methods through equivalent circuit and model applications

2.5.1 Impedance spectroscopy

Nyquist plots are used to show how the impedance (or response) of a system changes with frequency [19,61]. Using the Thévenin battery equivalent circuit we can formulate equations to calculate the Nyquist plot for this particular battery circuit. For the equivalent circuit in Fig. 2.10 the battery impedance (Z) is the sum of the individual impedances,

$$Z = R_{\mathrm{T}} + Z_{\mathrm{D}} + Z_{\mathrm{P}} \tag{2.39}$$

where,

$$Z_{\mathrm{D}} = \frac{R_{\mathrm{D}} Z_{C_{\mathrm{D}}}}{R_{\mathrm{D}} + Z_{C_{\mathrm{D}}}} \qquad \text{and} \qquad Z_{\mathrm{P}} = \frac{R_{\mathrm{P}} Z_{C_{\mathrm{P}}}}{R_{\mathrm{P}} + Z_{C_{\mathrm{P}}}} \tag{2.40}$$

It must be noted that the voltage source is "shorted" to calculate the Thévenin impedance. Similarly the corresponding equations for the bulk-surface equivalent circuit of Fig. 2.11, are

$$Z = R_{\mathrm{T}} + \frac{Z_{\mathrm{B}} Z_{\mathrm{S}}}{Z_{\mathrm{B}} + Z_{\mathrm{S}}}, \tag{2.41}$$

where,

$$Z_{\mathrm{B}} = R_{\mathrm{B}} + Z_{C_{\mathrm{B}}} \qquad \text{and} \qquad Z_{\mathrm{S}} = R_{\mathrm{S}} + Z_{C_{\mathrm{S}}} \tag{2.42}$$

These formulas were implemented in MATLAB to produce Figures 2.12, 2.13 and 2.14.

Figure 2.12 shows a decomposition of the individual components of the Thévenin battery circuit as a function of frequency. The graphs show that the magnitude of the imaginary component of the impedance decreases as the frequency decreases below the lowest resonant frequency peak. This is contradictory to what the Warburg impedance theory tells us. The 45° phase angle suggested by Warburg's impedance would indicate that both real and imaginary components of the cell impedance should increase as frequency decreases. If however multiple, or an infinite sum as suggested by Greenleaf [38], resonant peaks are stacked appropriately placed in the low frequency area of these curves then the electrical circuit model can be made to appear to behave like a Warburg impedance. Kuhn et al. [40] present an interesting paper which shows data relating measured NiMH impedance plots to impedance plots produced with a Thévenin equivalent circuit. The paper presents modelled data with multiple RC pairs and

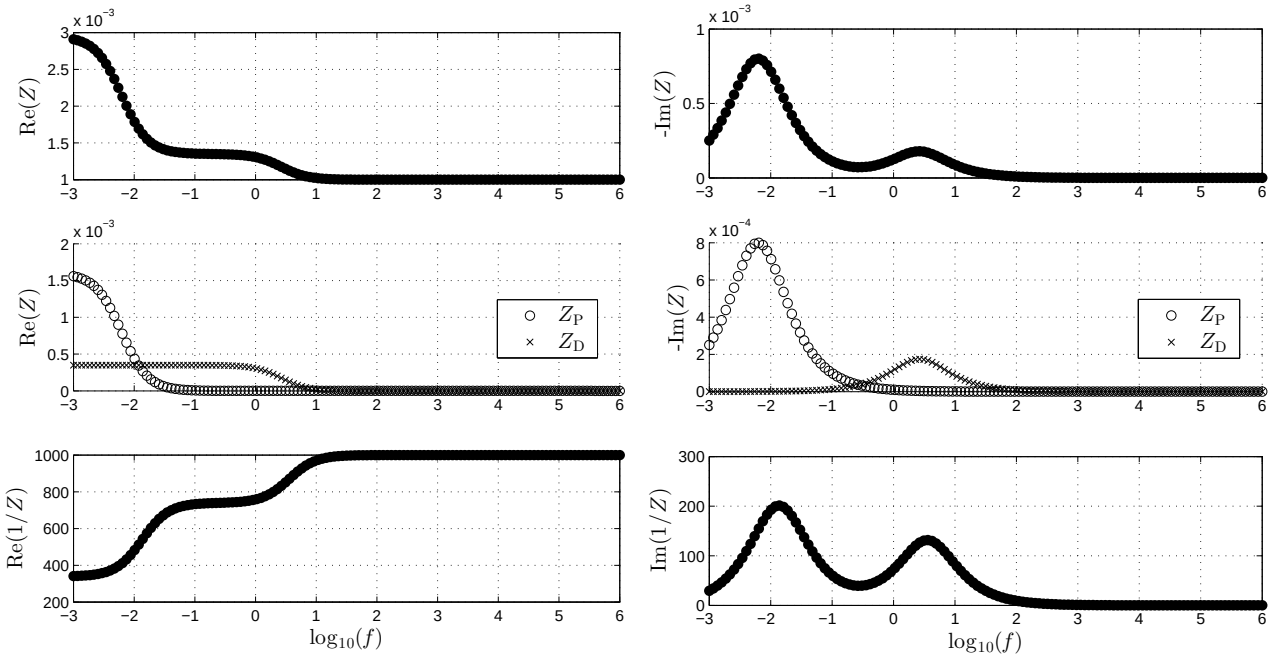

(a) (b)

Figure 2.12: Thévenin battery equivalent circuit plots of (a) real part of the impedance and (b) imaginary part of the impedance for a frequency range between 1 mHz and 1 MHz

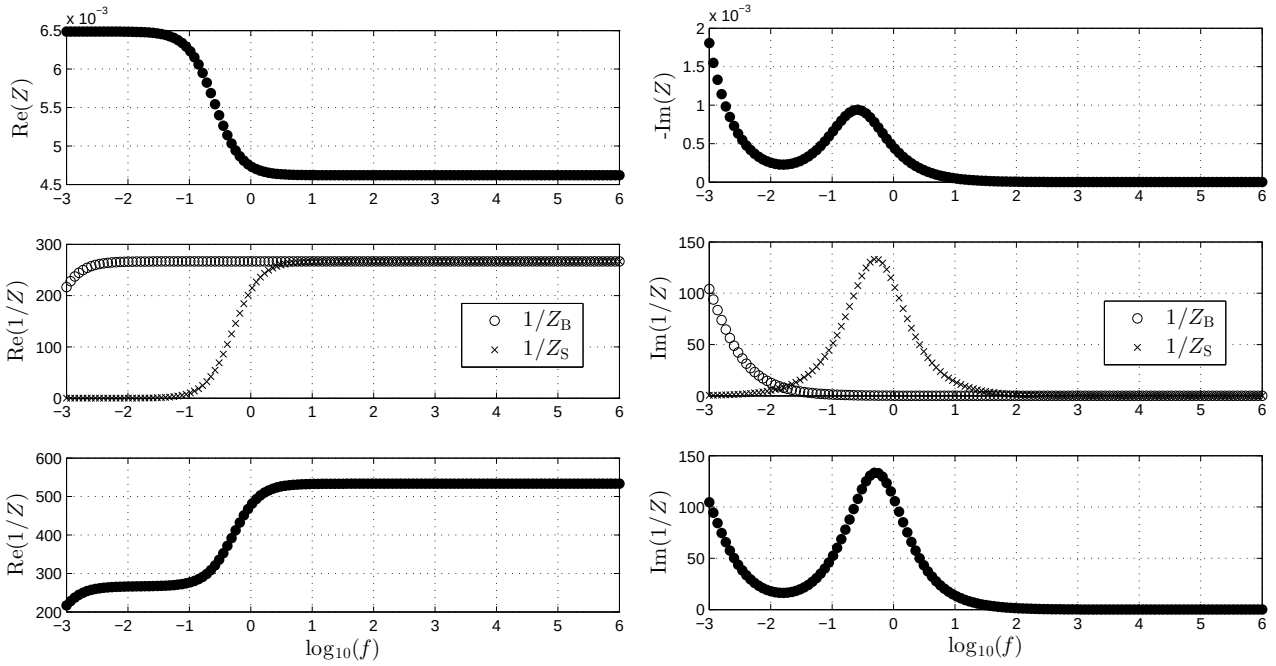

(a) (b)

Figure 2.13: Bulk-surface battery model plots of (a) real part of the impedance and (b) imaginary part of the impedance for a frequency range between 1 mHz and 1 MHz

investigates the error decrease as more *RC* pairs are used. Kuhn states that four *RC* pairs gave the best trade-off between equivalent circuit accuracy and computational complexity.

Figure 2.13 shows the decomposition of the individual impedance components for the bulk-surface battery equivalent circuit. The figure shows that the bulk-capacitor contributes to an increasing overall impedance value as the excitation frequency decreases, more closely modelling

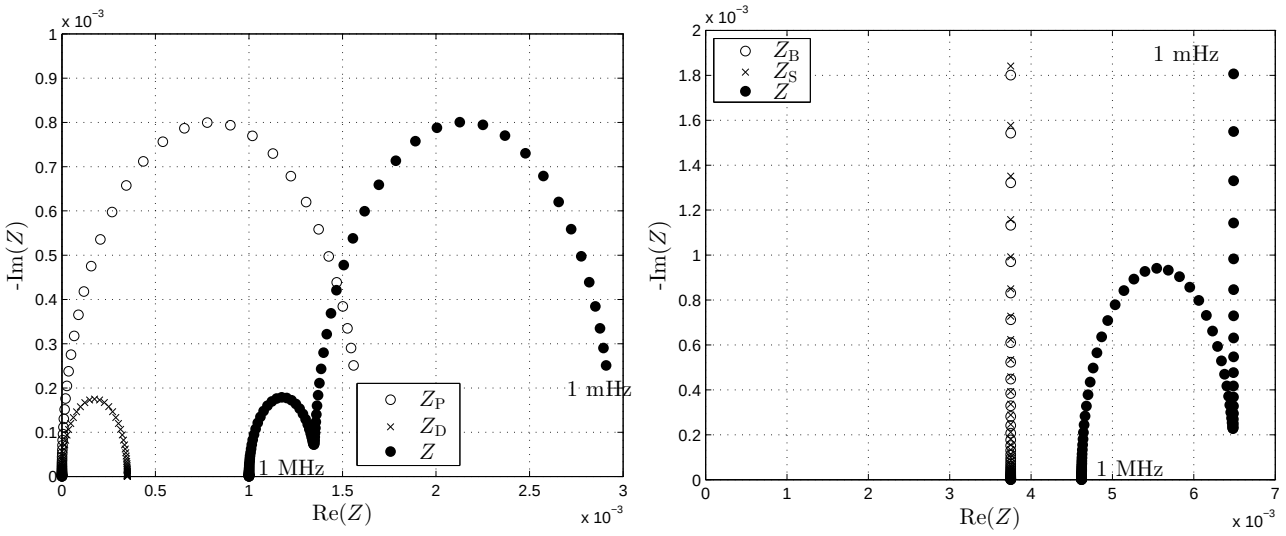

Figure 2.14: Nyquist plots of (a) Thévenin battery model and (b) bulk-surface model for a frequency range between 1 mHz and 1 MHz showing the contributions from the individual components

the Warburg impedance, but this could also be the rising edge of another resonant peak. However, the real component of the impedance remains constant as the frequency decreases, contradicting Z_{W}.

Figure 2.14(a) shows the Nyquist plot for the Thévenin battery equivalent circuit using the component values presented in Table 2.1; similarly Figure 2.14(b) shows the Nyquist plot for the bulk-surface equivalent circuit using the component values from Table 2.2. The Nyquist plots show that both models produce a similarly shaped curve in the high frequency region with the only differences between the two being the component values. However, the curves deviate significantly towards the lower frequencies.

Bhangu [31] identifies the bulk capacitance (C_{B}) as the primary SOH indicator. The Nyquist plot in Figure 2.14(b) shows that the impedances of the bulk and of the surface capacitances form a vertical line in the -Im(Z) plane intersecting the real axis at R_{B} and R_{S} respectively but from Table 2.2, $R_{\mathrm{S}} = R_{\mathrm{B}}$, so we cannot distinguish. Hence, calculating the bulk capacitance from the Nyquist plot can prove difficult. However, Huet [26] writes a compelling paper which argues that impedance spectrography is a useful tool for identifying battery failure, which is investigated in Chapter 5. He asserts that most authors consider discharge testing as the only accurate method for determining SOH.

In practical applications, impedance spectroscopy measures the voltage or current response of the battery when excited by a small-signal current or voltage around some DC bias current

or voltage, as discussed in Section 2.3.1. Some results obtained from Toyota Prius battery modules are presented in Section 5.1.

2.5.2 Kalman and extended Kalman filtering

Kalman filters and extended Kalman filters have also been used extensively in the field of battery parameter measurement [57, 62–73]. A Kalman filter is a recursive approximation method for modelling nonlinear systems whose state variables are periodically updated using actual measurements. Andre [62] presents a summary of Kalman theory.

The system equations must be expressed in state-space form (e.g. eqs (2.26) and (2.34)). These can be generalised as,

$$\dot{x}(t) = \mathbf{A}x(t) + \mathbf{B}u(t) \tag{2.43}$$

$$y'(t) = \mathbf{C}x(t) + \mathbf{D}u(t) \tag{2.44}$$

where $x(t)$ is the time-dependent state variable, $\mathbf{A}$ through to $\mathbf{D}$ are system matrices, $u(t)$ is some time-dependent input, and $y'(t)$ is the predicted measured quantity. For the battery model, $u(t)$ is battery current and $y'(t)$ is recovered terminal voltage and $y(t)$ is the physically measured terminal voltage.

The filter now becomes a two-step process. Step one is the prediction of the state of the system at time step $k + 1$, and step two is the correction. During the correction phase the Kalman gain, the state estimates and the error covariance are updated [70]. The error of estimation is calculated by taking the difference between the predicted ($y'(t)$) and measured ($y(t)$) quantity. The covariance of the mismatch error is calculated and minimized at every step, by adjusting the state-variable ($x(t)$).

The Kalman filter can be extended to nonlinear applications through a first-order Taylor expansion. Barbarisi [63] uses the extended Kalman filter (EKF) with an electrochemical model generating a state-space model of the battery from Fick's diffusion laws. The EKF is used to calculate SOC which is obtained by averaging the concentration of active material within the battery cell. The extended Kalman filtering approach can also be applied to the equivalent circuits described above in Sections 2.4.3 and 2.4.4 to track changes in the values of battery circuit components. Andre et al. [62] presents an EKF approach for finding the internal parameter value of R_{T} from the diffusion-polarisation (DP) battery model (Fig. 2.10). This

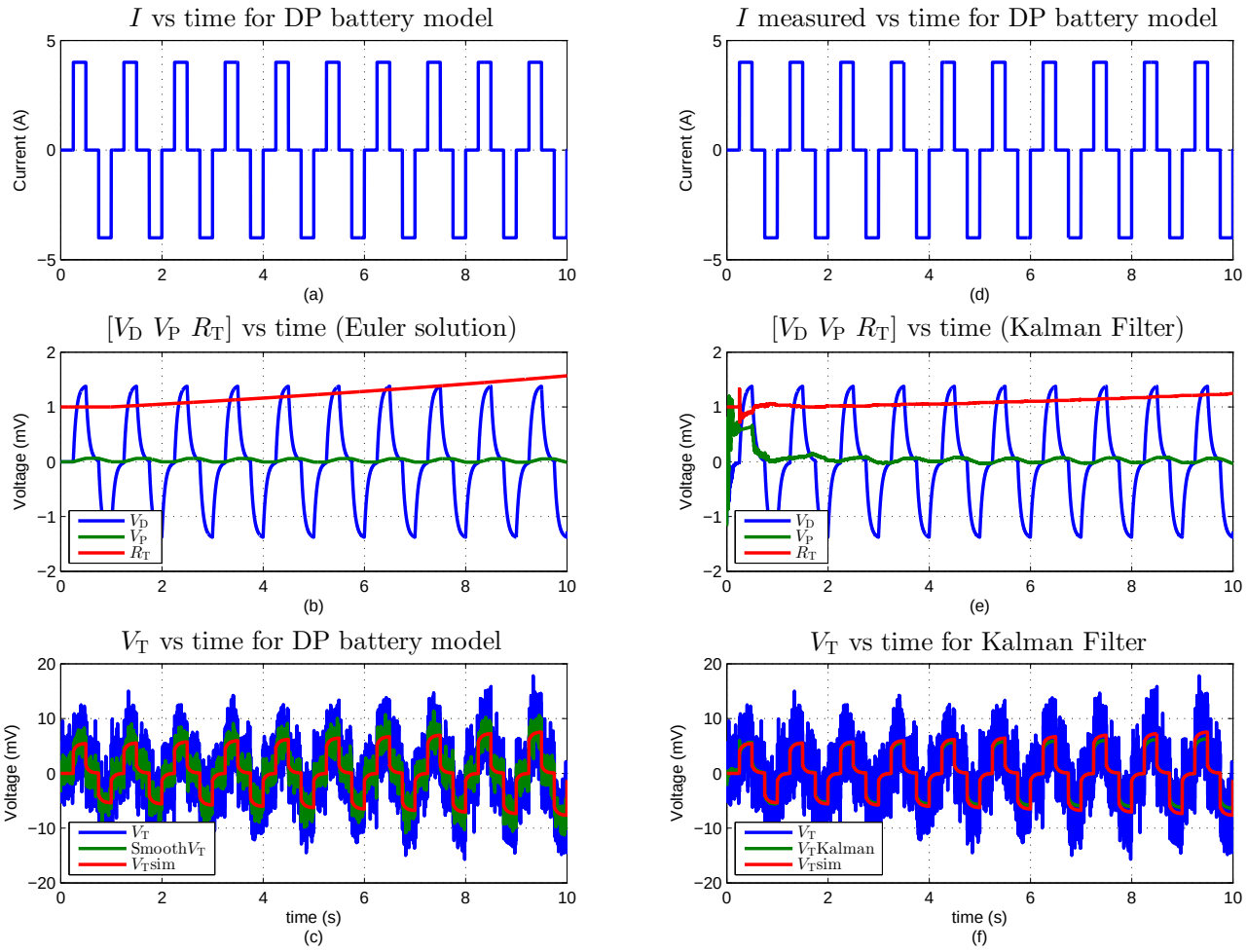

Figure 2.15: Extended Kalman filtering approach to estimating internal battery parameter R_T [62]

highlights that Kalman filtering can be applied to selected nonlinear systems provided that appropriate state-space equations can be formulated.

Figure 2.15 shows the results of the extended Kalman filter implementation. Figures 2.15(a) to (c) show the solution to the differential equations with an artificially ramped R_T value simulates an ageing battery. Figure 2.15(c) shows the simulation results for the terminal voltage variations around v_o (v_T sim), the measured voltage v_T and the standard MATLAB `smooth` command, which implements a moving average filter where span = 5, to filter the noise from the signal. This figure shows that even after the `smooth` command is applied there is still a large variation between the filtered measurement and v_T.

Figure 2.15(e) shows the extended Kalman filtering state variables and shows how the resistance R_T tracks up following the simulated ageing of the battery. Figure 2.15(f) shows how the actual battery voltage (v_T), the terminal voltage recovered from the Kalman Filtering (v_T Kalman) and the simulated terminal voltage (v_T sim) compare.

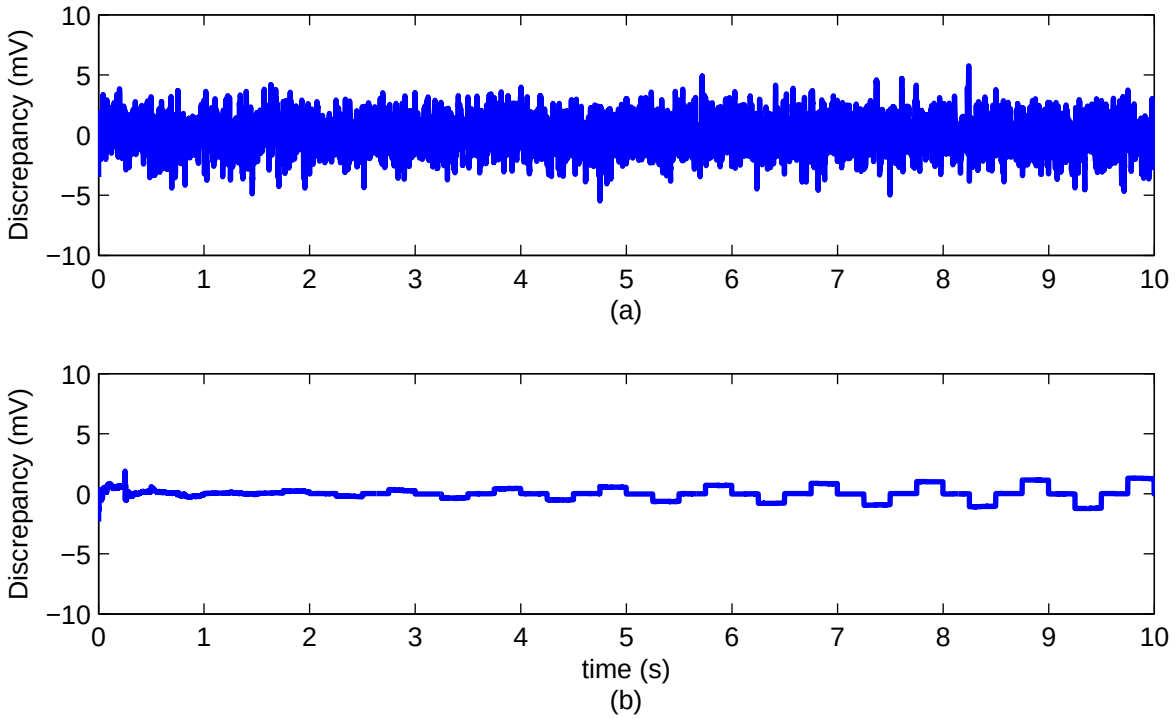

Figure 2.16: Discrepancy between (a) simulated terminal voltage and smoothed measured voltage and (b) terminal voltage and terminal voltage recovered using EKF

Figure 2.16 shows that the Kalman filter recovers the actual voltage better than the smoothing function; however, due to the changing internal resistance there is still some error in the filtered voltage. This error can be corrected by tuning the appropriate filter noise parameters as shown in Section 5.2.

A modification of the Kalman filter to an extended Kalman filter also allows the filtering technique to track changes in the internal parameters of the battery model from a noisy measurement. Applying this technique to NiMH battery voltage-response curves can identify an ageing cell, however the accuracy is limited and the simulation is very susceptible to noise.

2.6 Mapping circuits: Star-delta transformation

Section 2.5.1 shows that the bulk-surface and Thévenin equivalent circuits are unable to correctly show the effects of the Warburg impedance. Multiple papers mention the addition of more RC pairs as a suitable way of making the equivalent circuit show Warburg impedance effects with model complexity as a trade-off. The Thévenin equivalent circuit is better at describing small signal behaviour of the cell, whereas the bulk-surface equivalent circuit is better at describing the bulk behaviour of the cell. The latter is relevant for measuring SOH of battery modules.

A star-delta transformation can be applied to the DP equivalent circuit by removing the diffusion RC pair and mapping the component values onto its bulk-surface equivalent. Gould et al [57] shows the results of the mapping, please refer to the paper for the circuit drawings. The adapted formulas from [57], to match the circuit parameters shown in Figures 2.10 and 2.11, are

$$C_{\mathrm{S}} \approx \frac{C_{\mathrm{o}}^2}{(C_{\mathrm{o}} + C_{\mathrm{D}})} \tag{2.45}$$

$$C_{\mathrm{B}} \approx \frac{C_{\mathrm{o}} C_{\mathrm{D}}}{(C_{\mathrm{o}} + C_{\mathrm{D}})} \tag{2.46}$$

$$R_{\mathrm{S}} \approx \frac{R_{\mathrm{T}}(C_{\mathrm{o}} + C_{\mathrm{D}})^2}{C_{\mathrm{o}}^2} \tag{2.47}$$

where v_{o} in Figure 2.10 is replaced by a capacitor C_{o}.

In [57] a parallel resistance for self-discharge is also included, but for simplicity this resistance has been ignored here. Gould et al also do not include resistance R_{B} in their equivalent circuit, the assumption being that this resistance is included in R_{T}. The bulk characteristics of the battery can now be estimated by way of mapping the results obtained from small signal response data. But the small signal Thévenin battery model is a poor model for the Toyota Prius battery modules, highlighted in Section 5.3.

2.7 Chapter summary

In this chapter the NiMH battery has been explained in terms of electro-chemistry, equivalent circuits and models. Five battery models have been presented and their mathematics explained. It is clear from this chapter that there are a multitude of battery models appropriate to different situations. The bulk-surface equivalent circuit has been identified for describing a relationship between the internal bulk-capacitance C_{B} and battery SOH.

Chapter 3

Supercapacitor based energy transfer instrumentation

3.1 Desired outcomes

Efficient DC-DC voltage conversion is desired to charge and discharge the battery blocks during the analysis process. In order to waste as little energy as possible, energy is cycled through supercapacitors (as temporary storage) into a different battery under test. The design used in [2] uses variable linear power supply chips to provide and regulate the charging current. This design uses SMPS to increase efficiency. The battery modules are analysed by subjecting the cells to a charge-discharge cycle, whereas in [2] the cells were discharged into a shunt resistor hence dissipating the energy as heat. Methods such as the one mentioned in [74] utilise capacitors to balance SOC during battery operation i.e., in service balancing. Here, the supercapacitors are used as temporary energy storage during offline SOH measurement and SOC balancing.

This need for efficient energy cycling led to an investigation into various power supply topologies, their advantages, disadvantage, and voltage waveforms. Of these topologies, the chosen bidirectional switch-mode power-supply is discussed in the thesis. An investigation of relevant supercapacitor parameters is also reported.

3.2 Bidirectional buck–boost converter

The bidirectional buck–boost power supply shown in Figure 3.1 merges buck and boost topologies into one converter capable of stepping up the voltage in the forward direction governed by,

$$v_{\mathrm{o}} = \frac{1}{1 - d_1} v_{\mathrm{i}} \tag{3.1}$$

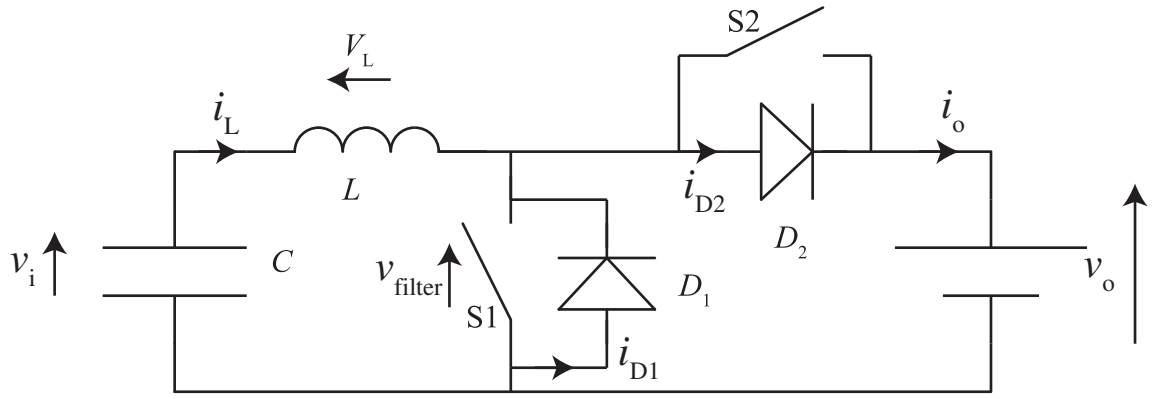

Figure 3.1: Bidirectional buck–boost power supply

where d_1 is the duty-cycle of switch S1 and stepping down the voltage in the reverse direction governed by,

$$v_\mathrm{i} = d_2 v_\mathrm{o} \tag{3.2}$$

where d_2 is the duty-cycle of switch S2. Figure 3.1 shows the basic layout of a bidirectional converter assuming ideal components.

The bidirectional converter works in two stages. In the first (boost) stage, switch S2 is open and S1 is driven by a pulse-width modulated signal. During boost, v_i is stepped up to v_o. Diode D_2 becomes forward conducting when the inductive transient produced as S1 opens exceeds $v_\mathrm{o} + v_\mathrm{D}$ where v_D is the forward voltage across diode D_2. In the second (buck) stage, switch S1 remains open and S2 is driven by a pulse-width modulated signal, stepping the voltage v_o down to v_i.

When the circuit operates in buck configuration it is essentially an LC filter exposed to a switching voltage input. An LC filter exposed to a voltage input step should, assuming ideal components, produce a sinusoidal current through the circuit (Eq. (3.5)) and a sinusoidal voltage across the capacitor. Writing Kirchhoff's voltage rule gives,

$$v_\mathrm{filter}(t) = \frac{1}{C}\int i_\mathrm{L}(t)\ dt + L\frac{di_\mathrm{L}(t)}{dt} \tag{3.3}$$

where, v_filter is the voltage step seen at the node joining the switch (S2), inductor (L) and diode (D_1). Taking the Laplace transform of Eq. (3.3) gives,

$$\frac{v_\mathrm{filter}(s)}{s} = \frac{1}{sC} i_\mathrm{L}(s) + sLi_\mathrm{L}(s) \tag{3.4}$$

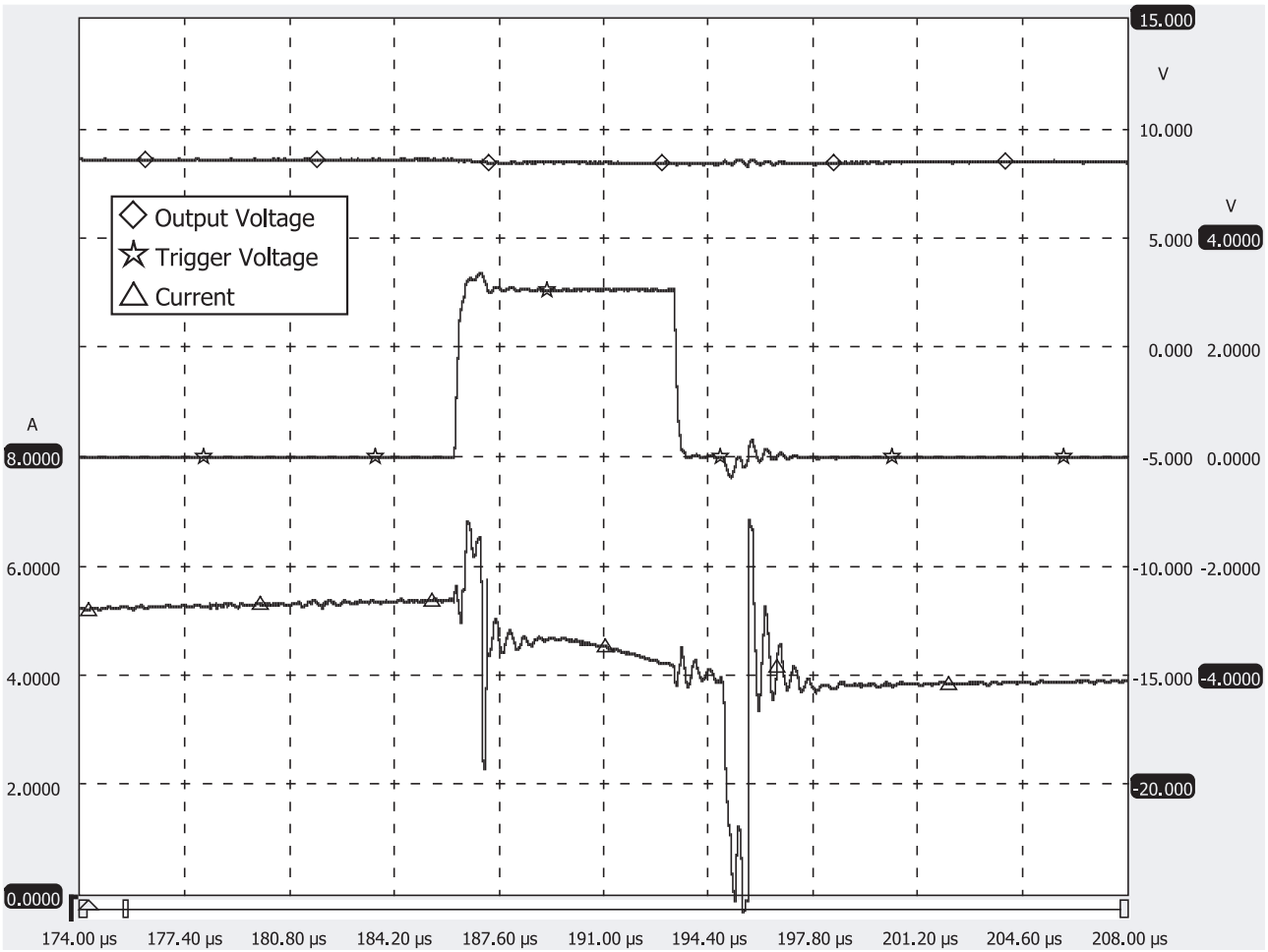

Figure 3.2: Scope trace of SMPS output voltage (the capacitor voltage in this case) v_{i}, switch trigger and inductor current i_{L} zoomed in to show damped oscillations around switching points

Taking the inverse Laplace transform and solving for $i_{\mathrm{L}}(t)$ predicts a cosinusoidal current,

$$i_{\mathrm{L}}(t) = \frac{v_{\mathrm{filter}}(t)}{L} \cos(t/\sqrt{LC}) \tag{3.5}$$

Adding a parasitic resistance in the circuit damps the oscillations, as seen in the waveforms in Figure 3.2 following the switching points.

The oscillation frequency shown in Fig. 3.2 is 2 MHz which is much higher than the predicted oscillation frequency $f = \frac{1}{2\pi\sqrt{LC}}$ of 0.9 Hz when $L = 10$ μH and $C = 55$ F. The higher actual oscillation frequency indicates that other parasitic capacitances such as the MOSFET output capacitance (C_{oss}) or diode junction capacitance are responsible for these oscillations.

The voltage trace in Fig. 3.3 shows a slight voltage ripple on the supercapacitor which can be reduced by increasing the frequency of switching and the size of the output capacitor [75].

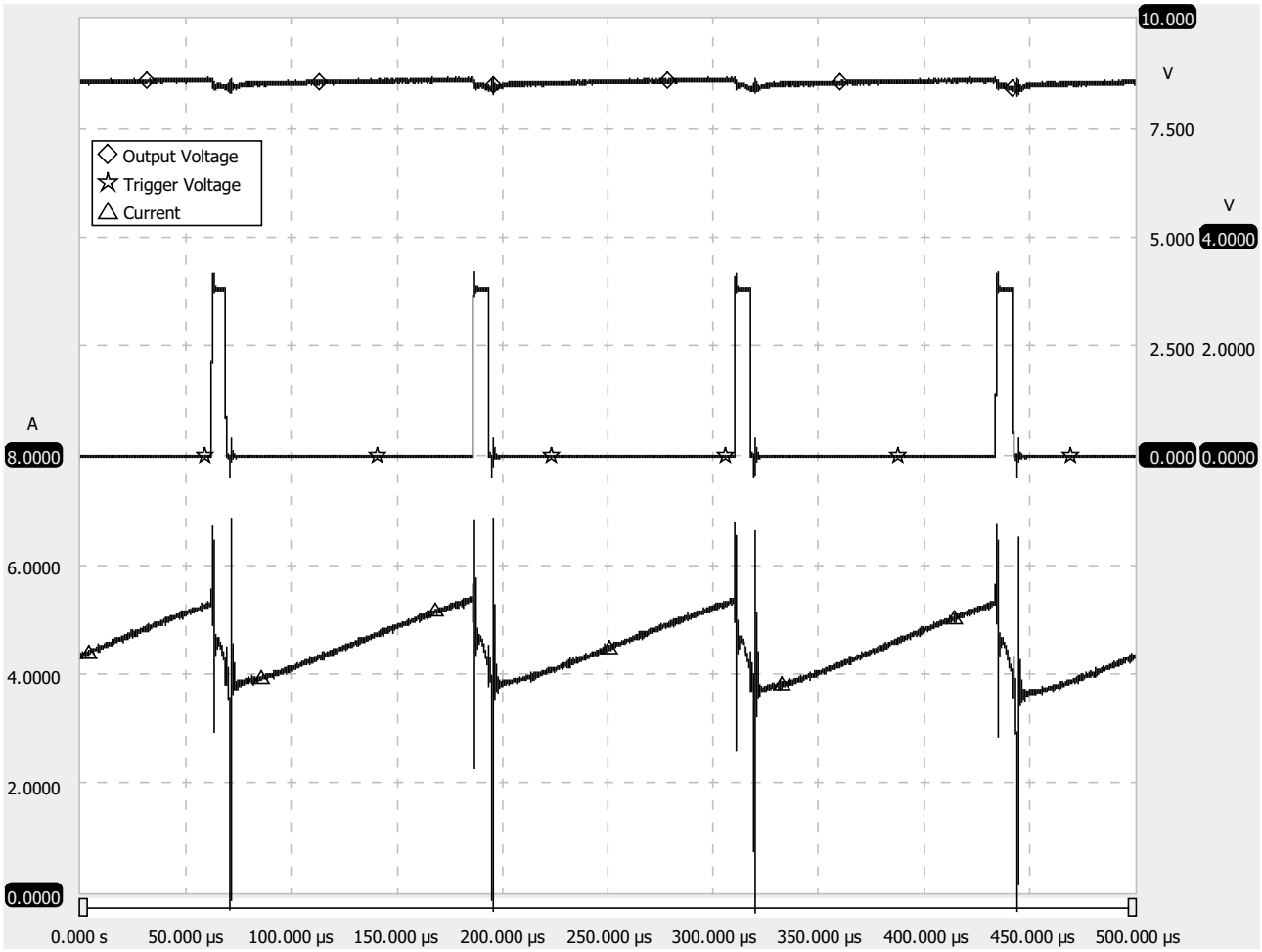

Figure 3.3: Scope trace of SMPS output voltage (the capacitor voltage in this case) v_{i}, switch trigger and inductor current i_{L}

The output voltage ripple (ΔV_o) can be estimated using,

$$\Delta v_{\mathrm{o}} = \frac{\Delta Q}{C} = \left(\frac{1}{C}\right)\left(\frac{\Delta i_{\mathrm{L}}}{f_{\mathrm{s}}}\right) \tag{3.6}$$

where C is the value of the output capacitor, i_{L} is the inductor current and f_{s} is the switching frequency.

In this topology v_{o} must always be greater than v_{i} otherwise the diode D_2 becomes forward conductive and drains all the energy from v_{i} through the inductor. v_{i} can be any positive voltage less than v_{o}. If C is a supercapacitor bank and v_{o} is a voltage source representing a battery module then this circuit realises both discharge and charge functions using minimal components. The control circuitry for this type of converter must be carefully designed so that it is not possible for both S1 and S2 to be activated (closed or switched-on) at the same time otherwise the supercapacitor bank and battery module will be short-circuited.

3.3 Energy conversion considerations

The flow of energy between the supercapacitor and the batteries through the circuit is important and relates very closely to how efficient the circuitry is; this is detailed in Chapter 4. The desired outcome of this section is to decide on a suitable energy flow circuit to ensure maximum efficiency i.e., drawing the least amount of power from an external source such as a bench top power supply during battery analysis. Utilising the existing vehicle wiring loom the charger/analyser system is connected to the battery blocks; the wiring loom has a sensing wire connected to the outer terminals of each battery block. This sensing wiring loom (shown in Figure 1.1 as the wires connecting the battery module pairs to the PhotoMOS relay and isolation amplifier) will be used to charge and discharge the battery blocks during the analysis cycle.

3.3.1 Energy flow

Figures 3.4 to 3.5 show how the current flows between the battery blocks, an external 12 V source and the supercapacitor bank. The arrows show the direction of current flow: red for discharging and green for charging. In order to start the analysis the battery blocks need to be brought to a known state e.g., 100% SOC as indicated when the battery reaches its end-of-charge voltage.

Figure 3.4(a) shows battery block n being discharged into the supercapacitor bank; during this stage the block voltage and current are monitored. Figures 3.4(a) and 3.4(b) show how the energy from battery block n is charged into battery block $n+1$. This method of recycling the

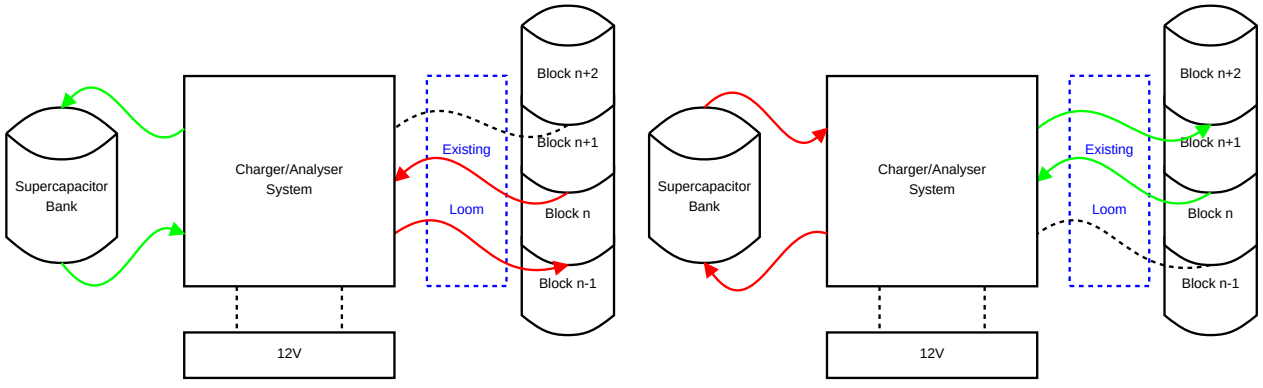

Figure 3.4: Energy flow from block n to block $n+1$ where (a) shows block n discharged into the supercapacitor bank and (b) shows block $n+1$ charged from the supercapacitor bank

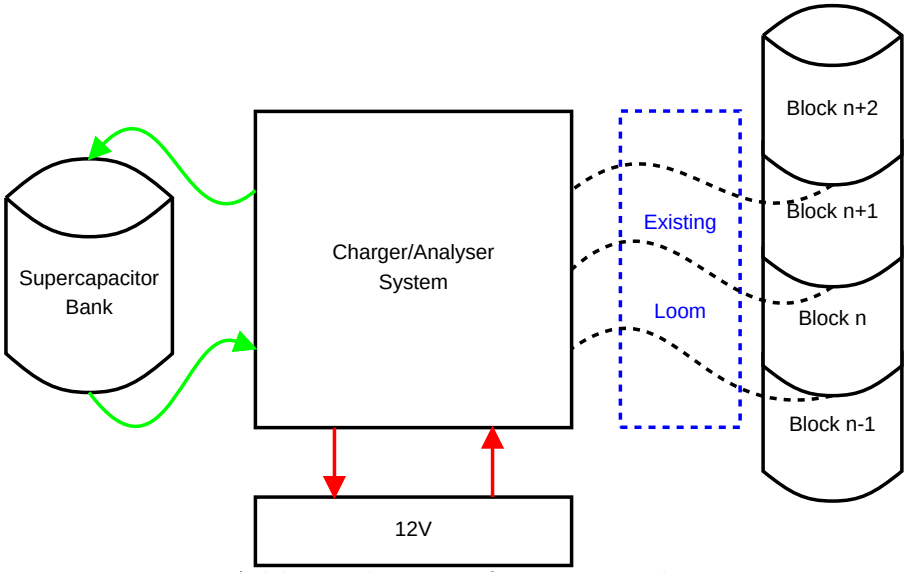

Figure 3.5: Additional energy from external 12 V source

energy extracted from battery block n means that the energy required from the external 12 V source is minimised.

It is not possible to achieve 100% energy transfer, so Figure 3.5 shows the supercapacitor bank being charged from an external 12 V source. Externally-supplied energy is required to fully charge block $n+1$ when block n has reached its end-of-discharge voltage, bringing the battery block $n+1$ to 100% SOC so that the block is ready to be analysed. Charging the blocks from 12 V is repeated in the final stage making the battery pack fit for use in the vehicle again.

The process shown in Figure 3.4 where one battery block is discharged into the next battery block can be reversed to analyse the voltage characteristics of battery block $n+1$ under discharge. The supercapacitor bank only holds a fraction of the total energy stored within the battery block, therefore the process shown in Figure 3.4 has to be repeated many times during the analysis process and it is important that this process be as efficient as possible.

Charging the external 12 V source from the supercapacitor bank is possible in theory allowing excess energy from one block pair to be passed onto the next block pair. The bench-top power supply used during testing does not have the ability to store excess energy from a block pair. As a result, energy flows need to be carefully designed in such a way that one block pair does not end up having excess energy which subsequently cannot be recycled. If, instead, a 12 V battery were to be connected to the charger-analyser system as the external power source then it would be possible to pass energy from one block pair to another.

The energy flow is therefore designed in such a way that the energy from battery block $n+1$ is used initially to charge block n to 100% SOC. This leaves block $n+1$ at 0% SOC assuming

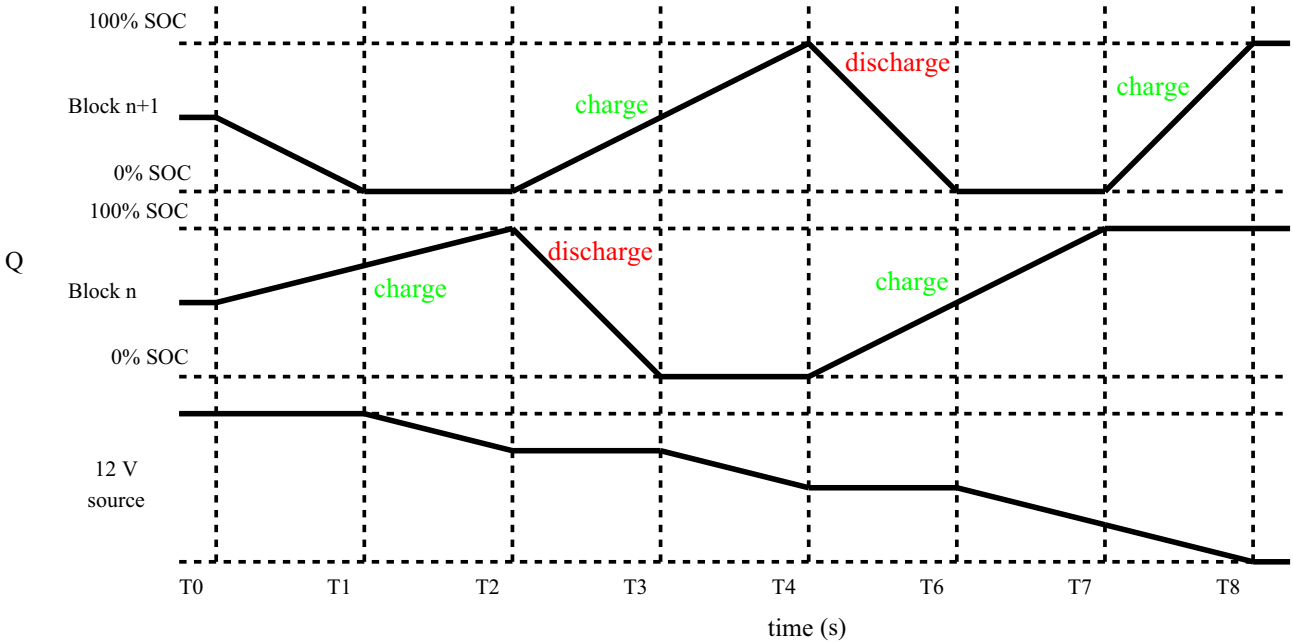

Figure 3.6: Energy flow summary assuming battery blocks start at 50% SOC and 50% energy conversion efficiency; y-axis indicates state-of-charge, x-axis is time in seconds

both battery blocks started at 50%, and that the energy conversion is ideal. However, 100% energy conversion is unobtainable so energy will be required from the external source to achieve 100% SOC on block n. Current and voltage monitoring during the charge and discharge cycles give the (Q, V) points required to calculate state-of-health; this will become clear in Chapter 6 (a sample dataset is shown in appendix C).

Figure 3.6 shows the predicted energy flow assuming that both battery blocks start at 50% SOC with the same SOH. The figure shows that 50% of the energy (SOC) removed from battery block $n + 1$ results in a 25% change in SOC for battery block n at time T1. The remainder of the energy needs to be sourced from the 12 V external supply from T1 to T2. Note that the 12 V source charge-line only changes when energy is drawn from it. Each battery block undergoes one charge-discharge-charge cycle as shown in the figure.

If one of the four battery modules (two battery blocks) connected to the battery analyser is of significantly lower state-of-health (SOH) than the other three modules, then analysis of this pair of battery blocks becomes difficult. The block of lower SOH will be unable to source enough energy to significantly contribute to the charging of the other block in this pair. In addition the block with low SOH will not be able to store the discharge energy from the healthy battery block. Intelligent software will need to be designed in order to detect and eliminate the low state-of-health battery block from the analysis process.

3.3.2 Fractional energy transfer

Section 3.3.1 discussed how the first battery block (block n) is fully charged from block $n+1$ and an external source before analysis begins. If an accurate battery model is available, then it may be possible to transfer a small fraction of the full battery energy and analyse the voltage and current response during this cycle.

3.3.3 Dissipating energy

In cases where battery block mismatch is severe it is also possible to dissipate excess energy as heat in the circuit boards. This process requires repeated charge and discharge cycles of the battery block whose SOC is too great. The successive cycling of the battery block means that the energy is dissipated in all the parasitic series resistances which exist throughout the circuit and within the battery block itself. However, dissipating excess energy as heat in the parasitic resistances is undesirable and should be avoided.

The user will be informed when the battery voltages are too high for analysis and will be advised to drain excess energy from the battery pack through the HEV system by, for example, reversing the vehicle for a short period of time to reduce the SOC of the battery pack.

3.4 Supercapacitor description and characteristics

A supercapacitor or electrochemical capacitor stores its electrical energy in the interface between an electrolyte and a solid electrode [76, 77]. Supercapacitors are desirable as an energy storage medium because they have very good reversible energy storage characteristics which means that they are able to withstand many charge-discharge cycles at high charge-discharge rates [77–80]. Supercapacitors follow the same basic principles as ordinary capacitors however they generally have much higher capacitances and much lower ESR. Capacitances can be as high as 5000 F with ESR as low as 0.28 mΩ [81] in single-cell devices. This means that supercapacitor time-constants can be in the order of several milliseconds to seconds due to their low internal resistances and high capacitance values. Due to the large capacitance of a supercapacitor it is able to store many times more energy than a conventional capacitor, however supercapacitors in general have lower maximum DC voltage rating compared to conventional capacitors.

Figure 3.7 shows three different energy storage devices: a 3300 μF, 450 V capacitor from a Prius inverter, a 110 F 2.5 V supercapacitor and a 1.5 V AA battery. Table 3.1 compares the

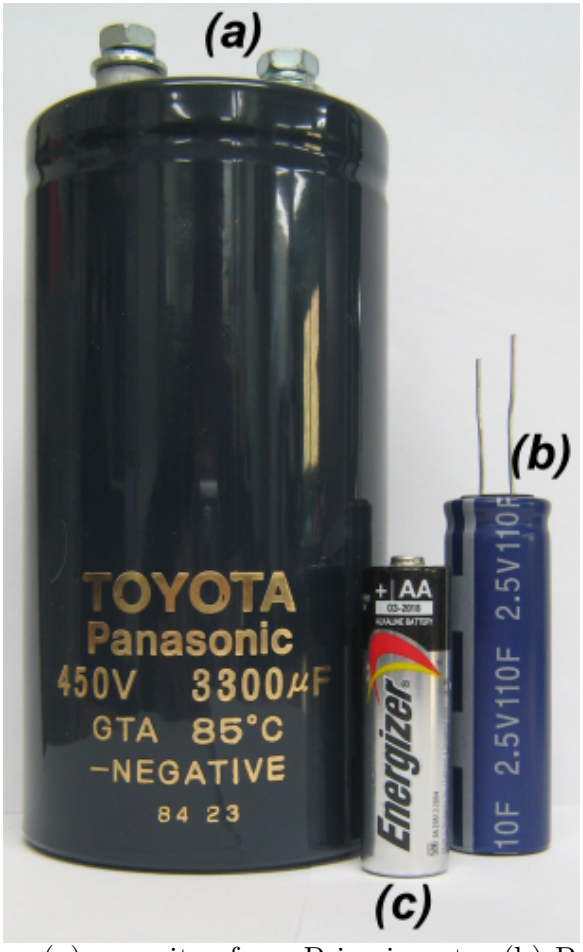

Figure 3.7: Size comparison (a) capacitor from Prius inverter (b) PowerStor Aerogel supercapacitor (c) Energizer AA battery

amount of energy that each device from Figure 3.7, and a 10 μH inductor carrying 10 A, can store. The table clearly identifies the dangers involved in storing large amounts of energy in conventional capacitors. The 3300 μF capacitor is charged to 450 V can be deemed dangerous due to the high voltage and energy content. The photo (figure 3.7) shows how the sizes of these components vary. The supercapacitor and the Panasonic capacitor both store similar amount of energy however, the Panasonic capacitor is many times larger than the supercapacitor indicating that the supercapacitors have higher energy density than conventional capacitors. The AA battery however still has the largest energy density but has lower energy efficiency due to higher internal resistance compared to the capacitors.

Supercapacitors are also referred to as double-layer capacitors. Charge interfaces between the electrolyte and the capacitor electrode are formed at both ends of the capacitor. The electrode-electrolyte interface consists of a porous electrode soaked in liquid electrolyte, effectively increasing the area (A) of the capacitor plates which, in turn effects the capacitance. Some supercapacitors have an electrode area recorded as large as $1000 - 2000$ m^2/cm^3 [78]. The two electrodes are separated by a thin separator plate to avoid internal shorting of the

Table 3.1: Energy storage comparison

Component	Value	Voltage/Current	Energy
Panasonic capacitor	3300 μF,	450 V	$\frac{1}{2}CV^2 =$ **334 J**
Supercapacitor	110 F	2.5 V	$\frac{1}{2}CV^2 =$ **343 J**
AA battery	2500 mAh, 9000 As	1.2 V	$ItV =$ **10800 J**
Inductor	10 μH	10 A	$\frac{1}{2}LI^2 =$ **0.5 mJ**

supercapacitor, meaning that d is small [77]. The electric field within the capacitor is formed as a result of ion diffusion within the electrolyte so, ϵ_r is large [82].

3.5 Supercapacitor equivalent circuits

There are many supercapacitor models. In some papers [77, 82] the supercapacitor is modelled by an impedance consisting of a series of RC ladder networks. The porous nature of the capacitor plates mean that diffusion processes are important, but modelling the capacitor to represent the diffusion related components falls outside the scope of the thesis. Therefore the ideal capacitor and a first-order capacitor model are introduced.

3.5.1 Capacitor first-order equivalent circuit

In [83] the first-order equivalent circuit for a capacitor is expressed as an RCL network, but the equivalent series inductance of the capacitor is ignored in this thesis. Figure 3.8 shows the RC equivalent circuit of a supercapacitor. This circuit can be extended to include diffusion effects by including additional RC pairs [84–87].

The maximum current drawn by the first-order model is limited by the ESR (R_C). The energy delivered to the first-order capacitor, by applying a voltage to the terminal (v_T), will not equal the final energy stored within the capacitive element because some energy will be lost through the series resistance.

The energy balance equation for this circuit becomes,

$$\int P_\mathrm{T}\ dt = \int v_\mathrm{T} i\ dt = \int R_\mathrm{C} i^2\ dt + \frac{1}{2} C v_\mathrm{C}^2 \tag{3.7}$$

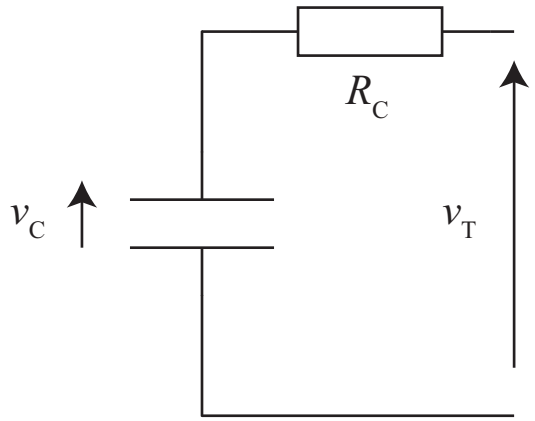

Figure 3.8: First-order supercapacitor model

where P_T is the power at the terminal, v_T is the terminal voltage and i is the current through the capacitor. When the current returns to zero, or $v_C = v_T$ the instantaneous power loss through the resistor equals zero. However, the energy lost through the resistor while current is flowing is not captured in the electric field of the capacitor.

The supercapacitor equivalent circuit can be made more complex [87–89], for example, by adding a leakage current to the capacitor model with an equivalent parallel resistance (EPR). Leakage within the supercapacitor only becomes significant if the capacitors are used as a long-term energy storage; in this project the supercapacitor bank is used for temporary storage only so leakage can be ignored.

3.6 Parameter variation and dependences

Maxwell Technologies, previously one of the largest supercapacitor manufacturers, specify a test procedure for quantifying the internal supercapacitor parameters assuming a first-order equivalent circuit as described in Section 3.4. The voltage measured at the terminals, which is the only voltage measurement which can be done, is a sum of the voltage in the capacitor and the voltage drop across the series resistance. So for a constant charging current, the series resistance R_C can be determined from,

$$R_C = \frac{(v_T - v_C)}{I} \tag{3.8}$$

where v_C is measured to be the terminal voltage in an open-circuit situation i.e., no current flowing. The capacitance can be calculated using,

$$C = \frac{I\Delta t}{(V_{\text{measure\_end}} - V_{\text{measure\_start}})} \tag{3.9}$$

where I is a constant input current and Δt is the time that it takes for the capacitor to charge from $V_{\text{measure\_start}}$ to $V_{\text{measure\_end}}$. A test procedure can now be implemented to record these parameters. Figure 3.9 shows the measurements taken when a supercapacitor is subjected to the Maxwell test procedure.

The capacitance can be calculated using,

$$C = \frac{I_{\text{ch}}(t_2 - t_1)}{(V_2 - V_1)} \tag{3.10}$$

or,

$$C = \frac{I_{\text{disch}}(t_5 - t_4)}{(V_4 - V_5)} \tag{3.11}$$

and the equivalent series resistance can be calculated using,

$$R_C = \frac{(V_2 - V_3)}{I_{\text{ch}}} \tag{3.12}$$

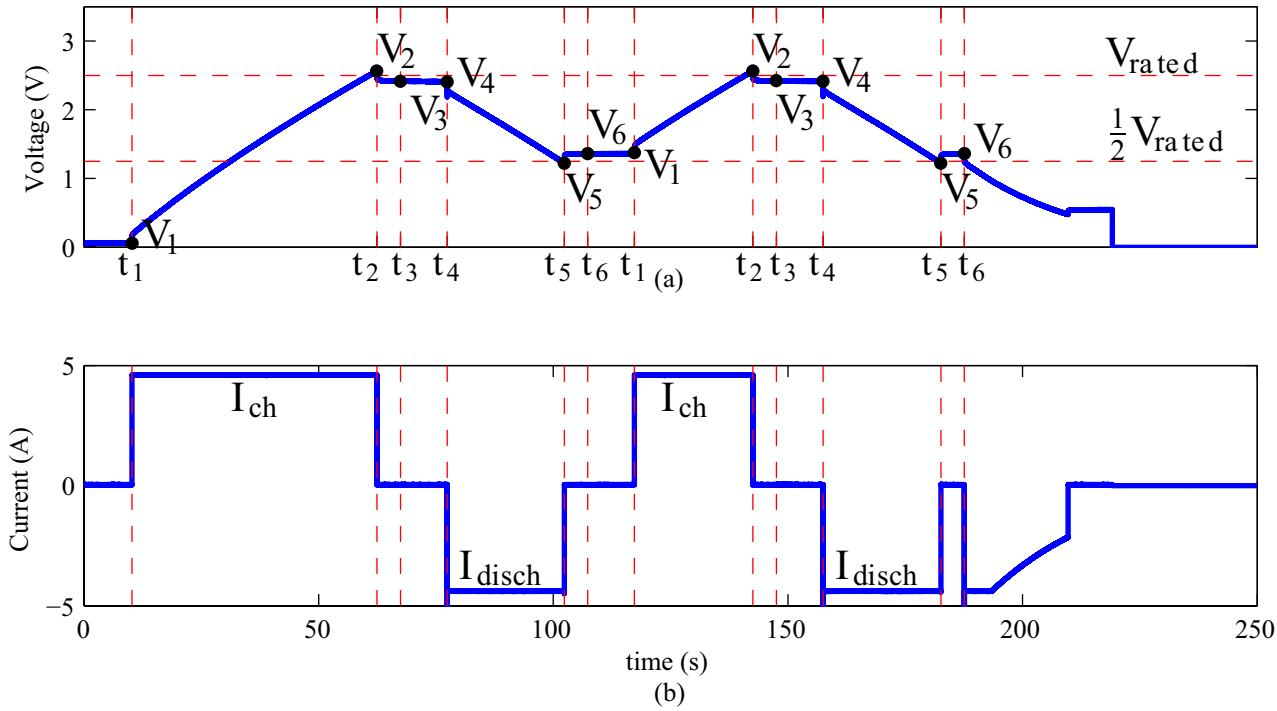

Figure 3.9: Maxwell test procedure showing (a) supercapacitor terminal voltage (v_T) variation with (b) terminal current (i)

or,

$$R_{\mathrm{C}} = \frac{(V_6 - V_5)}{I_{\mathrm{disch}}} \tag{3.13}$$

Figure 3.10 shows the variation in capacitance, ESR, mean and standard deviation measured on 20 PowerStor Series HB 2.5 V 110 F supercapacitors used in this project. The results were obtained using the Maxwell test procedure.

The mean capacitance for both the discharge and charge case lie approximately 10% below the rated capacitance of 110 F, Fig. 3.10. The Maxwell test procedure specifies a test current of 75 mA/F which equates to a test current of 8.25 A for the PowerStor capacitors; however, the test results have been obtained using a current of 4.5 A. This difference in test currents could be responsible for the 10% deviation from rated capacitance.

Xu et al [90] discuss dynamic voltage equalisation of supercapacitor banks. Dynamic voltage equalisation is necessary when there is a mismatch between the capacitances of the capacitor in a series-connected capacitor bank leading to the risk of overcharging and damaging one capacitor within the bank. Obviously if the supercapacitor bank is connected in parallel the voltages at the capacitor terminals will be equal in a no-current situation, however energy can be wasted during balancing if there are large variations in capacitor ESR. Researchers [88, 91] also relate changes in supercapacitor capacitance to charging voltage, current and temperature. For example, Cheng shows in [91] that the apparent capacitance of their device increases as the terminal voltage of the capacitor increases, and this is confirmed in [88]. Both papers also

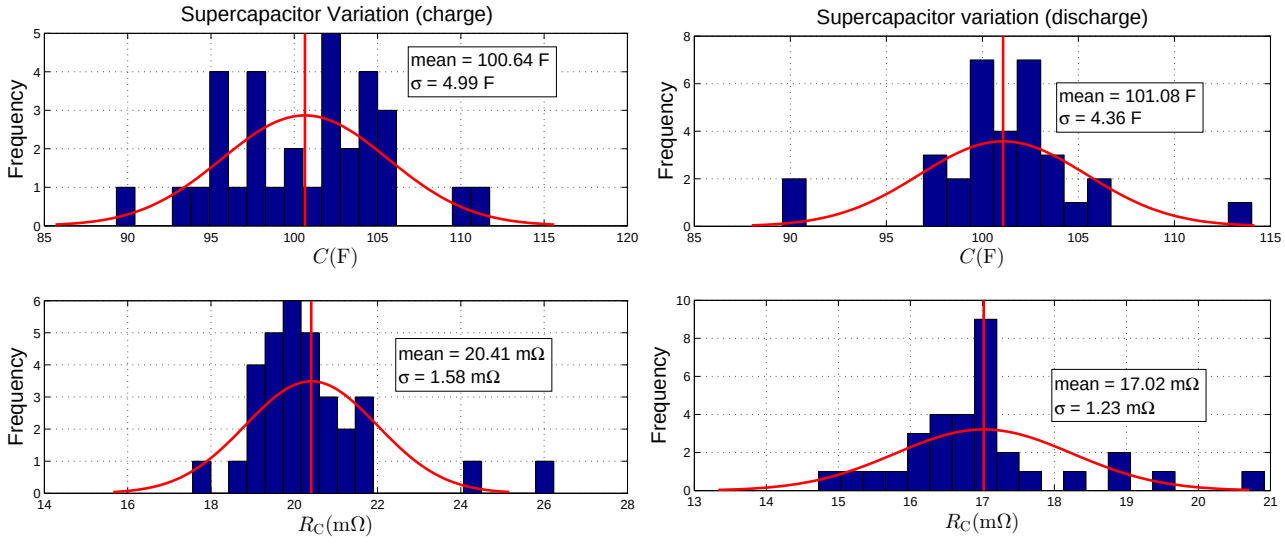

(a) (b)

Figure 3.10: Maxwell test results for PowerStor Series HB 110 F supercapacitors; (a) charge capacitance and ESR, (b) discharge capacitance and ESR.

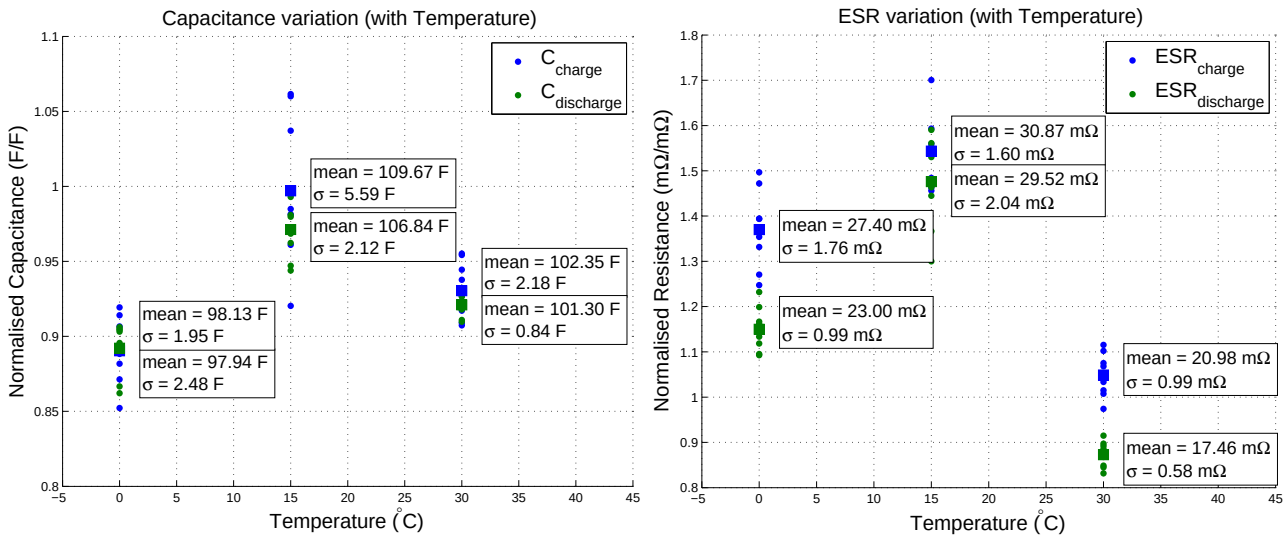

(a) (b)

Figure 3.11: Maxwell test results for PowerStor Series HB 110 F capacitors; (a) capacitance variation with temperature, (b) ESR variation with temperature.

mention sensitivity of ESR to charge rates and terminal voltages. The effects of temperature on ESR (R_C) and capacitance (C) are of particular importance to this project since changes in these two parameters change the cyclic energy efficiency of the hardware. The two parameters that are investigated in this thesis are capacitance variation from the nominal rated capacitance and capacitance variation with temperature.

Figure 3.11 shows the variation with temperature of the capacitance and of the ESR measured using the Maxwell test procedure. The graphs show capacitance and ESR normalised to the datasheet values of 110 F and 20 mΩ. There are variations in capacitance of 15% from the rated capacitance as the temperature drops to 0°C. ESR is also measured to be larger than the datasheet parameter by a maximum of 170% at 15°C.

3.7 Chapter summary

Based on the measurements taken and the prototypes built it can be concluded that the bidirectional buck–boost power-supply is most desirable circuit design because it requires a minimal number of components to transfer power to and from battery and supercapacitor. Fractional energy transfer between battery block and supercapacitor bank is the preferred method as this decreases the analysis time and energy lost during conversion. Chapter 6 will cover the relationship between battery state-of-health and the data gathered using this method.

Two basic supercapacitor equivalent circuits have been discussed, both the ideal capacitor model and the first-order equivalent circuit taking into account only the equivalent series resistance. More complex models exist that take into account effects such as the double-layer charge boundaries. The simple first-order equivalent circuit is suitable for this project as the capacitor bank will be used for temporary storage of energy during the battery module analysis cycle. Maxwell's test procedure has been used to investigate the variation of capacitance and ESR between supercapacitors and with temperature, confirming the parameter variation quoted on the datasheet for the PowerStor supercapacitors used in this project.

Chapter 4

Efficiency considerations for charging supercapacitors through a bidirectional converter

4.1 Desired outcome

The aim of this chapter is to investigate the efficiency increase gained by switching a supercapacitor bank between series and parallel configurations during energy recycling in a Toyota Prius battery pack. Before simulating the circuit through its full operating range the accuracy of the results at each switching period is checked. Here, MATLAB is used to produce the main set of results which are cross-checked against output generated by the Spice circuit simulator. The fundamental equations describing the circuit behaviour are built by analysing the ideal model. Some realistic first-order component losses are then added to the ideal circuit to produce a realistic result. Throughout this chapter a smaller 550 μF capacitance value was used to verify simulation performance before scaling to the full 55 F supercapacitor value. The smaller capacitance value reduces simulation run time and shows greater voltage variation with current.

4.2 Circuit modelling

Figure 4.1 shows the bidirectional switch-mode power-supply using ideal components i.e., all equivalent series resistances, diode forward voltage drops and switching losses are set to zero. The equations below outline the operation of the switching converter in buck mode.

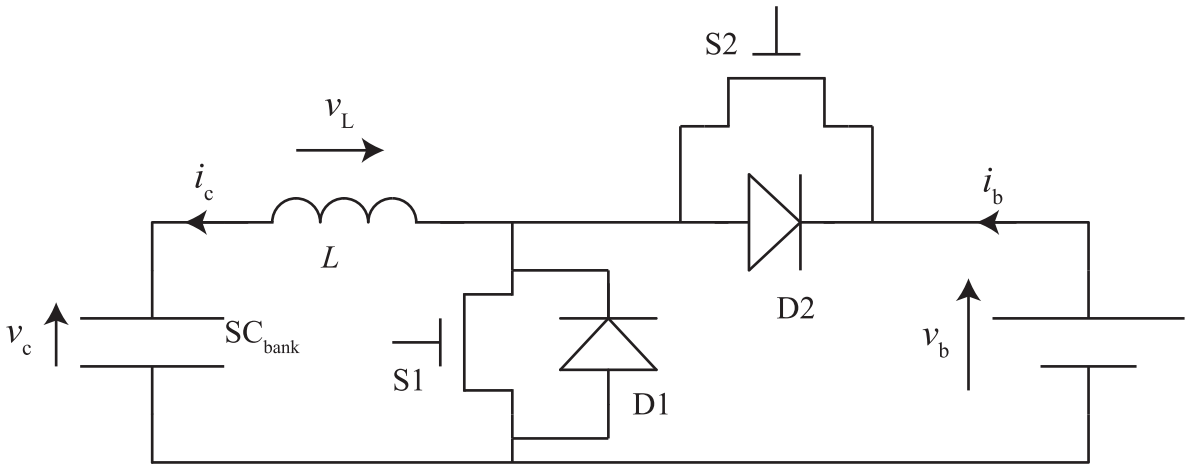

Figure 4.1: Bidirectional buck-boost power supply assuming ideal components. D1 and D2 are separate diodes paralleled with the MOSFET switches.

4.2.1 Ideal model

The buck converter stage is used to charge the supercapacitor bank while discharging the battery blocks. In this case switch S2 is controlled and the governing equations are,

$$v_{\mathrm{L}} = L\frac{di}{dt} = \begin{cases} v_{\mathrm{b}} - v_{\mathrm{c}}, & \text{switch S2 closed} \\ -v_{\mathrm{c}}, & \text{switch S2 open} \end{cases} \tag{4.1}$$

$$i_{\mathrm{c}} = C\frac{dv_{\mathrm{c}}}{dt} = i \tag{4.2}$$

$$i_{\mathrm{b}} = \begin{cases} i, & \text{switch S2 closed} \\ 0, & \text{switch S2 open} \end{cases} \tag{4.3}$$

where the symbols are defined in Table 4.1. These equations are integrated numerically in MATLAB to produce the appropriate voltage and current traces.

Spice software allows the user to import component models generated by the manufacturer which contain the correct parasitic effects, hence Spice simulations will be used to validate the MATLAB solutions and give an indication as to how significant particular parasitic effects are. However, it is difficult to code logic or digital circuits in Spice. MATLAB was used to implement the equations above because of the large digital component in the circuit simulations. Euler integration and Laplace transform methods can also be used to solve these differential equations. The power transistors drawn in Figure 4.1 are driven with a duty-cycle controlled signal produced by a microcontroller with a switching period (T_{s}) of 15 μs.

Table 4.1: Symbol definitions and constants for the bidirectional switching converter

Symbol	Description	Unit
v_{L}	voltage across the inductor	V
v_{b}	battery block voltage	V
v_{c}	supercapacitor bank voltage	V
v_{D}	diode forward voltage	mV
i_{c}	current through the supercapacitor bank	A
i_{b}	current through the battery block	A
i	instantaneous current through the inductor	A
L	inductance	μH
R_{L}	series parasitic resistance of inductor	mΩ
$\mathrm{SC}_{\mathrm{bank}}$	supercapacitor bank capacitance, changes whether in series or parallel arrangement	F
R_{C}	series parasitic resistance of supercapacitor bank	mΩ
R_{DS}	series resistance of MOSFET	mΩ
t_{on}	MOSFET turn-on delay time	ns
t_{off}	MOSFET turn-off delay time	ns
Q_{rr}	body diode reverse recovery charge	nC
C_{oss}	output capacitance	pF
V_{D}	voltage drop across diode PN junction	V
R_{D1}	series resistance of diode	mΩ
D	duty-cycle of switches, the on-time as a ratio of cycle time	%
T_{s}	switching period	μs
n	simulation step	

Figure 4.2 shows the results of Spice simulation with fixed duty-cycle gate drive. The figure also highlights the difference between continuous conduction mode (CCM) and discontinuous conduction mode (DCM), where the current flowing through the capacitor drops to zero during one cycle. The output current at the changeover between CCM and DCM is calculated from,

$$I_{o_{\mathrm{lim}}} = \frac{v_{\mathrm{i}}}{2L}(1-D)DT_{\mathrm{s}} \tag{4.4}$$

Clearly as D approaches 1, $I_{o_{\mathrm{lim}}}$ approaches zero. However, in this case $I_{o_{\mathrm{lim}}} = 2.25$ A after substituting the component values ($v_{\mathrm{b}} = 12$ V, $L = 10$ μH, $D = 0.5$ and $T_{\mathrm{s}} = 15$ μs). Equations (4.1) to (4.3) show the ideal case and Figure 4.2 shows the Spice simulated traces. The correct formulas for calculating the output current relationship with input and output voltage are derived, using the data presented in Figure 4.2.

Figure 4.3 sketches how the currents behave throughout the switching cycle in continuous conduction mode and in discontinuous conduction mode. The variables marked in Figure 4.3

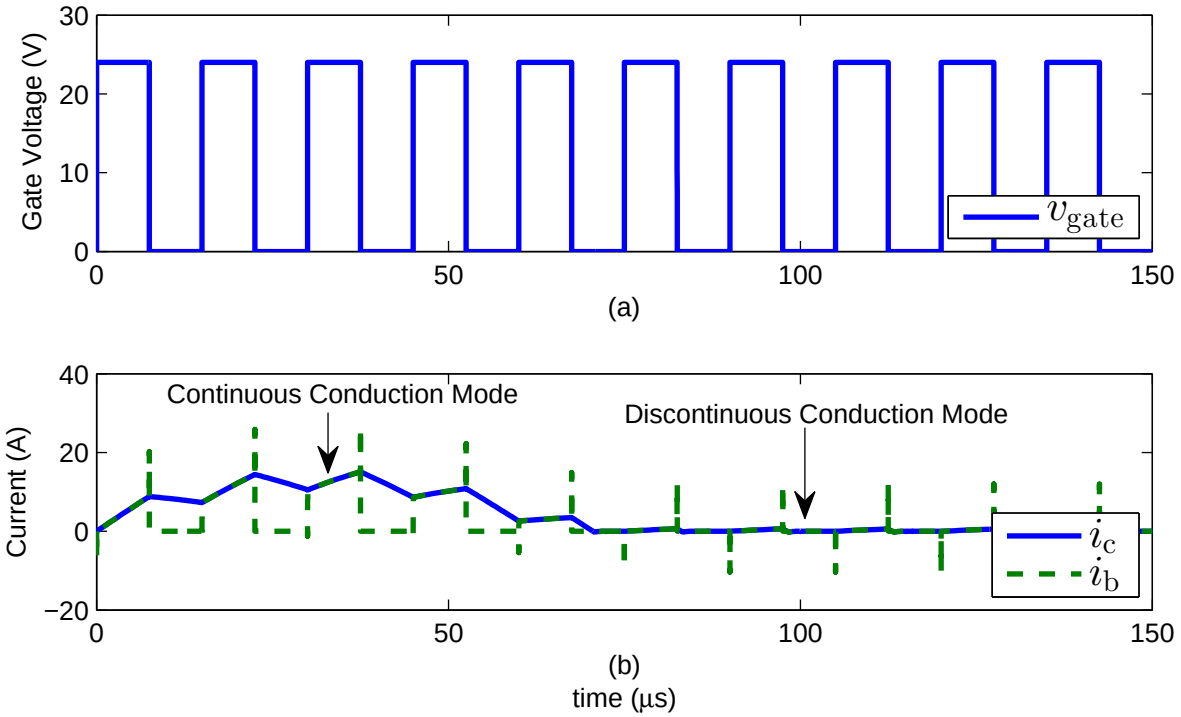

Figure 4.2: Spice simulation results of buck stage with fixed 50% duty-cycle showing (a) gate voltage (v_{gate}) for MOSFET S2 and (b) capacitor and battery current (i_{c}, i_{b}), highlighting the change from continuous to discontinuous conduction modes when I_{c} drops below 2.25 A

can be used to derive the following equations,

$$D(n) = \frac{v_{\text{c}}(n-1)}{v_{\text{b}}} = \frac{I_{\text{B}}}{i_{\text{c}}(n-1)}, \qquad 0 \leq D(n) \leq 1 \tag{4.5}$$

where n is the simulation index the battery voltage (v_{b}) is assumed constant throughout a cycle and the average battery current (I_{B}) is assumed constant for the calculation of the duty-cycle in Eq. (4.20). However, the capacitor voltage (v_{c}) still needs to be calculated. To calculate

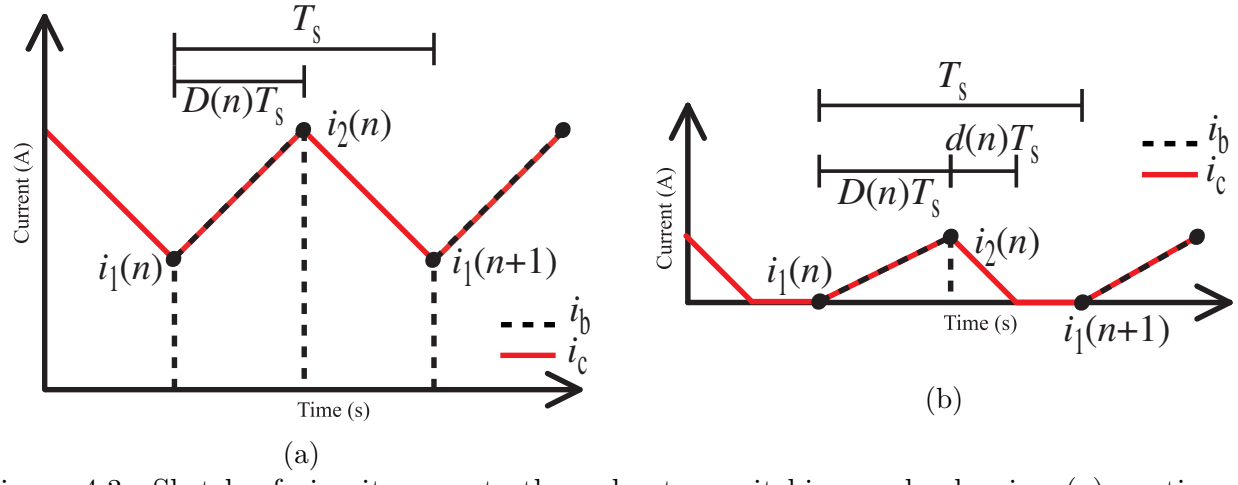

Figure 4.3: Sketch of circuit currents throughout a switching cycle showing (a) continuous conduction mode and (b) discontinuous conduction mode. Here, n is the simulation index, the black trace is battery current and the red trace is capacitor current.

the capacitor voltage the capacitor current (i_c) is integrated i.e., calculate the area below the current curve, which requires calculation of the points i_1 and i_2,

$$\Delta i = \frac{1}{L} v_L \Delta t \tag{4.6}$$

$$i_2(n) = \frac{1}{L}(v_b - v_c(n-1))D(n)T_s + i_1(n) \tag{4.7}$$

Once $i_2(n)$ is calculated the capacitor voltage can be updated before calculating $i_1(n+1)$ which is done by integrating the capacitor equation for the time period $D(n)T_s$, where T_s is the MOSFET switching period. With the updated capacitor voltage, $i_1(n+1)$ can be calculated using,

$$i_1(n+1) = i_2(n) + \frac{1}{L}(v_D - v_c(n))D(n)T_s \tag{4.8}$$

At this stage a check whether or not the converter is in CCM or DCM is performed, which affects the capacitor current. If $i_1(n+1)$ is greater than or equal to zero the converter is in CCM and average capacitor current (I_c) for one switching cycle is calculated using,

$$I_c = \frac{i_1(n) + i_2(n)}{2} \tag{4.9}$$

If $i_1(n+1)$ drops below zero the point in time at which the capacitor current drops to zero is calculated,

$$dT_s = \frac{i_2(n)}{\frac{1}{L}(v_D - v_c(n-1))} \tag{4.10}$$

With this information I_c can be calculated,

$$I_c = \frac{i_1(n) + i_2(n)}{2} D(n) + \frac{i_2(n)}{2} d \tag{4.11}$$

remembering that $i_1(n+1)$ now equals zero for the next switching round. The capacitor voltage is the integral of the capacitor current and is calculated using,

$$v_c(n+1) = \frac{1}{C} I_c T_s \tag{4.12}$$

Figure 4.4 shows the Spice simulation results compared with the MATLAB implementation

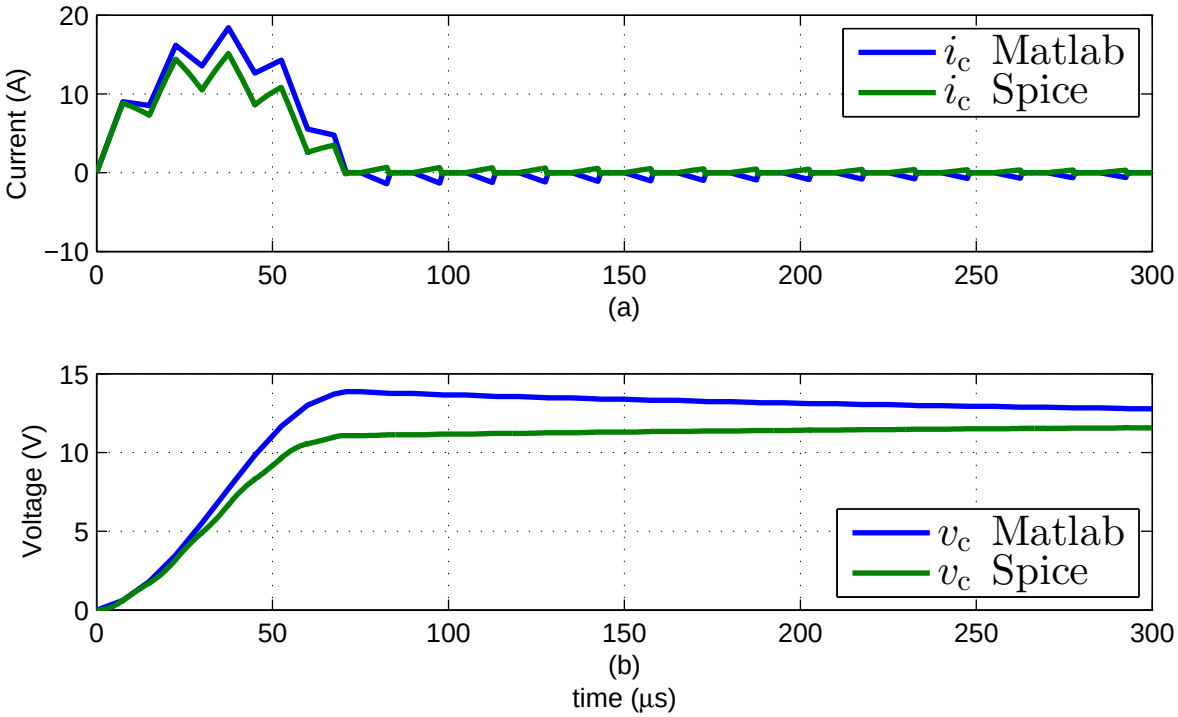

Figure 4.4: MATLAB and Spice simulation results for (a) capacitor current and (b) capacitor voltage for equations (4.6) to (4.12)

(see Appendix E) of equations (4.6) to (4.12) for a fixed duty-cycle case showing the effects that the parasitic elements have on the voltage and current traces. For the Spice simulation the parasitic effects (series resistances and forward voltage drops of the MOSFET switch and diode) are simulated. A full explanation of these calculations will follow leading to the first-order model of the switching power supply.

4.2.2 First-order model

The voltage across the inductor (v_L) changes when parasitic resistances are added to the circuit, which in turn effects the rate of change of capacitor current (i_c), Eq. (4.1). Figure 4.5(a) shows the first-order losses in the circuit with the switch closed.

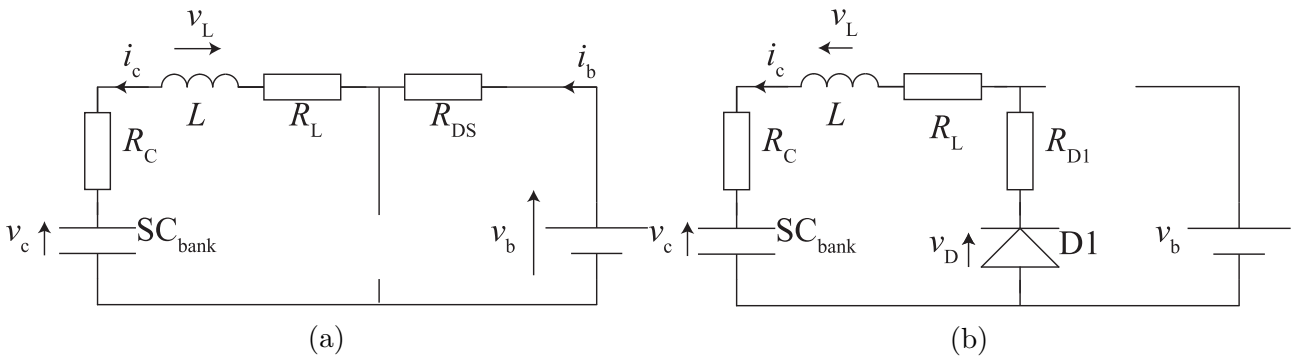

Figure 4.5: Circuit diagram of first-order model showing (a) switch S2 closed and (b) switch S2 open

Figure 4.5(a) is scrutinised to develop the characteristic equations for this situation. Simplistically the buck converter is an RLC filter circuit driven by a step input voltage. The voltage around the circuit can be summed using Kirchhoff's voltage rules to be,

$$v_{\mathrm{b}} = \frac{1}{C}\int i_{\mathrm{c}}(t)\ dt + L\frac{di_{\mathrm{c}}(t)}{dt} + Ri_{\mathrm{c}}(t) \tag{4.13}$$

where R is the lumped parasitic resistance. This equation can be solved using numerical integration methods such as Euler integration, however as discussed earlier a small time-step is necessary to accurately solve the differential equations. But, if Laplace's method for solving differential equations is used the current and voltage at specific points in time can be calculated. So, taking the Laplace transform of Eq. (4.13) gives,

$$v_{\mathrm{b}} = \frac{1}{sC}i_{\mathrm{c}}(s) + v_{\mathrm{c}}(0) + sLi_{\mathrm{c}}(s) - Li_{\mathrm{c}}(0) + Ri_{\mathrm{c}}(s) \tag{4.14}$$

Solving for i_{c} gives,

$$i_{\mathrm{c}}(s) = \frac{V}{R + sL + 1/sC} \tag{4.15}$$

where $V = v_{\mathrm{b}} - v_{\mathrm{c}}(0) + Li_{\mathrm{c}}(0)$. This is the voltage across the RLC components and their parasitic elements. When the switch is closed V is a scaled step function $Vu(t)$ with Laplace transform $V \cdot 1/s$. So Eq. (4.15) becomes,

$$i_{\mathrm{c}}(s) = \frac{V \cdot 1/s}{(R + sL + 1/sC)} = \frac{V}{L}\left(\frac{1}{s^2 + s\frac{R}{L} + \frac{1}{LC}}\right) \tag{4.16}$$

with inverse Laplace transform,

$$i_{\mathrm{c}}(t) = \frac{V}{L}e^{-\alpha t}\left(\beta\cos(\omega t) + \frac{\gamma - \alpha\beta}{\omega}\sin(\omega t)\right) \tag{4.17}$$

where, $\alpha = \frac{R}{2L}$, $\beta = 0$, $\gamma = 1$ and $\omega = \sqrt{-\alpha^2}$, an imaginary number, representing both phase and frequency of the damped sinusoid discussed in Section 3.2. Eq. (4.17) is the time-series representation of the current through the circuit which can be calculated at time DT_{s} or $(1 - D)T_{\mathrm{s}}$. So these calculations become,

$$i_2(n) = \frac{V}{L}e^{-\alpha DT_{\mathrm{s}}}\left(\beta\cos(\omega DT_{\mathrm{s}}) + \frac{\gamma - \alpha\beta}{\omega}\sin(\omega DT_{\mathrm{s}})\right) + i_1(n) \tag{4.18}$$

where $V = v_b - v_c - i_1(n)R$ and $R = (R_L + R_C + R_{DS})$ for the switch-closed situation. The equations for switch open (Fig. 4.5(b)) are very similar,

$$i_1(n) = \frac{V}{L} e^{-\alpha(1-D)T_s} \left(\beta \cos(\omega(1-D)T_s) + \frac{\gamma - \alpha\beta}{\omega} \sin(\omega(1-D)T_s) \right) + i_2(n) \tag{4.19}$$

where $V = v_D - v_c - i_2(n)R$ and $R = (R_L + R_C + R_{D1})$.

Figure 4.6 demonstrates good agreement between first-order Spice results and MATLAB simulations for a range of duty-cycles from 0 to 60%. Figure 4.7 shows that the two methods agree with an RMS error less than 0.2 V and 0.2 A which equates to less than 2% error of the maximum voltage and current seen throughout the simulation.

The data presented later in Section 5.2 highlight the fact that Kalman filtering works best with a *uniform current profile* i.e., regularly occurring current pulse of the same amplitude. Figure 4.6 shows that a buck circuit in which the MOSFET switch is driven by a fixed duty-cycle gives a large initial current which reduces once the capacitor voltage rises. So, to produce a uniform current profile the duty-cycle needs to be varied to keep the average battery current constant throughout the discharge duration.

The circuit is now simulated for a fixed battery current, the losses within the circuit are analysed and the efficiency improvements achieved by switching the capacitors from a series to

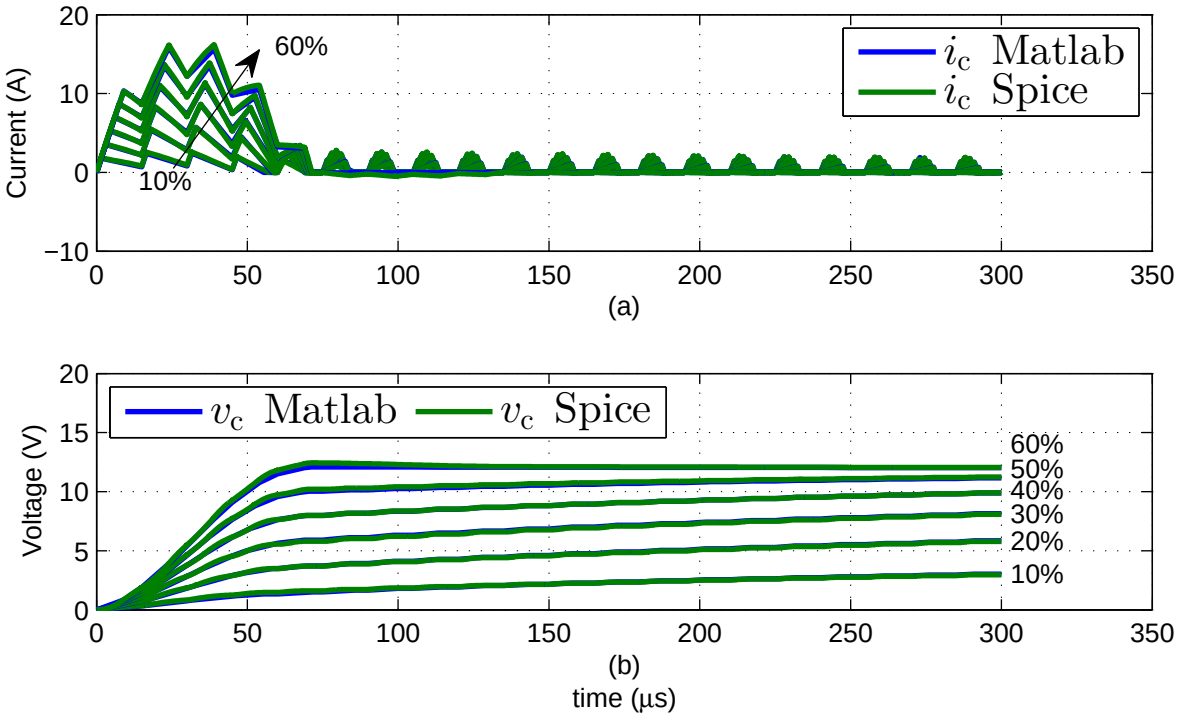

Figure 4.6: MATLAB and Spice simulation results for (a) capacitor current and (b) capacitor voltage for different fixed duty-cycle values

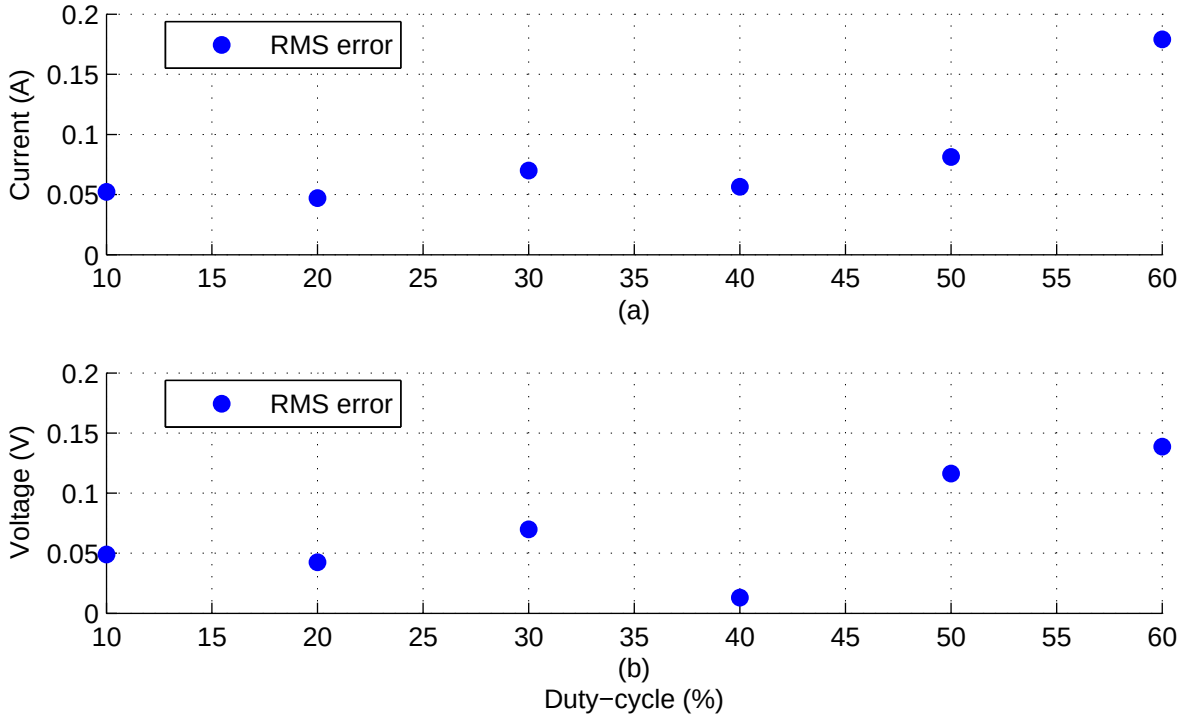

Figure 4.7: RMS error between MATLAB and Spice simulation results for (a) capacitor current and (b) capacitor voltage plotted against duty-cycle

parallel arrangement and vice versa are investigated. Justification for switching the capacitor bank from series to parallel will become clear in Section 4.3.

4.3 Reduced capacitor-size circuit loss analysis

Figure 4.2 shows that battery current is far from the uniform profile required for accurate Kalman filtering if the duty-cycle is kept constant at 50%. The duty-cycle can be varied to keep the average battery-current constant which means that the battery is exposed to a slight current ripple whose frequency is equal to the switching frequency of the power supply. The switching period $T_s = 15$ μs is much shorter than the battery time-constants $\tau_{bulk} = 12.5$ s and $\tau_{surf} = 18$ ms, using component values from Table 5.2. So the battery will not be affected by the switching cycles.

In the simulations the battery current is fixed to an average current of 4 A. A microcontroller continuously tunes the duty-cycle of the power transistor to keep the average battery current (I_b) at 4 A. The duty-cycle is calculated as,

$$D(n) = \frac{I_b}{I_c}, \qquad 0 \leq D \leq 0.8 \tag{4.20}$$

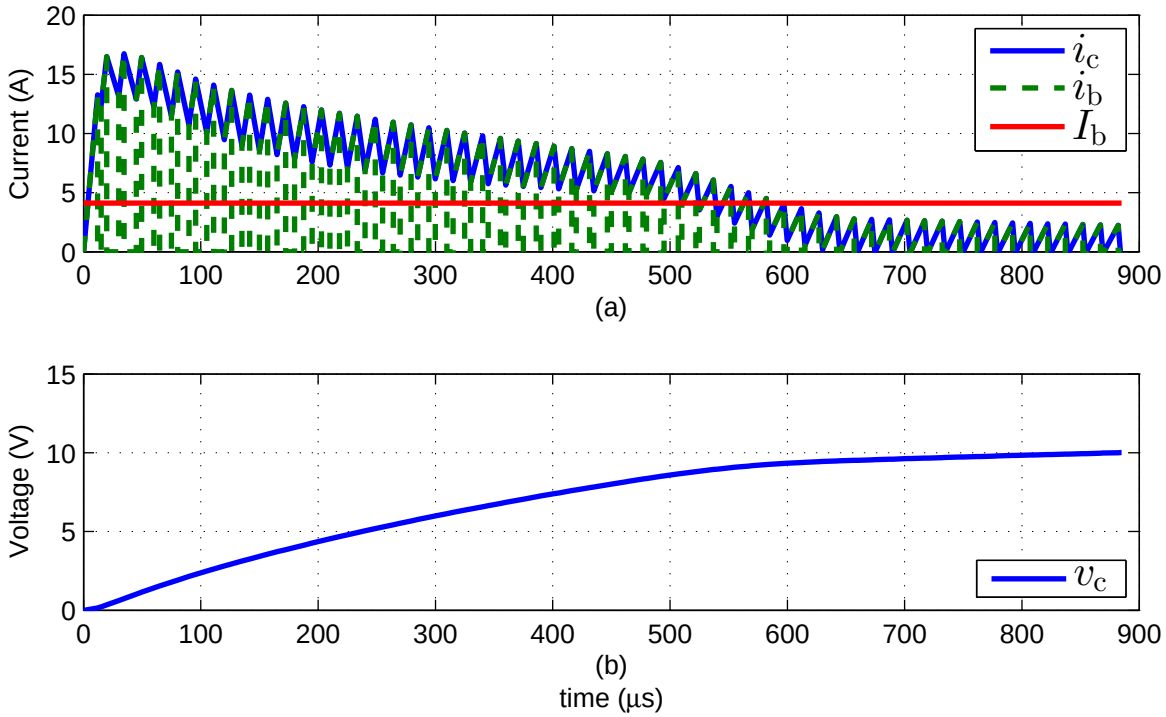

Figure 4.8: MATLAB simulation results for (a) circuit currents and (b) capacitor voltage where the duty-cycle is varied to keep the average battery current (I_b) at 4 A

and limited to a maximum value of 80%. Figure 4.8 shows capacitor current and voltage. This type of control is difficult to implement in Spice since it does not handle variable duty-cycling well.

There are many sources of energy losses in the circuit which reduce conversion efficiency of the buck power supply. These include,

- static losses in parasitic resistances (R_C, R_L, R_{DS} and R_{D1}) and forward volt drops (v_D)
- dynamic losses in switching elements such as diode reverse recovery and MOSFET switching transitions
- MOSFET gate drive losses, and
- control circuit losses i.e., microcontroller power consumption etc.

Static losses resulting from first-order component models can be calculated as I^2R and IV power dissipations in the parasitic elements,

$$P_{\text{static}} = P_{R_C} + P_{R_{DS}} + P_{R_{D1}} + P_{V_D} + P_{R_L} \tag{4.21}$$

where,

$$P_{R_{\mathrm{C}}} = \begin{cases} i^2 R_{\mathrm{C}}, & \text{switch closed} \\ i^2 R_{\mathrm{C}}, & \text{switch open} \end{cases} \tag{4.22}$$

with i being the current flowing through the associated parasitic component at that point in time. Similar calculations can be done for $P_{R_{\mathrm{L}}}$. For $P_{R_{\mathrm{DS}}}$ and $P_{R_{\mathrm{D1}}}$, current is only flowing through the MOSFET switch when the switch is closed so,

$$P_{R_{\mathrm{DS}}} = \begin{cases} i^2 R_{\mathrm{DS}}, & \text{switch closed} \\ 0, & \text{switch open} \end{cases} \tag{4.23}$$

Current is only flowing through the diode when the switch is open,

$$P_{R_{\mathrm{D1}}} = \begin{cases} 0, & \text{switch closed} \\ i^2 R_{\mathrm{D1}}, & \text{switch open} \end{cases} \tag{4.24}$$

and the diode is forward biased,

$$P_{V_{\mathrm{D}}} = \begin{cases} 0, & \text{switch closed} \\ i v_{\mathrm{D}}, & \text{switch open} \end{cases} \tag{4.25}$$

The dynamic losses for the MOSFET can be estimated using,

$$P_{\text{dynamic}} = P_{\text{switch}} + P_{\text{body diode}} + P_{C_{\text{oss}}} \tag{4.26}$$

where,

$$P_{\text{switch}} = \frac{v_{\mathrm{b}} i_{\mathrm{c}}}{2T_{\mathrm{s}}}(t_{\text{on}} + t_{\text{off}}) \tag{4.27}$$

with, t_{on} and t_{off} being the turn-on and turn-off delay times respectively. Also,

$$P_{\text{body diode}} = Q_{\text{rr}} v_{\mathrm{b}} \frac{1}{T_{\mathrm{s}}} \tag{4.28}$$

where Q_{rr} is the body diode reverse-recovery charge. The final dynamic loss term is,

$$P_{C_{\text{oss}}} = \frac{C_{\text{oss}} v_{\mathrm{b}}^2}{2T_{\mathrm{s}}} \tag{4.29}$$

where C_{oss} is the MOSFET output capacitance.

Using datasheet parameters ($t_{\text{on}} = 13$ ns, $t_{\text{off}} = 29$ ns, $Q_{\text{rr}} = 1.4$ nC and $C_{\text{oss}} = 600$ pF) and the worst case current ($i_{\text{c}} = 17$ A) and voltage ($v_{\text{b}} = 16$ V) we get,

$$P_{\text{dynamic}} = 0.3808 + 0.00149 + 0.00512 = 0.387 \text{ mW} \tag{4.30}$$

The observed losses $P_{\text{body diode}}$ and $P_{C_{\text{oss}}}$ equate to around 2% of the dynamic losses and are therefore ignored. The simulations need only account for the added losses of P_{switch}. The dynamic losses in the diode, D1, can be calculated using Eq. (4.28) with Q_{rr} being replaced with the reverse recovery charge of the Schottky diode. However, because the capacitance of the Schottky diode is a thousand times smaller than that of the MOSFET, the dynamic effects of the diode can be ignored. The gate drive and control circuitry are powered from a separate external power supply and therefore do not play part in the power conversion efficiency calculations.

Figure 4.2 shows how battery current (i_{b}) and capacitor current (i_{c}) vary with time. Relating this back to i_1 and i_2 it was observed that a trapezoidal integration between the current points multiplied by the voltage drop at that point in time will give the rate of energy dissipation in the circuit.

An energy balance calculation can be used to check if all energy is accounted for. Here all energy not stored in the capacitor is grouped as wasted energy (E_{waste}),

$$E_{\text{waste}} = \int P_{\text{waste}} \; dt + E_{\text{L}} \tag{4.31}$$

where E_{L} is the energy stored in the inductor,

$$E_{\text{L}} = \frac{1}{2} L i^2 \tag{4.32}$$

Figure 4.10 shows that the energy stored in the inductor does not contribute to the wasted energy. Now,

$$E_{\text{in}} = E_{\text{waste}} + E_{\text{c}} \tag{4.33}$$

where E_{c} is calculated as,

$$E_{\text{c}} = \frac{1}{2} C v_{\text{C}}^2 \tag{4.34}$$

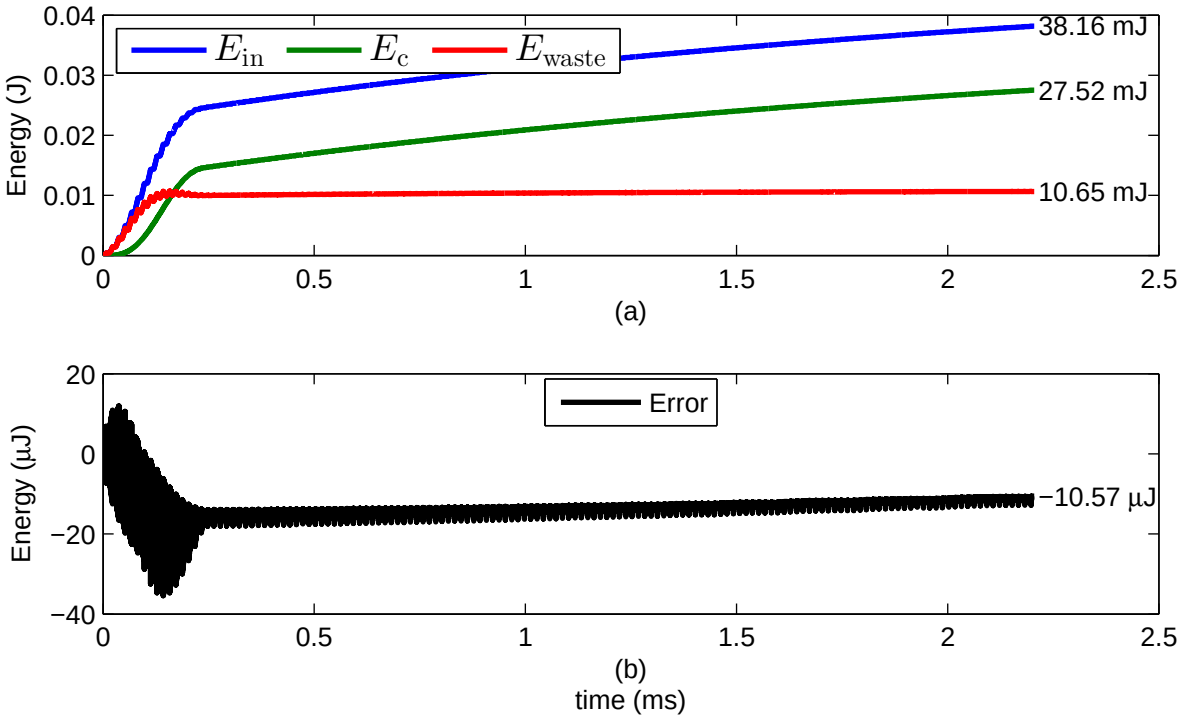

Figure 4.9: MATLAB simulation results for (a) input energy (E_{in}), stored energy (E_{c}) and wasted energy (E_{waste}) for duty-cycle fixed at 50% and (b) discrepancy between input energy and (stored energy plus wasted energy) showing a maximum error less than 0.5%

The overall circuit efficiency can be calculated as,

$$\eta = \frac{E_{\text{in}} - E_{\text{waste}}}{E_{\text{in}}} \times 100 \tag{4.35}$$

Figure 4.9 shows the results of the energy balance calculation from the MATLAB simulation. The sum of the energies agrees with an error of less than 0.5%.

Figure 4.10 shows an area graphic highlighting which parasitic components contribute to the wasted energy. It can be observed that the I^2R losses through the capacitor and MOSFET parasitic resistances contribute the most at 32% and 20% respectively, closely followed by the static I^2R losses in the diode at 19%. Minimizing the current through the output stage will minimise the energy lost in these components. Note, Figs. 4.9 and 4.10 are for a fixed duty-cycle case charging a 550μF capacitor to 10 V.

Figure 4.11 shows the same simulation run but now the duty-cycle of the MOSFET is allowed to change in order to keep the average battery current constant at 4 A. Here the energy stored in the capacitor remains the same $\approx$ 27.5 mJ. Importantly though the wasted energy has reduced by over 20%, allowing the duty-cycle to vary has reduced the time to full charge from over 2 ms to under 1 ms.

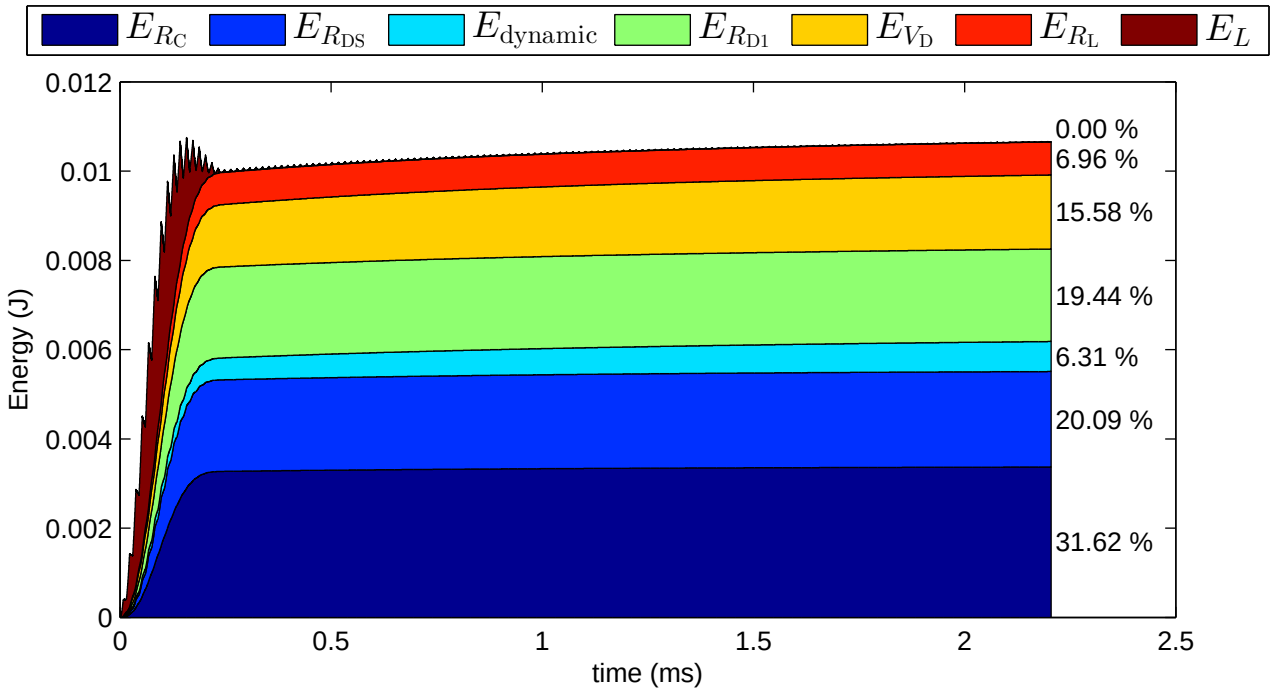

Figure 4.10: MATLAB simulation results showing breakdown of wasted energy into individual energy components with percentage contribution of each parasitic component and E_L for 50% dutycycle

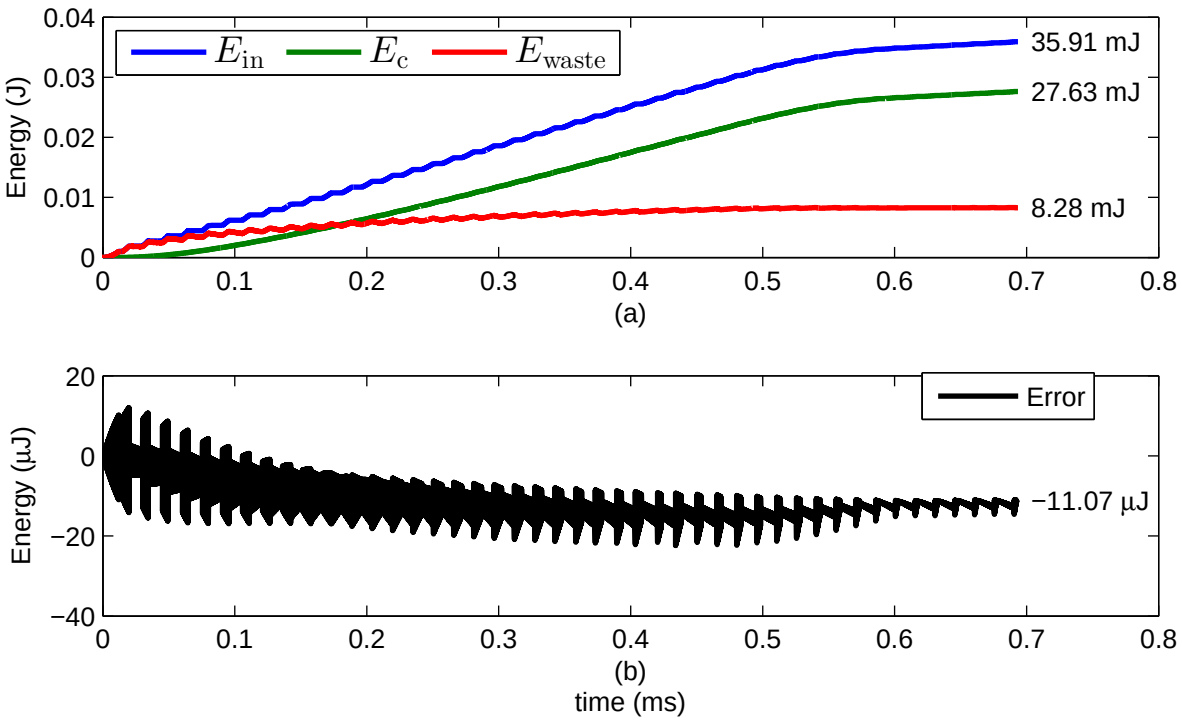

Figure 4.11: MATLAB simulation results for (a) input energy (E_{in}), stored energy (E_c) and wasted energy (E_{waste}) for constant input current (variable duty-cycle) and (b) discrepancy between input energy and (stored energy plus wasted energy)

Figure 4.12 shows how each parasitic effect contributes to the overall wasted energy. An interesting observation can be made on how the energy dynamics shift between the different parasitic effects. For example the resistive losses in the switch now contribute a lesser percentage

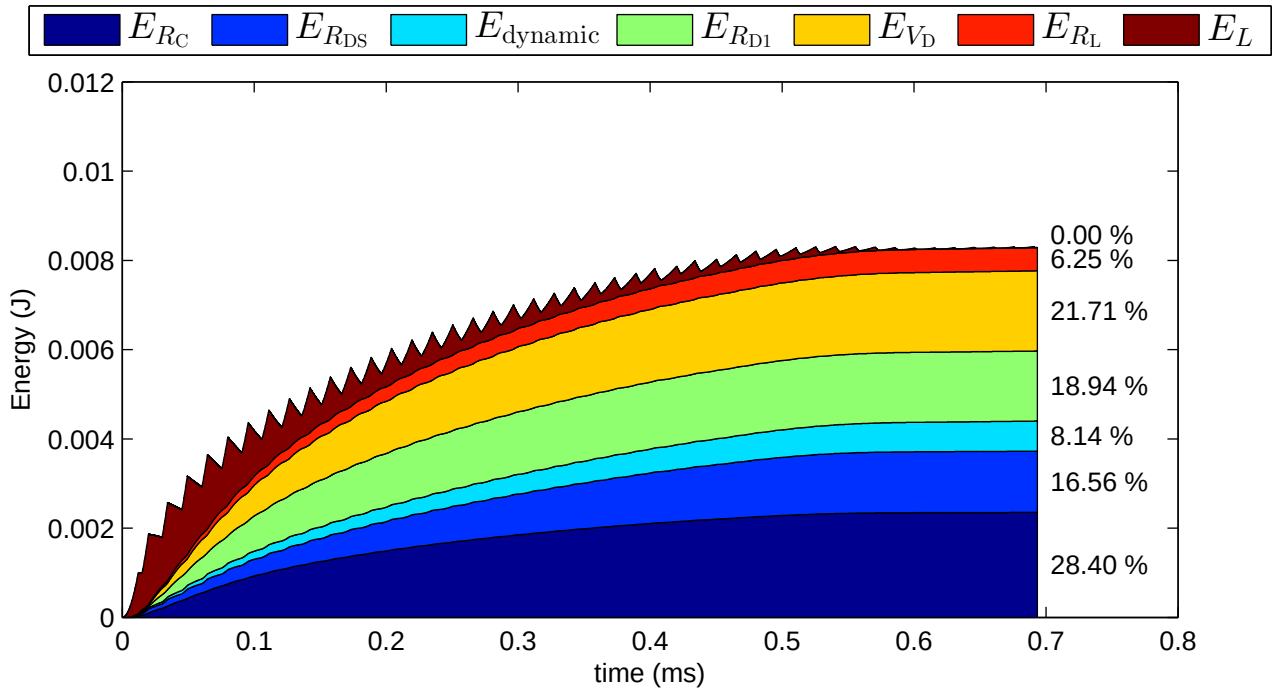

Figure 4.12: MATLAB simulation results showing breakdown of wasted energy into individual energy components with percentage contribution of each parasitic component and E_L for constant input current (variable duty-cycle).

of the wasted energy whereas the IV losses across the diode contribute a higher percentage loss. From a design point of view these graphics provide insights into which parameters need to be tuned in-order to maximise conversion efficiency. The power equations show that minimising the average current (i_c) flowing through these components will give lower E_{waste} values. Given that v_b and i_b are both assumed constant, the only mechanism for reducing i_c would be to increase capacitor voltage more rapidly. This can be achieved by reducing the capacitance value, but the storage capacity of the capacitor bank should not be compromised. So, arranging a capacitor bank in a series configuration will increase the capacitor voltage rapidly and reduce the output current through increased series resistance. Switching the capacitor bank to a parallel configuration when a high enough voltage level is reached maintains the capacitor-banks original storage capacity. The effect of series/parallel switching on overall efficiency is investigated next.

Figure 4.13(a) shows that with capacitors arranged in series the parasitic resistance is doubled. Figure 4.13(b) shows the capacitors arranged in parallel: this configuration increases the capacitor bank storage capacity and reduces the overall parasitic resistance. The super-capacitor bank consists of eight PowerStor capacitors (details in Chapter 3) arranged in two banks of four capacitors giving the bank in a parallel configuration a maximum voltage of 10 V.

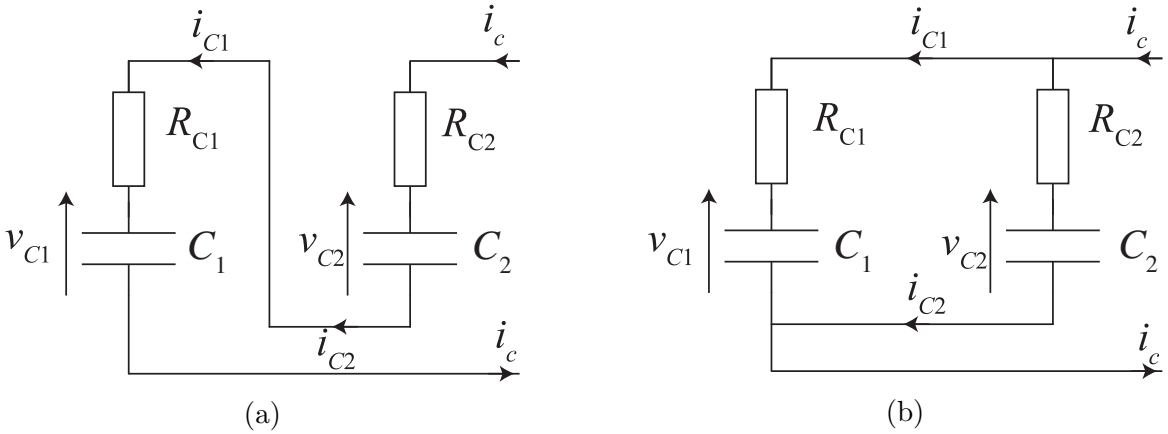

Figure 4.13: Diagram showing (a) capacitors arranged in series and (b) in parallel.

When arranged in series the maximum bank voltage increases to 20 V, however the capacitor bank cannot be charged to more than the battery voltage (as explained in Section 3.2). So, the control system is programmed to charge the capacitor bank to 1.5 V less than the battery voltage before switching to a parallel arrangement. Finally the bank is charged to a maximum voltage of 10 V to achieve the same energy storage as the above cases. Figure 4.14 shows the current and voltage behaviour for the capacitor bank when the battery voltage is 12 V.

Capacitors with different capacitance values and ESR will contribute an additional energy loss when these capacitors are switched from series to parallel. This additional energy loss also needs to be considered. Section 3.6 investigated the variation in supercapacitor parameters

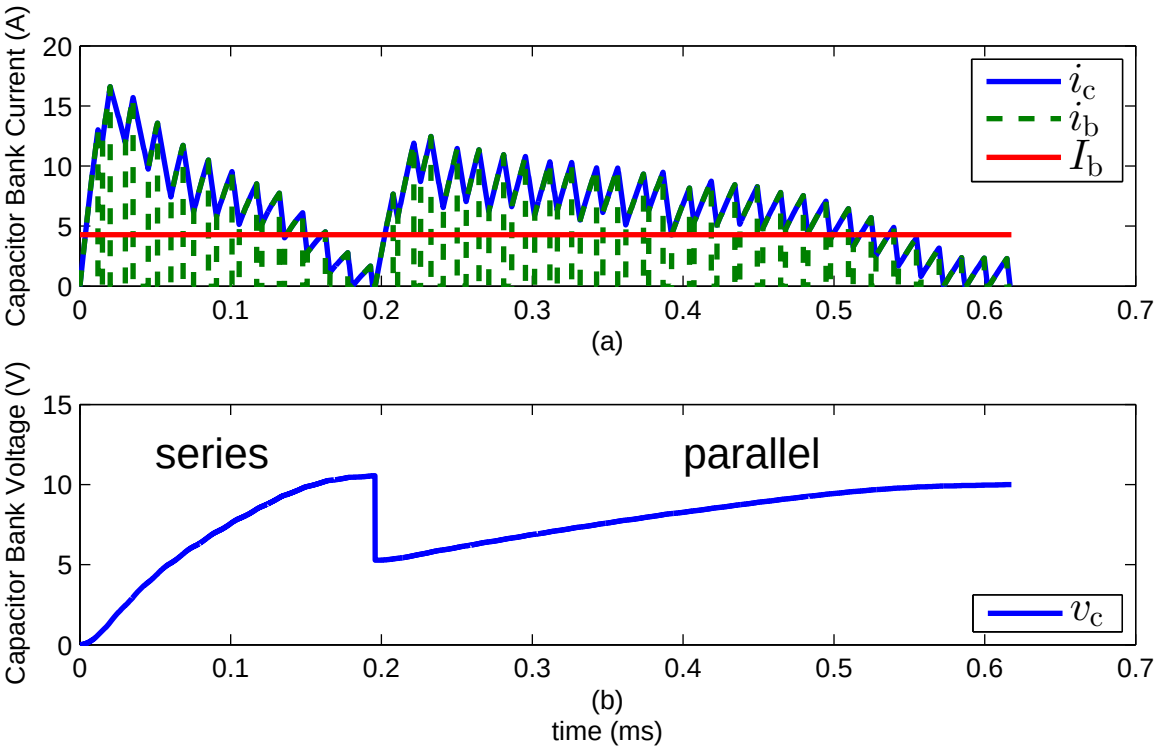

Figure 4.14: MATLAB simulation results for (a) circuit currents and (b) capacitor bank voltage showing the switch from series to parallel at ≈ 0.2 ms

showing that both ESR and capacitance can vary by 20% from the quoted datasheet values. If the worst-case mismatch situation ±20% on both ESR and capacitance is considered, then the energy lost during series-to-parallel switching can be calculated by taking the difference between V_{C1} and V_{C2} at the end of the series-charging stage. Using the relationship between capacitor current and voltage the difference in voltage was calculated as,

$$\Delta V(t) = v_{C1}(t) - v_{C2}(t) = \left(\frac{1}{C_1} - \frac{1}{C_2}\right) \int_0^{t_1} i_{\mathrm{c}}\ dt \tag{4.36}$$

where t_1 is the point in time where the capacitor bank is switched from series to parallel. The instantaneous power wasted during balancing can now be calculated as,

$$P_{\mathrm{balancing}}(t) = \frac{\Delta V(t)^2}{R_{C1} + R_{C2}} \tag{4.37}$$

However, as time progresses ΔV reduces therefore the integral of power over time needs to be calculated to get the total energy wasted during balancing. A simple Euler simulation of this process produced the results shown in Figure 4.15 where the supercapacitor bank was charged to a maximum of 16 V to maximise $\Delta V(0)$. Alternatively,

$$E_{\mathrm{balancing}} = \frac{1}{2}\frac{C_1 C_2}{C_1 + C_2}\Delta V(0)^2 \tag{4.38}$$

To produce Fig. 4.15, the supercapacitor values and resistances were set to give worst case mismatch ($\pm 3\sigma$ from the mean, Fig. 3.10): $C_1 = 237.5\ \mu$F, $R_{C1} = 24.8\ \mathrm{m}\Omega$ and $C_2 = 312.5\ \mu$F, $R_{C2} = 24.8\ \mathrm{m}\Omega$. Note: the capacitor charging current is fixed to 10 A in this simulation for simplicity; this does not effect the energy wasted during balancing as no external current is flowing during balancing. The energy wasted during balancing can now be calculated by integrating I^2R for the period after 21.2 s which gives $E_{\mathrm{balance}} = 0.26$ mJ. Figure 4.16 shows the energy balance for series-parallel switching case where $E_{\mathrm{waste}} = 4.96$ mJ so the energy wasted during supercapacitor balancing equates to 5% at worst case, and is therefore ignored.

Figure 4.16 shows the energy balance calculation for series/parallel switching. Significantly the wasted energy has dropped further, with nearly a 50% improvement relative to the fixed duty-cycle case. Figure 4.17 shows how each parasitic component contributes to the wasted

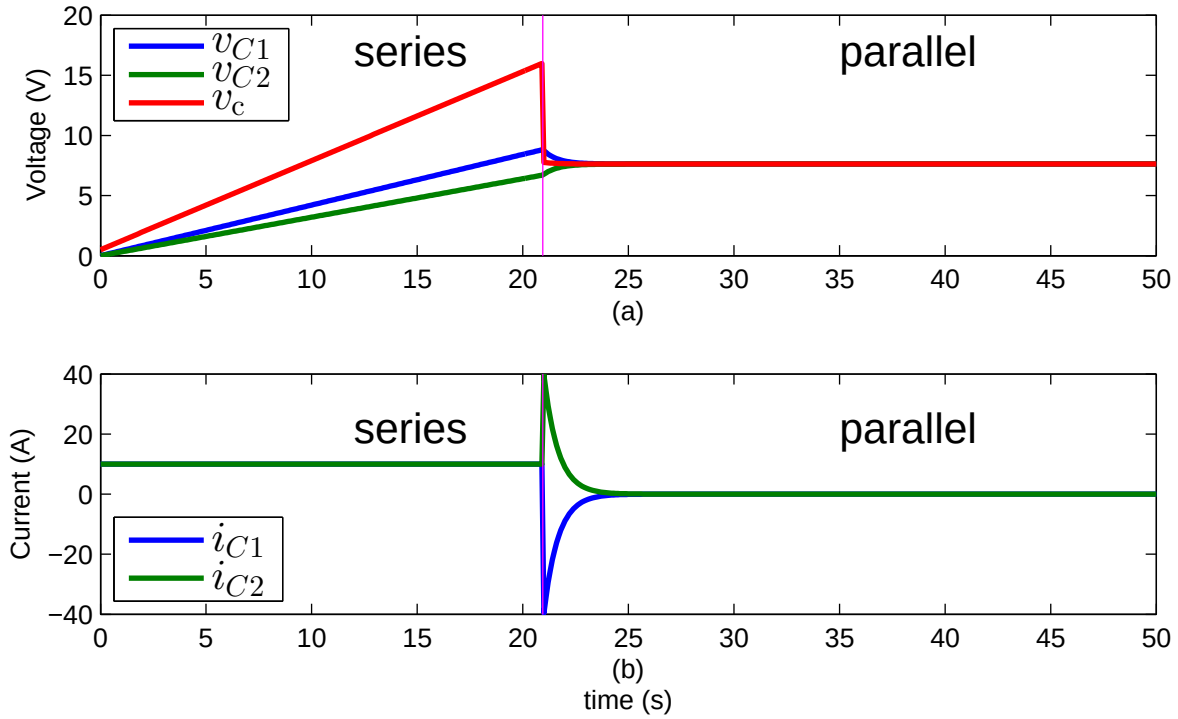

Figure 4.15: MATLAB simulation of supercapacitor balancing process showing (a) capacitor voltages and (b) capacitor currents. At $t = 21.2$ s, the capacitors are switched from series to parallel configuration

energy. The figure shows that the contribution from the capacitor ESR (E_{R_C}) has increased as a percentage of E_{waste} from 28.4% to 30.65%; this is unavoidable and preferably this contribution

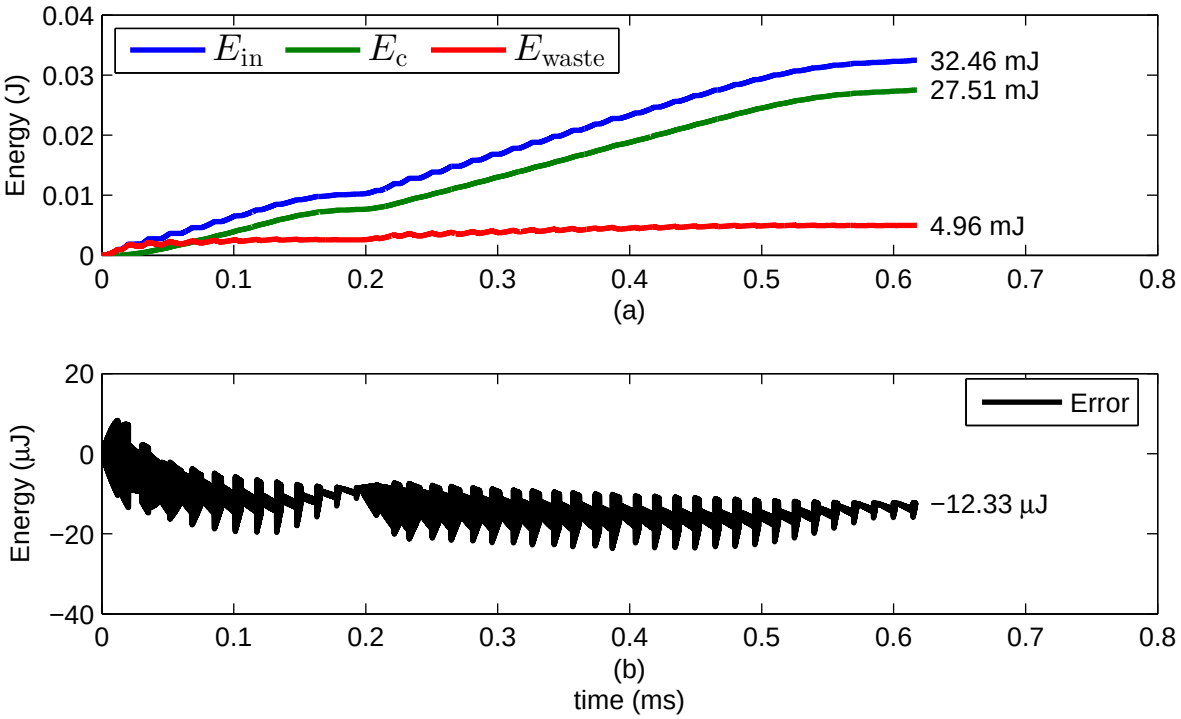

Figure 4.16: MATLAB simulation results for (a) input energy (E_{in}), stored energy (E_c) and wasted energy (E_{waste}) and (b) discrepancy between input energy and stored energy plus wasted energy

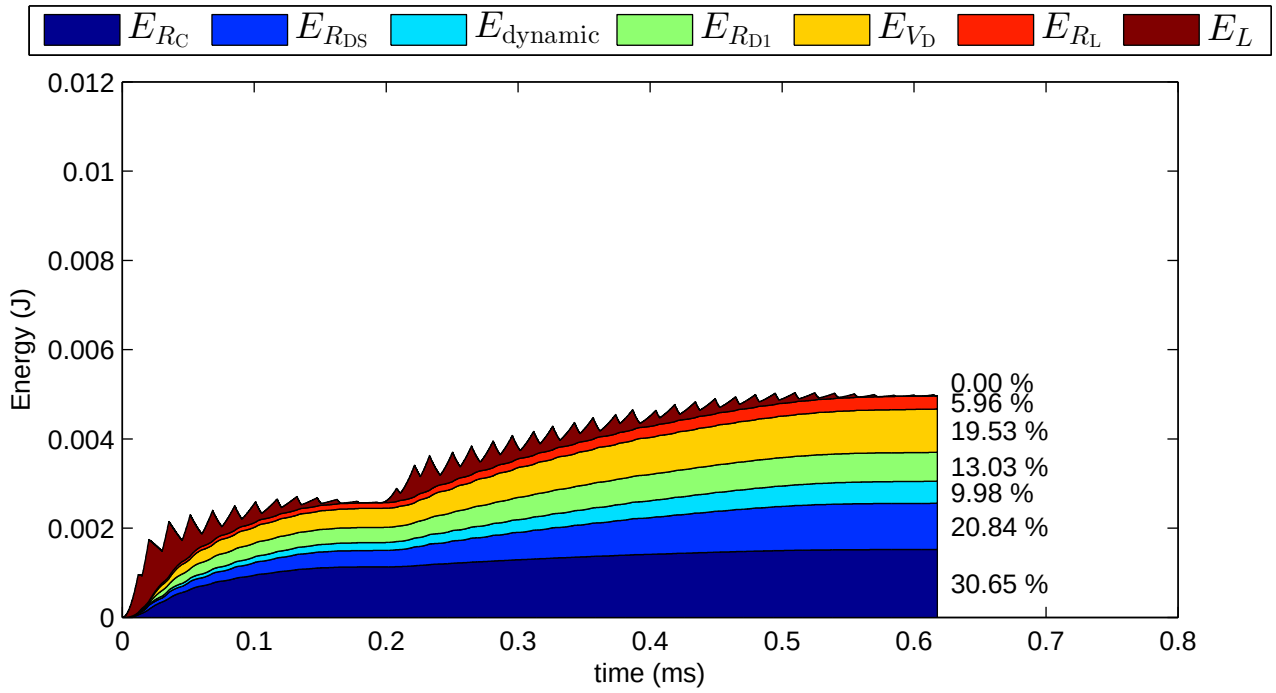

Figure 4.17: MATLAB simulation results showing breakdown of wasted energy into individual energy components with percentage contribution of each parasitic component and E_L. Note the same vertical scale is used as in Figure 4.12 and 4.10

should be 100% of the wasted energy.

The assumption made here is that the circuitry required to switch the supercapacitor bank is lossless which, when realised with solid-state switches, is a reasonable assumption. The series/parallel switching regime can be extended by adding two more capacitor banks and with appropriate switching techniques arranged in series and parallel. This extended implementation gives a wasted energy of 3.69 mJ which is a further improvement on the energy efficiency of the switching circuit. Table 4.2 summarises these improvements for different input voltages.

Table 4.2: Simulated efficiency improvements for series/parallel switching 550 μF capacitors

Power supply regime	**Input voltage**	**Energy wasted**	η
Fixed duty-cycle	12 V	10.65 mJ	72.1%
	16 V	17.66 mJ	60.9%
Variable duty-cycle	12 V	8.28 mJ	76.9%
	16 V	10.96 mJ	71.8%
Series/parallel 2 capacitors	12 V	4.96 mJ	84.7%
	16 V	5.96 mJ	82.4%
Series/parallel 4 capacitors	12 V	3.69 mJ	88.2%
	16 V	4.25 mJ	86.8%

Table 4.2 shows that adding more capacitor banks to the series/parallel switching regime further improves the efficiency but at a diminishing rate. Between the variable duty-cycle situation and the four capacitor series/parallel switching regime there is a 16% efficiency improvement in the simulations for the same input voltage. This efficiency could be increased further by use of more advanced power converters such as a SEPIC converter, by implementing zero-current switching, or other forms of more advanced switch-mode power-supply.

4.4 Full capacitor-size circuit loss analysis

The proof-of-concept simulation results for 550 μF capacitors presented can be scaled to full simulations for the 55 F supercapacitor values. Figure 4.18 shows simulation results for the 55 F supercapacitor bank showing the difference in energy wasted between a parallel-only configuration and series/parallel switching regime.

Figure 4.19 shows the actual measured energy balance between the parallel-only configuration and series/parallel switching regime. There are slight differences between the simulations and the measurements, namely: E_{waste} is slightly lower in the simulations and the energy stored in the supercapacitor bank is slightly lower in the measurements. The lower simulated E_{waste} is a result of using simplified models and not including additional parasitic losses within each component and also the simulation assumes that the circuitry responsible for the series/parallel switching has zero series resistance. The difference in stored energy between simulation and measurements arises because the microcontroller, responsible for terminating supercapacitor charging, does not take into account the raised supercapacitor terminal voltage resulting from the voltage drop across R_{C}.

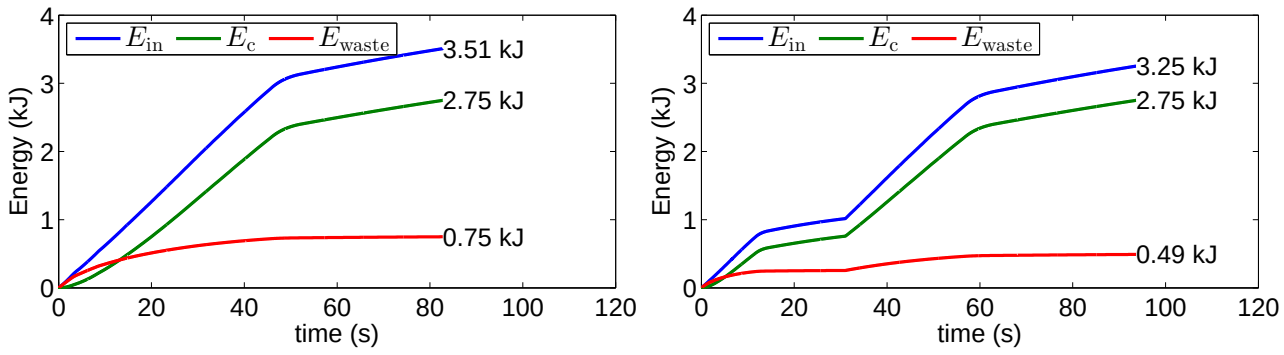

(a) (b)

Figure 4.18: MATLAB simulation results for (a) input energy (E_{in}), stored energy (E_{c}) and wasted energy (E_{waste}) for the variable duty-cycle case and (b) energy balance for series/parallel switching regime for 55 F supercapacitors

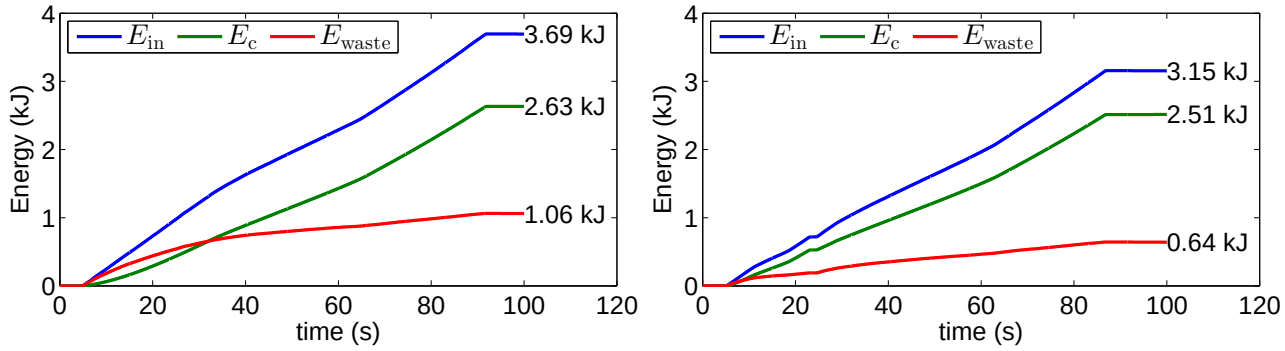

(a) (b)

Figure 4.19: Measured results for (a) input energy (E_{in}), stored energy (E_c) and wasted energy (E_{waste}) for the variable duty-cycle case and (b) energy balance for series/parallel switching regime using 55 F supercapacitors

Table 4.3: Simulated versus actual efficiency improvements for series/parallel switching 55 F supercapacitor

Power supply regime	**Input voltage**	**Energy wasted**	η
Variable duty-cycle simulated	12 V	0.75 kJ	78.6%
Series/parallel 2 cap simulated	12 V	0.49 kJ	84.9%
Variable duty-cycle measured	12 V	1.06 kJ	71.3%
Series/parallel 2 cap measured	12 V	0.64 kJ	79.7%

Table 4.3 summarises these results and shows that the simulations overestimate the actual efficiency by $\approx 6\%$. However the efficiency improvement afforded by series/parallel switching is around 8%, and this figure can be improved further as discussed in this Section.

4.5 Chapter summary

In this chapter a switching power supply used to charge a supercapacitor bank from a battery is successfully modelled. The losses associated with first-order component models are analysed and compared. Switching the capacitor bank from series to parallel configuration during the charging process reduces the amount of energy wasted by as much as a factor of two compared to fixed duty-cycle charging. An efficiency improvement of 8% was measured when the series/-parallel switching scheme was implemented. This is a significant improvement for such a simple circuit and can be improved further by selecting components with lower parasitic resistances or using more advanced switch-mode power-supply topologies.

Chapter 5

NiMH battery equivalent circuit parameter extraction and evaluation

The test results shown in this chapter are of a moderately healthy battery module considered to be at 75% state-of-health, unless stated otherwise. The following sections describe two methods, impedance spectroscopy and extended Kalman filtering, for extracting equivalent circuit parameters and confirming the battery equivalent circuits covered in Section 2.4.

5.1 Impedance spectroscopy

5.1.1 Internal resistance

Impedance spectroscopy (EIS) was covered in Section 2.5.1 where the impedance response curves for two battery equivalent circuits are created based on parameter values found in the literature. Figs. 2.12 to 2.14 in Section 2.5.1 showed how the individual components of the battery circuit contribute to the overall impedance curve, but in reality these internal parameters cannot be accessed with measurement devices so the individual internal parameters can only be estimated based on terminal measurements. EIS is a small-signal terminal measurement technique for estimating these internal parameters at a particular bias point. Figure 2.14 shows a plot of battery impedance (Z) measured at the battery terminals. Recreating these figures with actual battery data should allow estimation of the internal parameters. This section will focus on the internal resistance component which was identified as the intersection of the Nyquist plot with the real axis.

Figure 5.1 shows the impedances of four battery modules of which Module 0 has suffered "catastrophic" battery failure while the remaining three modules are of similar SOH. A quick impedance measurement at 0.1 Hz could be a good indicator for catastrophic battery failure.

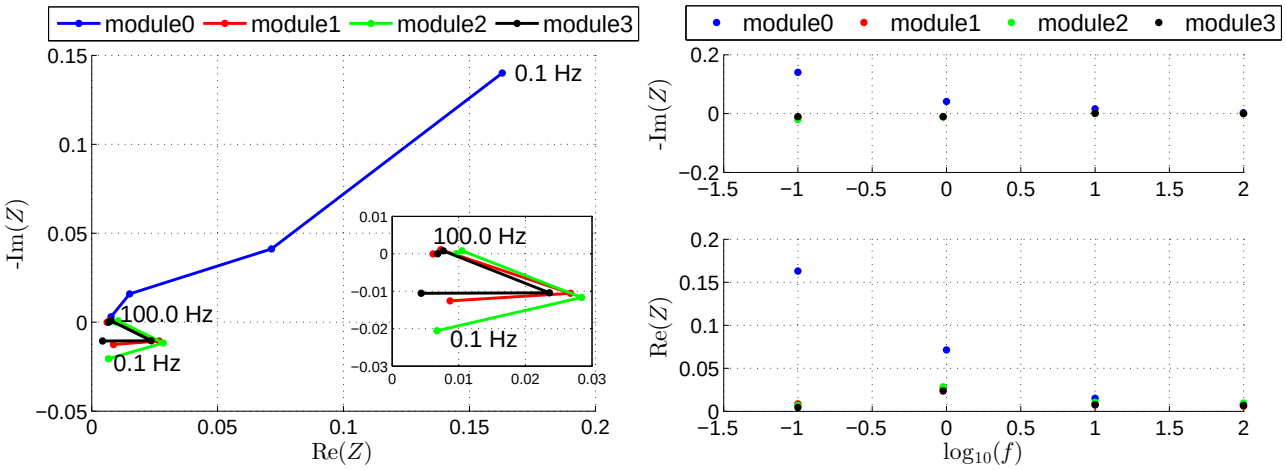

(a) (b)

Figure 5.1: Comparison between four battery modules (a) Nyquist plots (b) Impedance versus frequency

The real impedance of the battery modules shows a slight resonant peak at 1 Hz, however the imaginary impedances do not show such behaviour. When there is no apparent peak in the imaginary impedance of the battery module it is difficult to quantify the capacitive components of the battery equivalent circuit. The imaginary impedances of the battery modules become negative which is an indication of an inductive component within the battery.

5.1.2 Diffusion-polarisation and bulk-surface time constants

RC pairs (diffusion and polarisation or bulk-surface) show as a bump on the Nyquist plots. The Nyquist plots in Figure 5.1 do not show this effect as outlined in [40]. It is likely that the results presented by Kuhn et al [40] have not been reproduced here because of differences in measurement equipment and batteries. Module 0 does show the predicted effects of the Warburg impedance (Section 2.3.3) i.e. a 45° impedance curve at low frequencies. The *RC* time constants cannot be predicted from these measurements.

5.2 Kalman filtering approach

Some of the properties of extended Kalman filtering need to be investigated before detailing the EKF approach. The Optimal State Estimation text [92] provided useful guidance for battery modelling and the EKF technique.

5.2.1 Extended Kalman filtering

A Kalman filter continuously updates state-estimates as more measurement data become available i.e., states are periodically updated based on actual measurements from a system. The filter output is projected into the future through knowledge of the system (system model) which is easily done for a linear system. Batteries and battery models are inherently nonlinear which hinders the filter's ability to predict the next state. The extended Kalman filter (EKF) attempts to linearise the system through a first-order Taylor expansion of the state equation, which introduces errors.

The errors that are introduced as a result of linearisation need to be absorbed in the noise-covariance matrices $\mathbf{P}$, $\mathbf{Q}$ and $\mathbf{R}$. $\mathbf{P}$ is the covariance of the estimation error i.e., the confidence in our state-estimate, $\mathbf{Q}$ is the covariance of process noise i.e., how accurate is the system model; and $\mathbf{R}$ is the covariance of the measurement error. The filter can be empirically tuned to compensate for linearisation errors, i.e., guess and check values for the noise-covariance matrices until the results are satisfactory.

A known voltage response was generated by simulating current through a battery equivalent circuit with known internal parameters (refer to Section 2.4 for model equation). Because the simulated voltage traces are generated by a known model, all error-covariance matrices are known. This gives the ability to estimate the correction factor required as a result of linearisation errors. However, there is still one flaw in this approach when it is applied to actual voltage and current traces measured from a battery: the battery model chosen may not exactly match the battery responses hence confidence ($\mathbf{Q}$) is difficult to estimate. Chapter 2 highlighted the many short comings of the various battery models; these model deficiencies map to an increase in $\mathbf{Q}$ i.e., reduced confidence in the system model.

A simplified battery model, Figure 5.2, is used to tune the filter. The state equations describing this model behaviour are similar to those presented in Section 2.4.3.

The discrete-time system equations, slightly modified from Section 2.5.2, are,

$$\begin{aligned} \mathbf{x}_k &= f_{k-1}(\mathbf{x}_{k-1}, u_{k-1}, w_{k-1}) \\ \mathbf{y}_k &= h_k(\mathbf{x}_k, \mathbf{v}_k) \\ w_k &= (0, Q_k) \\ \mathbf{v}_k &= (0, R_k) \end{aligned} \tag{5.1}$$

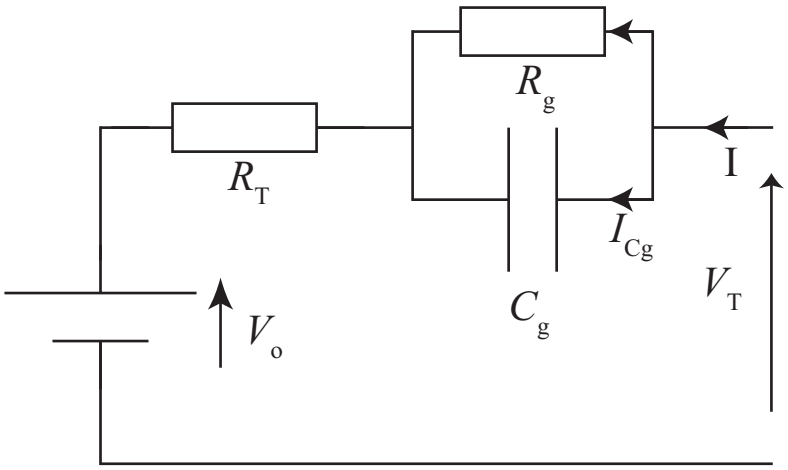

Figure 5.2: Simplified battery model used to investigate tuning of EKF noise-covariance parameters. R_g and C_g are grouped diffusion and polarisation resistance and capacitance respectively

where the k subscript indicates the time step, $\mathbf{x}_k$ is the state-vector, u is a time dependent input, ω is zero-mean Gaussian process noise with $\sigma^2 = Q$, $\mathbf{y}_k$ is the measurement vector, v is zero-mean Gaussian measurement noise with $\sigma^2 = R$.

An initial estimate of the state variable is required to start the Kalman filter. The sections that introduce actual battery measurements therefore first start with a section on initial estimation of internal battery parameters before examining the extended Kalman filter results. Theoretically the filter is initialised with,

$$\begin{aligned} \hat{\mathbf{x}}_0^+ &= E[\mathbf{x}_0] \\ \mathbf{P}_0^+ &= E[(\mathbf{x}_0 - \hat{\mathbf{x}}_0)(\mathbf{x}_0 - \hat{\mathbf{x}}_0)^{\mathrm{T}})] \end{aligned} \tag{5.2}$$

where the $\hat{\mathbf{x}}_k^+$ notation is the predicted state *estimate* at time k updated with measurement information, the $E[\cdot]$ notation is the expected value and $\mathbf{A}^{\mathrm{T}}$ denotes the matrix (or vector) transpose.

The nonlinear system equations are linearised through Taylor's approximation so the partial-derivatives of the matrices are also calculated,

$$\begin{aligned} \mathbf{F}_{k-1} &= \left.\frac{\partial f_{k-1}}{\partial \mathbf{x}}\right|_{\hat{\mathbf{x}}_{k-1}^+} \\ \mathbf{L}_{k-1} &= \left.\frac{\partial f_{k-1}}{\partial \mathbf{w}}\right|_{\hat{\mathbf{x}}_{k-1}^+} \end{aligned} \tag{5.3}$$

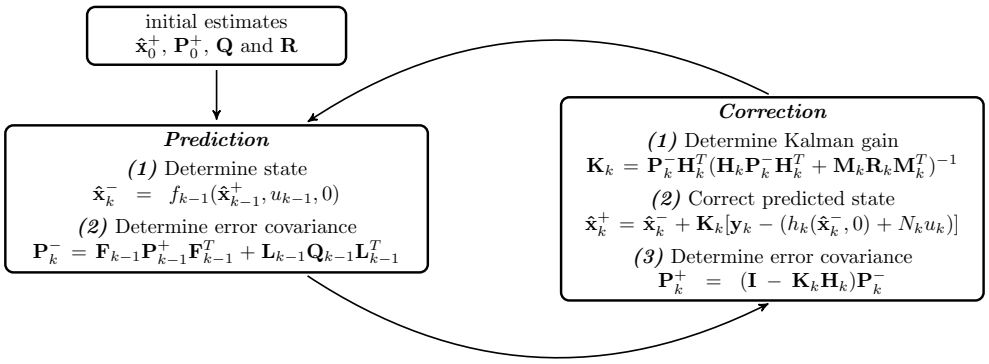

Figure 5.3: Kalman filter update loop where the flow through both prediction and correction phases is from top to bottom.

With these matrices in place the state estimate and estimation-error covariance can be updated using the following two equations,

$$\begin{aligned} \mathbf{P}_k^- &= \mathbf{F}_{k-1}\mathbf{P}_{k-1}^+\mathbf{F}_{k-1}^{\mathrm{T}} + \mathbf{L}_{k-1}\mathbf{Q}_{k-1}\mathbf{L}_{k-1}^{\mathrm{T}} \\ \hat{\mathbf{x}}_k^- &= f_{k-1}(\hat{\mathbf{x}}_{k-1}^+, u_{k-1}, 0) \end{aligned} \tag{5.4}$$

where $\hat{x}_k^-$ notation is the predicted state estimate at time k before it is updated with measurement information. The prediction can now be updated with the measurements so the following partial derivatives are calculated,

$$\begin{aligned} \mathbf{H}_k &= \left.\frac{\partial h_k}{\partial \mathbf{x}}\right|_{\hat{\mathbf{x}}_k^+} \\ \mathbf{M}_k &= \left.\frac{\partial h_k}{\partial \mathbf{v}}\right|_{\hat{\mathbf{x}}_k^+} \end{aligned} \tag{5.5}$$

Now the state estimate is updated with the measured data as follows,

$$\begin{aligned} \mathbf{K}_k &= \mathbf{P}_k^-\mathbf{H}_k^{\mathrm{T}}(\mathbf{H}_k\mathbf{P}_k^-\mathbf{H}_k^{\mathrm{T}} + \mathbf{M}_k\mathbf{R}_k\mathbf{M}_k^{\mathrm{T}})^{-1} \\ \hat{\mathbf{x}}_k^+ &= \hat{\mathbf{x}}_k^- + \mathbf{K}_k[\mathbf{y}_k - h_k(\hat{\mathbf{x}}_k^-, 0)] \\ \mathbf{P}_k^+ &= (\mathbf{I} - \mathbf{K}_k\mathbf{H}_k)\mathbf{P}_k^- \end{aligned} \tag{5.6}$$

The overall Kalman filter update loops are shown in Figure 5.3. For the battery model shown in Figure 5.2,

$$\begin{aligned}\mathbf{x}_k &= f_{k-1}(\mathbf{x}_{k-1}, u_{k-1}, w_{k-1}) \\ &= \begin{bmatrix} 1 - \frac{\Delta t}{C_\mathrm{g} R_\mathrm{g}} & 0 \\ 0 & 0 \end{bmatrix} \mathbf{x}_{k-1} + \begin{bmatrix} \frac{\Delta t}{C_\mathrm{g}} \\ R_\mathrm{T} \end{bmatrix} u_{k-1} + w_{k-1} \\ \mathbf{y}_k &= h_k(\mathbf{x}_k, \mathbf{v}_k) \\ &= v_\mathrm{o} + \begin{bmatrix} 1 & 1 \end{bmatrix} \mathbf{x}_k + \mathbf{v}_k \end{aligned} \tag{5.7}$$

An arbitrary set of component values were used in a Euler simulation to generate the voltage responses from the battery model as a result of a square-wave current input. The result of the simulation is shown in Figure 5.4. The open-circuit voltage is set to zero to further simplify the model ($v_\mathrm{o} = 0$ V).

Kalman filtering only works if the battery model parameters i.e., R_T, R_g and C_g, are known. Extended Kalman filtering can be used to identify the battery model parameters by adding extra variables to $\mathbf{x}_k$ and some arbitrary noise, w_p, to allow the filter to adjust. For this simplified

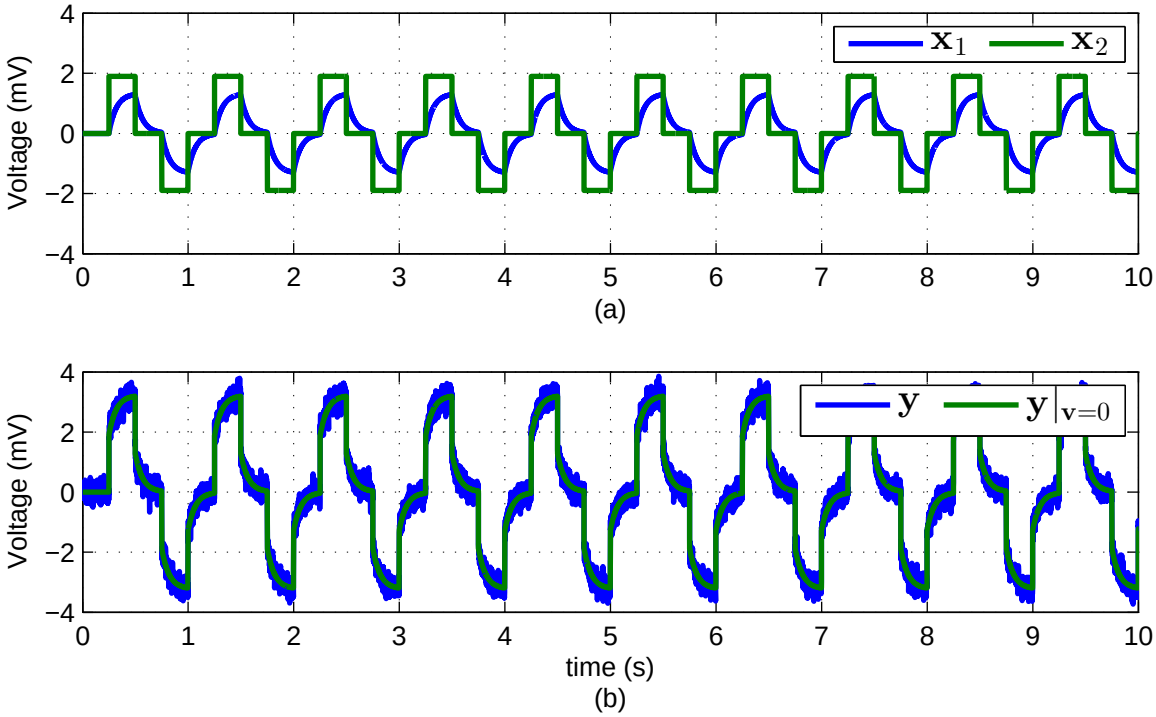

Figure 5.4: Euler simulation results of the simplified battery model presented in Figure 5.2 subjected to 0.25 s of ±3.8 A current pulse with 0.25 s rest between subsequent positive and negative pulses. Panel (a) shows the voltage across C_g (x_1) and the voltage across R_T (x_2); (b) shows y and y without noise where $R = 0.2$ mV, $R_\mathrm{T} = 0.5$ mΩ, $R_\mathrm{g} = 0.35$ mΩ and $C_\mathrm{g} = 200$ F.

model there are three different variables which need to be identified which can be grouped into an unknown parameter array, $\mathbf{p}$. So $\mathbf{x}_k$ becomes,

$$\mathbf{x}_k = \begin{bmatrix} \mathbf{x}_1 & \mathbf{x}_2 & \mathbf{p} \end{bmatrix}^{\mathrm{T}} \tag{5.8}$$

and w_k becomes,

$$w_k = \begin{bmatrix} (0, Q_k) & w_p \end{bmatrix}^{\mathrm{T}} \tag{5.9}$$

where, $(0, Q_k)$ represents the process noise associated with the state variables i.e., $\mathbf{x}_1$ and $\mathbf{x}_2$ and w_p represents the process noise associated with the additional elements of $\mathbf{p}$. If more unknown parameters are added to the EKF state-equations the computational complexity of the filter will increase as the size of all matrices is proportional to the dimension of $\mathbf{p}$. The EKF can be expanded to identify all the component values of the model presented in Figure 5.2 from the simulated voltage responses presented in Figure 5.4. The state equations now become,

$$\mathbf{x}_k = \begin{bmatrix} \mathbf{x}_1 & \mathbf{x}_2 & a & b & c \end{bmatrix}^{\mathrm{T}} \tag{5.10}$$

where, $a = 1/C_{\mathrm{g}}$, $b = 1/R_{\mathrm{g}}$ and $c = R_{\mathrm{T}}$. Here, a and b are chosen to be the reciprocals of C_{g} and R_{g} respectively because this simplifies the partial differentials required to complete the EKF equations. The overall equations now become,

$$\begin{aligned} \mathbf{x}_k &= f_{k-1}(\mathbf{x}_{k-1}, u_{k-1}, w_{k-1}) \\ &= \begin{bmatrix} (1 - ab\Delta t)\mathbf{x}_1|_{k-1} + a\Delta t u_{k-1} + w_{k-1} \\ cu_{k-1} + w_{k-1} \\ a + w_p \\ b + w_p \\ c + w_p \end{bmatrix} \\ \mathbf{y}_k &= h_k(\mathbf{x}_k, \mathbf{v}_k) \\ &= \begin{bmatrix} v_{\mathrm{o}} + \mathbf{x}_1 + \mathbf{x}_2 + \mathbf{v}_k \end{bmatrix} \end{aligned} \tag{5.11}$$

and the partial differentiations required for the filter can be calculated to get,

$$\mathbf{F}_{k-1} = \begin{bmatrix} 1 - ab\Delta t & 0 & -b\Delta t\mathbf{x}_1 + \Delta t u_{k-1} & -a\Delta t\mathbf{x}_1 & 0 \\ 0 & 0 & 0 & 0 & u_{k-1} \\ 0 & 0 & 1 & 0 & 0 \\ 0 & 0 & 0 & 1 & 0 \\ 0 & 0 & 0 & 0 & 1 \end{bmatrix} \tag{5.12}$$

$$\mathbf{L}_{k-1} = \begin{bmatrix} a\Delta t & c & 0 & 0 & 0 \end{bmatrix} \tag{5.13}$$

$$\mathbf{H}_k = \begin{bmatrix} 1 & 1 & 0 & 0 & 0 \end{bmatrix} \tag{5.14}$$

$$\mathbf{M}_k = \begin{bmatrix} 1 & 0 & 0 & 0 & 0 \end{bmatrix} \tag{5.15}$$

Figure 5.5 shows the extended Kalman filtering equations implemented to recover the values of C_g, R_g and R_T from an initial estimation error of 10% for each variable. Using this method of first simulating the state equations, and then recovering the state variables from a noisy measurement, allows the accuracy of the EKF to be investigated and allows correct calculation of $\mathbf{P}$, $\mathbf{Q}$, and $\mathbf{R}$.

The extended Kalman filter appears to correctly identify the three unknown state variables given a 10% initial estimation error. Figure 5.6 shows the EKF estimated values $\hat{C}_\mathrm{g}$, $\hat{R}_\mathrm{g}$ and $\hat{R}_\mathrm{T}$ plotted against the actual values used in the Euler simulation.

The filter in this case was initialised with an artificial process noise $w_p = 0.1$ to allow a, b and c to converge. The initial estimation errors were calculated using,

$$p_{\mathbf{x}_0} = \mathrm{rms}(\mathbf{x_0} - \bar{\mathbf{x}})^2 \tag{5.16}$$

which can be done because the average ($\bar{\mathbf{x}}$) or actual value is known. This poses a practical problem when the EKF is implemented on real battery voltage responses because estimation error covariance matrix ($\mathbf{P}$) can no longer be estimated. Filter convergence cannot be determined either because, looking at Figure 5.6 the filter keeps on adjusting its state estimates. Concluding that any state-space model that is built to simulate battery response will have some form of error and that the linearisation of the EKF introduces an extra error. The effects of

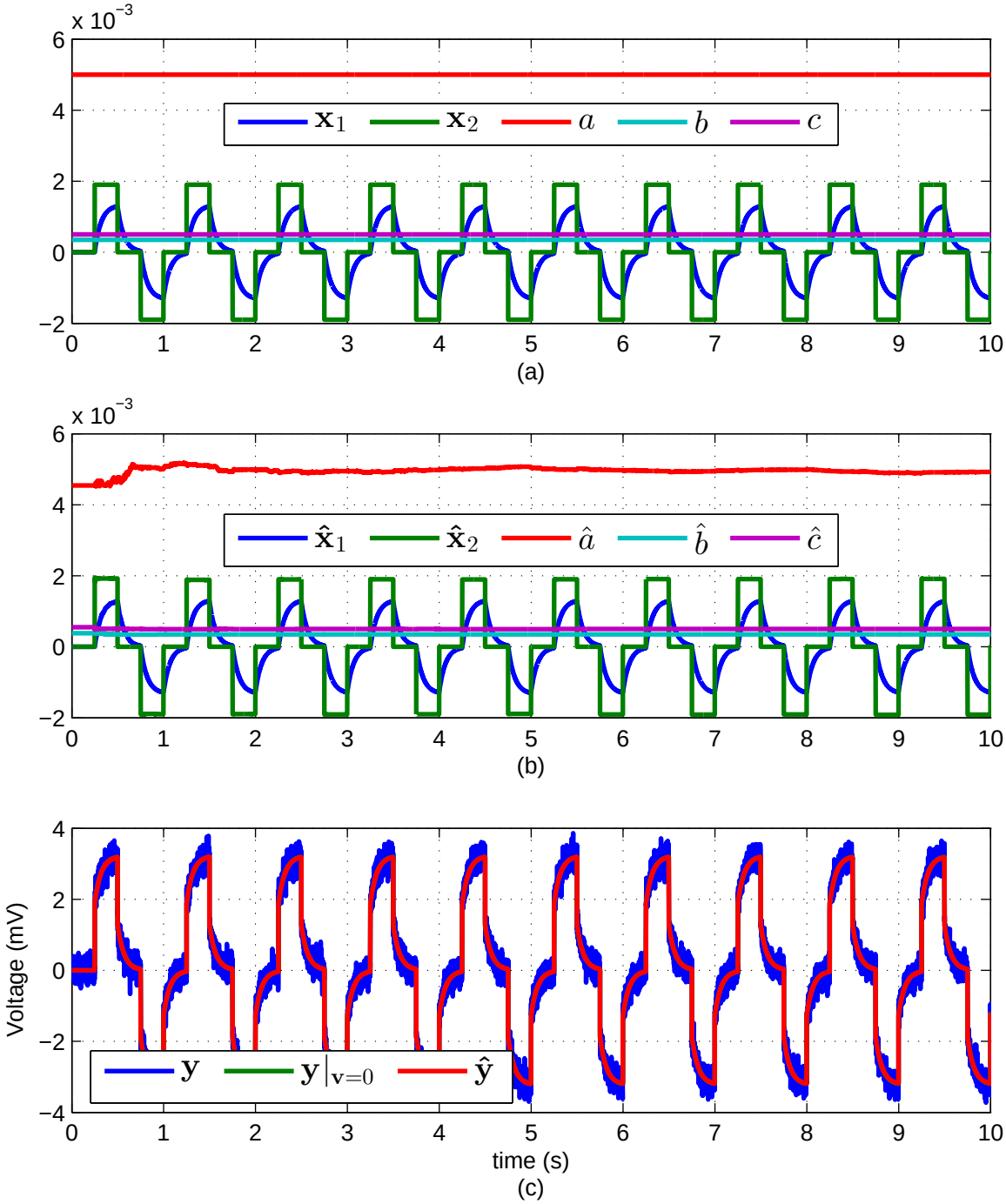

Figure 5.5: Extended Kalman Filter implemented to identify C_g, R_g and R_T initialised with an estimation error of 10% on each of the three variables. (a) Actual state variables obtained by Euler simulation; (b) the estimated state variables obtained through EKF; (c) measured voltage trace $\mathbf{y}$, simulated voltage trace $\mathbf{y}|_{v=0}$, and the EKF estimate of the voltage $\hat{\mathbf{y}}$

these errors need to be absorbed in the process error covariance matrix ($\mathbf{Q}$) both of which are unknown and can at best only be estimated. Hence, empirical tuning seems to be standard practice.

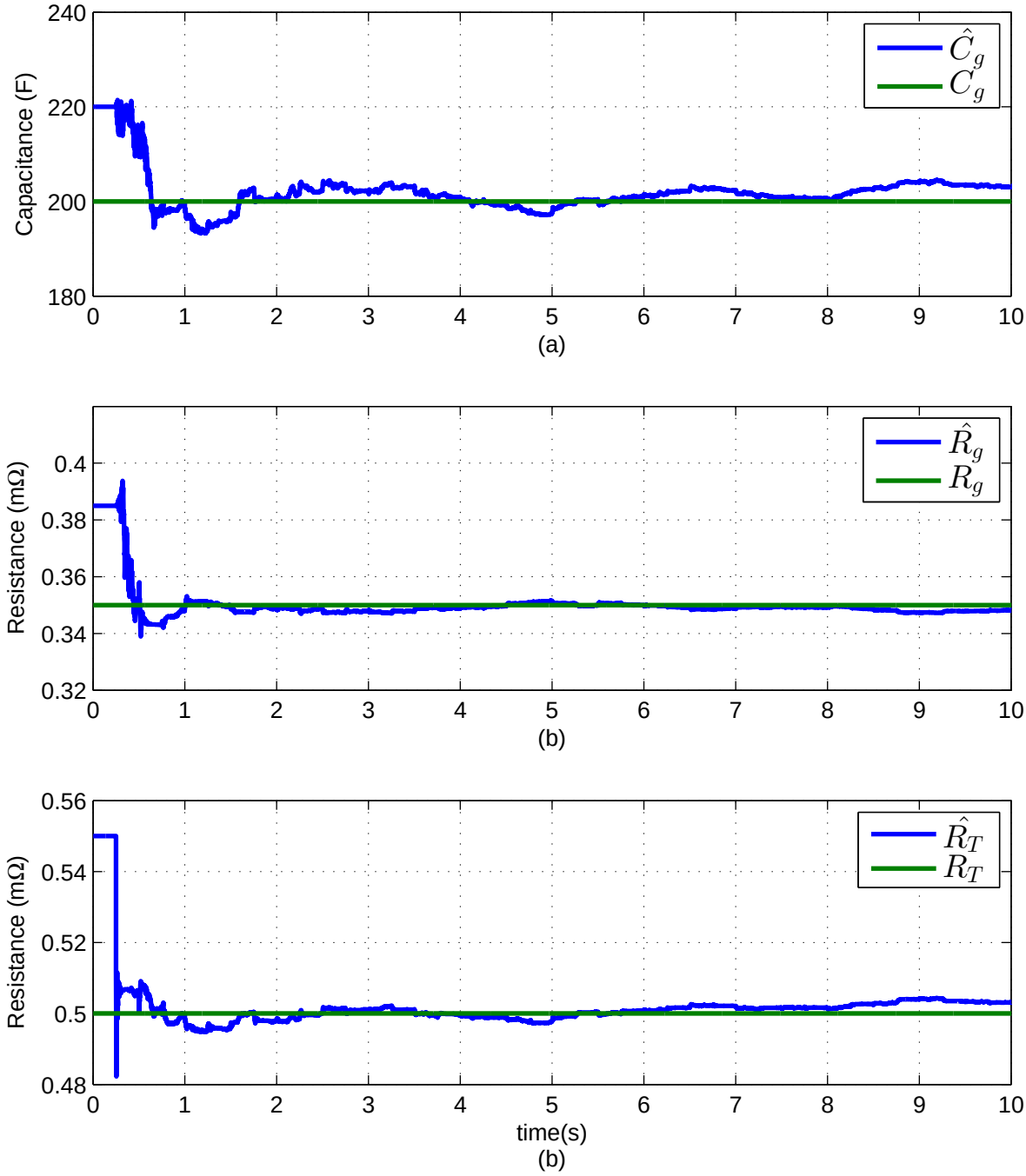

Figure 5.6: Estimated and actual values for (a) C_{g}, (b) R_{g} and (c) R_{T} showing how the filter converges from a 10% estimation error but seems to never settle on the actual value

5.2.2 Internal resistance

Initial estimation

The simple battery model, Figure 2.8, consists of a voltage source with an internal series resistance (R_{T}). The internal resistance can be calculated using,

$$R_{\mathrm{T}} = \frac{v_{\mathrm{o}} - v_{\mathrm{T}}}{I} \tag{5.17}$$

where v_o is the open-circuit voltage when no current is drawn and v_T is the terminal voltage when current I is drawn from the cell. This idealised measurement can provide an initial estimate for the actual internal resistance of a real battery.

Extended Kalman filtering

The EKF matrices for the simple battery model are,

$$\mathbf{F}_{k-1} = \begin{bmatrix} 1 & 0 \\ 0 & 1 \end{bmatrix} \qquad \mathbf{L}_{k-1} = \begin{bmatrix} 0 & 0 \end{bmatrix} \tag{5.18}$$

$$\mathbf{H}_k = \begin{bmatrix} 1 & I \end{bmatrix} \qquad \mathbf{M}_k = \begin{bmatrix} 1 & 0 \end{bmatrix} \tag{5.19}$$

Figure 5.7 show the EKF implementation to estimate R_T for the simple battery model shown in Figure 2.8. The initial estimate for R_T was 47 mΩ. Figure 5.7(c) shows that R_T apparently increases with time. However, panel (b) shows that the voltage estimate ($\hat{\mathbf{y}}$) does not correctly follow the actual voltage ($\mathbf{y}$) and that the increase in R_T with time is actually a side effect of the terminal voltage reducing with SOC which the simple model cannot account for. The figure shows that the Kalman filter has adjusted R_T to 53 mΩ after the first discharge pulse which is likely to be a better estimate of R_T than the initial estimate.

5.2.3 Diffusion and polarisation time constants

Initial estimation

Hu et al [55, 93] introduce a cost minimising method for determining the internal parameters for the DP battery model. The paper contains the full mathematical description of this method which is not repeated here. However, this method produces unrealistic (negative resistance and imaginary capacitance values) when implemented to this dataset. It is therefore not used. A set of values for R_D, C_D, R_P and C_P (Fig. 2.10) needs to be found to initialise the Kalman

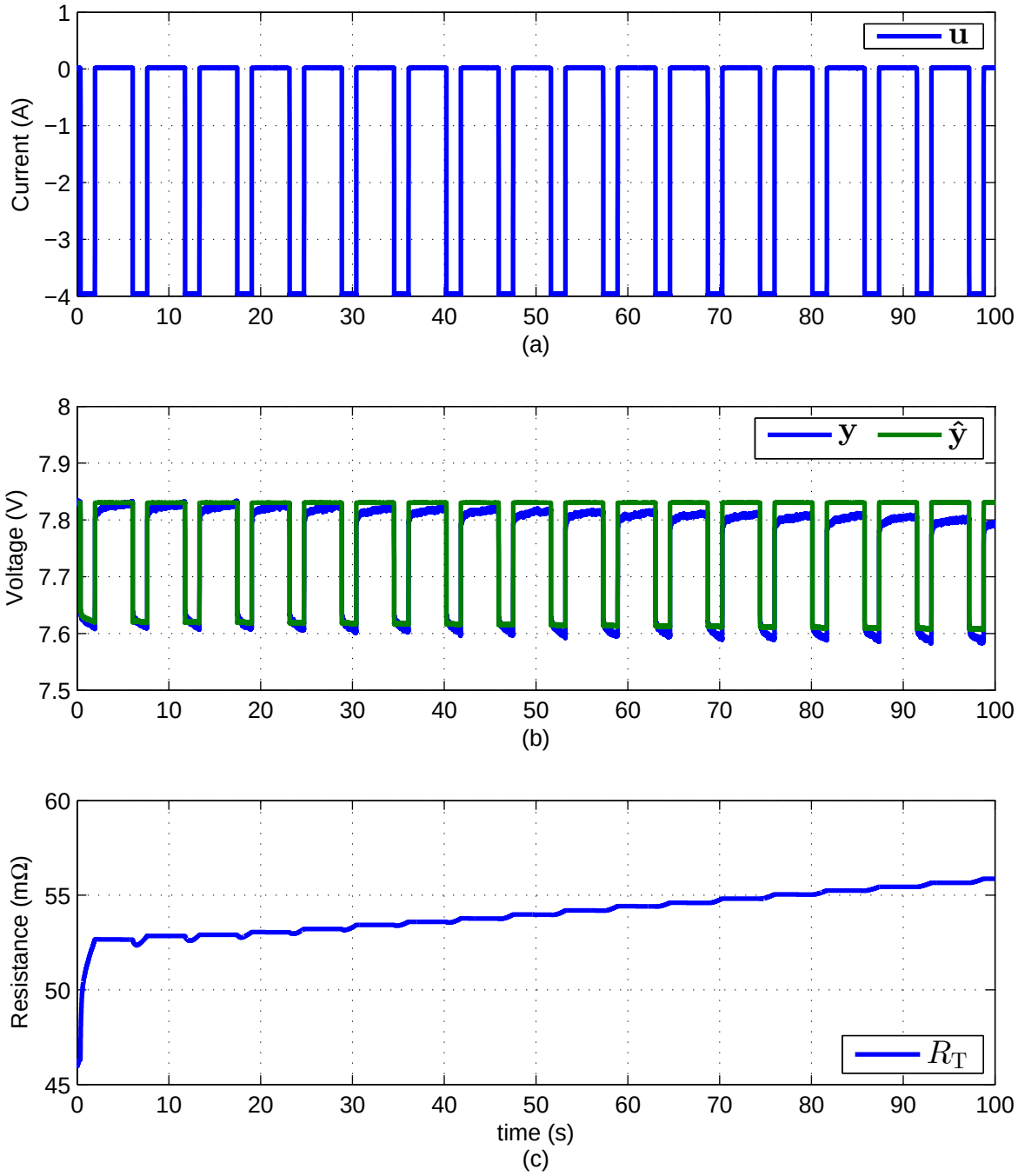

Figure 5.7: Extended Kalman filter implemented to estimate R_T for the simple battery model of Figure 2.8 showing: (a) current through battery and model; (b) measured terminal voltage ($\mathbf{y}$) and estimated battery voltage ($\hat{\mathbf{y}}$); and (c) estimated R_T for 100 seconds

filter. The time dependent equation for one discharge pulse is described by,

$$v_T(t) = v_o + R_T I + R_D I(1 - e^{-t/R_D C_D}) + R_P I(1 - e^{-t/R_P C_P}) \tag{5.20}$$

where $R_T = 47$ mΩ is a good estimation for the terminal resistance. Figure 5.8 shows the battery voltage response when subjected to a 4 A discharge pulse with the first two terms of Eq. (5.20) removed.

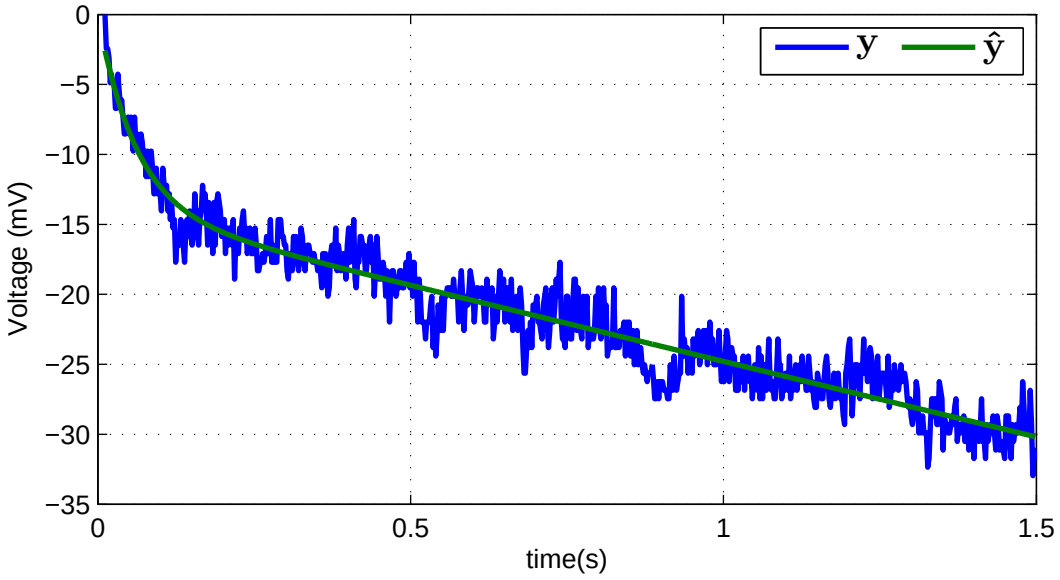

Figure 5.8: Initial estimation of Thévenin equivalent circuit model components by fitting exponential decay curves using MATLAB curve fitting tool

The MATLAB curve fitting tool was then used to fit,

$$\hat{y} = -\alpha(1 - e^{-t/\beta}) - \gamma(1 - e^{-t/\delta}) \tag{5.21}$$

where α, β, γ and δ are the fit constants. When subjected to a fixed amplitude current pulse the component values summarised in Table 5.1 are obtained. These values are used to initialise the EKF.

Table 5.1: Diffusion and polarisation component values initial estimates

Component	**Initial Estimate**	**EKF recovered**
R_{P}	174 mΩ	171 ± 1.2 mΩ
C_{P}	363 F	3113 ± 155 F
R_{D}	3.46 mΩ	5.089 ± 0.023 mΩ
C_{D}	17 F	17.1 ± 0.023 F
R_{T}	47 mΩ	47 mΩ

Extended Kalman filtering

The Kalman filtering state vector for the diffusion-polarisation model is,

$$\mathbf{x}_k = \begin{bmatrix} \mathbf{x}_1 & \mathbf{x}_2 & a & b & c & d \end{bmatrix}^{\mathrm{T}} \tag{5.22}$$

where $a = 1/C_{\mathrm{D}}$, $b = 1/R_{\mathrm{D}}$, $c = 1/C_{\mathrm{P}}$ and $d = 1/R_{\mathrm{P}}$, $\mathbf{x}_1$ and $\mathbf{x}_2$ are the voltages across the diffusion and polarisation RC pairs respectively. The reciprocals of the component values were chosen for the state vector because this simplifies the differentiations required for the Kalman filter update equations. The extended Kalman filter matrices are,

$$\mathbf{F}_{k-1} = \begin{bmatrix} (1 - ab\Delta t)\mathbf{x}_1|_{k-1} & 0 & F_{1,3} & -a\Delta t\mathbf{x}_1|_{k-1} & 0 & 0 \\ 0 & (1 - cd\Delta t)\mathbf{x}_2|_{k-1} & 0 & 0 & F_{2,5} & -c\Delta t\mathbf{x}_2|_{k-1} \\ 0 & 0 & 1 & 0 & 0 & 0 \\ 0 & 0 & 0 & 1 & 0 & 0 \\ 0 & 0 & 0 & 0 & 1 & 0 \\ 0 & 0 & 0 & 0 & 0 & 1 \end{bmatrix} \tag{5.23}$$

$$\begin{aligned} \mathbf{L}_{k-1} &= \begin{bmatrix} a\Delta t & c\Delta t & 0 & 0 & 0 & 0 \end{bmatrix} \\ \mathbf{H}_k &= \begin{bmatrix} 1 & 1 & 0 & 0 & 0 & 0 \end{bmatrix} \\ \mathbf{M}_k &= \begin{bmatrix} 1 & 1 & 0 & 0 & 0 & 0 \end{bmatrix} \end{aligned} \tag{5.24}$$

where,

$$\begin{aligned} F_{1,3} &= -b\Delta t\mathbf{x}_1|_{k-1} + \Delta t u_{k-1} \\ F_{2,5} &= -d\Delta t\mathbf{x}_2|_{k-1} + \Delta t u_{k-1} \end{aligned} \tag{5.25}$$

Figure 5.9 shows the current and voltage (measured and estimated) traces for the same dataset presented in Figure 5.7. Visual comparison of the estimated voltage traces between these two figures shows that the DP model is more suitable than the simple battery model even though the DP model still cannot adjust for changing open-circuit voltage, a problem discussed earlier.

Figure 5.10 shows the estimated component values describing the diffusion and polarisation effects seen within the battery. The figure shows that both R_{D} and R_{P} vary little once the filter has adjusted to a seemingly stable value, although R_{P} starts to drop towards the end of the recording. The capacitance values, C_{D} and C_{P} appear to be continually adjusting, with C_{D} seemingly not reaching a stable state within this time frame. This may be due to the model's inability to adjust for chances in open-circuit terminal voltage as the battery module is discharged. Further "tuning" of the filter may result in better convergence of these values.

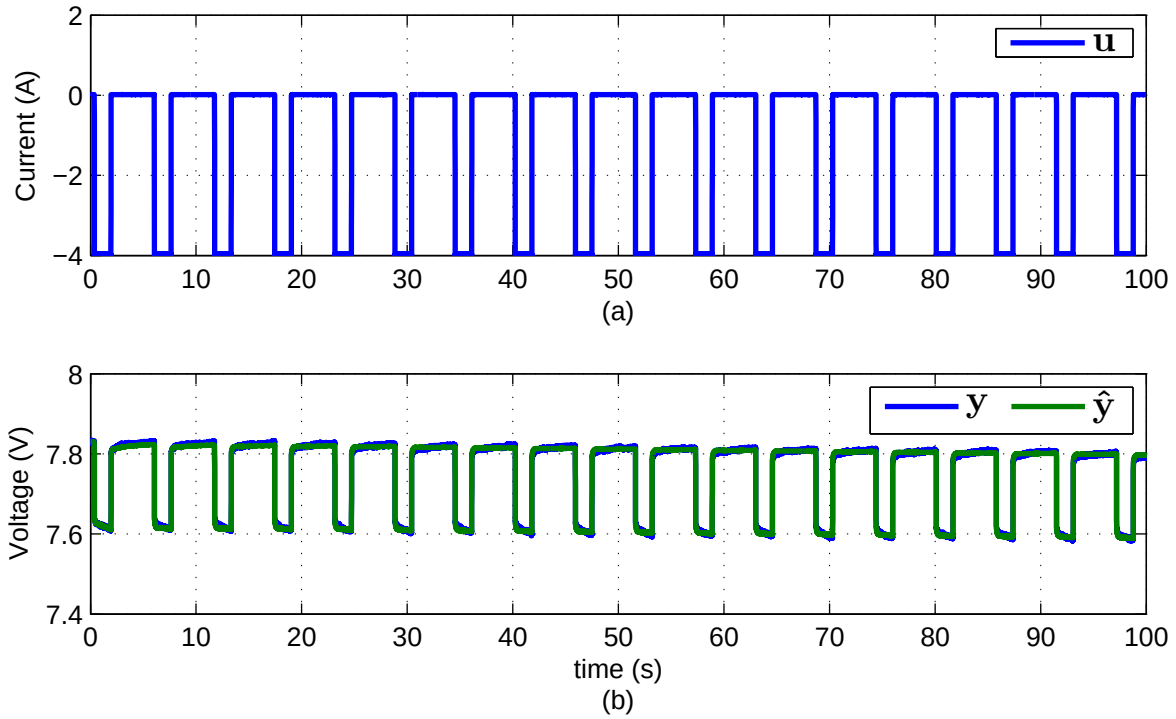

Figure 5.9: Extended Kalman filter implemented to estimate diffusion and polarisation time-constants for the model shown in Figure 2.10 initialised with the component values shown in Table 5.1 where (a) shows current trace and (b) shows measured terminal voltage ($\mathbf{y}$) and estimated battery voltage ($\hat{\mathbf{y}}$)

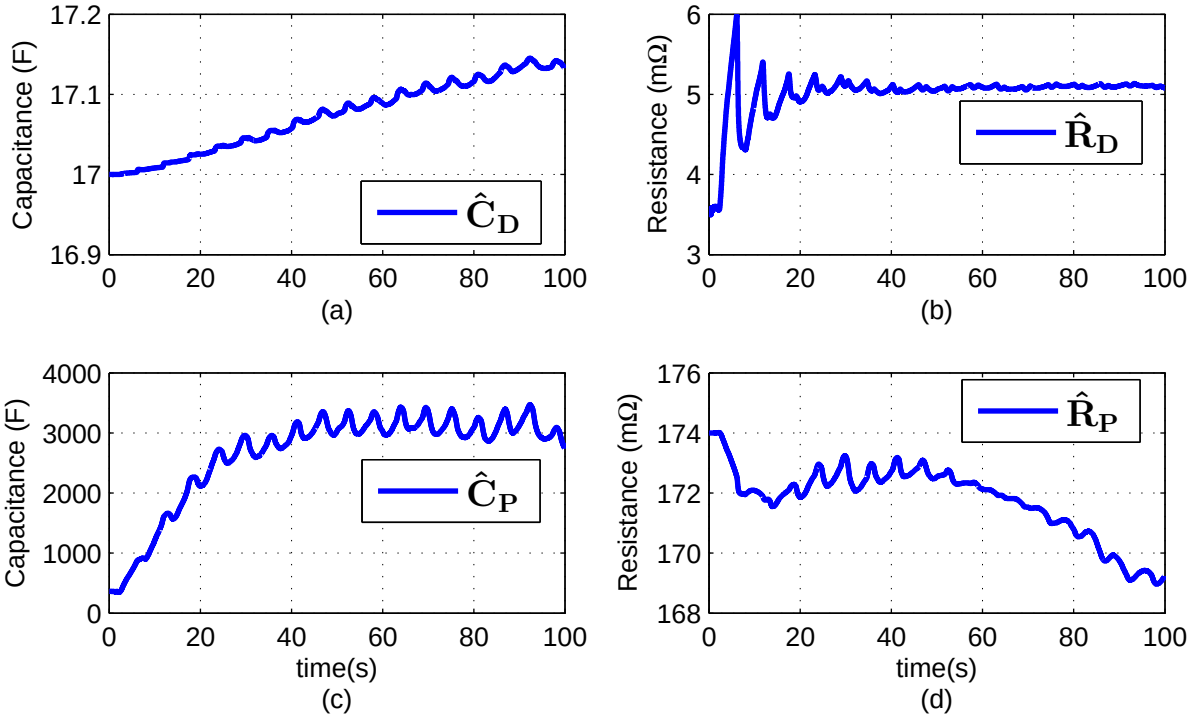

Figure 5.10: EKF filter estimated component values for (a) C_{D}, (b) R_{D}, (c) C_{P} and (d) R_{P} showing convergence in some values, initialised with values from table 5.1

5.2.4 Bulk-surface model parameters

Initial estimation

Bhangu et al [31] is followed to estimate internal battery parameters to initialise the Kalman filter. If the assumption is made that $C_{\mathrm{B}} \gg C_{\mathrm{S}}$ then the energy stored in the battery is

approximately equal to the energy stored in C_{B},

$$\begin{aligned} E_{\text{battery}} &\approx \frac{1}{2} C_{\mathrm{B}} \Delta v_{\mathrm{Cb}}^2 \\ &\approx \frac{1}{2} C_{\mathrm{B}} (v_{\mathrm{Cb}}^2|_{\mathrm{SOC}\,=100\%} - v_{\mathrm{Cb}}^2|_{\mathrm{SOC}\,=0\%}) \\ \int_{\mathrm{SOC}=0\%}^{\mathrm{SOC}=100\%} IV \ dt &\approx \frac{1}{2} C_{\mathrm{B}} (v_{\mathrm{Cb}}^2|_{\mathrm{SOC}\,=100\%} - v_{\mathrm{Cb}}^2|_{\mathrm{SOC}\,=0\%}) \\ Q v_{\mathrm{T}}|_{\mathrm{SOC}\,=100\%} &\approx \frac{1}{2} C_{\mathrm{B}} (v_{\mathrm{Cb}}^2|_{\mathrm{SOC}\,=100\%} - v_{\mathrm{Cb}}^2|_{\mathrm{SOC}\,=0\%}) \\ C_{\mathrm{B}} &\approx \frac{QV|_{\mathrm{SOC}\,=100\%}}{\frac{1}{2}(v_{\mathrm{Cb}}^2|_{\mathrm{SOC}\,=100\%} - v_{\mathrm{Cb}}^2|_{\mathrm{SOC}\,=0\%})} \end{aligned} \tag{5.26}$$

where v_{Cb} is the voltage across C_{B} and Q is the capacity of the module. Similarly if the assumption is made that C_{S} and its associated resistance is responsible for the high-frequency response of the battery, then the recovery time-constant (τ) can be measured and used to calculate C_{S}, R_{B} and R_{S} using,

$$C_{\mathrm{S}} \approx \frac{\tau}{R_{\mathrm{B}} + R_{\mathrm{S}}} \tag{5.27}$$

However, the values of R_{B} and R_{S} are not known. The instantaneous voltage drop, equation (5.17), seen when a discharge pulse is applied is a result of the series-parallel combination of all resistances. Bhangu et al make the assumption that R_{B} and R_{S} are equal and account for 75% of the total internal resistance. So,

$$\frac{v_{\mathrm{o}} - v_{\mathrm{T}}}{I} = R_{\mathrm{T}} + \left(\frac{R_{\mathrm{B}} R_{\mathrm{S}}}{R_{\mathrm{B}} + R_{\mathrm{S}}} \right) \tag{5.28}$$

where, v_{o} is the open-circuit voltage, $R_{\mathrm{B}} = R_{\mathrm{S}}$ and $R_{\mathrm{T}} = 0.75(v_{\mathrm{o}} - v_{\mathrm{T}})/I$ but R_{T} contributes much more than 75% of the total observed resistance by looking at the voltage response and the results gathered in section above. The initial estimates calculated using Bhangu's method are summarised in Table 5.2 along with tuned initial values obtained by trail and error.

The Kalman filter was initialised with the tuned estimates as it was found that the initial estimates obtained using Bhangu's method gave results that either did not converge or converged to unrealistic values. The section below shows the results and the Kalman filter equations.

Table 5.2: Initial and tuned first estimates for bulk-surface model component values and EKF recovered values

Component	Initial Estimate	Tuned Estimate	EKF recovered
C_{B}	2446 F	2446 F	3345 ± 26 F
R_{B}	18 mΩ	5 mΩ	6.740 ± 0.003 mΩ
C_{S}	37 F	37 F	68.5 ± 0.4 F
R_{S}	18 mΩ	0.5 mΩ	0.5141 ± 0.0003 mΩ
R_{T}	12 mΩ	47 mΩ	47 mΩ

Extended Kalman filtering

The Kalman filtering state vector for the bulk-surface model is,

$$\mathbf{x}_k = \begin{bmatrix} \mathbf{x}_1 & \mathbf{x}_2 & a & b & c & d \end{bmatrix}^{\mathrm{T}} \tag{5.29}$$

where $a = 1/C_{\mathrm{B}}$, $b = R_{\mathrm{B}}$, $c = 1/C_{\mathrm{S}}$ and $d = R_{\mathrm{S}}$; $\mathbf{x}_1$ and $\mathbf{x}_2$ are the voltages across the bulk and surface capacitors respectively. Resulting in the following EKF matrices for the bulk-surface model,

$$\begin{aligned} \mathbf{L}_{k-1} &= \begin{bmatrix} \frac{ad\Delta t}{b+d} & \frac{bc\Delta t}{b+d} & 0 & 0 & 0 & 0 \end{bmatrix} \\ \mathbf{H}_k &= \begin{bmatrix} \frac{d}{b+d} & \frac{b}{b+d} & 0 & 0 & 0 & 0 \end{bmatrix} \\ \mathbf{M}_k &= \begin{bmatrix} 1 & 1 & 0 & 0 & 0 & 0 \end{bmatrix} \end{aligned} \tag{5.30}$$

$$\mathbf{F}_{k-1} = \begin{bmatrix} 1 - \frac{a\Delta t}{b+d} & \frac{a\Delta t}{b+d} & F_{1,3} & F_{1,4} & 0 & F_{1,6} \\ \frac{c\Delta t}{b+d} & 1 - \frac{c\Delta t}{b+d} & 0 & F_{2,4} & F_{2,5} & F_{2,6} \\ 0 & 0 & 1 & 0 & 0 & 0 \\ 0 & 0 & 0 & 1 & 0 & 0 \\ 0 & 0 & 0 & 0 & 1 & 0 \\ 0 & 0 & 0 & 0 & 0 & 1 \end{bmatrix} \tag{5.31}$$

where,

$$
\begin{aligned}
F_{1,3} &= \frac{\Delta t}{b+d}\mathbf{x}_2|_{k-1} - \frac{\Delta t}{b+d}\mathbf{x}_1|_{k-1} + \frac{d\Delta t}{b+d}u_{k-1} \\
F_{1,4} &= \frac{a\Delta t}{(b+d)^2}\mathbf{x}_1|_{k-1} - \frac{a\Delta t}{(b+d)^2}\mathbf{x}_2|_{k-1} - \frac{ad\Delta t}{(b+d)^2}u_{k-1} \\
F_{1,6} &= \frac{a\Delta t}{(b+d)^2}\mathbf{x}_1|_{k-1} - \frac{a\Delta t}{(b+d)^2}\mathbf{x}_2|_{k-1} + \left(\frac{a\Delta t}{b+d} - \frac{ad\Delta t}{(b+d)^2}\right)u_{k-1} \\
F_{2,4} &= \frac{c\Delta t}{(b+d)^2}\mathbf{x}_2|_{k-1} - \frac{c\Delta t}{(b+d)^2}\mathbf{x}_1|_{k-1} + \left(\frac{c\Delta t}{b+d} - \frac{bc\Delta t}{(b+d)^2}\right)u_{k-1} \\
F_{2,5} &= \frac{\Delta t}{b+d}\mathbf{x}_1|_{k-1} - \frac{\Delta t}{b+d}\mathbf{x}_2|_{k-1} + \frac{b\Delta t}{b+d}u_{k-1} \\
F_{2,6} &= \frac{c\Delta t}{(b+d)^2}\mathbf{x}_2|_{k-1} - \frac{c\Delta t}{(b+d)^2}\mathbf{x}_1|_{k-1} - \frac{bc\Delta t}{(b+d)^2}u_{k-1}
\end{aligned}
\tag{5.32}
$$

Figure 5.11 shows how the Kalman filter reconstructs the battery terminal voltage more accurately than with the simple battery model and the Thévenin model. This is likely due to the model's ability to change open-circuit terminal voltage as the battery is discharged. Consequently the model parameters appear to converge to stable values shown in Figure 5.12; this behaviour was not observed for the other two battery models.

Figure 5.12 shows the time evolution of the recovered component values. The filter stabilises

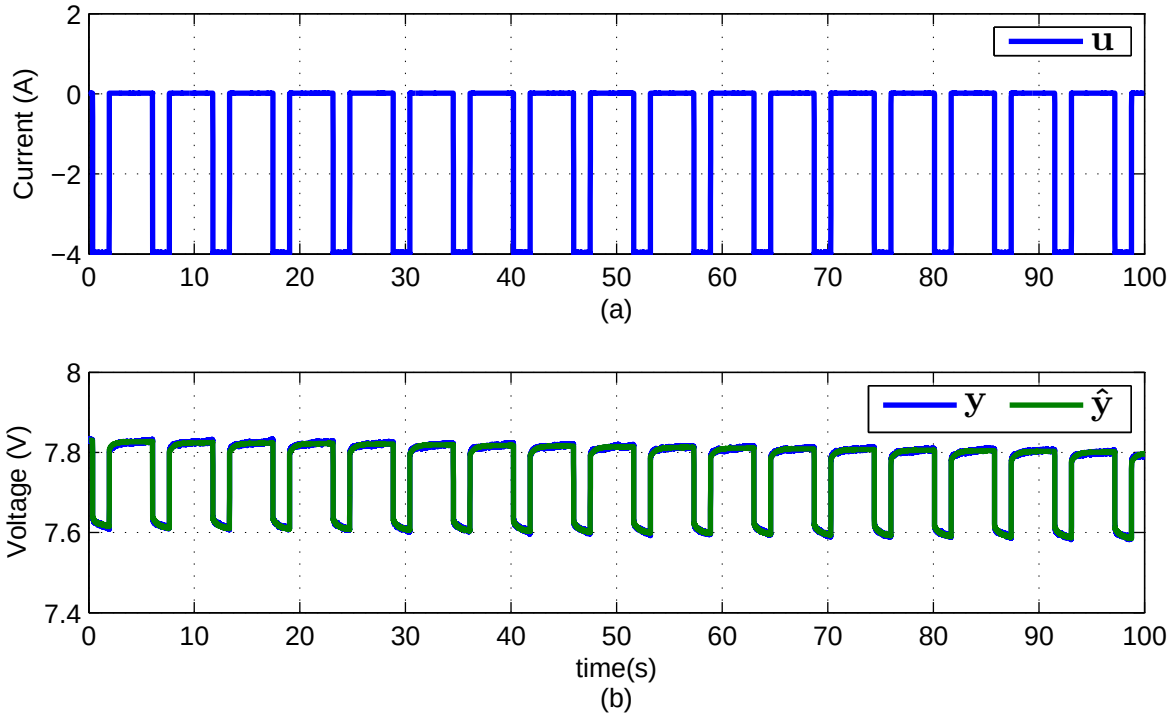

Figure 5.11: Extended Kalman filter implemented to estimate bulk-surface component parameters for the model shown in Figure 2.11 initialised with the component values shown in Table 5.2 panel (a) shows the current trace and (b) shows measured terminal voltage ($\mathbf{y}$) and estimated battery voltage ($\hat{\mathbf{y}}$)

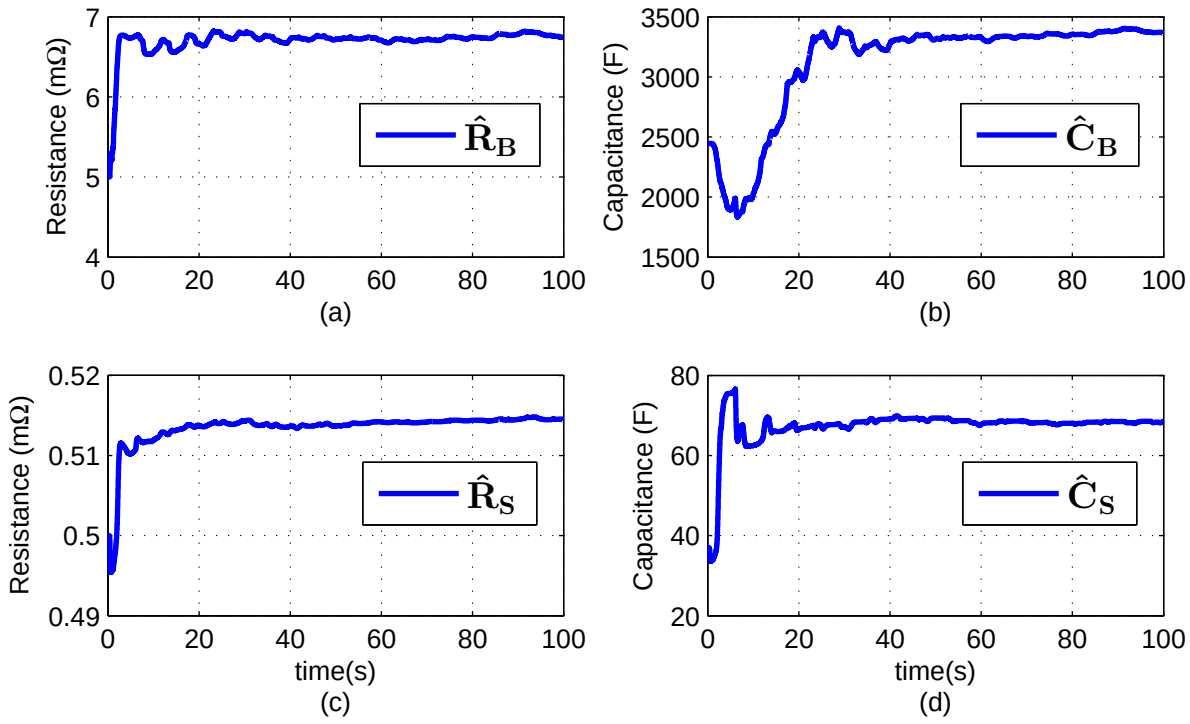

Figure 5.12: EKF filter estimated component values for (a) R_B, (b) C_B, (c) R_S and (d) C_S showing convergence in all values

after about 40 seconds with a residual $\approx 1\%$ variation about the mean. The Kalman-derived parameter values are listed in the final column of Table 5.2.

5.3 Equivalent circuit evaluation and suitability

Battery equivalent circuits were described in Section 2.4. The suitability of various component identification methods discussed in Section 5.1 and 5.2 are evaluated here. Impedance spectroscopy and extended Kalman filtering were used to identify battery component values from actual voltage and current traces. The results obtained from impedance spectroscopy were inconclusive and very susceptible to noise and/or impedances within the measurement equipment. It was therefore decided to not pursue impedance spectroscopy further. Kalman filtering was used to extract parameter values for the three battery-equivalent circuits. Table 5.3 summarises the RMS voltage error value for the 100 s data trace used for the Kalman filter (see Figures 5.7, 5.9 and 5.11).

RMS error is calculated using,

$$\text{RMS error} = \sqrt{\frac{1}{n}\sum_{i=1}^{n}(y_i - \hat{y}_i)^2} \tag{5.33}$$

Table 5.3: RMS errors for three battery models

Model	RMS error
Simple	19 mV
Thevinin	4.3 mV
Bulk-Surface	2.4 mV

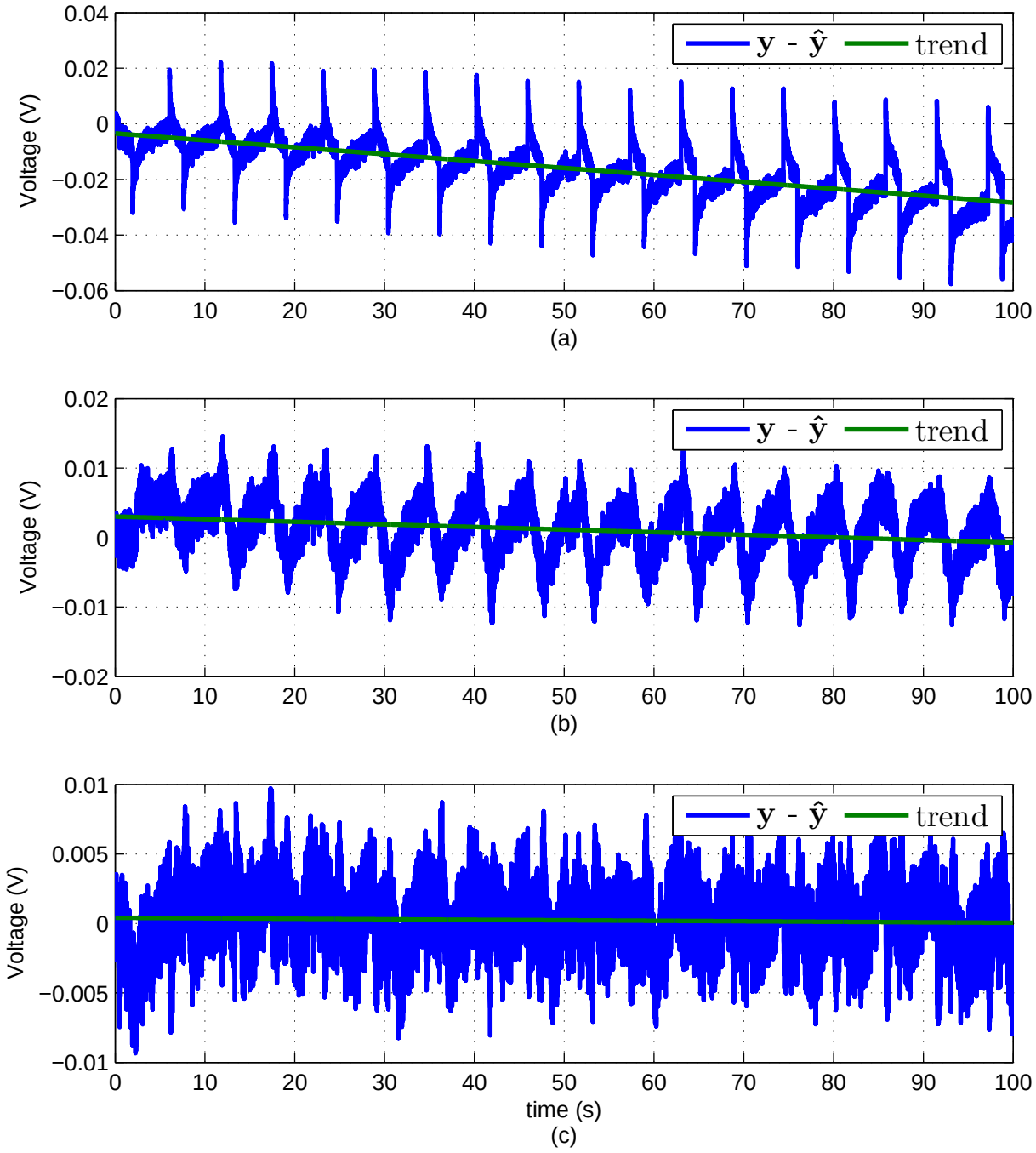

Figure 5.13: Residual error between measured voltage ($\mathbf{y}$) and estimated battery voltage ($\hat{\mathbf{y}}$) for (a) the simple battery equivalent circuit; (b) the Thévenin model and (c) the bulk-surface model showing the linear trend in each error plot.

The table shows that significant improvement in prediction accuracy is obtained by implementing the bulk-surface equivalent circuit which is capable of adjusting open-circuit terminal voltage. Figure 5.13 shows the residual errors for the three battery equivalent circuits plotted against time.

Figure 5.13(a) and (b) both show a deviation away from zero error, whereas panel (c) shows that the error maintains zero mean as time progresses. Concluding that the bulk-surface battery circuit is the most suitable equivalent circuit for the Prius battery module.

5.4 Application to battery data measured on vehicle

The extended Kalman filtering approach implemented in Section 5.2 assumed a regularly repetitive current waveform. Such regularity does not occur in a real-world driving situation where the current drawn from the battery pack is subject to driver demand. The same EKF equations are implemented, adjusted to also estimate R_{T}, to a 140 s recording of voltage and current measured from a Prius during a road test. Figure 5.14 shows the measured current ($\mathbf{u}$) and voltage traces ($\mathbf{y_1}$ and $\mathbf{y_2}$), and the corresponding estimated voltage ($\hat{\mathbf{y}}_\mathbf{1}$ and $\hat{\mathbf{y}}_\mathbf{2}$) traces for two battery modules.

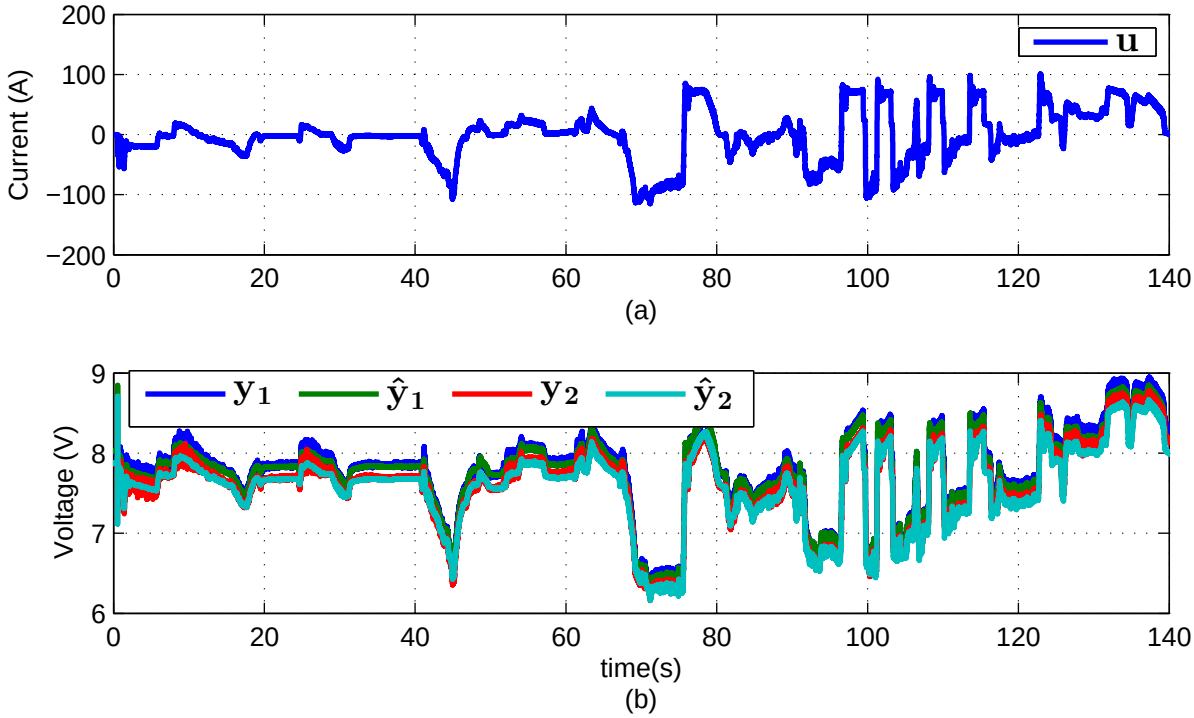

Figure 5.14: EKF implemented on 140 seconds of data measured during a road test (a) current and (b) two module voltages ($\mathbf{y_1}$ and $\mathbf{y_2}$) and estimated battery voltage ($\hat{\mathbf{y}}_\mathbf{1}$ and $\hat{\mathbf{y}}_\mathbf{2}$)

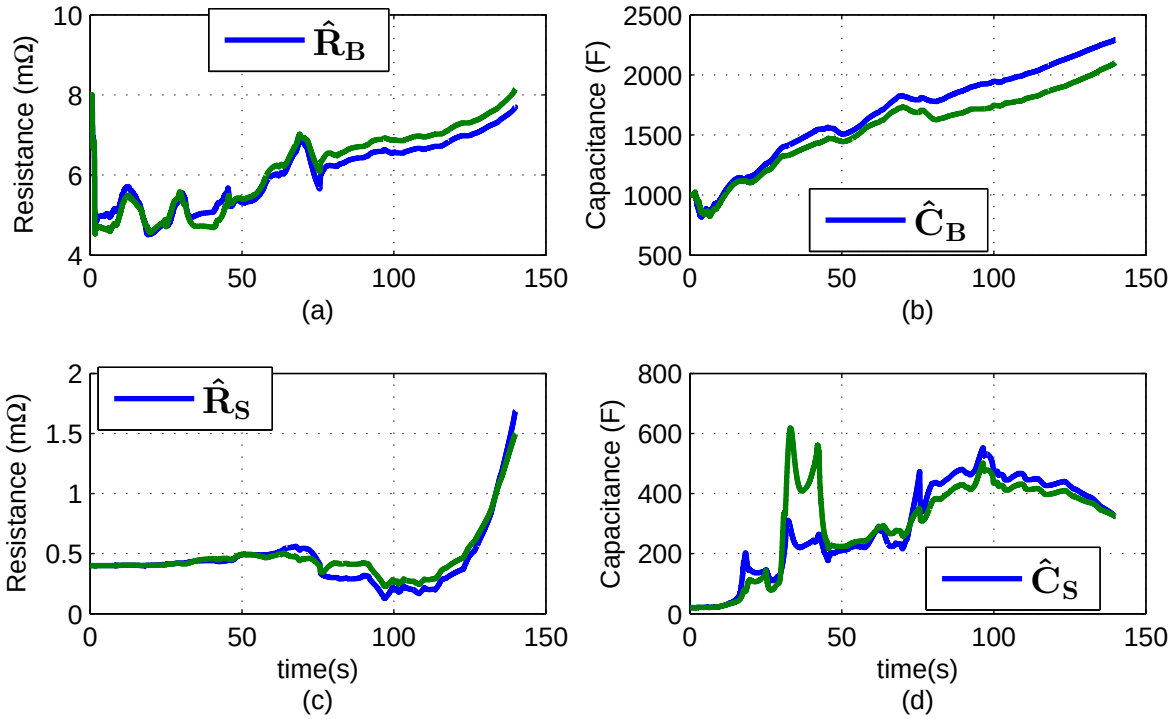

Figure 5.15: Bulk-surface model component values recovered using EKF from data measured during a drive. The blue trace is module 1 and the green trace is module 2.

The residual error between the measured and estimated battery module voltages is now about an order of magnitude higher then the error observed when the battery is excited with a regular current pulse. Figure 5.15 shows the recovered component values indicating that the filter no longer converges, though further empirical tuning may lead to better convergence. The lack of convergence in component values can also be linked to variation in component values with state-of-health, state-of-charge, current amplitude, temperature variation or any combination of parameters that may have changed throughout the 140 s road test. Figure 5.15 shows differences between the component values of the two modules which may be indicative of slight state-of-health mismatches.

5.5 Battery model parameter relationship with state-of-charge

The instabilities in the recovered values illustrated in Fig 5.15 may arise because of variation in battery equivalent component values with other parameters. This warrants further investigation. Section 5.3 showed that the bulk-surface battery circuit is most suitable for the NiMH battery modules found in Toyota Prius, so this equivalent circuit will be used this section. Figure 5.16 shows five different state-of-charge points throughout the discharge curve normalised

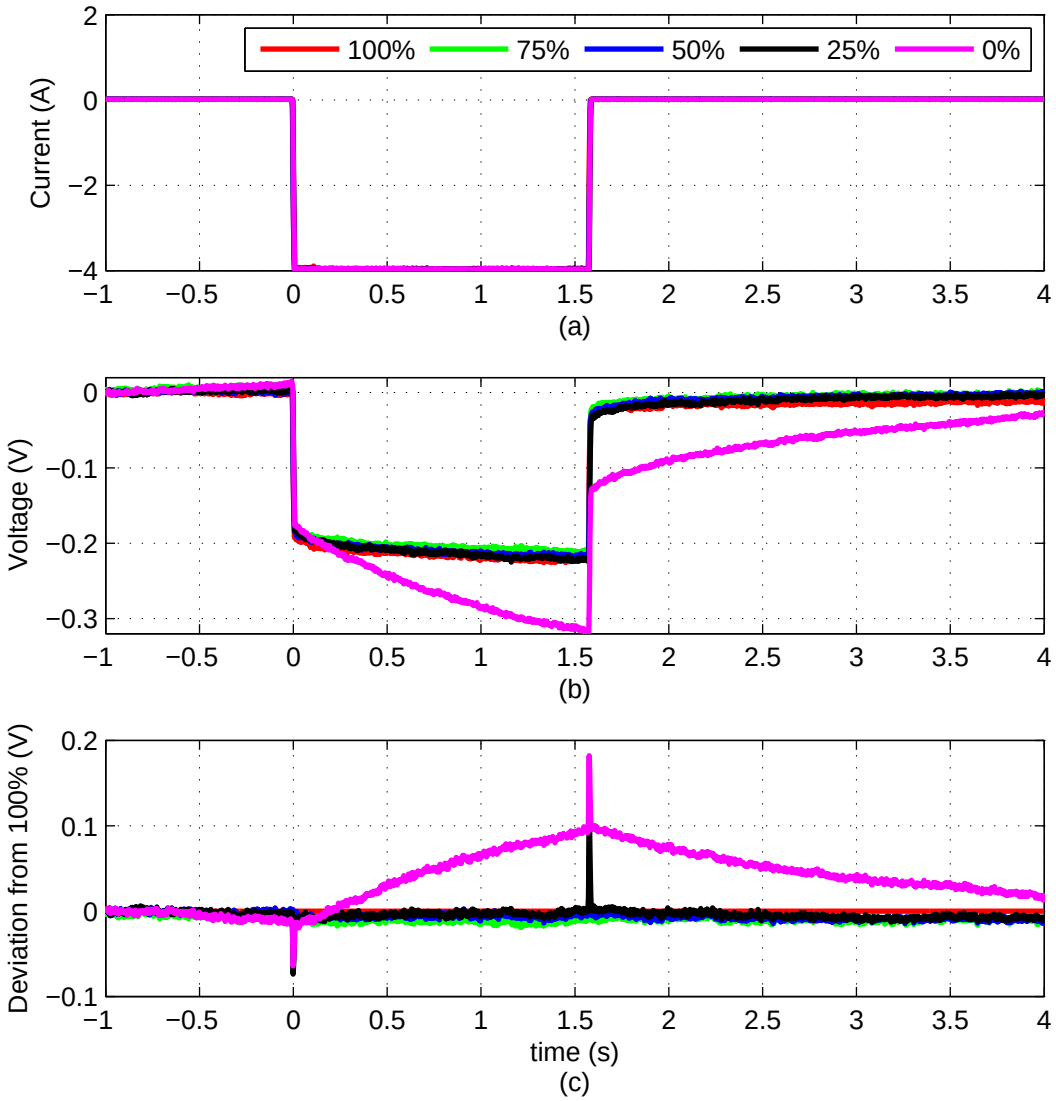

Figure 5.16: Battery voltage deviation from open-circuit voltage after a 4 A current pulse at five different states-of-charge showing (a) the current pulse, (b) the voltage response and (c) the deviation of each voltage response from the 100% SOC voltage response.

around the steady-state voltage of the battery at that SOC point. It can be seen that the battery responses are almost indistinguishable for SOC $\geq$ 25%; the only clearly different response occurs at 0% SOC.

5.5.1 Extended Kalman filter implementation

The extended Kalman filter described above was used to recover the battery model parameters at different state-of-charge points throughout the discharge curve. Figure 5.17 shows how the capacitances of the battery model vary with state-of-charge; a parabolic fit is well suited to the data despite the presence of some outliers.

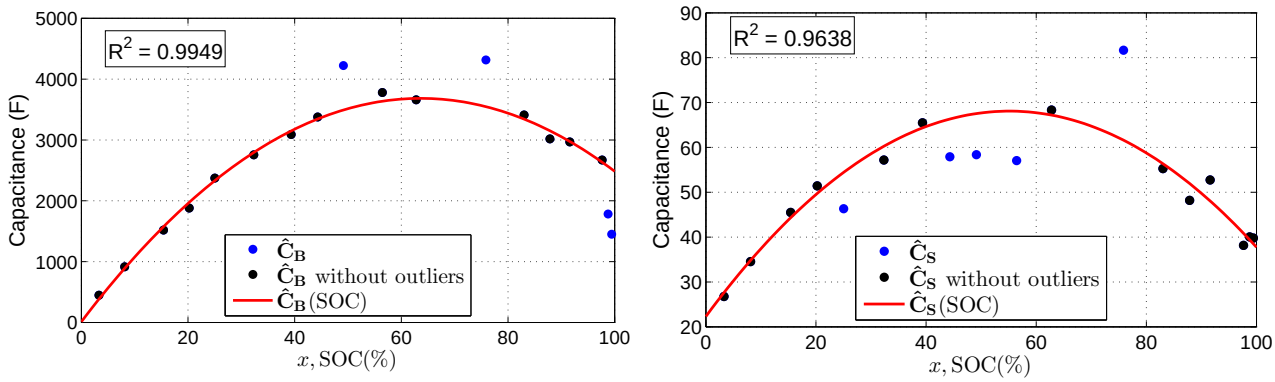

Figure 5.17: Variation in (a) bulk capacitance C_{B} and (b) surface capacitance C_{S} with state-of-charge with a parabolic fit ($C = ax^2 + bx + c$) plotted to each dataset. Here, $x = \mathrm{SOC}$.

The two subplots in Figure 5.17 show parabolic fits to the data. With outliers removed, the following equation describes the relationship between C_{B} and SOC,

$$C_{\mathrm{B}}(x) = -0.907x^2 + 115x + 11.3 \text{ F}, \tag{5.34}$$

and the fit for C_{S} is,

$$C_{\mathrm{S}}(x) = -0.0150x^2 + 1.66x + 22.3 \text{ F}, \tag{5.35}$$

where $x \equiv \mathrm{SOC}$. The outliers were removed based on data shown in Figure 5.18(d). The RMSE of the Kalman filter results increases below 10% SOC. The relationship between C_{B} and SOC suggests that at 0% SOC the value for $C_{\mathrm{B}} = 11.3$ F. The two equations show that there is a clear relationship between SOC and the capacitance values. However, due to the parabolic nature of the relationship two equally valid solutions exist when using either C_{B} or C_{S} as a measure of SOC. Figure 5.18(a) to 5.18(c) shows the resistance values of the equivalent circuit plotted against state-of-charge.

Outliers were removed using the same approach as described above. Fitted curves to the R_{B}, R_{S}, and R_{T} are exponential, parabolic, and quadratic respectively,

$$R_{\mathrm{B}}(x) = 0.0474e^{0.153x} + 9.87 \times 10^{-3} \ \Omega, \tag{5.36}$$

$$R_{\mathrm{S}}(x) = 1.05 \times 10^{-6}x^2 - 5.12 \times 10^{-5}x + 3.63 \times 10^{-3} \ \Omega, \tag{5.37}$$

$$R_{\mathrm{T}}(x) = -5.16 \times 10^{-10}x^4 + 1.16 \times 10^{-7}x^3 - 8.98 \times 10^{-6}x^2 + 2.73 \times 10^{-4}x + 0.0204 \ \Omega, \tag{5.38}$$

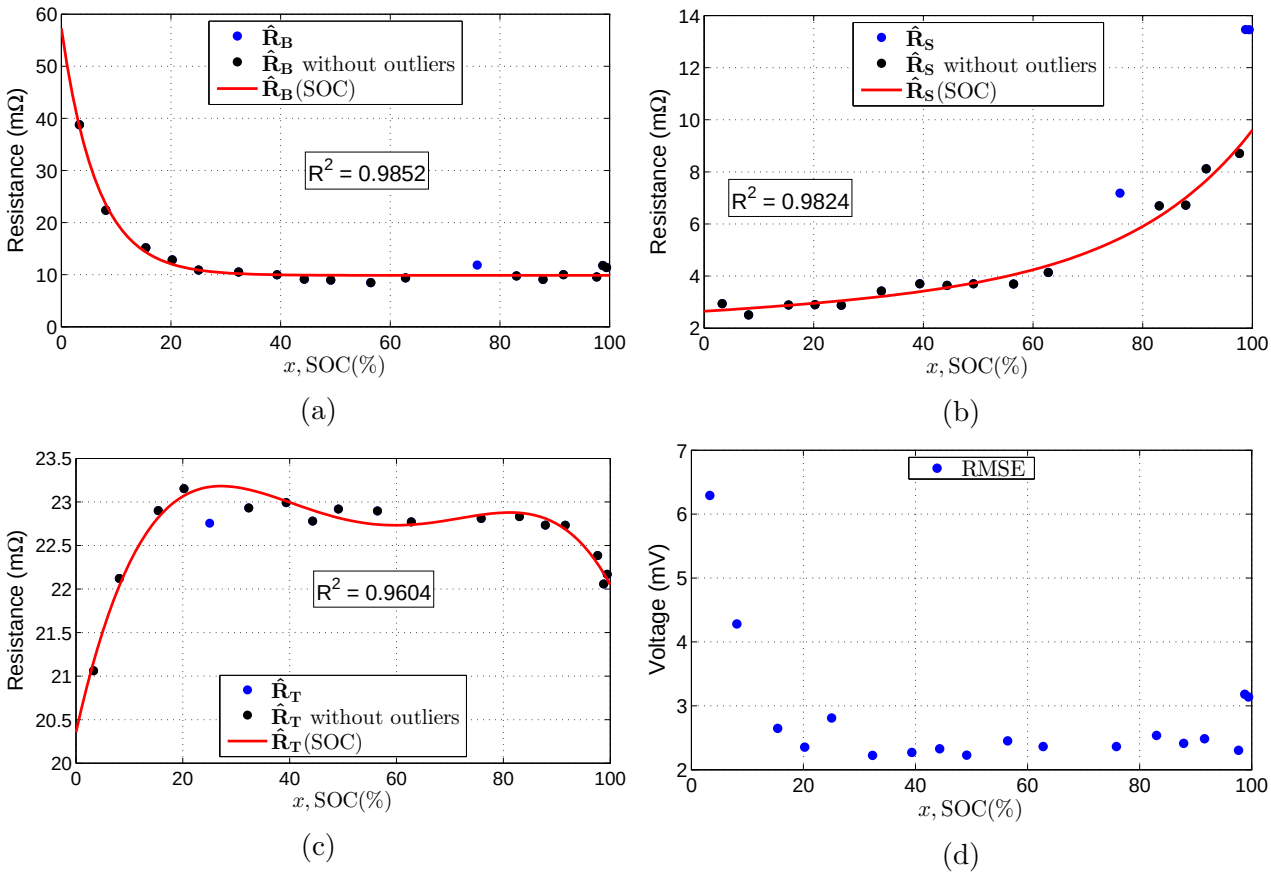

Figure 5.18: Variation in (a) bulk resistance R_B, (b) surface resistance R_S, (c) terminal resistance R_T and (d) RMSE error between the measured data and the voltage estimate recovered by Kalman filter with state-of-charge. A relationship is fitted between the resistance values and SOC.

5.5.2 Laplace transform of battery model

To calculate the time-based voltage response (seen in Fig. 5.16) for the bulk-surface model shown in Figure 5.19(a) the Laplace transforms are used to solve the differential equations relating the capacitor voltages with current. Figure 5.19(b) shows how the model is converted to Laplace space and adapted for a step discharge-current, where $\mathcal{L}\{x(t)\} \equiv X(s) = \int_0^\infty e^{-st}x(t)dt$, and $v_{\mathrm{Cb}}|_{t=0}$ is the voltage of the bulk-capacitor at time $t = 0$.

In the Laplace model, $I_\mathrm{B}(s) + I_\mathrm{S}(s) = I(s)$, i.e. the sum of the transformed branch currents is equal to the transformed load current. The terminal voltage is,

$$v_\mathrm{T}(s) = \frac{v_{\mathrm{Cb}}|_{t=0}}{s} - \frac{I_\mathrm{B}(s)}{sC_\mathrm{B}} - I_\mathrm{B}(s)R_\mathrm{B} - I(s)R_\mathrm{T} \tag{5.39}$$

The two parallel RC pairs must have equal voltages at the joining node so,

$$\frac{v_{\mathrm{Cb}}|_{t=0}}{s} - \frac{I_\mathrm{B}(s)}{sC_\mathrm{B}} - I_\mathrm{B}(s)R_\mathrm{B} = \frac{v_{\mathrm{Cs}}|_{t=0}}{s} - \frac{I_\mathrm{S}(s)}{sC_\mathrm{S}} - I_\mathrm{S}(s)R_\mathrm{S} \tag{5.40}$$

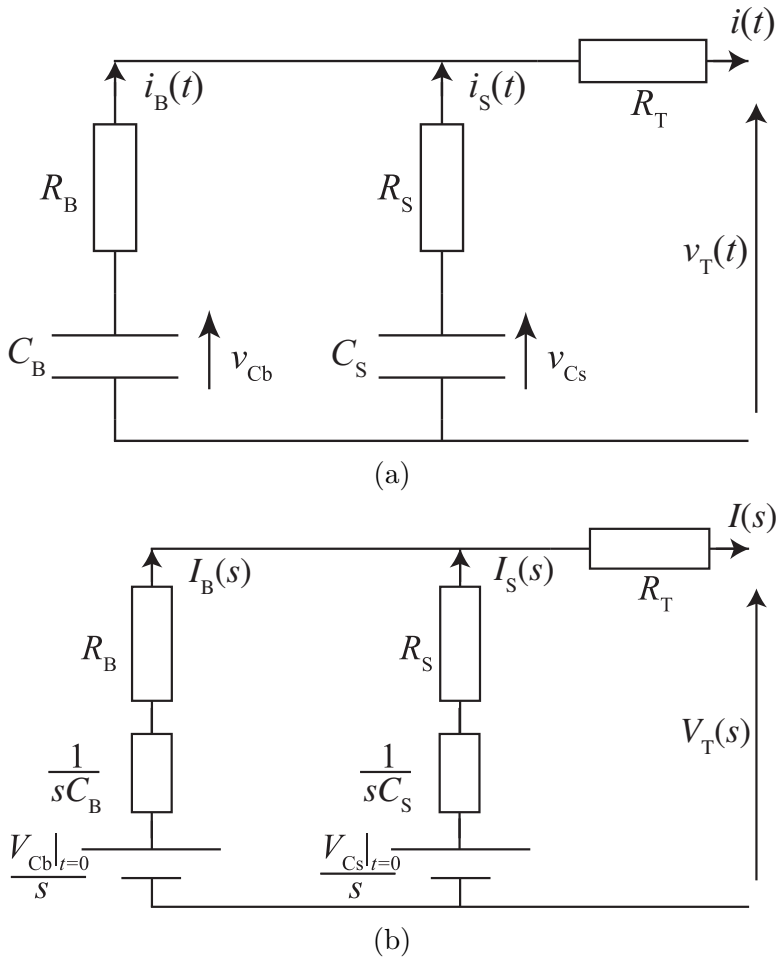

Figure 5.19: Laplace transform of the bulk-surface battery model showing (a) real bulk-surface battery model, (b) Laplace representation

Multiplying equation (5.40) by $sC_{\mathrm{B}}C_{\mathrm{S}}$ gives,

$$\begin{aligned} C_{\mathrm{B}}C_{\mathrm{S}}v_{\mathrm{Cb}}|_{t=0} - C_{\mathrm{S}}I_{\mathrm{B}}(s) - I_{\mathrm{B}}(s)sC_{\mathrm{B}}C_{\mathrm{S}}R_{\mathrm{B}} = C_{\mathrm{B}}C_{\mathrm{S}}v_{\mathrm{Cs}}|_{t=0} - C_{\mathrm{B}}I_{\mathrm{S}}(s) \\ -I_{\mathrm{S}}(s)sC_{\mathrm{B}}C_{\mathrm{S}}R_{\mathrm{S}} \end{aligned} \tag{5.41}$$

Substituting $I_{\mathrm{S}}(s) = I(s) - I_{\mathrm{B}}(s)$ and solving for $I_{\mathrm{B}}(s)$ gives,

$$I_{\mathrm{B}}(s) = \frac{C_{\mathrm{B}}C_{\mathrm{S}}(v_{\mathrm{Cs}}|_{t=0} - v_{\mathrm{Cb}}|_{t=0}) + I(s)(C_{\mathrm{B}} + sC_{\mathrm{B}}C_{\mathrm{S}}R_{\mathrm{S}})}{C_{\mathrm{B}} + C_{\mathrm{S}} + s(R_{\mathrm{B}} + R_{\mathrm{S}})C_{\mathrm{B}}C_{\mathrm{S}}} \tag{5.42}$$

where the first term of the numerator ($C_{\mathrm{B}}C_{\mathrm{S}}(v_{\mathrm{Cs}}|_{t=0} - v_{\mathrm{Cb}}|_{t=0})$) is zero for $t < 0$ because the load current ($I(s)$) is zero meaning that the system is in equilibrium therefore, $v_{\mathrm{Cs}}|_{t=0} = v_{\mathrm{Cb}}|_{t=0} = v_{\mathrm{o}}$. Similarly,

$$I_{\mathrm{S}}(s) = \frac{I(s)(C_{\mathrm{S}} + sC_{\mathrm{B}}C_{\mathrm{S}}R_{\mathrm{B}})}{C_{\mathrm{B}} + C_{\mathrm{S}} + s(R_{\mathrm{B}} + R_{\mathrm{S}})C_{\mathrm{B}}C_{\mathrm{S}}} \tag{5.43}$$

Thus,

$$\begin{aligned} I_{\mathrm{S}}(s) + I_{\mathrm{B}}(s) &= \frac{I(s)(C_{\mathrm{B}} + C_{\mathrm{S}} + sC_{\mathrm{B}}C_{\mathrm{S}}(R_{\mathrm{B}} + R_{\mathrm{S}}))}{C_{\mathrm{B}} + C_{\mathrm{S}} + s(R_{\mathrm{B}} + R_{\mathrm{S}})C_{\mathrm{B}}C_{\mathrm{S}}} \\ &= I(s) \end{aligned} \tag{5.44}$$

as expected. Substituting Eq. (5.42) into (5.39) gives,

$$v_{\mathrm{T}}(s) = \frac{v_{\mathrm{o}}}{s} - I(s)\left(R_{\mathrm{T}} + \left(\frac{C_{\mathrm{B}} + sC_{\mathrm{B}}C_{\mathrm{S}}R_{\mathrm{S}}}{C_{\mathrm{B}} + C_{\mathrm{S}} + s(R_{\mathrm{B}} + R_{\mathrm{S}})C_{\mathrm{B}}C_{\mathrm{S}}}\right)\left(\frac{1}{sC_{\mathrm{B}}} + R_{\mathrm{B}}\right)\right) \tag{5.45}$$

The step response of the battery is investigated here so let $i(t) = Ju(t)$, a step function of amplitude J, then $I(s) = J/s$. Taking the inverse Laplace transform of Eq. (5.45) gives,

$$\begin{aligned} v_{\mathrm{t}}(t) = v_{\mathrm{o}} - JR_{\mathrm{T}} - \frac{J}{(C_{\mathrm{B}} + C_{\mathrm{S}})^2}\Bigg((C_{\mathrm{B}} + C_{\mathrm{S}})t + R_{\mathrm{B}}C_{\mathrm{B}}^2 + R_{\mathrm{S}}C_{\mathrm{S}}^2 \\ - \frac{(C_{\mathrm{B}}R_{\mathrm{B}} - C_{\mathrm{S}}R_{\mathrm{S}})^2}{R_{\mathrm{B}} + R_{\mathrm{S}}}e^{-(\alpha+\beta)t}\Bigg) \end{aligned} \tag{5.46}$$

where,

$$\alpha = \frac{1}{C_{\mathrm{B}}(R_{\mathrm{B}} + R_{\mathrm{S}})}, \quad \beta = \frac{1}{C_{\mathrm{S}}(R_{\mathrm{B}} + R_{\mathrm{S}})} \tag{5.47}$$

At $t = 0$ Eq. (5.45) simplifies to,

$$v_{\mathrm{t}}(t) = v_{\mathrm{o}} - J\left(R_{\mathrm{T}} + \frac{R_{\mathrm{B}}R_{\mathrm{S}}}{R_{\mathrm{B}} + R_{\mathrm{S}}}\right) \tag{5.48}$$

as expected. Similarly the inverse Laplace transform of the branch currents leads to,

$$\begin{aligned} i_{\mathrm{b}}(t) &= \frac{J}{C_{\mathrm{B}} + C_{\mathrm{S}}}\left(C_{\mathrm{B}} - \frac{C_{\mathrm{B}}R_{\mathrm{B}} - C_{\mathrm{S}}R_{\mathrm{S}}}{R_{\mathrm{B}} + R_{\mathrm{S}}}e^{-(\alpha+\beta)t}\right) \\ i_{\mathrm{S}}(t) &= \frac{J}{C_{\mathrm{B}} + C_{\mathrm{S}}}\left(C_{\mathrm{S}} - \frac{C_{\mathrm{B}}R_{\mathrm{B}} - C_{\mathrm{S}}R_{\mathrm{S}}}{R_{\mathrm{B}} + R_{\mathrm{S}}}e^{-(\alpha+\beta)t}\right) \end{aligned} \tag{5.49}$$

and both $i_{\mathrm{b}}(t)$ and $i_{\mathrm{S}}(t)$ equal $JR_{\mathrm{B}}/(R_{\mathrm{B}}+R_{\mathrm{S}})$ at $t=0$. Now the individual capacitor voltages can also be calculated using,

$$v_{\mathrm{Cb}}(t) = v_{\mathrm{o}} + \frac{1}{C_{\mathrm{B}}}\int i_{\mathrm{b}}(t)dt, \quad v_{\mathrm{Cs}}(t) = v_{\mathrm{o}} + \frac{1}{C_{\mathrm{S}}}\int i_{\mathrm{S}}(t)dt \tag{5.50}$$

The above equations (Eq. 5.39 to 5.50) only describes the behaviour of the terminal voltage at the leading edge of the current pulse. When the current pulse ends i.e., terminal current ($I=0$) the terminal voltage is determined by the voltage between R_{S} and R_{B} as there is no volt drop across R_{T}. The terminal voltage now depends on the balancing of the bulk and surface capacitances through the R_{S} and R_{B} resistors. Eq. (5.42) is adapted but now $v_{\mathrm{Cs}}|_{t=0} \neq v_{\mathrm{Cb}}|_{t=0}$ and $I(s)=0$ so,

$$I_{\mathrm{B}}(s) = -I_{\mathrm{S}}(s) = \frac{C_{\mathrm{B}}C_{\mathrm{S}}(v_{\mathrm{Cs}}|_{t=0} - v_{\mathrm{Cb}}|_{t=0})}{C_{\mathrm{B}}+C_{\mathrm{S}}+s(R_{\mathrm{B}}+R_{\mathrm{S}})C_{\mathrm{B}}C_{\mathrm{S}}} \tag{5.51}$$

However, as the capacitors balance their respective voltages also change so Eq. (5.51) becomes,

$$I_{\mathrm{B}}(s) = -I_{\mathrm{S}}(s) = \frac{C_{\mathrm{B}}C_{\mathrm{S}}(v_{\mathrm{Cs}} - v_{\mathrm{Cb}})}{C_{\mathrm{B}}+C_{\mathrm{S}}+s(R_{\mathrm{B}}+R_{\mathrm{S}})C_{\mathrm{B}}C_{\mathrm{S}}} \tag{5.52}$$

Taking the inverse Laplace transform results in,

$$i_{\mathrm{b}}(t) = -i_{\mathrm{S}}(t) = \frac{v_{\mathrm{Cs}}(t) - v_{\mathrm{Cb}}(t)}{R_{\mathrm{B}}+R_{\mathrm{S}}} e^{-\frac{C_{\mathrm{B}}+C_{\mathrm{S}}}{C_{\mathrm{B}}C_{\mathrm{S}}(R_{\mathrm{B}}+R_{\mathrm{S}})}t} \tag{5.53}$$

where the capacitor voltages are updated using Eq. (5.50). The terminal voltage can now be calculated using,

$$v_{\mathrm{t}}(t) = v_{\mathrm{Cb}}(t) + R_{\mathrm{B}}i_{\mathrm{b}}(t) \tag{5.54}$$

These theoretical voltage traces are compared with Euler numerical integration of the differential equation (2.34) for the individual capacitor voltages. Figure 5.20 shows good conformity between the Euler integration method and the Laplace transform integration of the battery model differential equations as well as a Spice simulation and the actual terminal voltage measurements. The component values used in the equations are those recovered using EKF from Table 5.2.

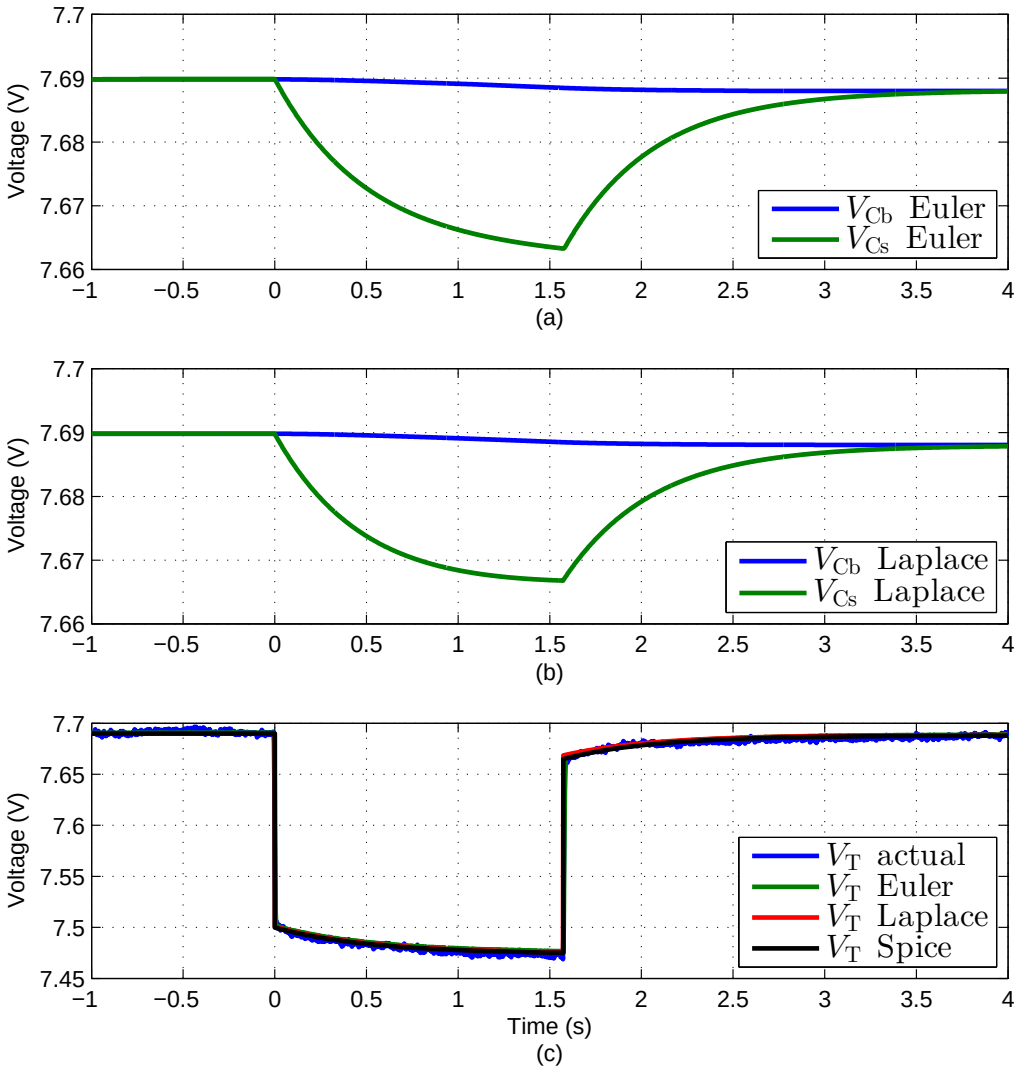

Figure 5.20: Bulk capacitor voltage (v_{Cb}) and surface capacitor voltage (v_{Cs}) calculated using (a) Euler integration and (b) Laplace transform for the step current pulse. Figure (c) shows the actual terminal voltage (v_{T} actual) and the terminal voltage modelled using Euler integration, Laplace transform and Spice with good results.

5.5.3 Results

For simplicity only the voltage response at the leading edge of the current pulse is examined. Equation (5.46) shows the time-dependent equation for the terminal voltage which can be rearranged as,

$$v_{\mathrm{t}}(t) = v_{\mathrm{o}} - J\left[R_{\mathrm{T}} + \frac{1}{(C_{\mathrm{B}}+C_{\mathrm{S}})^2}\left((C_{\mathrm{B}}+C_{\mathrm{S}})t + R_{\mathrm{B}}C_{\mathrm{B}}^2 + R_{\mathrm{S}}C_{\mathrm{S}}^2 - \frac{(C_{\mathrm{B}}R_{\mathrm{B}} - C_{\mathrm{S}}R_{\mathrm{S}})^2}{R_{\mathrm{B}}+R_{\mathrm{S}}}e^{-(\alpha+\beta)t}\right)\right] \tag{5.55}$$

which is in the form,

$$v_{\mathrm{t}}(t) = v_{\mathrm{o}} - JR(t, \mathrm{SOC}) \tag{5.56}$$

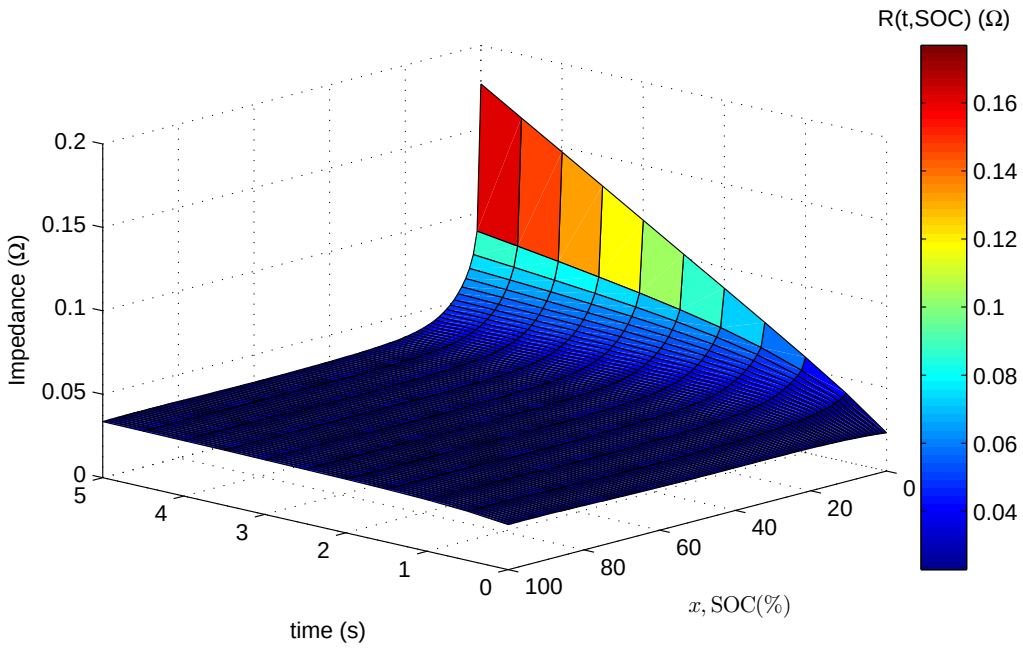

Figure 5.21: Time and SOC dependent impedance ($R(t, \mathrm{SOC})$) plotted against time and SOC

where $R(t, \mathrm{SOC})$ is the overall time and state-of-charge dependent impedance. Figure 5.21 shows $R(t, \mathrm{SOC})$ plotted against time factoring in the changes in the (C_B, C_S, R_B, R_S and R_T) component values with state-of-charge.

The figure shows that $R(t, \mathrm{SOC})$ for the leading edge of the discharge pulse remains relatively constant in both time and SOC planes for SOC $> 20\%$, explaining why the voltage responses seen in Figure 5.16 are so similar.

5.6 Chapter summary

Identifying component values of a battery-equivalent circuit requires sensitive measurements coupled with advanced techniques for recovering the internal parameters from a time-series recording of battery voltage and an applied excitation signal. Compared to what is quoted in the literature, impedance spectroscopy was found to give very poor results with the available equipment. In contrast extended Kalman filtering, applied to the bulk-surface equivalent circuit, lead to more accurate parameter estimations. The state vector $\mathbf{x}$ for the bulk-surface model is 6^{th} order, so the associated matrix operations required to implement the Kalman filter make it impractical to implement for microcontroller applications. The high sample rate (1kHz) at which the data is collected is not achievable using sensibly priced microcontrollers considering that a max of 38 measurement channels need to be available to analyse a complete battery pack. Nevertheless this investigation has identified the bulk-surface equivalent circuit as the most appropriate model for the NiMH battery modules found in Toyota Prius.

Chapter 6

Effective capacitance as a measure of state-of-health

In this chapter a new useful battery parameter called *effective capacitance* is introduced and used to identify battery block state-of-health and failure modes. It is observed that peak effective capacitance estimated throughout the discharge curve has a direct relationship to the conventional definition of state-of-health and that the location of this peak on the charge–voltage plane is indicative of different failure modes.

6.1 Background

Increasing interest in both hybrid electric vehicles (HEV) and electric vehicles (EV) means that accurate and appropriate measures of battery health are essential, particularly as these vehicles age. Many recent reviews of state-of-art battery health measurement techniques and research results have been published [94–96]. Barré et al [94] describes how battery ageing manifests as capacity fades and with resistive film growth. Capacity fade is the loss of active material within the battery; resistive film growth is the accumulation of resistive contaminants on the battery electrodes arising from unwanted side reactions. Capacity fade reduces the energy storage capability of the battery whereas resistive film growth reduces the maximum power available at the battery terminal due to increased internal resistance of a cell. These two performance-limiting phenomena are affected by different environmental conditions and usage patterns, making ageing assessment a difficult task [94]. Rezvanizaniani et al [95] assert that a battery's internal electrochemical processes are both nonlinear and time-varying, making them nearly impossible to quantify. This nonlinear behaviour of battery internal components is demonstrated in Chapter 5. Here the nonlinear aspects are simplified to an effective capacitance (C_{eff}) measure explained in Section 6.3.

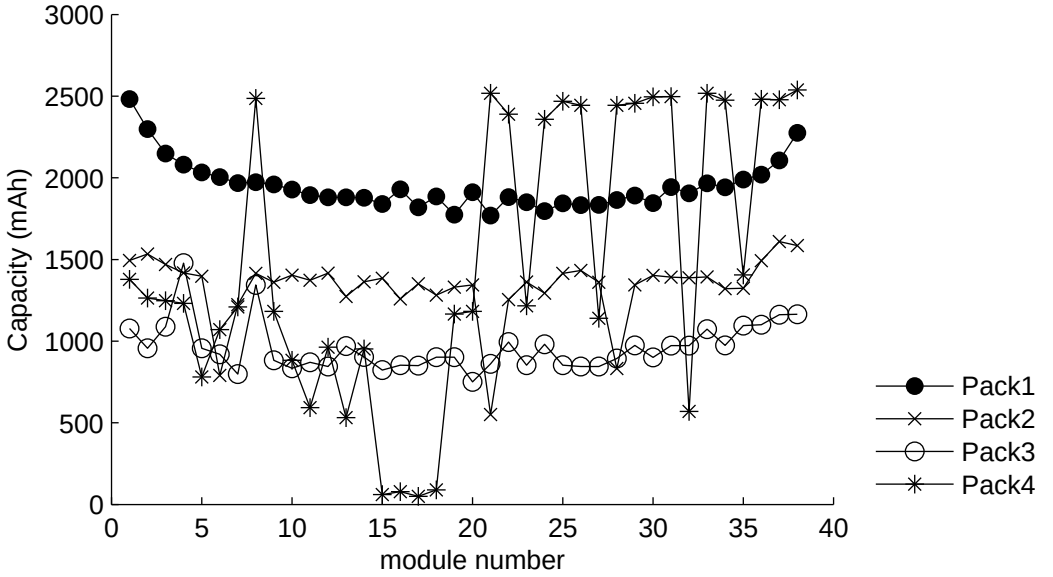

Figure 6.1: Capacity distribution of aged battery packs from four different Prius vehicles [copy of Fig. 1.4]

Figure 6.1 shows the measured capacities per battery module from several Prius HEVs, using a coulomb-counting algorithm between end-of-discharge and end-of-charge points, for four identical battery packs, but with distinct state-of-health conditions, repeated here from Chapter 1. Pack 1 shows "bath-tub" (concave) capacity distribution due to accelerated ageing of battery modules in the centre of the pack (where the temperature is higher). Pack 2 shows a similar relationship, however some modules are failing through other mechanisms. Pack 3, which is more degraded than Pack 1, also shows the concave capacity distribution. Pack 4 shows a faulty pack in which some modules retain good health whereas others have failed completely with less than 200 mAh capacity.

Zheng et al [97] discuss how capacity variation in series-connected cells affects overall pack capacity. They quantify pack capacity by coulomb counting (refer to Eq. (6.12)) during discharge, from when a given cell, Cell A, within the pack is fully-charged until another cell, Cell B, is fully discharged; cells A and B are in the same pack. The pack consisting of n series-connected cells, where a battery management system (BMS) monitors the terminal voltages of each cell, is considered to be *fully charged* when cell A is at 100% SOC. That is, the voltage of cell A is equal to the voltage at 100% SOC for that particular chemistry while the other $(n-1)$ cells have SOC less than 100%. The pack is considered *fully discharged* when cell B is at 0% SOC, that is the voltage of cell B is equal to the terminal voltage at 0% SOC for that particular chemistry while the other $(n-1)$ cells have SOC greater than 0%. Coulomb counting from when cell A is fully charged (100% SOC) to when cell B is fully discharged (0% SOC) will give

overall pack capacity. Now if one cell in such a series-connected pack is of significantly lower state-of-health, the BMS will consider the pack to be "flat" earlier, and fully charged earlier, reducing the apparent capacity of the entire pack. It can be seen from Figure 6.1, where all modules are series connected, that the energy storage capability will be restricted by the lowest performing battery module. Unfortunately, measurements of individual cell SOC is not possible on the Prius system due to the battery management configuration [2]; however, end-of-charge and end-of-discharge can be determined for each *pair* of modules.

In a series-connected battery pack, such as in the Toyota Prius, matching state-of-health, i.e., capacity, of battery modules throughout the battery pack will improve pack performance and extend vehicle service life compared to driving with a mismatched battery pack.

6.2 Model-based approach to state-of-health measurement

The most common battery model described in the literature is shown in Figure 6.2(a) [5–7, 18, 19, 26, 28, 29, 47–49, 51–53, 55, 98]. This model is used to describe the small-signal behaviour of a battery about some DC bias point, taken in this case as the $i = 0$ steady-state terminal voltage i.e., v_{o}.

Many of the aforementioned research papers establish a link between the internal parameters of the battery model shown in Figure 6.2(a) and state-of-charge (SOC). As battery SOC changes, so does the open-circuit voltage. This behaviour can be approximately modelled by replacing the fixed voltage source (v_{o}) in Figure 6.2(a) with a storage capacitor. Hence, the approximate model in Figure 6.2(b) is more suitable for modelling large-signal battery behaviour. These two battery models can be related through a star-delta transformation [57].

However, for the EKF to work correctly, an accurate estimate of other battery parameters (surface capacitance and series resistances) is also required. Estimated parameter values were used by Bhangu et al. [31] and they assume that the other battery parameters remain constant, which is not the case as shown in Figs 5.17 and 5.18.

Modelling the battery using large capacitors as in Figure 6.2(b) better reflects reality. However, when we look closely at the charge and discharge curves it can be seen that the relationship between state-of-charge and open-circuit voltage does not follow the linear trend expected of a fixed capacitor, as seen from Fig. 2.9. It is observed that $C_{\mathrm{B}} \gg C_{\mathrm{S}}$ hence the effects of the

surface capacitance on battery storage capability are negligible. The storage capacitor must instead be modelled by some nonlinear function with multiple inputs,

$$C_{\mathrm{B}} = f(\text{charge}, V, \text{SOH}, \text{temp}, \text{X}), \tag{6.1}$$

where "X" represents the remaining battery parameters such as charge-rate or hysteresis effects [29].

The battery models presented in Fig. 6.2 are appropriate for single-cell research where only the voltage responses of two (positive and negative) electrodes are considered, but cannot directly extend to multi-cell batteries [94]. Practical automotive batteries rarely have terminals exposed to allow individual measurements at cell level. Lithium technologies are an exception due to the dangers of single cells reaching run-away temperatures resulting from over-charge or excessive discharge. Toyota Prius battery modules consist of six series-connected NiMH cells; two series-connected modules constitute a block. As a result Eq. (6.1) becomes increasingly complex. If there is no difference between cells then we could consider the module as a single

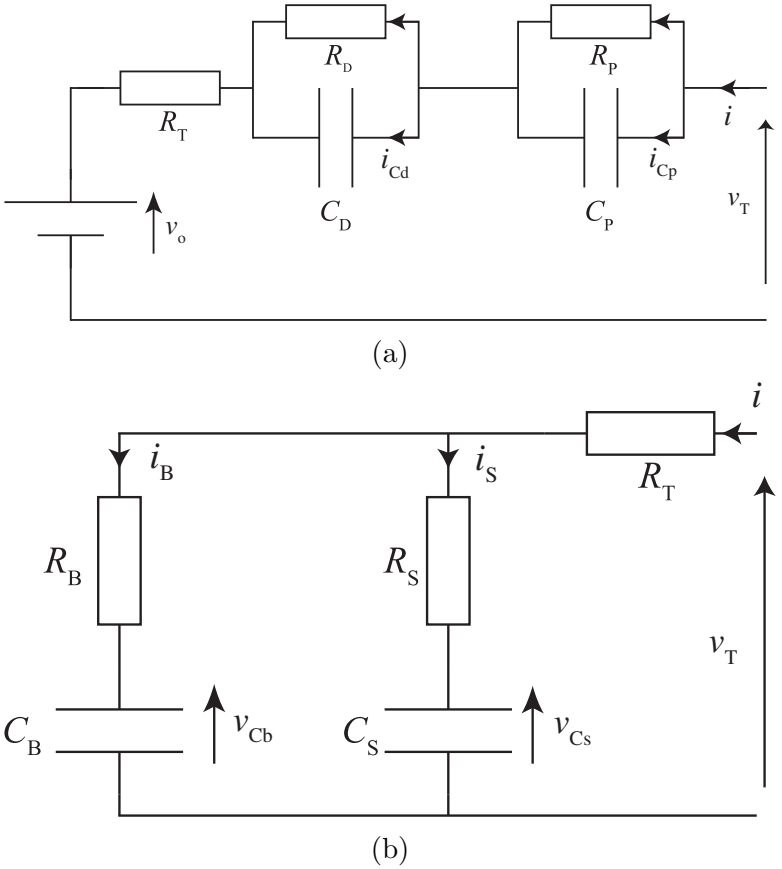

Figure 6.2: Two commonly-used battery equivalent circuits. (a) Thévenin or diffusion-polarisation equivalent circuits describes the small-signal voltage recovery after a current pulse. Bulk-surface equivalent circuits (b) describes the bulk behaviour of the battery due to capacitor energy storage by linking charge to terminal voltage [31, 57]. [copy of Figs. 2.10 and 2.11]

cell, however in reality individual cells are never identical [97]. The total bulk capacitance of the battery block now becomes a function of the 12 individual bulk capacitances,

$$C_{\mathrm{B}}^{\mathrm{tot}} = f(C_{\mathrm{B}}|_1, C_{\mathrm{B}}|_2, ..., C_{\mathrm{B}}|_{12}), \tag{6.2}$$

which in turn becomes a function of the 12 individual battery parameters,

$$C_{\mathrm{B}}^{\mathrm{tot}} = f(\mathrm{charge}|_n, V|_n, \mathrm{SOH}|_n, \mathrm{temp}|_n, \mathrm{X}|_n), \tag{6.3}$$

where the $|_n$ notation symbolises the parameter evaluated at cell n where $n = 1, 2, \ldots, 12$ for the 12 series-connected cells. Building a model to estimate all of these individual parameters, given only battery terminal current and voltage, and ambient temperature, is not practical. Hence a new grouped parameter, the *effective capacitance*, is proposed as a measure of battery state-of-health. This new measure should be useful in practical systems such as the Prius.

6.3 Effective capacitance estimation

Little work has been done on the development of suitable off-line techniques for determining state-of-health of a series-connected multi-cell battery. Most battery models presented in the literature contain some form of charge-dependant voltage source such as, in its simplest form, a capacitor (Fig. 6.2(b)). Many models such as that presented in [31] relate this storage element to state-of-health. However due to the nonlinear interaction between the multiple battery-model components of Eq. (6.1), it is extremely challenging to parameterise its capacitance. A determination of the "effective capacitance" is presented here as a reliable indicator of state-of-health of a battery block (in this case 12 series-connected NiMH cells), used in applications such as the Toyota Prius battery pack.

Effective capacitance is defined as the local slope of the charge-vs-voltage curve,

$$C_{\mathrm{eff}} = \frac{dQ}{dV}, \tag{6.4}$$

which is the small-signal equivalent of the bulk capacitance definition, $C = Q/V$; assuming that C is independent of V. Here, C_{eff} takes into account any inherent nonlinearities because it is calculated on a point-by-point basis along the discharge curve. Figure 6.3 shows how

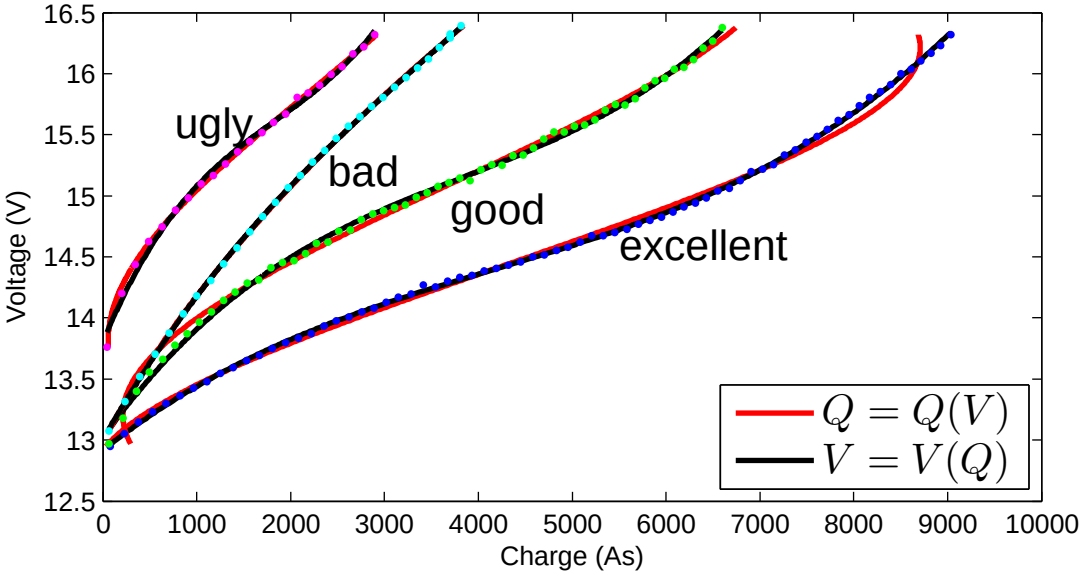

Figure 6.3: Discharge curves comparing third-order polynomial fits $Q = Q(V)$ and $V = V(Q)$ for four battery blocks (series-connected pairs of modules) whose states-of-health are, from visual inspection, grouped into four categories. The basis for this grouping is on length and shape of the discharge curve. Note: The colour scheme identifying the family of (Q, V) data points is retained in Fig. 6.4.

C_{eff} deviates from the linear relationship expected between state-of-charge and voltage for an ordinary capacitor.

To calculate C_{eff} charge-vs-voltage, (Q, V), is measured using a prototype battery diagnostic tool [99]. A supercapacitor-based energy circulation system was developed to sample the required data-points (see Appendices A to C for details). The diagnostic system connects to the sensing wires on the Toyota Prius battery pack to enable voltage and current measurements at each battery-block terminal.

If the true functional form for $Q(V)$, battery-charge as a function of battery-voltage was known, then the capacitance could be calculated from the gradient of the Q-vs-V curve. But $Q(V)$ is not known; instead a sequence of point values for (V, Q) along the discharge path are gathered. These point values are inevitably noisy, so a simple ratio of first-differences will produce very noisy gradient estimates. Therefore a smoothing technique is applied to the measurements to increase the accuracy of the gradient estimates. Inspection of the curves in, Fig. 6.3, suggests that, over the range of these measurements, the voltage V can be approximately expressed as a cubic polynomial of charge Q,

$$V(Q) = a_3 Q^3 + a_2 Q^2 + a_1 Q + a_0, \tag{6.5}$$

or alternatively charge can be approximately expressed as a cubic polynomial of voltage,

$$Q(V) = b_3V^3 + b_2V^2 + b_1V + b_0 \tag{6.6}$$

It can be seen in Figure 6.3 that both equations (6.5) and (6.6) match the measured data reasonably well. The effective capacitance can now be determined. From Eq. (6.6),

$$C_{\text{eff}} = \frac{dQ}{dV} = 3b_3V^2 + 2b_2V + b_1 \tag{6.7}$$

which is a quadratic relationship between voltage and C_{eff}, implying that C_{eff} can approach $+\infty$ or $-\infty$ when $V \to \infty$, depending on the sign of the b_3 coefficient. Such unbounded behaviour for C_{eff} is clearly undesirable. Fortunately the $V(Q)$ fitting (described next) produces a bounded and well-behaved expression for C_{eff}.

From equation (6.5) we get an inverse-quadratic function,

$$C_{\text{eff}} = \left(\frac{dV}{dQ}\right)^{-1} = \frac{1}{3a_3Q^2 + 2a_2Q + a_1}, \tag{6.8}$$

which is a bell-shaped curve with an asymptote at $C_{\text{eff}} = 0$. If Q is set to zero then $C_{\text{eff}} = 1/a_1$, which is positive for all discharge curves; this could be interpreted as the component of the capacitance of the cell that is not related to any chemical changes. For example, $C_{\text{eff}}|_{Q=0}$ could be an indication of plate area, separation distance, and electrolyte permittivity, where smaller a_1 values indicate a healthier battery i.e., larger plate area, smaller separation distance or better electrolyte permittivity. Additionally, the charge at which the C_{eff}-vs-Q curve reaches its maximum ($Q|_{C_{\text{eff}}^{\max}}$) can be calculated by locating the turning-point,

$$\frac{dC_{\text{eff}}}{dQ} = -\frac{6a_3Q + 2a_2}{(3a_3Q^2 + 2a_2Q + a_1)^2} = 0, \tag{6.9}$$

so,

$$Q|_{C_{\text{eff}}^{\max}} = \frac{-a_2}{3a_3} \tag{6.10}$$

therefore,

$$C_{\text{eff}}^{\max} = \frac{3a_3}{3a_1a_3 - a_2^2} \tag{6.11}$$

where a larger $C_{\text{eff}}^{\max}$ indicates a healthier battery i.e., better energy storage capability. From Eq. (6.5) it can be seen that a_0 is the terminal voltage of the cell when there is no charge.

In order to test this measurement technique, four battery modules are identified as "excellent", "good", "bad" and "ugly" after referring to their apparent state-of-health based on inspection of their respective discharge curves plotted in Fig. 6.3. Figure 6.3 shows that "ugly" has a higher value for a_0, but careful inspection of Fig. 6.8(b) shows that batteries that suffered catastrophic failures, end-of-life failures and ordinary ageing present with similar values for a_0, hence there is no direct relationship between a_0 and battery health.

Graphs of the residual error for the two fits of Fig. 6.3 are shown in Fig. 6.4. The maximum residual error, expressed as a percentage, for $Q = Q(V)$ fit is 4.4%, and for $V = V(Q)$ fit is 0.9%, confirming that $V = V(Q)$ gives a more accurate description of the voltage-discharge characteristics for these battery blocks.

Effective capacitance trends calculated from the local gradients of the cubic $V = V(Q)$ polynomial fits of Figure 6.3 are shown in Fig. 6.5 plotted against charge and voltage. The maximum effective capacitances are marked with a dot. [$C_{\text{eff}}^{\max}$ was also calculated using the $Q = Q(V)$ cubic fit, and a maximum difference between the two values for $C_{\text{eff}}^{\max}$ of 17% was found, (not shown).]

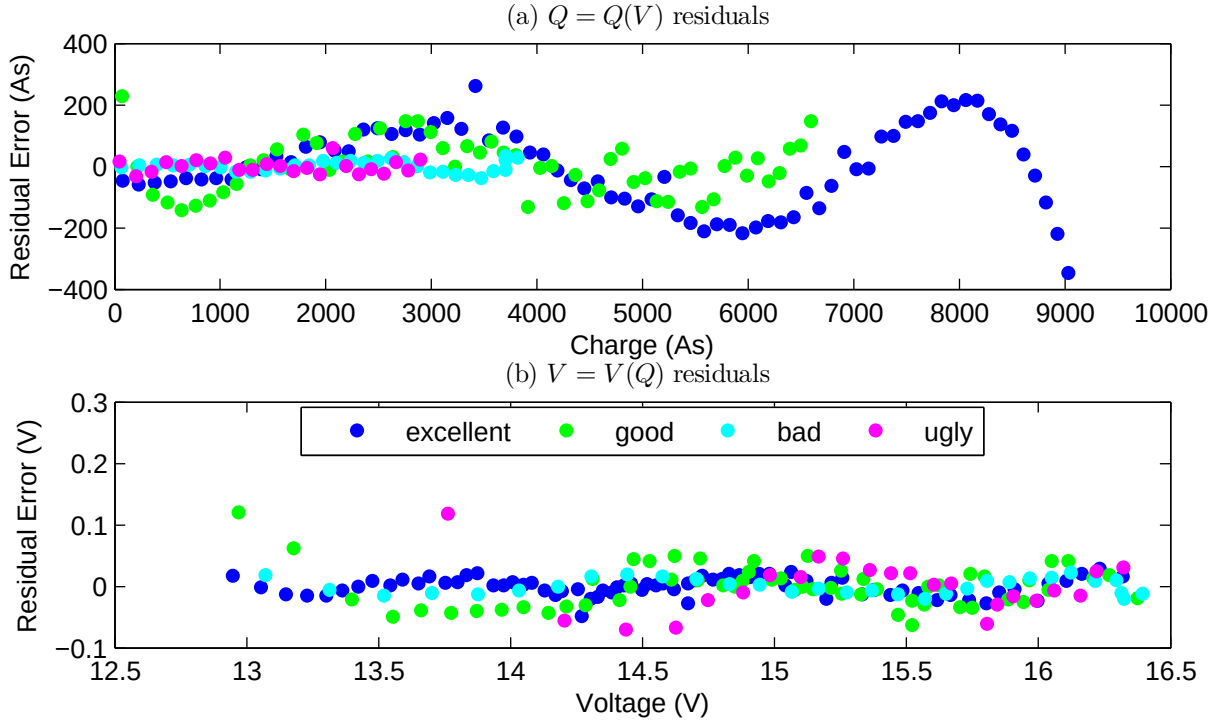

Figure 6.4: Residual error between measurements and (a) $Q = Q(V)$ cubic fit, and (b) $V = V(Q)$ cubic fit for the four battery blocks shown in Figure 6.3 confirming that $V = V(Q)$ is the better approximation for this dataset.

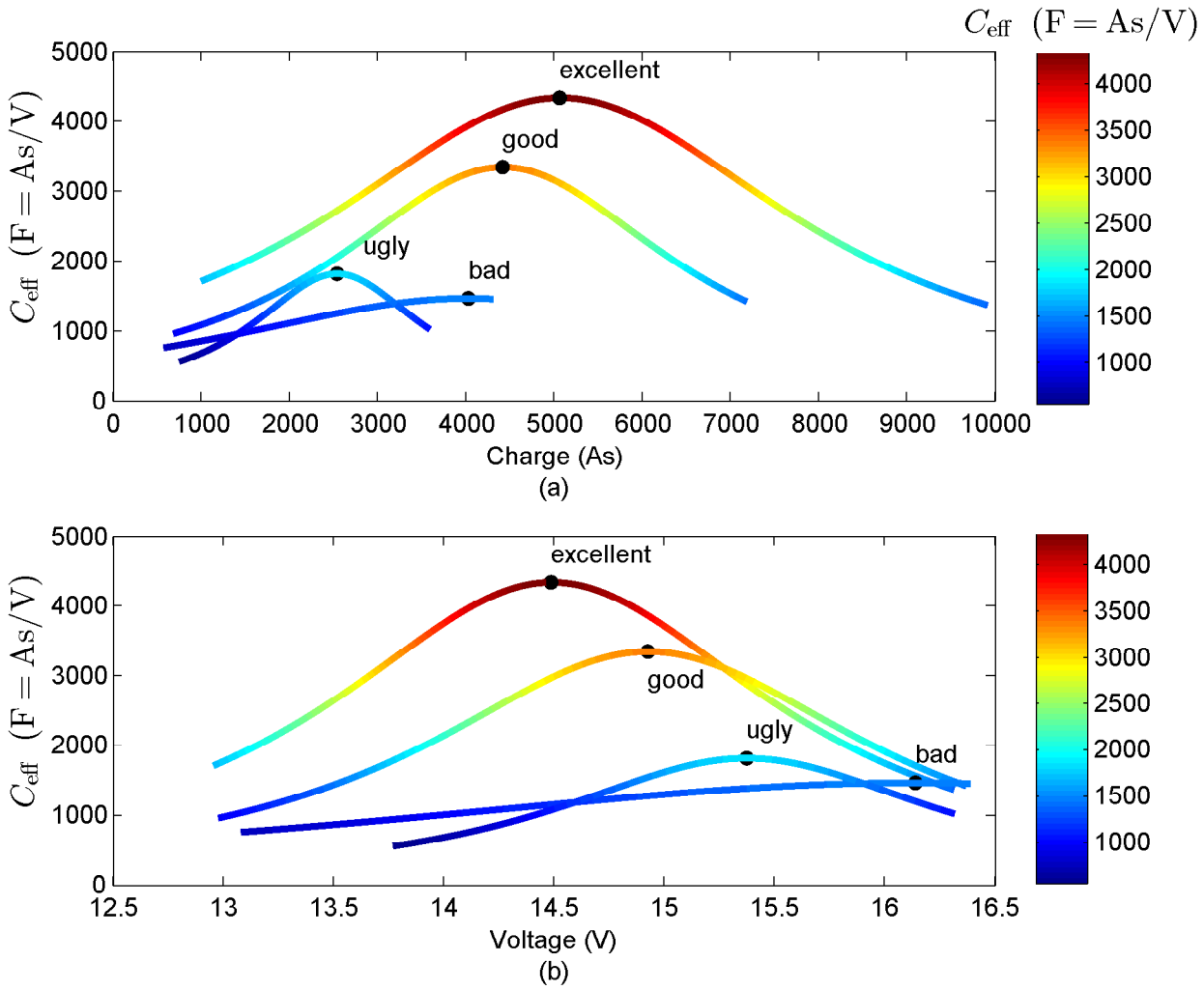

Figure 6.5: Effective capacitance calculated using $C_{\text{eff}} = (dV/dQ)^{-1}$ for the cubic polynomial fit $V(Q) = a_0 + a_1 Q + a_2 Q^2 + a_3 Q^3$ plotted against (a) charge and (b) voltage for the four battery blocks shown in Fig. 6.3. The dots mark the location of maximum effective capacitance, $C_{\text{eff}}^{\text{max}}$, and the colour scale indicates the magnitude of C_{eff}. The same colour scheme is used in Fig. 6.8.

Maximum effective capacitance occurs where the battery voltage response is most linear around the point of inflection, highlighting the nonlinear behaviour of the battery-model bulk-capacitance (C_{B}) shown in Fig. 6.2(b). This changing behaviour of the series battery block is a result of a complex series of electrochemical processes. A NiMH battery is fully charged when all chemical species have oxidised from Ni(II) to Ni(III), the electrolyte and the two electrodes now effectively forming a capacitor (charged plates separated by a distance). For constant-current discharge, the voltage-vs-charge curve should be linear if the cell behaves as a perfectly linear capacitor. However, this theoretical capacitor, formed by the electrodes and electrolyte, is charged by the electrochemical redox reactions occurring within the electrodes with ion diffusion through the electrolyte [17]. The chemical reactions effectively charge the theoretical capacitor and the voltage deviates from the expected linear relationship. This

phenomenon highlights the electrochemical aspects of the battery and indicates that modelling the battery as a fixed capacitor is an approximation at best. The hypothesis that the location of $C_{\text{eff}}^{\max}$ on the voltage–charge plane, and the value of $C_{\text{eff}}^{\max}$ itself, are primary indicators for battery state-of-health is tested using 40 sets of data.

6.4 Results and discussion

The data in Figures 6.6 to 6.8 were obtained from a variety of Toyota Prius battery packs, some from vehicles that remain in service, and others from battery packs which have failed in the field. All measurements were taken at an ambient temperature of 15°C, drawing a constant 4 A for 35 seconds every 180 seconds, giving the battery 145 s to rest and recover before recording the open-circuit voltage. In most publications researchers start with a battery or a single cell of a particular chemistry and do the required analysis and modelling to quantify ageing relationships w.r.t. environmental factors such as temperature. Instead for this battery prognostics project measurements from 40 battery blocks, of different ages, of which usage characteristics are not available, are presented.

A measurement of capacity ($Q_{\max}$) can be obtained by integrating the current between the end-of-charge and end-of-discharge points,

$$Q_{\max} = \int_{t_0}^{t_1} I dt, \tag{6.12}$$

where, $t_1 - t_0$ is the time taken to charge the module from end-of-discharge to end-of-charge and I is the time-varying current through the module. State-of-health is defined as,

$$\text{SOH} = \frac{Q_{\max}}{Q_{\text{rated}}} \cdot 100\%, \tag{6.13}$$

but for these battery blocks Q_{rated} is not readily available from battery manufacturers. So, for this battery type, SOH cannot be expressed as a percentage. An attempt was made at finding a relationship between the fit coefficients (a_0, a_1, a_2 and a_3) and $Q_{\max}$ however no clear relationship was found. Hence a relationship between capacity and $C_{\text{eff}}^{\max}$ is suggested.

Figure 6.6(a) shows capacity plotted against $C_{\text{eff}}^{\max}$ for the full dataset. While a linear relationship is clearly visible, it is skewed by outliers. The outlying data-points represent a number of possible failures such as short-circuited cells, reversed electrodes or end-of-life

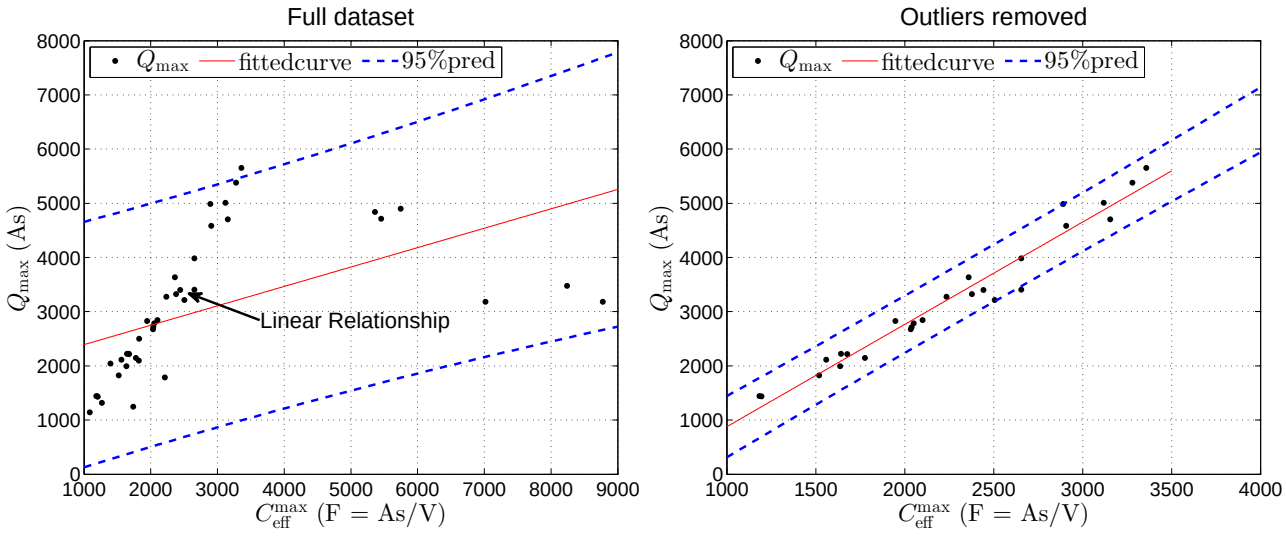

(a) (b)

Figure 6.6: Capacity, fitted curve ($mx + c$) and 95% prediction interval plotted against local maximum C_{eff} for (a) complete dataset including outliers and (b) with outliers removed. For (b), the fit parameters are $m = 1.891$ AsF^{-1} and $c = -1025$ As.

failures. Considering that the measurements are of a battery *block* where the individual cell terminals are not accessible means that it is not possible to determine which type of failure has occurred. In Figure 6.8 the location of $C_{\text{eff}}^{\text{max}}$ on the charge-voltage plane is examined to distinguish between catastrophic failures and end-of-life failures. Figure 6.6(b) removes the outliers to reveal the underlying linear relationship between capacity Q_{max} and $C_{\text{eff}}^{\text{max}}$,

$$Q_{\text{max}} = 1.891\, C_{\text{eff}}^{\text{max}} - 1025. \tag{6.14}$$

Although researchers commonly describe capacity-fade ageing effects seen in battery model parameters as an exponential decay over time [100] such relationship was not suitable for this dataset as time-series ageing data are not available. If capacity reduces to zero, an effective capacitance ($1/a_1$) of ≈ 550 F remains; this residual 550 F can be pictured as the capacitance of the battery when no active species are present, so no ion transfer through the electrolyte is possible [101].

The relationships between maximum effective capacitance ($C_{\text{eff}}^{\text{max}}$) and the (Q_x, V_x) coordinate at which the point of inflection occurs (shown in Fig. 6.7) with the outliers removed are,

$$\text{Charge} = 1.32 \times 10^{-5}\, (C_{\text{eff}}^{\text{max}})^{2.33} + 934 \quad \text{As} \tag{6.15}$$

More significant however is the relationship between voltage and C_{eff},

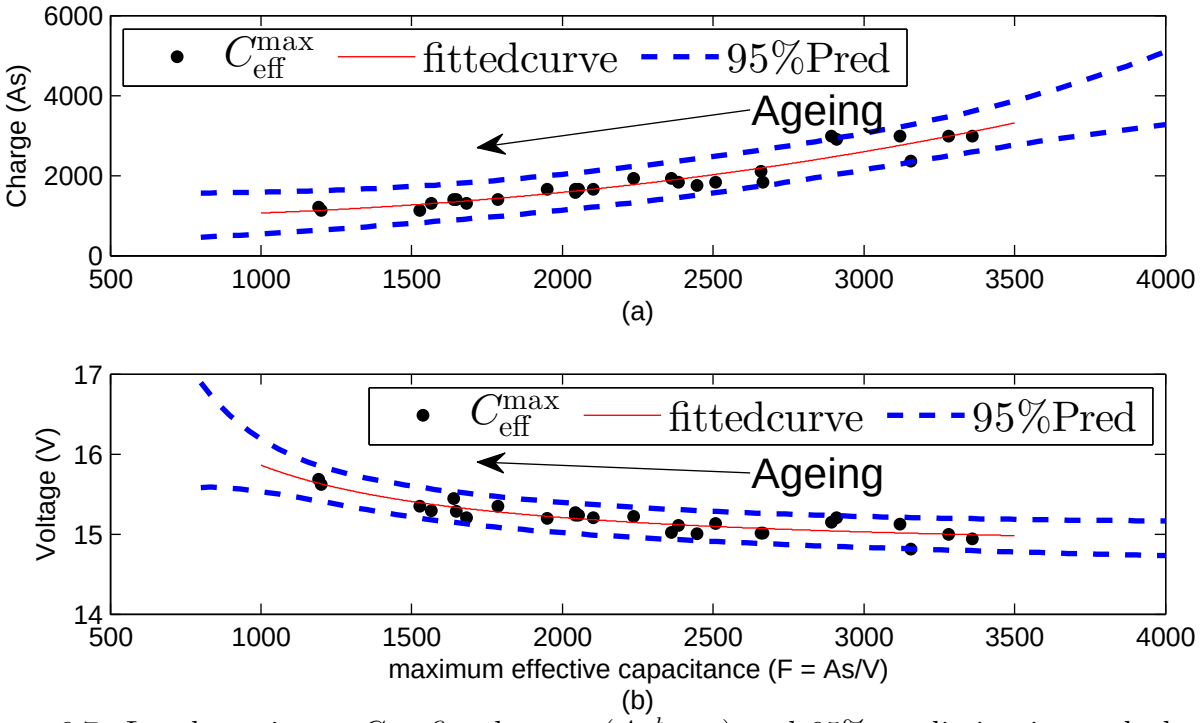

Figure 6.7: Local maximum C_{eff}, fitted curve ($Ax^b + c$) and 95% prediction interval plotted against (a) charge [$A = 1.32 \times 10^{-5}, b = 2.33$, $c = 934$] and (b) voltage [$A = 1.1 \times 10^4, b = -1.34$ and $c = 14.8$].

$$\text{Voltage} = 1.1 \times 10^4 \, (C_{\text{eff}}^{\max})^{-1.34} + 14.8 \quad \text{V} \tag{6.16}$$

which suggests that as battery health increases, corresponding to increasing $C_{\text{eff}}^{\max}$ shown in Fig. 6.6(b), the voltage where $C_{\text{eff}}^{\max}$ occurs approaches 14.8 V. These relationships are plotted on Fig. 6.8 to highlight the locus of $C_{\text{eff}}^{\max}$ during ageing. For a block of 12 series-connected NiMH cells, 14.8 V relates to a nominal voltage of between 1.2 and 1.3 V per cell. This suggests that the cubic-fitting approach may be transferrable to different battery chemistries after an appropriate adjustment to the constants in Eqs. (6.16) and (6.15). Where, Eqs. (6.15) and (6.16) describe the movement of $C_{\text{eff}}^{\max}$ through the voltage–charge plane as a result of *ordinary battery ageing* which manifests as a gradual fading of capacity. This relationship is plotted on Fig. 6.8(a).

Figure 6.8(b) superimposes the dataset outliers. Here two clear regions can be identified: battery *end-of-life* and *catastrophic* failures. The *end-of-life* region highlights the unpredictability of battery behaviour at this point shown by the scatter in $C_{\text{eff}}^{\max}$. Batteries with peak effective capacitance that fall in the end-of-life region, but also within the ordinary ageing bounds, may still be suitable for reuse, however the battery-pack may fail within a short time-frame.

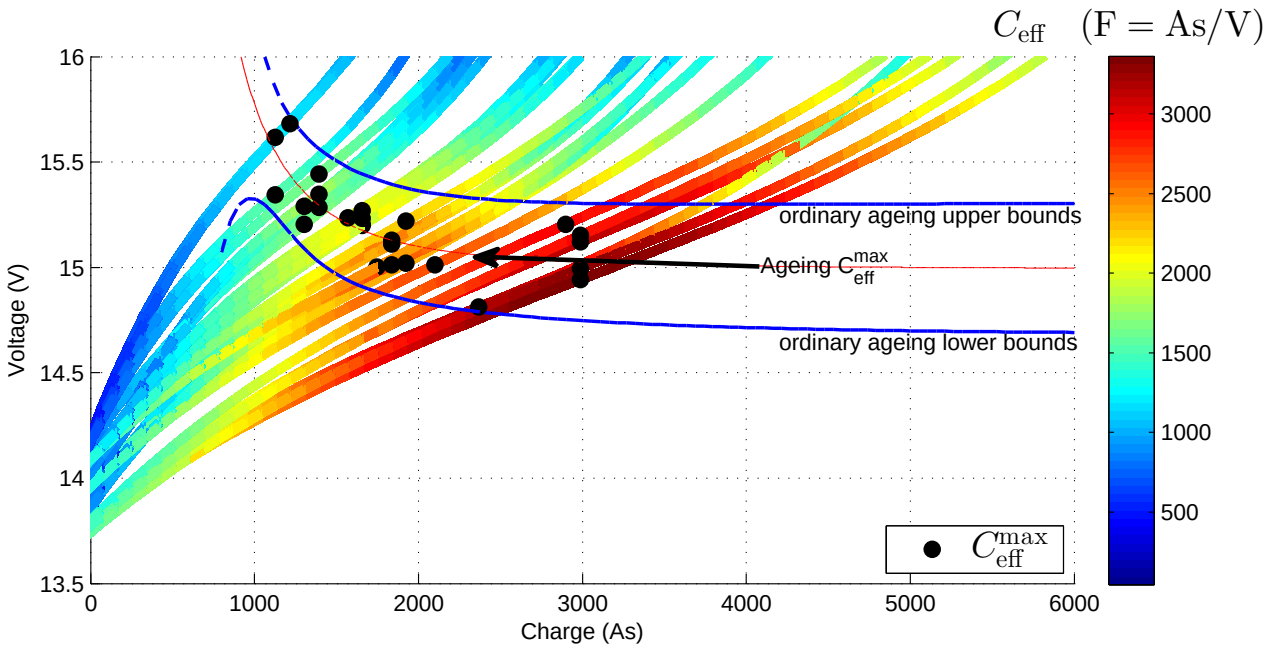

(a)

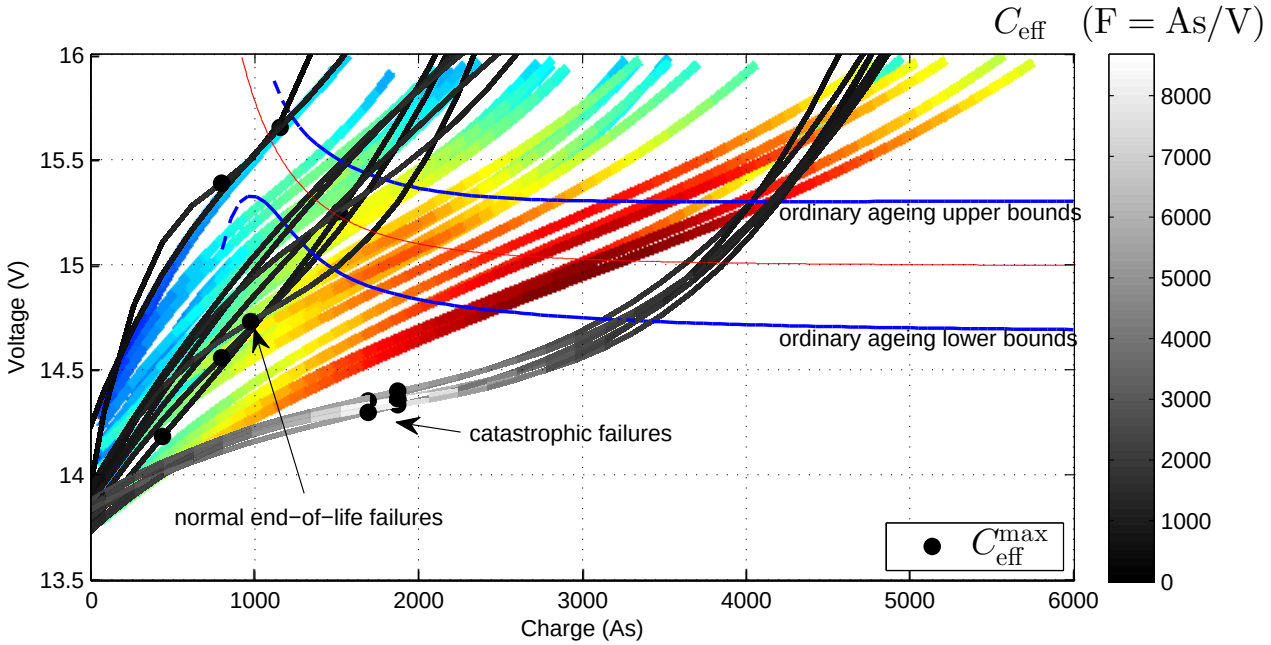

(b)

Figure 6.8: Effective capacitance, indicated by the colour bars (as defined in Figure 6.5), plotted along the battery block discharge curve for (a) *ordinary ageing* dataset showing relationship between $C_{\text{eff}}^{\max}$ (black dots), charge and voltage and 95% prediction interval i.e. the ordinary ageing locus and (b) with outliers (catastrophic and end-of-life failures) included. These plots highlight the unpredictable failure modes when battery-health reduces (end-of-life) and "catastrophic" battery failure such as short-circuited cells where $C_{\text{eff}}^{\max}$ falls outside ordinary ageing bounds.

The *catastrophic* failure region shows blocks exhibiting either short-circuited cells or electrode reversal. If one of the 12 series-connected cells is short-circuited, it is still possible to charge the battery block to 16 V; however, this results in 11 severely over-charged cells. When the block is subsequently discharged the rate-of-change in voltage with respect to charge is

higher as the over-charge is removed from the electrodes. The voltage at which $C_{\text{eff}}^{\max}$ occurs is now lower, outside of ordinary ageing bounds, as only 11 cells contribute to the overall storage capability of the block. Electrode reversal also shows a similar accelerated drop in voltage when the battery block is discharged [41].

It must also be noted that the numerical value of $C_{\text{eff}}^{\max}$ is much higher for the catastrophic failures than ordinary cells: 8000 F as opposed to 3000 F. This is a side-effect of the C_{eff} calculation: the rate-of-change of slope is much higher at the turning point for the catastrophic failure due to the steep initial voltage drop. What is of importance in this case is that $C_{\text{eff}}^{\max}$ lies outside of the ordinary ageing region.

6.5 Conclusion

Maximum effective-capacitance calculated from a third-order polynomial fit to (Q, V) data-points and its position on the voltage–charge plane accurately distinguishes catastrophic and end-of-life battery failure from ordinary battery ageing processes causing capacity fade effects. The coefficients of the third-order fit $V = V(Q)$ can be used as design parameters to optimise battery pack performance. However, no clear relationship exists between the fit coefficients and state-of-health. Rather, the suggested method shows ordinary ageing bounds within which $C_{\text{eff}}^{\max}$ must lie, with $C_{\text{eff}}^{\max}$ having a positive linear relationship with SOH capacity. These bounds are calculated through a power-law relationship between $C_{\text{eff}}^{\max}$, V_x and Q_x.

Chapter 7

Conclusions and further work

7.1 Conclusions

The main aim of this thesis was to develop a method for identifying hybrid-electric vehicle NiMH battery state-of-health. Several other areas that required investigation were identified. Here the three main technical tracks that this thesis has followed are summarised.

7.1.1 Bidirectional switch-mode power-supply efficiency

During this work hardware required to cycle energy from the battery block through a super-capacitor bank to an adjacent battery block was developed. The bidirectional switch-mode power-supply realises both buck and boost functionality using the same basic hardware. In order to improve the cycling efficiency, simulations showed that the energy wasted in the circuit depends largely on the current flowing in the output stage of the buck converter. To minimise the current in the output loop, the output or capacitor voltage needs to be higher. The output voltage increases faster if the capacitance of the storage bank is reduced. Switching the capacitor bank to be a series configuration, charging to a certain voltage then switching to parallel to finish charging, accomplishes this. The series-parallel switching scheme improves converter efficiency by a factor of two compared to a fixed duty-cycle charging scheme. Adding more series-parallel switching cycles further improves efficiency but by smaller amounts.

7.1.2 Battery parameter measurement

The thesis introduces a range of different battery parameters and battery models, and discusses various practical and numerical methods for identifying these parameters. The three different battery models are investigated and extended Kalman filtering was applied to these models and measured data to recover values for the internal battery model components. It was concluded

that the bulk-surface battery model is the most appropriate model of the NiMH batteries found in Toyota Prius.

This is because the bulk-surface model has the ability to adjust its open-circuit terminal voltage due to the bulk storage capacitors. The ability to adjust gives the EKF the lowest RMS error of 2.4 mV compared to 19 and 4.3 mV for the simple and Thévenin battery models respectively. By taking a closer look at the voltage response of the battery with respect to current during a driving cycle and applying EKF to recover the model component values, the values no longer converged. Here the conclusion was drawn that Kalman filtering only converges to a stable value when the battery is subjected to a regular current pulse. In fact what was observed was that the battery component values changed due to environmental factors, such as temperature changes, and battery state-of-charge. Further investigation showed that even though the voltage response is uniform during discharge the individual component values exhibit nonlinearity. The relationships between component values and state-of-charge are identified and it was shown that the total terminal impedance remains constant for SOC $\geq 25\%$.

The nonlinear responses of each battery component and their complex interrelationships maked it nearly impossible to implement extended Kalman filtering as a reliable method for estimating state-of-health. Even though it is theoretically possible, the number of different relationships that need to be quantified to gain suitable results makes it impractical. Therefore a new and practical measure of battery SOH: effective capacitance was proposed.

7.1.3 Effective capacitance

Effective capacitance is calculated by taking the local slope of the charge–voltage curve. Due to the battery nonlinearity this results in a point of inflection in the discharge curve which translates to a maximum in effective capacitance. The numerical value of maximum effective capacitance is linearly related to battery capacity which makes it a suitable measure for state-of-health. Batteries however fail in a variety of ways which are difficult to differentiate through conventional methods. The relationship between maximum effective capacitance, voltage and charge defines a locus of ordinary ageing on the charge–voltage plane. If maximum effective capacitance falls outside of the ordinary ageing region, the battery has failed catastrophically or reached end-of-life. So, the numerical value of, and the position on the charge–voltage plane are used together to determine the state-of-health of the battery module.

7.2 Further work

7.2.1 Bidirectional switch-mode power-supply efficiency

The simulation results only look at the buck stage of the converter and only consider first-order parasitic component losses. Should further researchers be interested simulation of the losses due to higher-order parasitic components and of the boost stage of the converter will be a useful addition to the work. Also the reasonable assumption is made that the switches required to implement the series parallel switching are lossless. Altering the simulation code to include these losses would also be a useful addition.

7.2.2 Battery parameter measurement

This thesis only details some battery parameter measurement techniques, where the main mathematical approach covered is extended Kalman filtering. Extended Kalman filtering is a large area of research and it is an impossible task to cover and investigate all aspects of Kalman filtering. Nevertheless, further work could be done investigating other variants of KF. The initial estimation problem remains unanswered, so techniques such as expectation maximisation could be investigated. Further work can be done on for example, investigating neural networks as a means of measuring the battery model internal parameters, parametrising further relationships between internal battery components and battery condition.

7.2.3 Effective capacitance

In Chapter 6 the hypothesis was made that this method could also apply to batteries of different chemistries after suitable relationships have been found. This is something that has been left as further work. More interesting however would be to investigate the possibility of calculating C_{eff} by just looking at one portion of the discharge curve i.e., only discharging from 15 to 14 V.

Appendix A

Design details

A.1 Hardware design

A.1.1 Desired outcomes

This section discusses and shows the steps taken to achieve the final design. The desired outcome of this chapter is to clearly explain the design steps taken and the reasoning behind some of the major design decisions.

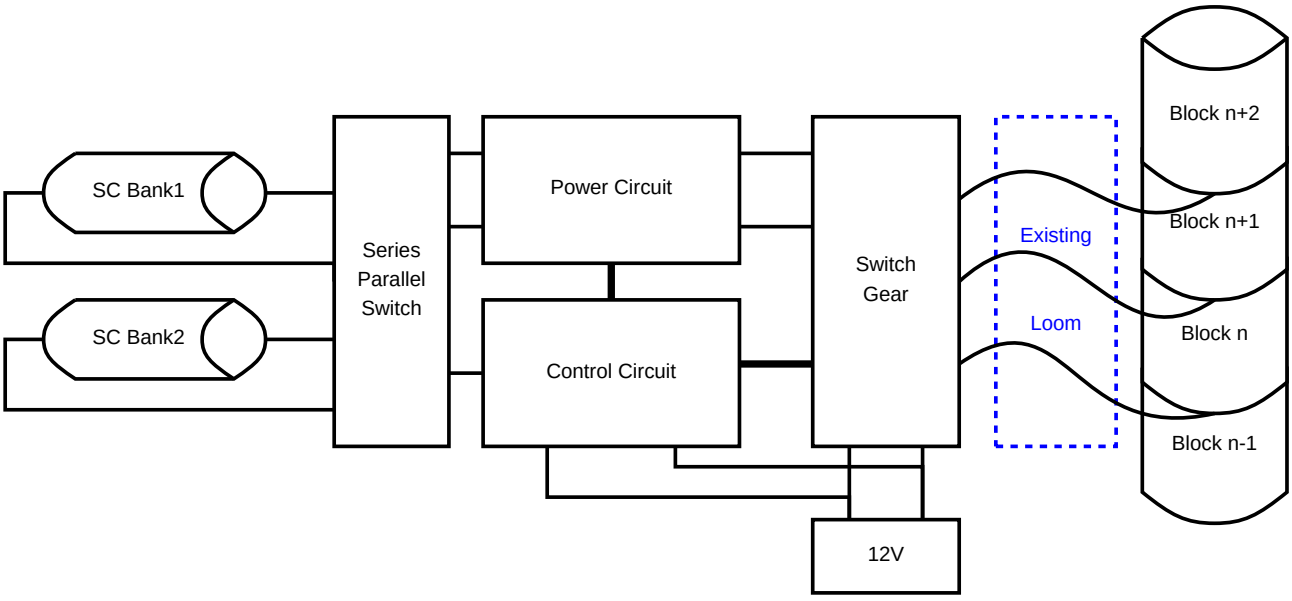

Figure A.1: Battery analyser system overview

A.1.2 Power circuitry

The power circuits used in this design can be split into three distinct sections, the bidirectional switch mode power supply hardware which is responsible for all the voltage conversions, the series/parallel switch which is used to switch two banks of supercapacitors from a series configuration to a parallel configuration and the Switch Gear used to multiplex the charger/analyser

units with and external 12 V source and two battery blocks. The following three sections describe the hardware design.

Bidirectional power supply circuit

The bidirectional Power Supply Circuit consists of an inductor, two power switches and two diodes. A schematic print of the power circuitry is included in Appendix B.2. The power switch used is the IRFZ34 is selected for its current capabilities and high breakdown voltages. The internal body diode of the IRFZ34 has a forward voltage drop of approximately 1.6 V this means that using the body diode as a flyback/flyforward diode in the switch mode power supply results in relatively large power losses and thermal strain on the FETs. As a result the mosfets are paralleled with a fast switching low forward voltage schottky barrier rectifier diode (1N5822) which has a forward voltage drop of only 0.5 V at 4 A. The power lost in the diodes can be reduced further if the mosfet is driven to allow current to flow through, however due to the nature of the converter this is difficult to implement as a there is no clear measurable transition between continuous and dis-continuous conduction without complicating the design. Driving the mosfets while the converter is in discontinuous conduction can lead to short-circuiting of either the capacitor bank or battery blocks.

The mosfets are all driven by HCLP-3020 isolated gate drive ICs in order to isolate the power circuitry from the control circuitry. An ACS711 hall sensor differential current monitor chip is placed in the current path to the battery blocks, the output of this sensor is used to determine the duty-cycle of the power switches and also to integrate the current flow through the battery blocks, this is covered in more detail in appendix A.2. The inductor used is a 10 uH bar type inductor capable of handling up to 10 A. This inductor was chosen because it was readily available and it was able to handle the peak currents which occur in the power supply.

The Power mosfet used for the buck stage (PS_Q2 in appendix B.2) is placed in a negatively switched configuration, this simplifies the gate drive circuitry as no bootstrapping is required. This does however mean that the source of the boost power transistor (PS_Q1 in appendix B.2) is floating, this complicates the drive circuitry. PS_D3, PS_D4, PS_R3 and PS_C2 insure that the isolated gate drive IC PS_U1 always has sufficient power supply (minimum of 10 V maximum of 35 V). PS_D3 is a 20 V Zener diode which when biased through PS_R3 clamps the power supply to PS_U1 to 20 V. The capacitor PS_C2 acts as a bootstrapping capacitor and links the source of PS_Q1 to PS_U1.

Series/parallel capacitor switch

The series/parallel capacitor switch is a unique piece of electronics which requires only one digital input to switch the two capacitor banks from series to parallel. The reasons behind the need for such a switch are covered in 4.

The switch consists of two high-side mosfet drive ICs (LTC1154), three power mosfets, an isolating opto-coupler and a series of RC timer circuits to insure sufficient deadband between switching. The LTC1154 has an internal charge pump capable of driving the gate beyond the supply voltage [102], which makes it the ideal component as minimal additional components are required. Table A.1 shows how the input signals to the LTC1154s are related to insure switching with appropriate deadband.

Table A.1: LTC1154 truth table

IN	$\overline{EN}$	GATE
L	X	L
H	L	H

The two LTC1154 need to output complementary gate drive voltages with some deadband delay to insure that the supercapacitors are not short circuited during switching. From the truth table it can be seen that if the IN of one driver is connected to the $\overline{EN}$ of the second driver and the IN of the second driver is always high that this would produce a complementary gate drive situation. Figure A.2 shows how the two gate drive IC outputs behave, the circuit diagram for this circuit is included in Appendix B.4.

Switch gear

The switch gear is used to multiplex two battery blocks and an external 12 V source to one charger/analyser unit. Simple 12 V relays are used to ensure full electrical isolation between the batteries and the control circuitry. Fuses are also built onto the switch gear circuit board for additional safety. The relay coils are driven through a simple transistor circuit from the main microcontroller.

A.1.3 Sensor design

The ILD74 opto-coupler is used for the voltage sensing, the ACS711 is used to sense the current and a MCP9700 temperature chip is used to sense temperature [103].

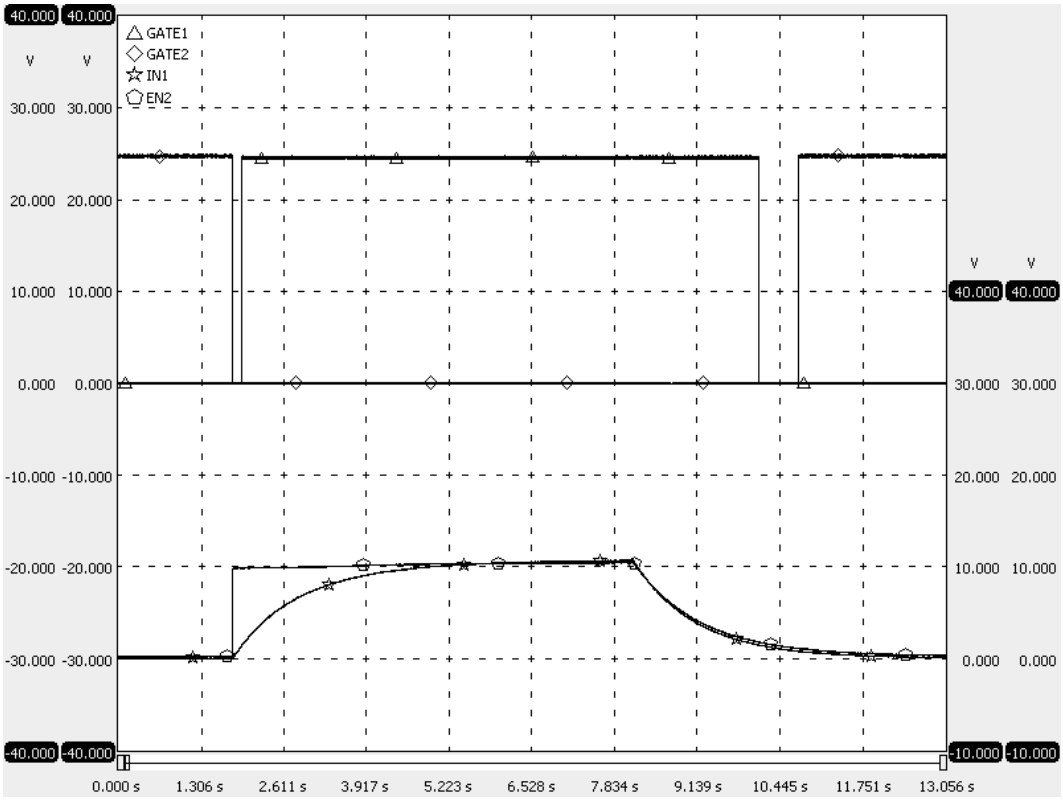

Figure A.2: Series/parallel gate drive signals showing RC time constants and deadband

The transfer characteristics of the ILD74 were measured for a range of input voltages. A linear relationship was created between input and output voltage throughout the range required for this project, the results and the linear relationship are shown in Figure A.3.

The resulting relationship is:

$$V_{\text{in}} = -0.0204\, V_{\text{digital}} + 24.447 \tag{A.1}$$

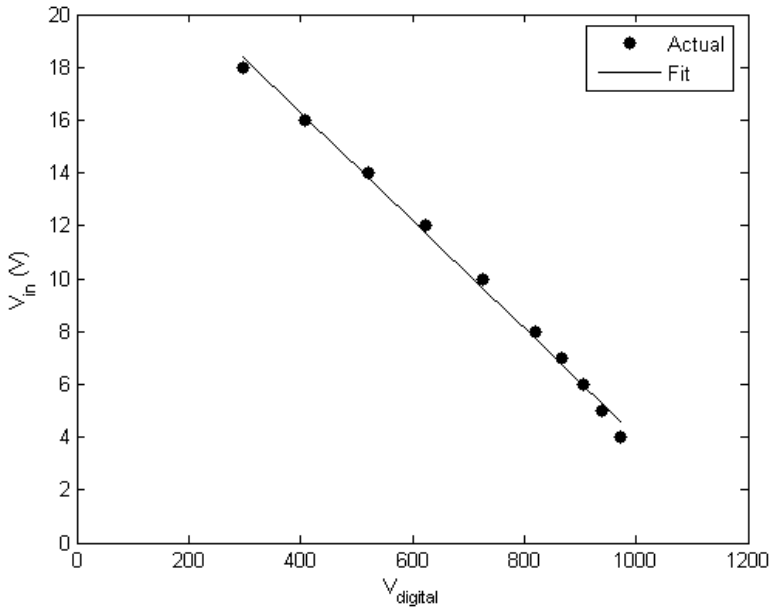

Figure A.3: Voltage transfer relationship of the voltage sensing circuit.

The relationship shown in equation (A.1) fits the dataset with an R^2 value of 0.9954. This relationship is used in the firmware to calculate and compare battery and supercapacitor voltages. A simple two point gain offset calibration routine has been programmed into the microcontroller which allows for periodic checking and adjustment of this relationship.

The ACS711 is a positive and negative current sense IC therefore the output voltage of this chip is half the supply voltage when no current is flowing. The specifications of this current sensor state that the output voltage varies with 110 mV per amp [104]. However this application requires the sensor to measure an average from a 62kHz current signal. A simple *RC* filter circuit was built on the output of the sensor to filter out the high frequency switching signal. The filter was designed to have a cut-off frequency of approximately 500Hz by using a 1kΩ and a 0.33μF capacitor.

Adding this filter to the design meant that the over all gain between the current flowing through the sensor and the voltage at the microcontroller input was different from the value stated in the data-sheet. Not only was the gain different but the gain for positive current and for negative current were also different. So to accurately measure the current this sensor needed to be calibrated using a three point calibration routine. The sensor output voltage is directly related to the supply voltage of the sensor which in turn is also the reference voltage for the ADC inside the microcontroller. The calibration routines are discussed in appendix A.2.2.

The MCP9700 is a Linear active thermistor, this means that there is a linear relationship between voltage and temperature which is not the case for NTC or PTC thermistors. The relationship between temperature and voltage for the MCP9700 is shown in equation (A.2) [103].

$$V_{temp} = T_{\mathrm{C}} T_{\mathrm{A}} + T_{0^{\circ}C} \tag{A.2}$$

Where T_C is the temperature coefficient, T_A is the ambient temperature and $T_{0^{\circ}C}$ is the voltage output at 0°C. The datasheet suggests the values shown in table A.2 for these parameters, however some calibration may be required.

Table A.2: MCP9700 temperature sensor parameters.

Parameter	Value
T_C	10 mV/°C
$T_{0^{\circ}C}$	500 mV

The MCP9700 measures temperature by monitoring the voltage drop across a diode, the low impedance thermal path to the diode is provided by the pins of the sensor [103]. Therefore the temperature sensor can accurately measure the temperature of the PCB board, this may not be an accurate representation of the battery temperature.

A.1.4 Control circuitry

The main component of the control circuitry is a PIC16F1827 table A.3 describes the functionality of the microcontroller. Appendix B.1 shows how the microcontroller is connected to all the various components of the power circuitry, the series/parallel switch, the sensor circuitry and the communications circuitry.

Table A.3: PIC16F1827 functionality.

Program Memory	Data Memory												
Words	SRAM	Data EEPROM	I/O's	10-bit ADC (ch)	CapSense (ch)	Comparators	Timers (8/16-bit)	EUSART	MSSP	ECCP (Full-Bridge)	ECCP (Half-Bridge)	CCP	SR Latch
4K	384	256	16	12	12	2	4/1	1	2	1	1	2	Yes

The PIC16F1827 was chosen for the control circuitry because it was able to operate at a relatively high frequency 32 MHz internal clock frequency. This has as advantage that no external clocking source was required reducing both complexity of the design and footprint of the circuitry. The microcontroller also has both 10bit analogue to digital converters and a 10bit pulse width modulation output. This means that there is enough resolution in both the inputs and the outputs to accurately measure and control the various parameters surrounding the design.

A.1.5 Communication hardware

The communication hardware consists of two XBee Series 2 Pro wireless modules and two 8 channel multiplexers. The XBees behave like a wireless serial port extension and communicate with each other using API commands. The Master XBee which is connected via a FTDI USB to serial converter to the PC is configured as an API coordinator. The Slave XBees RX and TX lines are connected to two 1-8 multiplexers. Four digital IO lines are connected from the Slave

XBee to the select and enable lines of the multiplexer. This allows the XBee to switch its RX and TX lines to the 8 analyser units, allowing for duplex (bidirectional) communication between the PC and the analyser units. Figure A.4 shows a block diagram of the layout. Appendix B.5 shows the design of the communication system.

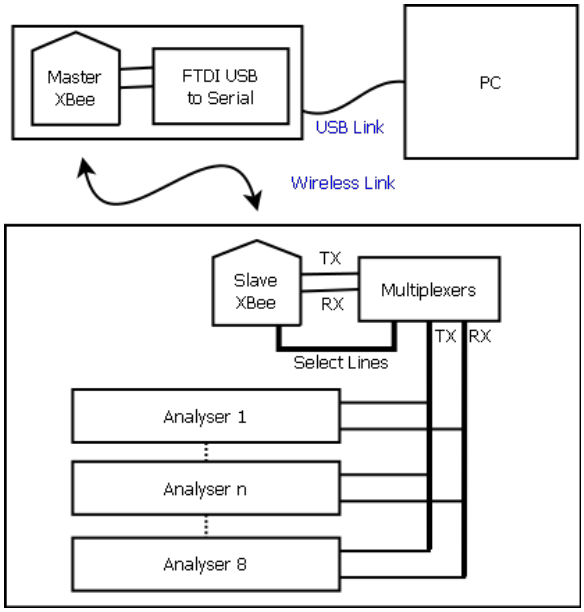

Figure A.4: Communication system block diagram.

The RX input on the microcontroller cannot be left floating otherwise induced noise on the pin could be interpreted as communication. Therefore each RX pin arriving at the communication board is connected to ground through a 10kΩ resistor. The 10kΩ resistor is big enough to not have an effect on the communication signals.

A.2 Firmware design

This section describes in detail how the various sections of the firmware are developed.

A.2.1 Special variables

Object orientated programming is very common in higher level languages such as C# and Java. The concept of object orientated programming is that an object (class) is created which contains within it all the variables and functions associated with that object (class). In microcontroller C such a concept does not exist. As a result various work-around solutions are used to create the same/similar effect in a lower level language. The concepts of `struct` and `union` type definitions are described well in [105]. A `struct` is a collection of related elements or variables that can be accessed by a common name [105].

Battery variable

The battery description needs to contain a number of different variables such as voltage, block number, status and capacity. For this reason a structure was created which contains the different elements related to the battery, the code is shown in Listing A.1. Four battery variables are created as shown in line 12. This represents the two battery blocks that can be connected to the bidirectional power supply, the external 12 V supply and none which disconnects everything from the bidirectional power supply.

Listing A.1: Battery Structure Typedef

```
1  typedef struct {
2      short int voltage;
3      unsigned char blockNr;
4      unsigned char status;
5      unsigned int capacityMSB;
6      unsigned int capacityLSB;
7      unsigned int AsMSB;
8      unsigned int AsLSB;
9      unsigned int sampleCount;
10 } battery_tdef;
11
12 battery_tdef battery1, battery2, twelve_volts, none;
```

Grouping all the variables related to the battery in one simple battery structure means that writing to and reading from these variables in a range of different methods (or subroutines) is simplified. The battery variable can either be passed directly into a method or the pointer to the battery structure can be passed into the method. Passing the pointer to the structure

into a method means that code within the method can alter the variable, much like object orientated programming. Passing pointers to data instead of passing the data into the variable also greatly reduces the size of the program code.

A.2.2 Voltage, current and temperature sensing

The voltage sensing hardware has been discussed in appendix A.1.3, this hardware produces a 0-3.3 V signal which is passed into the PIC. The PIC microcontroller has a 10bit analogue to digital converter which converts the input voltage to a digital equivalent value (V_{digital}). The conversion is shown in equation (A.3).

$$V_{\text{digital}} = \frac{V_{\text{in}}}{3.3\ \text{V}} 1024 \tag{A.3}$$

The V_{digital} value of both the supercapacitor voltage and the battery block voltage is used throughout the firmware. The relationship between V_{digital} and supercapacitor voltage is shown in equation (A.1).

The current sensing IC described in appendix A.1.3 is also connected to an analogue to digital converter. The output voltage of this current sensing IC is half of the supply voltage when there is no current flowing. This means that V_{digital} will be 512 when no current is flowing. This needs to be taken into account during the design of the firmware. It was found during use of the sensor that the relationship between sensor output voltage and current varied depending on whether or not positive or negative high speed switching current was passed through the sensor. So a three point calibration routine was programmed which initially calibrated the zero point, then positive current and finally negative current. Choosing the calibration points that lie close to the actual operating currents minimises errors.

Temperature sensing is also done with an analogue to digital converter.

The values measured by the analogue to digital converter need to be translated into a term that can be read and understood by a human. For example, 512 needs to be converted to zero. This is done by providing some calibration data. One form of calibrating is using a two point method. For example if there is a linear relationship between the measured and actual values then a two point gain zero calibration method will provide enough information to accurately predict the actual value from the measured value.

Calibration is handled in the firmware by responding to a series of API commands which indicate that the calibration process has started. The firmware waits for a specific command from the user (through the graphical user interface) indicating that the conditions for zero calibration have been met. This for example requires placement of a jumper wire across the super-capacitor pins after removing a fuse. This means that zero voltage will be measured. The digital value for zero voltage is written to non-volatile EEPROM memory. The firmware then waits till the user has provided the second calibration point, 20 V for example. This may involve connecting a fixed voltage source to the sensor. The actual value and the measured value are then written to the EEPROM.

Calibration of the battery voltage is a bit more involved due to the set-up of the sensing circuit. If a zero voltage calibration point if provided then the voltage regulator used to power the PIC micro and provide the reference voltage will also be zero. Therefore the first calibration point cannot be zero and must be greater than 3.3 V. With the addition of the zener diode to this circuit the calibration point needs to exceed the zener voltage (10 V in this case). It is best to chose calibration points as close as possible to the actual values that are being measured therefore calibration points of 12-20 V are suitable for calibrating the input voltage sensor.

A.2.3 Discharge firmware

The battery blocks need to be discharged to record the (Q, V) points during discharge. Figure A.5 shows a flow diagram of one of the sub-routines responsible for controlling the discharge of the battery block.

The section of the flow chart labelled "discharge battery" represents a PID loop which holds the discharge current steady at 4 A. The current is controlled by altering the duty cycle of the appropriate power switch. A steering control register is altered which determines the physical pin of the microcontroller that carries the PWM signal. This steering control is altered to give the bidirectional power supply the appropriate function i.e., charge or discharge.

The flow chart in Figure A.5 also shows which configuration the super-capacitor is switched to throughout the discharge cycle. The first decision block determines whether or not the super-capacitor is already full. This is done by checking the configuration and the voltage. For example if the supercapacitors are switched in parallel and the super-capacitor voltage is 10 V then the super-capacitor bank is deemed to be full.

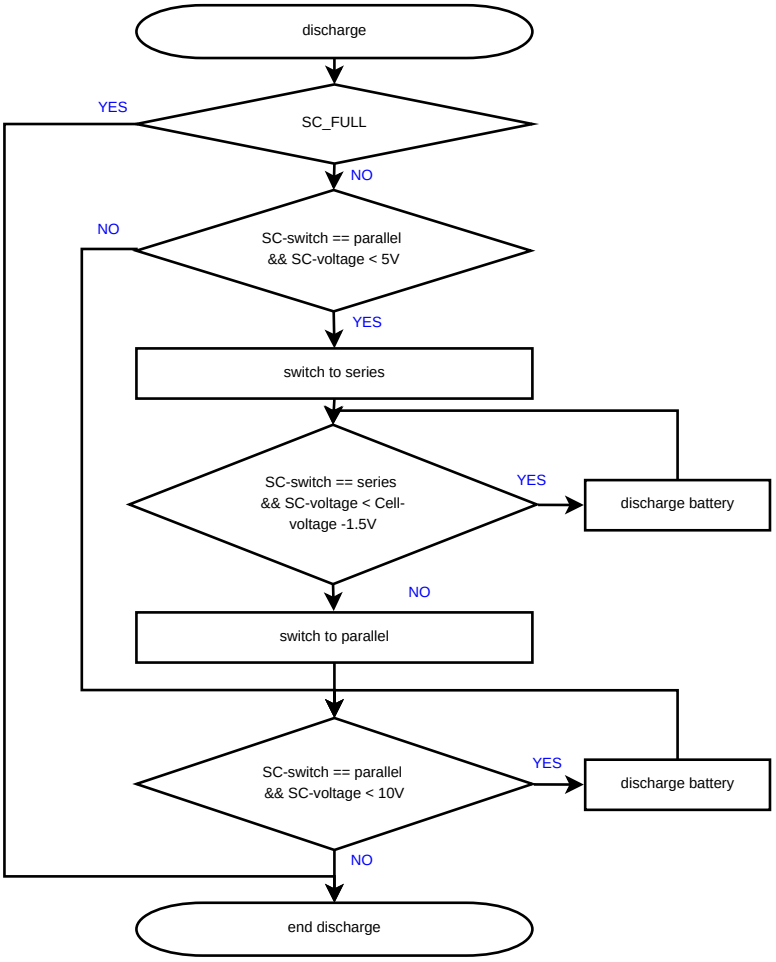

Figure A.5: Flowchart depicting discharge control flow

The second decision block in the flow chart checks to see if the super-capacitor bank is in a parallel configuration and if the voltage is less than 5 V. If this is the case than the capacitor banks are switched to series in order to increase the efficiency of the converter by increasing the output voltage. After the switch to series has completed the code enters a loop where the battery blocks are discharged until the series connected super-capacitor bank voltage is 1.5 V below the battery block voltage.

When the series connected capacitor bank reaches this voltage it is switched to a parallel bank in which case the voltage halves. The code then enters another loop which charges the now parallel connected bank to 10 V. The capacitor bank is now considered to be full and the discharge routine is finished. If an API command is sent to the battery charger while it is in the "discharge battery" PID loop the battery charger will reply with the battery voltage, the super-capacitor voltage and the state of the integrator. A pointer to the battery variable described in section A.1 is passed into the PID loop, this ensures that the battery data is always up to date.

The firmware uses the calibration data stored in EEPROM to accurately calculate the

battery and super-capacitor voltages. For example the two calibration points are used to calculate the gain and offset for the linear relationship between the V_{digital} value and the actual battery voltage. The formulas below show how the gain and offset are calculated, (x_1, y_1) and (x_2, y_2) are the two calibration points.

$$y = ax + b \tag{A.4}$$

$$a = \frac{y_1 - y_2}{x_1 - x_2} \tag{A.5}$$

$$b = y_1 - ax_1 \tag{A.6}$$

Floating point calculations on a microcontroller take a lot of time and use a relatively large amount of memory to compute. Therefore the battery and super-capacitor voltages are calculated in a millivolt scale, this means that the scaling factors a and b are also multiplied by 1000. Listing (A.2) shows how the super-capacitor voltage is calculated in the firmware based on the relationship shown in equation (A.1).

Listing A.2: Super-capacitor voltage calculation

```
1 int calc_scVoltage(void)
2 {
3     return (24447-20*readSCVoltage());
4 }
```

A.2.4 Charge firmware

The battery blocks need to be charged in order to correct any charge imbalances throughout the battery pack. Figure A.6 shows how the firmware handles the charging operation.

The first decision block determines whether or not the super-capacitor bank is in series or parallel. If the bank is in a parallel configuration then the battery block is charged until the super-capacitor voltage drops below half the battery voltage. The block named “charge battery” represents a piece of code that implements the standard boost formula for calculating duty cycle shown in equation (3.1). If the super-capacitor voltage drops below half the battery voltage then the capacitor bank is switched to a series configuration effectively doubling the input voltage to the converter. As a result the duty cycle required to boost the capacitor voltage to the battery voltage is reduced.

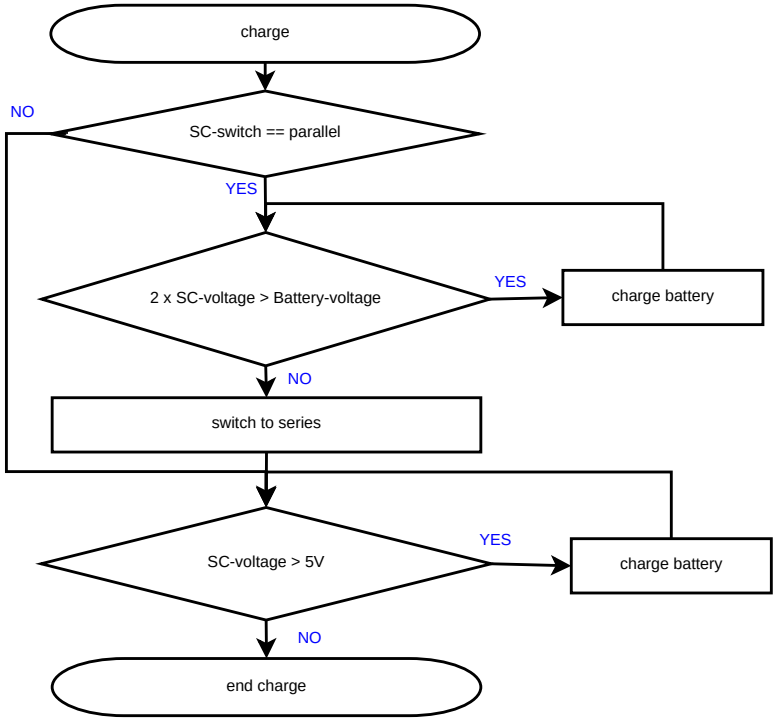

Figure A.6: Flowchart depicting charge control flow.

The firmware in this loop also responds to an API command by returning the battery voltage, super-capacitor voltage and current integration value. The reply from the charge unit in this fashion also indicate to the GUI that the charger is busy, this will become more apparent in section A.3.

A.2.5 Coulomb counting

Coulomb counting is effectively an integral of the current flowing into or out of a battery. This is achieved in firmware by periodically sampling the output of the current sensor. To get an accurate integral, the time interval dt between samples needs to be small. On a digitally controlled system this is very difficult to achieve and requires large amounts of processing power. Therefore the sampling is done in a timer interrupt service routine to insure that the current is sampled at a consistent time interval. The instantaneous current (sample) is measured and summed to give a total current value. Figure A.7 shows the discrete integration process.

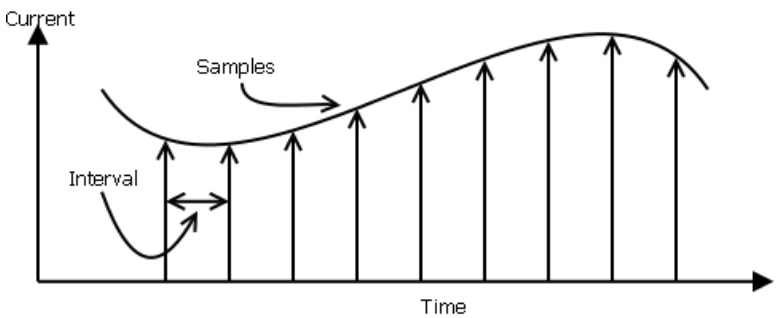

Figure A.7: Discrete integration

Equation (A.7) shows the continuous calculation for an integral

$$Q = \int_0^T I(t)\ dt \approx \sum_{n=0}^{N} I_n \Delta t \tag{A.7}$$

where $I(t)$ is the instantaneous current at time t and $N = T/\ dt$. In equation (A.7) the variable I_n represents the ADC read performed by the microcontroller of the current sensor voltage. The ADC read is not directly related to the current due to the offset of approximately half the supply voltage in the sensor output voltage. Therefore to get an accurate representation of the actual current this offset needs to be subtracted from the ADC value. Only now can the digital representation of the capacity be converted to an actual capacity using the sensor calibration data.

Overflow of the digital representation of the capacity variable needs to also be taken into account i.e., if the integration exceeds 0xFFFF. The firmware accounts for this situation by checking to see if the total current value exceeds 60000 and if this is the case another variable is incremented to insure that all the data is captured correctly.

The data from the integrator is written to the battery variable described in appendix A.1. The firmware knows which battery variable to write to the integral data too based on the block number and the state of the digital IO pins used to select a specific block. The energy taken from the 12 V source is not integrated.

A.2.6 Communication system

The communication system on the individual microcontrollers makes use of the hardware EUSART serial port on the microcontroller. The hardware implementation of the serial port means that interrupts are triggered when data is received and when the transmit buffer has been emptied. This hardware controlled system makes the communication firmware easier to develop.

The baud rate of the serial port on the microcontroller is changed using set-up registers within the microcontroller or a register can be configured so that the baud rate is automatically detected. The synchronisation character used is `0x55`. The microcontroller upon receiving this character sets the appropriate baud-rate registers to the correct values. As a result the communication baud rate of the microcontroller matches the communication baud rate of the slave XBee and the effect of slight variations of clock speeds are removed.

The standard C `printf` command is used to send data from the microcontroller out of the standard output port of the chip. The standard output needs to be assigned. This requires the user to program their own implementation of the `putch(char c)` method and a transmit ring buffer which are both used by the printf library.

During development it was found that the `printf` library is large and memory hungry. Each implementation of printf, i.e., printf with one argument or printf with four arguments, meant that the whole printf code was duplicated in program memory. As a result the program memory of the PIC16F1827 was full after only a few different printf commands. It was therefore decided that only two variations of the printf command will be used in two different methods, a `printTwelve` subroutine which implements a printf statement with 12 arguments and a `printFive` subroutine which implements a printf statement with 5 arguments. If the response to an API command does not contain 5 or 12 characters of data the remaining arguments are set to 0x00. This reduced the program code for each call to printf dramatically. Similarly a subroutine named `printBatt` which implements printTwelve was created. A pointer to a battery variable is passed into this subroutine and it subsequently prints all the relevant battery data, voltage, status, capacity etc.

A special structure was programmed for the receiving string shown in listing A.3. The `str_cnt` variable in the typedef keeps track of the length of the received command, the array holds the characters that have been received through the hardware serial port. A series of `if` statements in the RX interrupt service routine (ISR) check to see if the start delimiter for the communication packet has been received, the start delimiter was chosen to be `0x24` which corresponds to the '$' character. The end of packet byte is `0x0D` or the carriage return character.

Listing A.3: Receive Buffer Typedef

```
1 typedef struct {
2     uchar       str_cnt;
3     uchar       str[UART_BUF_SIZE];
4 } str_ptr_t;
```

The communication system needs to be duplex due to its nature i.e. one master communicating with up to eight end devices (the micro controllers). Therefore each microcontroller is given a unique ID which is stored in the EEPROM. This ID is always transmitted back to the master (the PC) allowing it to decipher which microcontroller has replied to its command.

No checksum is transmitted from the PC to the microcontroller because the networked nature of the XBee communication means that an acknowledgement of transmission is sent back to the PC, see Listing A.4. Also the command transmissions are followed with a verification reply from the microcontroller. For example, if the temperature is requested from the microcontroller then it immediately replies with the temperature. A catch for unknown commands has been built into the microcontroller API firmware, if an unknown command is received a negative acknowledge byte is returned. A checksum is however transmitted from the microcontroller back to the PC because the data transmitted to the PC contains critical information and no acknowledgement system is built into the microcontroller or slave XBee firmware.

The master XBee is configured as an API coordinator. This means that the full API command stream is transmitted to the PC, the API commands include information such as acknowledgement of transmissions etc. Setting the Master XBee to an API coordinator allows commands to be sent to the slave XBee to change the status of digital IO pins.

The slave XBee is configured to be an AT router/end device. This means that only the transmitted packet is sent out of the serial port. For example if the command,

```
7E 00 11 10 01 00 13 A2 00 40 61 62 E4 D3 9B 00 00 24 DC 0D D7
```

is sent to the master from the PC then only the command

```
24 DC 0D
```

comes out of the slave XBee serial port. This means that the microcontroller which is connected to the XBee serial port via the multiplexer receives a lot less data than what the PC actually transmitted. As a result the serial input buffer on the microcontroller can be smaller. The XBee datasheet explains how the API commands work.

During testing it was found that the 16 bit network address of the slave XBee sometimes changed, the reasoning behind this is unknown. As a result the slave XBee is only addressed by its serial number and by a generic broadcast 16 bit network address. This resulted in more stable communication between the master XBee and the slave XBee. The Node Detect API command was used to determine the network address of the slave XBees connected to the Master PAN Network.

A.3 Software design

This section describes in detail how the various sections of the software and user interface are developed. The software language used to program the user interface was C# using .NET 4.0. The .NET 4.0 toolboxes give access to a range of system components such as serialports, timers and graphing displays.

A.3.1 Classes

C# and other programming languages in the Windows environment are becoming more object orientated [106]. Object orientated programming revolves around classes. A class can be seen as a page of code which contains methods and variables that relate to that particular object. In [106] a line object is used as an example, the line class contains all the variables that relate to the line such as width, start and end point etc. The class also contains methods that relate to the line such as draw, which draws the line on the user interface.

The software created for this project is also object orientated and contains numerous classes to describe all the different aspects of the program. For example there is a communication class which holds all the serial communication methods such as APItransmit and analyse packet. There are also classes describing the individual TX and RX packets. Object orientated programming allows objects to be created, duplicated and destroyed. This means that there is only one class describing a battery block which is duplicated in the class that describes the battery analyser/charger which in turn is duplicated in the form i.e., one instance of battery analyser class is created for each battery analyser unit connected to the PC. Figure A.8 show a UML class diagram for the battery object.

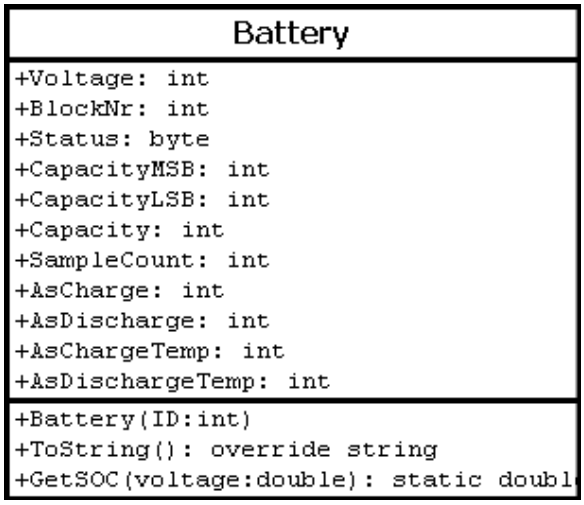

Figure A.8: UML class diagram for battery object.

Figure A.8 shows how the battery class stores all the raw data from the battery in integer form. The battery has three methods associated with it. The first method is a constructor which is passed the ID of the battery analyser unit which the battery is connected to. The second method is an override of the standard ToString() method which is included as standard in every class. The third method calculates the SOC of a battery based on a voltage, this method implements the battery model discussed in Chapter 2. The variables in the UML class diagram shown also correspond to the special battery variable created in the firmware (listing A.1) with some additional variables.

A.3.2 Threading

Threading in a Windows environment is a way of processing tasks in parallel. For example, the user interface is one thread whereas other lengthy or time consuming operations such as database searches may run on a parallel thread. Figure A.9 shows how the program flow of the receive functionality of the software is put together.

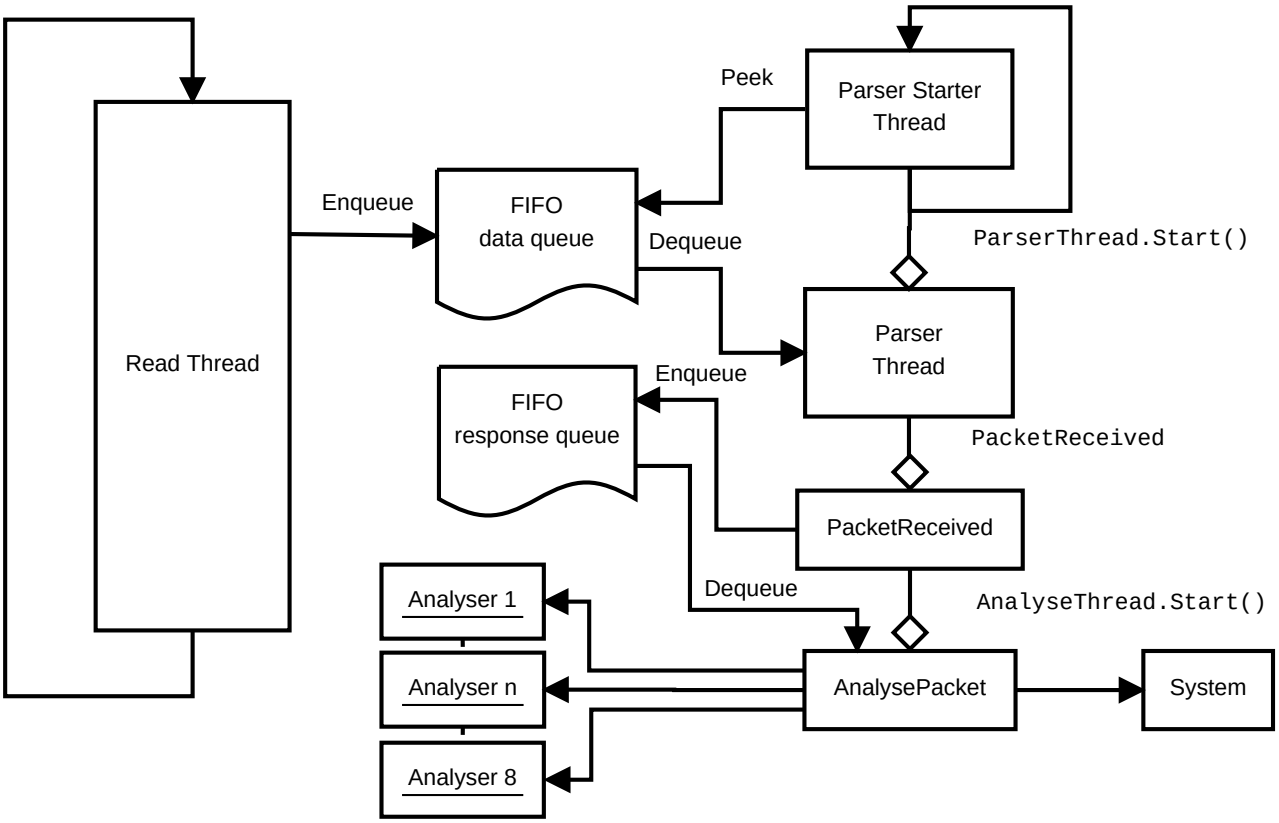

Figure A.9: Program flow of the receive section of the software showing the relationships between different threads

The Read Thread continuously reads a byte from the serial port. The .NET serial port class has a number of different read methods. The main ones are `Read()`, `ReadLine()` and

`ReadByte()`. The `ReadByte()` method was used because it reads only one byte from the serial port buffer at a time, the readbyte method blocks program flow when there is no data available in the serial port buffer. Implementing this method in a thread ensured that all data that arrived via the serial port was read and the user interface thread was not blocked if there was no data available in the serial port buffer. The read thread implementation writes the received byte into a FIFO (First In First Out) data queue.

Queue is also a class in the .NET library which provides `Enqueue()`, `Peek()` and `Dequeue()` methods amongst others. The `Enqueue()` method adds data to the Queue, the `Peek()` method returns the first object from the queue without removing it from the queue and the `Dequeue()` method removes the first object form the queue.

The Parser Starter Thread peeks at the data in the queue to see if the API start delimiter byte (`0x7E`) has been received. When the start delimiter byte has been added to the queue a new thread (Parser Thread) is started which proceeds to parse the data from the queue into a valid packet, when a byte is added to the packet it is Dequeued (removed) from the data queue. However `0x7E` is also a valid data byte so a check is performed in the parser starter thread to see if the parser thread is alive or not. If the parser thread is alive then a packet is in the process of being parsed and the parser starter thread waits for this process to be completed. This avoids data collision and false packet generation.

Once the data has been successfully parsed then a data received event is triggered. The parsed packet is written to a FIFO response queue in the data received event handler, this ensures that no packets are missed. An analyse packet thread is started from the data received event.

The analyse packet thread determines the nature of the packet and performs the appropriate operations based on the data that has been received. In this case the data received can either be an answer from one of the analyser microcontrollers in which case the response is written to the corresponding analyser object. Or the response can be a reply from the master XBee in which case the response is relayed to the system. System can either be the main user interface or the method call that requires the response; for example when the digital IO lines are switched each transmission (command from master to slave XBee) is followed by a response. So the analyse packet thread needs to signal to the system that the response has been received before sending the next transmission. Figure A.10 shows this process.

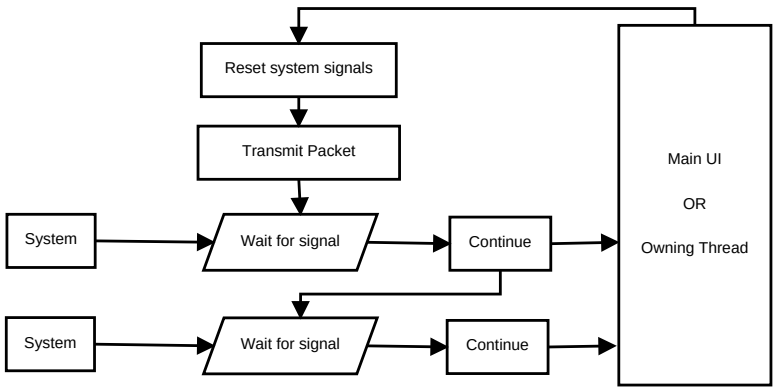

Figure A.10: Flow diagram showing how the software behaves when a command has been sent

Figure A.10 shows how the transmissions interact with the receive threads shown in Figure A.9. When a transmission is sent the software expects either one response or two responses depending on whether or not the transmission is aimed at the slave XBee or a the microcontroller. The "wait for signal" block in the flow diagram is a thread wait process. The thread wait process blocks the owning thread. It is therefore important that all transmission occur on a different thread then the User Interface. If the UI is blocked by a thread wait procedure then the UI becomes unresponsive. Manual reset events are used to synchronise the API transmission and the responses.

Listing A.4 shows the packets sent and received during a typical cycle.

Listing A.4: Typical XBee TX-RX sequence

```
1  TX: 7E 00 0F 17 01 00 13 A2 00 40 61 62 E4 D3 9B 02 25 56 60
2  RX: 7E 00 11 97 01 00 13 A2 00 40 61 62 E4 D3 9B 25 56 00 0B 10 C7
3  TX: 7E 00 10 17 01 00 13 A2 00 40 61 62 E4 D3 9B 02 44 33 05 5F
4  RX: 7E 00 0F 97 01 00 13 A2 00 40 61 62 E4 D3 9B 44 33 00 E6
5  TX: 7E 00 10 17 01 00 13 A2 00 40 61 62 E4 D3 9B 02 44 30 04 63
6  RX: 7E 00 0F 97 01 00 13 A2 00 40 61 62 E4 D3 9B 44 30 00 E9
7  TX: 7E 00 10 17 01 00 13 A2 00 40 61 62 E4 D3 9B 02 44 31 04 62
8  RX: 7E 00 0F 97 01 00 13 A2 00 40 61 62 E4 D3 9B 44 31 00 E8
9  TX: 7E 00 10 17 01 00 13 A2 00 40 61 62 E4 D3 9B 02 44 32 04 61
10 RX: 7E 00 0F 97 01 00 13 A2 00 40 61 62 E4 D3 9B 44 32 00 E7
11 TX: 7E 00 10 17 01 00 13 A2 00 40 61 62 E4 D3 9B 02 44 33 04 60
12 RX: 7E 00 0F 97 01 00 13 A2 00 40 61 62 E4 D3 9B 44 33 00 E6
13 TX: 7E 00 11 10 01 00 13 A2 00 40 61 62 E4 D3 9B 00 00 24 DC 0D D7
14 RX: 7E 00 07 8B 01 D3 9B 00 00 00 05
15 RX: 7E 00 12 90 00 13 A2 00 40 61 62 E4 D3 9B 01 24 00 DC 00 03 FC 65
```

Lines 1,3,5 to 11 show the transmitted packets in order to set the appropriate digital IO lines high or low to select a specific microcontroller/analyser unit. Lines 2,4,5 to 12 show the acknowledge response from the remote XBee. Line 13 is a TX packet directed at the microcontroller with a payload of `24 DC 0D`, the API command for request temperature. Line 14 is the acknowledge from the remote XBee indicating that the packet has been successfully

received and transmitted to the microcontroller. Line 15 is the response from the microcontroller with a payload of `24 00 DC 00 03 FC`. Where, `0x24` is the start delimiter, `0x00` is the analyser unit ID, `0x0003` is the 10 bit analogue value representing the temperature and `0xFC` is the checksum. Listing A.4 shows that a transmission from the master to the analyser unit expect two responses (lines 13 to 15).

A.3.3 Multiple forms

C# and the .NET framework has the ability of creating user interfaces with multiple forms, a form can also be referred to as a window. Each form runs on its own unique thread, the previous section describes threading. Passing variables from one form the next is difficult to handle because each form runs on a different thread. To avoid unnecessary complications with variables that are required across multiple forms a separate class was created which contains all the variables that are shared between the forms.

Main form

The main form is the main user-interface of the software giving the user access to the other forms to perform either calibration of the sensors or change the settings of the communication port. The main form provides the user with the different analysis options i.e., fully charge the battery blocks, analyse the battery blocks, voltage check, etc.

Calibration form

The calibration form figure A.12 is hidden behind a password protected section of the software so that only a dedicated service technician is able to calibrate the tool. The user is prompted for a password through the password form shown in Figure A.11

Figure A.11: Password form

The calibration form gives the user the opportunity to select which charger has to be calibrated. The software then queries the selected charger/analyser unit for its calibration data which is read from the PIC microcontroller EEPROM and displayed on the form. Three different calibration techniques are implemented due to the nature of the sensors used in this project.

Figure A.12 shows which parameters are able to be calibrated for each different item. For example current requires a zero calibration, positive current calibration and negative current

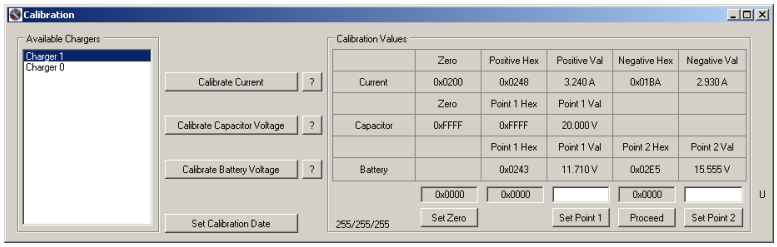

Figure A.12: Calibration form

calibration. The super-capacitor voltage only requires a gain/offset calibration which is performed by doing a zero calibration and a point calibration. The complex nature of the battery voltage curve means that a two point calibration is required. The calibration points used for the two point calibration of the battery voltage must be greater than the drop out voltage of the linear regulator whose output voltage is used as a reference voltage and the series connected zener diode responsible for improving the accuracy of the voltage measurement.

Port settings form

The Port Settings form shown in figure A.13 gives the user the ability to change the serial port settings of the master XBee device. The settings changes made in this form are saved to a settings file so that each time the software is started it remembers the port settings of the last session.

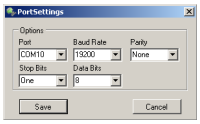

Figure A.13: Settings form

The port settings form also behaves like a class it has properties such as portsettingsform.Port which returns the string name of the port which has been selected. These properties are used by the main form to pass the correct port settings into the communication class.

Appendix B

Circuit diagrams

The following circuit diagrams detail the overview given in Figure A.1

B.1 Control Circuitry Design/Analyser Overview

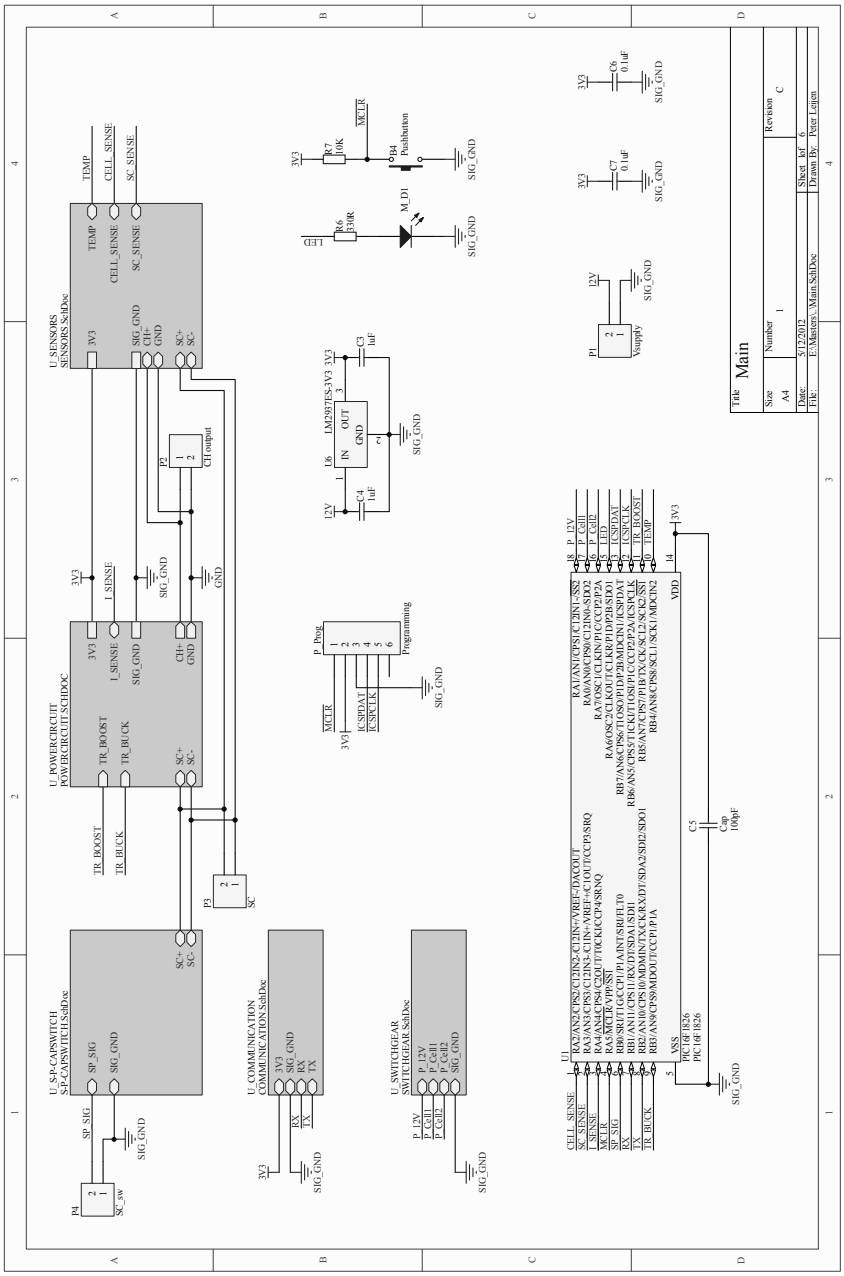

Figure B.1: Schematic print showing an overview of the complete system and how the following sheets are connected together

B.2 Bidirectional SMPS Design

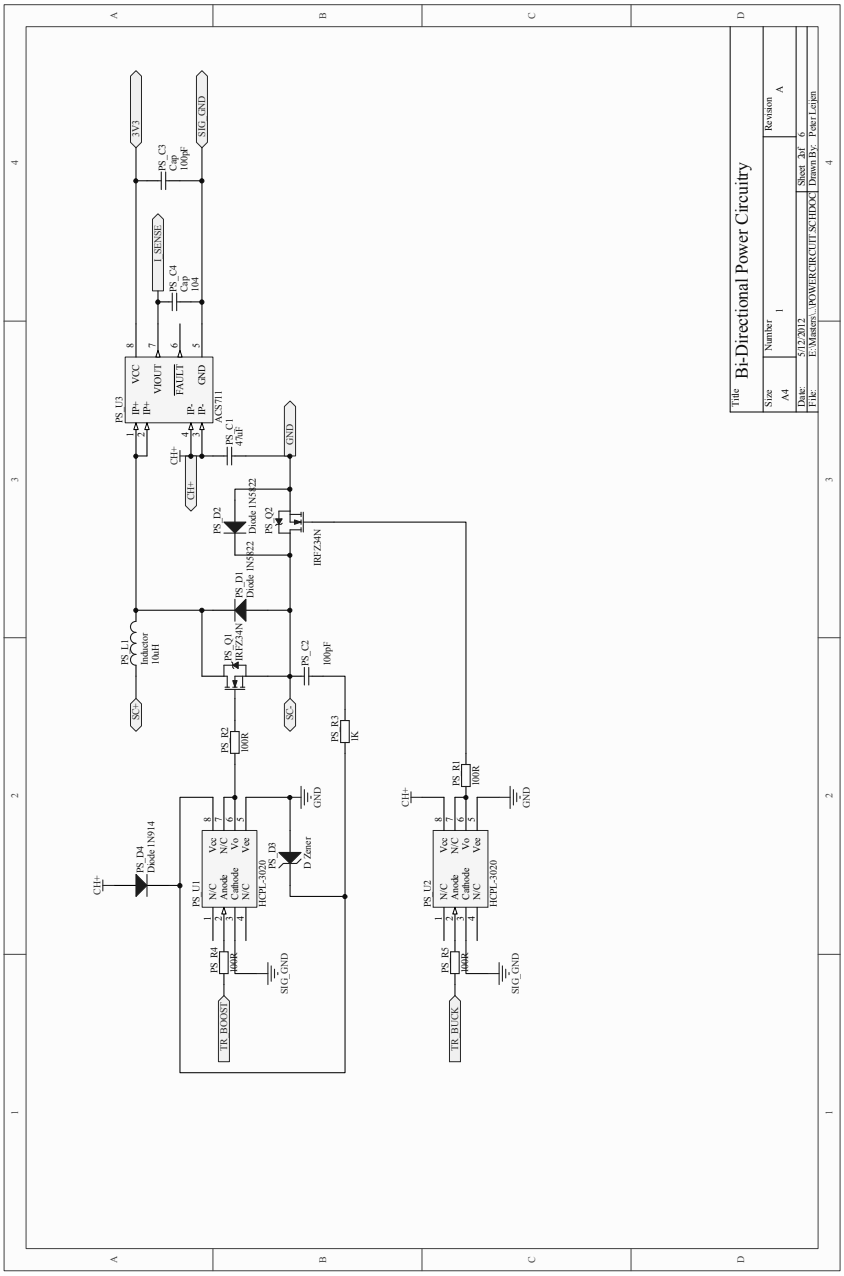

Figure B.2: Schematic print showing bidirectional switch-mode power-supply

B.3 Sensor Design

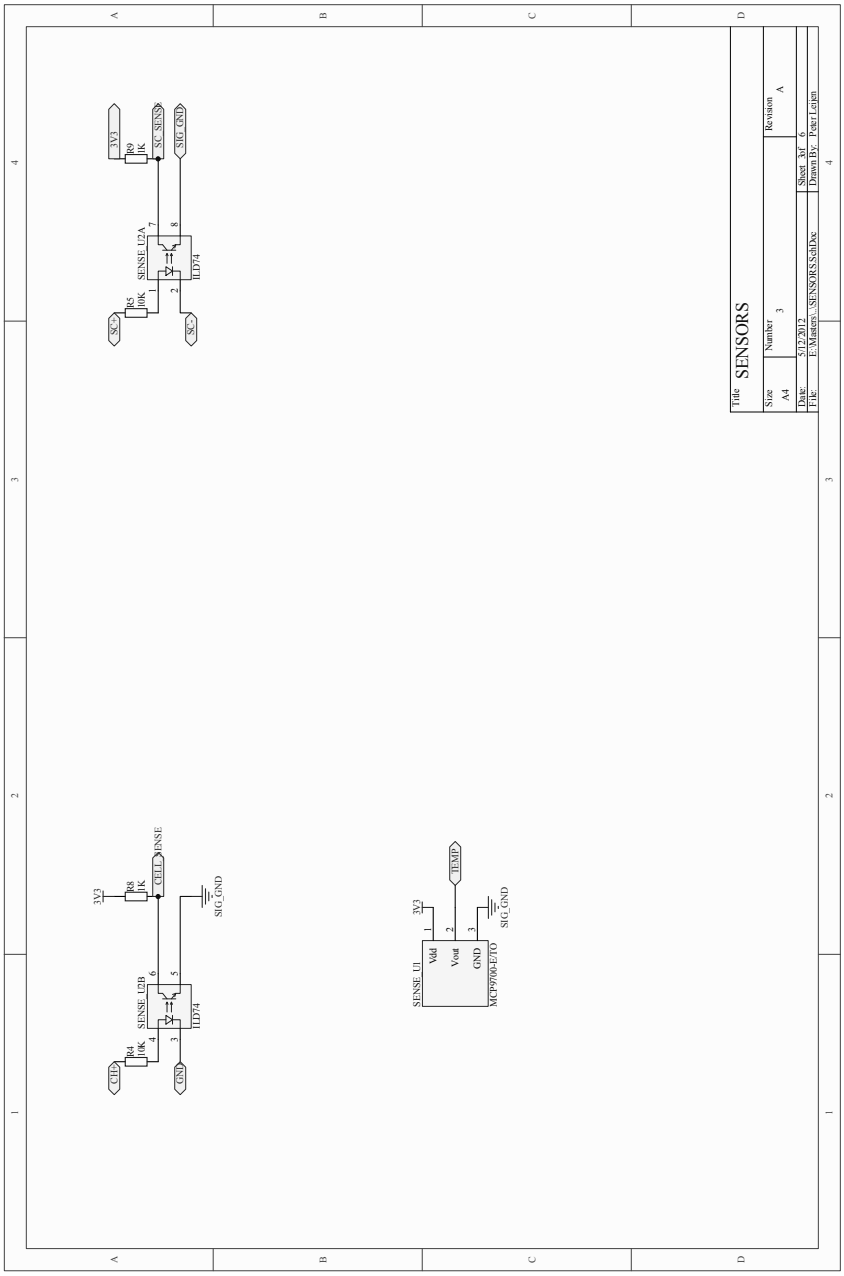

Figure B.3: Schematic print showing how the supercapacitor and battery voltage sensors are connected

B.4 Series Parallel Switch Design

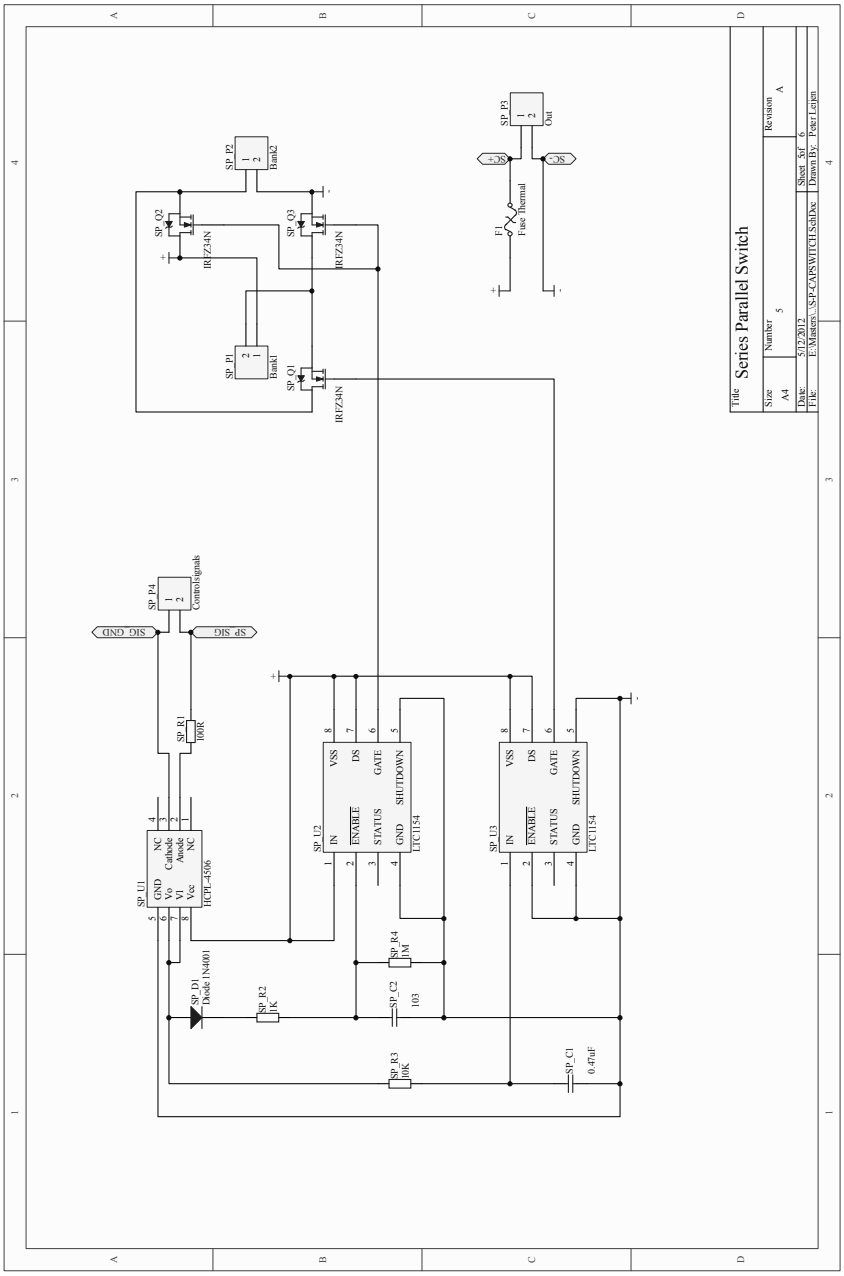

Figure B.4: Schematic print showing the series-parallel switching hardware with two capacitor banks

B.5 Communication System Design

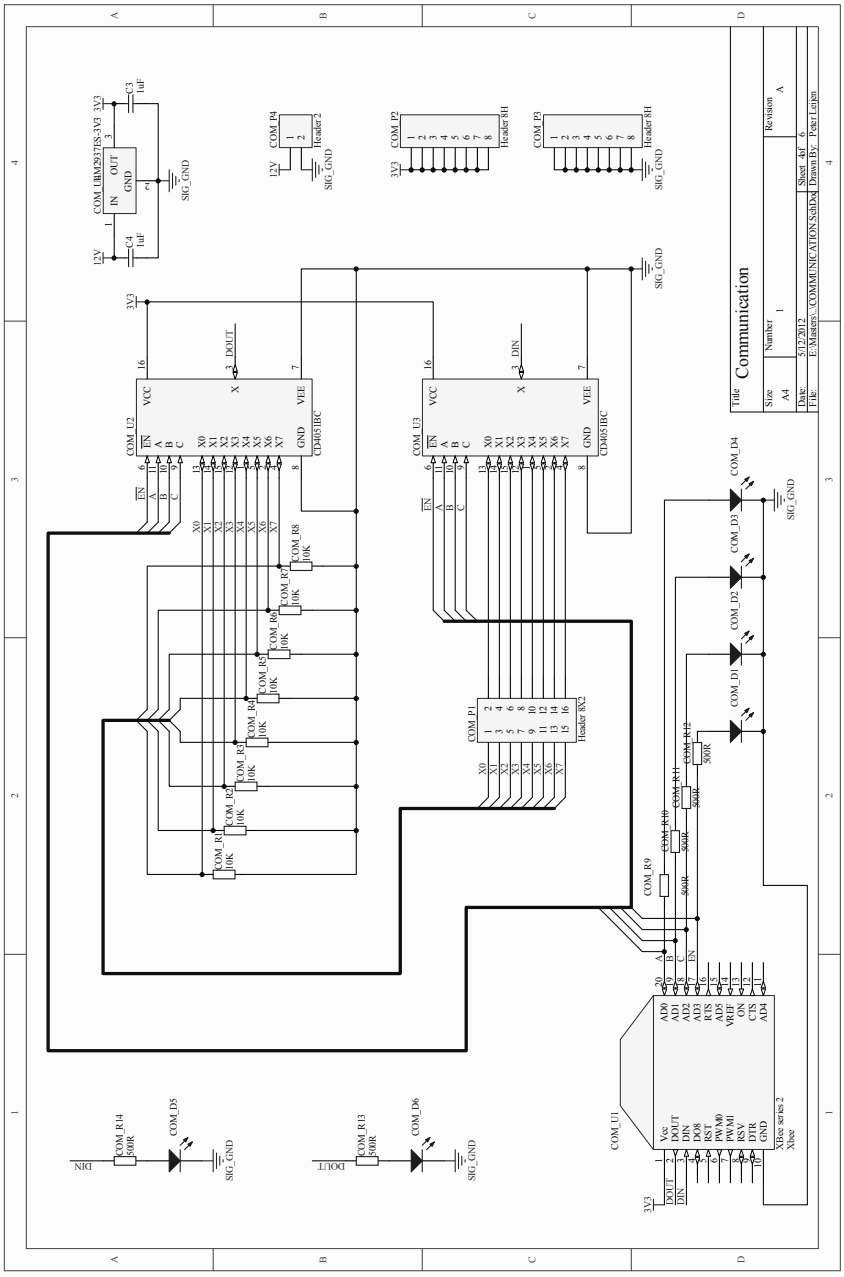

Figure B.5: Schematic print showing how the individual charger/analyser units are connected to the XBee wireless serial controller to transmit data back to the PC

Appendix C

Sample data set from battery analyser

The following shows a sample data file from the charger/analyser system.

```
 1  9:34:25 a.m.,createFiles
 2  9:34:25 a.m.,00,0/0/768,13.1 C ,12.060V,0,0,9.596,0.000,0.000,0.000,0.000,0.000,
 3  9:34:37 a.m.,CapacitiesTest 0
 4  9:34:37 a.m.,00,0/0/768,13.1 C ,12.054V,1005,670,14.095,0.000,0.000,0.000,0.000,0.000,
 5  9:34:37 a.m.,charge 0
 6  9:34:37 a.m.,00,0/0/768,13.1 C ,12.054V,1005,670,14.095,0.000,0.000,0.000,0.000,0.000,
 7  9:37:42 a.m.,00,0/0/768,13.4 C ,12.064V,1007,842,15.247,50.798,0.000,68858.000,0.000,5772.000,
 8  9:40:52 a.m.,00,0/0/768,13.8 C ,12.069V,1006,872,15.446,103.471,0.000,140259.000,0.000,11547.000,
 9  9:44:21 a.m.,00,0/0/768,13.8 C ,12.075V,994,889,15.560,157.022,0.000,212849.000,0.000,17351.000,
10  9:47:32 a.m.,00,0/0/768,14.1 C ,12.073V,995,912,15.711,211.246,0.000,286351.000,0.000,23183.000,
11  9:50:45 a.m.,00,0/0/768,14.1 C ,12.073V,993,925,15.799,265.498,0.000,359891.000,0.000,29026.000,
12  9:53:58 a.m.,00,0/0/768,14.4 C ,12.070V,993,935,15.863,320.131,0.000,433948.000,0.000,34910.000,
13  9:57:06 a.m.,00,0/0/768,14.4 C ,12.077V,993,946,15.937,374.933,0.000,508234.000,0.000,40694.000,
14  10:00:12 a.m.,00,0/0/768,14.4 C ,12.083V,994,954,15.991,429.472,0.000,582164.000,0.000,46514.000,
15  10:03:19 a.m.,00,0/0/768,14.4 C ,12.077V,994,962,16.044,483.707,0.000,655681.000,0.000,52353.000,
16  10:06:32 a.m.,00,0/0/768,14.4 C ,12.077V,993,968,16.085,538.833,0.000,730406.000,0.000,58382.000,
17  10:09:42 a.m.,00,0/0/768,14.4 C ,12.083V,992,976,16.138,592.834,0.000,803606.000,0.000,64342.000,
18  10:12:58 a.m.,00,0/0/768,14.4 C ,12.083V,992,981,16.172,646.436,0.000,876266.000,0.000,70370.000,
19  10:16:09 a.m.,00,0/0/768,14.4 C ,12.090V,992,991,16.239,699.534,0.000,948241.000,0.000,76505.000,
20  10:19:23 a.m.,00,0/0/768,14.4 C ,12.090V,992,994,16.259,751.994,0.000,1019353.000,0.000,82692.000,
21  10:22:39 a.m.,00,0/0/768,14.4 C ,12.090V,992,1000,16.300,803.541,0.000,1089227.000,0.000,88936.000,
22  10:25:53 a.m.,00,0/0/768,14.4 C ,12.090V,992,1005,16.333,855.129,0.000,1159156.000,0.000,95261.000,
23  10:29:18 a.m.,00,0/0/768,14.4 C ,12.090V,992,1009,16.360,906.055,0.000,1228188.000,0.000,101636.000,
24  10:33:06 a.m.,00,0/0/768,14.4 C ,12.077V,992,1012,16.380,955.635,0.000,1295395.000,0.000,108044.000,
25  10:36:23 a.m.,00,0/0/768,14.4 C ,12.077V,992,1017,16.414,1006.251,0.000,1364006.000,0.000,114551.000,
26  10:39:41 a.m.,00,0/0/768,14.4 C ,12.077V,992,1020,16.434,1056.095,0.000,1431571.000,0.000,121091.000,
27  10:43:01 a.m.,00,0/0/768,14.4 C ,12.083V,992,1022,16.447,1105.883,0.000,1499061.000,0.000,127680.000,
28  10:43:27 a.m.,finalVoltage 0
29  10:43:27 a.m.,00,0/0/768,14.4 C ,12.077V,991,1017,16.414,1105.883,0.000,1499061.000,0.000,127680.000,
30  10:43:27 a.m.,discharge 0
31  10:43:27 a.m.,00,0/0/768,14.4 C ,12.077V,991,1017,16.414,1105.883,0.000,1499061.000,0.000,127680.000,
32  10:54:21 a.m.,00,0/0/768,14.4 C ,12.036V,1006,865,15.393,964.754,0.000,1499061.000,205653.000,129424.000,
33  11:03:46 a.m.,00,0/0/768,14.4 C ,12.030V,1008,774,14.782,805.552,0.000,1499061.000,437644.000,131390.000,
34  11:12:51 a.m.,00,0/0/768,14.4 C ,12.016V,1006,753,14.641,646.439,0.000,1499061.000,669503.000,133355.000,
35  11:21:34 a.m.,00,0/0/768,14.4 C ,12.023V,1005,729,14.480,483.918,0.000,1499061.000,906329.000,135369.000,
36  11:30:08 a.m.,00,0/0/768,14.1 C ,12.026V,1005,707,14.335,321.288,0.000,1499061.000,1143315.000,137382.000,
37  11:38:33 a.m.,00,0/0/768,14.1 C ,12.026V,1007,679,14.147,156.121,0.000,1499061.000,1383996.000,139430.000,
38  11:46:38 a.m.,00,0/0/768,14.4 C ,12.030V,1006,650,13.950,-11.987,0.000,1499061.000,1628964.000,141521.000,
39  11:54:26 ...
        a.m.,00,0/0/768,14.1 C ,12.032V,1005,622,13.764,-182.836,0.000,1499061.000,1877926.000,143647.000,
40  12:02:11 ...
        p.m.,00,0/0/768,14.1 C ,12.026V,1005,593,13.570,-356.644,0.000,1499061.000,2131199.000,145816.000,
41  12:07:37 ...
        p.m.,00,0/0/768,14.4 C ,12.030V,1005,564,13.372,-533.639,0.000,1499061.000,2389117.000,148069.000,
42  12:11:45 ...
        p.m.,00,0/0/768,14.4 C ,12.043V,1006,534,13.171,-714.100,0.000,1499061.000,2652085.000,150334.000,
43  12:15:47 ...
        p.m.,00,0/0/768,14.4 C ,12.056V,1008,512,13.023,-895.187,0.000,1499061.000,2915966.000,152615.000,
44  12:18:56 ...
        p.m.,00,0/0/768,14.4 C ,12.056V,1006,485,12.842,-1079.519,0.000,1499061.000,3184575.000,154936.000,
45  12:18:57 p.m.,voltage too low
46  12:18:57 ...
        p.m.,00,0/0/768,14.4 C ,12.056V,1006,485,12.842,-1079.519,0.000,1499061.000,3184575.000,154936.000,
47  12:22:05 ...
        p.m.,00,0/0/768,14.4 C ,12.063V,1006,493,12.896,-1079.519,0.000,1499061.000,3184575.000,154936.000,
48  12:25:17 ...
        p.m.,00,0/0/768,14.4 C ,12.070V,1005,462,12.688,-1258.925,0.000,1499061.000,3446005.000,157201.000,
49  12:25:18 p.m.,voltage too low
50  12:25:18 ...
        p.m.,00,0/0/768,14.4 C ,12.070V,1005,462,12.688,-1258.925,0.000,1499061.000,3446005.000,157201.000,
51  12:28:26 ...
        p.m.,00,0/0/768,14.7 C ,12.067V,1005,472,12.752,-1258.925,0.000,1499061.000,3446005.000,157201.000,
52  12:28:26 p.m.,voltage too low
```

Appendix D

Extended Kalman filter code

Chapter 5.2 starts by producing voltage responses from a simplified Thévenin battery equivalent circuit initialised with a generic set of parameter values to be later recovered by EKF. The code below shows the Euler integration of the simplified state-space equations.

```
%% generate known data set with known internal battery parameters
% define sampling interval and time-span
Fs = 1000;      % sampling rate
dt = 1/Fs;      % sampling interval
tspan = [0 : dt : 20]';
Nsteps = length(tspan);
Rt = 0.5;    % mΩ  R_T
Rg = 0.35;   % mΩ  R_g
Cg = 200;    % F   C_g
% allocate space for solution vector
[Vg Vr I Y] = deal(zeros(Nsteps, 1));
[Yn KA] = deal(zeros(Nsteps, 3));
% define measurement noise parameters, assume 0 mean and Gaussian PD
v = 0.2;  % mV
% set initial voltages: [Vg(t = 0); Vr(t = 0)]
Vg(1) = 0;  % assume capacitor initially uncharged
Vr(1) = 0;  % assume zero current flowing
X = [Vg(1); Vr(1)]; % convert to state vector (column)
% matices for state space model
A = [1-dt/(Rg*Cg) 0; 0 0];
B = [dt/Cg; Rt];
C = [1 1];
D = 0;
for k = 2: Nsteps
    t = k*dt;
    s = ceil(t);
    % define a bipolar 3.8-A pulse current
    i = 3.8*(t > s-0.75 & t < s-0.5) - 3.8*(t > s-0.25 & t < s);
    I(k) = i;
    X = (A*X + B*i);    % Euler update
    Y(k) = C*X + D*i;
    [Vg(k) Vr(k)] = deal(X(1), X(2));
end
% ideal measurement without noise (y|_{v=0})
Eout = Y;
% actual measurement (y) Note: v_o = 0 for simplicity
Eout_meas = Eout + v*randn(Nsteps, 1);
```

The two vectors `Eout_meas` and `I` are the only externally measurable quantities and are used in the EKF code to reproduce the `Vg`, `Vr` matrices and C_g, R_g and R_T. We need to initialise the Kalman filter first by creating all the Jacobian matrices

```
1  %% set up Extended Kalman Filtering Jacobians
2  %note Cg, Rg and Rt different from actual values to see how well kalman ...
       filter estimates.
3  a = 1/(Cg*1.1); %â_0
4  b = 1/(Rg*1.1); %b̂_0
5  c = Rt*1.1;     %ĉ_0
6  %define main variables
7  xk= [0; 0; a; b; c]; %initized state x̂_0
8
9  %observation matrix for EKF
10 H = [1 1 0 0 0];
11 %noise paramaters
12 w = 0;  % process noise 100% confidence in model
13 wp = w+0.1; %artificial noise added to â, b̂ and ĉ to allow filter to ...
       compensate
14 r = rms(Eout_meas - Eout)^2;     %measurement noise rms(y − y|_{v=0})^2
15 pc = rms(a-1/Cg)^2;              %estimation error cov Cg
16 pr = rms(b-1/Rg)^2;              %estimation error cov Rg
17 prt = rms(c-Rt)^2;               %estimation error cov Rt
18
19 % covariance of process noise
20 Q = [w^2 0 0 0 0; 0 w^2 0 0 0; 0 0 wp 0 0; 0 0 0 wp 0; 0 0 0 0 wp];
21 % covariance of measurement noise
22 R = [r 0 0 0 0; 0 r 0 0 0; 0 0 0 0 0; 0 0 0 0 0; 0 0 0 0 0];
23 % covariance of estimation error
24 P = [0 0 0 0 0; 0 0 0 0 0; 0 0 pc 0 0; 0 0 0 pr 0; 0 0 0 0 prt];
```

Note in line 14 we assume that the actual terminal voltage $y|_{v=0}$ and in lines 15-16 we assume that the actual component values for C_{g}, R_{g} and R_{T} are known. This is not the case when the extended Kalman filter is applied to real battery data. We can assume the we know the measurement noise associated with out equipment so `r` is known. However, for `pc`, `pr` and `prt` I have simply used the RMS of the initial estimate. The following code implements the extended Kalman filter.

```
1  %% Do kalman filtering
2  %initize estimation variables
3  Xhat = []; %state estimate matrix
4  Yhat = []; %battery voltage estimate
5
6  for k = 1:length(Eout)
7      % Predict next state of the battery voltages with the last state and ...
           current.
8      I(k); %actual current measurement
9      Eout_meas(k); %actual voltage measurement note: no E0 for simplicity
10
11     % update Jacobians around current operating point
12     a = xk(3);
13     b = xk(4);
14     c = xk(5);
15
16     F = [1-dt*a*b    0    -dt*xk(1)*b+dt*I(k) -dt*a*xk(1) 0;
17          0 0 0 0 I(k);
18          0 0 1 0 0;
19          0 0 0 1 0;
20          0 0 0 0 1];
```

```
21
22      L = [dt*a c 0 0 0];
23
24      M = [1 0 0 0 0];
25
26      A = [1-a*b*dt 0 0 0 0;
27              0 0 0 0 0;
28              0 0 1 0 0;
29              0 0 0 1 0;
30              0 0 0 0 1];
31
32      B = [dt*a; c; 0; 0; 0];
33
34      % update estiamtion error covariance
35      P = F * P * F' + L * Q * L';
36      % update estiamted state
37      xk = (A*xk + B*I(k));
38      % update Kalman gain
39      K = P * H' * inv(H * P * H' + M*R*M');
40      % update state estimate post measurement
41      xkp = xk + K * (Eout_meas(k) - (H * xk));
42      % update estimation error cov post measurement
43      P = (eye(5) - K*H)*P;
44      %Store for plotting
45      Xhat = [Xhat; xkp'];
46      Yhat = [Yhat; (xkp(1) + I(k)*Rt)'];
47      %current = predicted
48      xk = xkp;
49  end
```

Appendix E

SMPS code: Spice and Matlab

E.1 Spice

The bidirectional switch-mode-power-supply simulation results presented in Chap. 4 use the following LTSpice and MATLAB codes. Figure E.1 shows the first-order Spice model diagram used to generate all the first-order results.

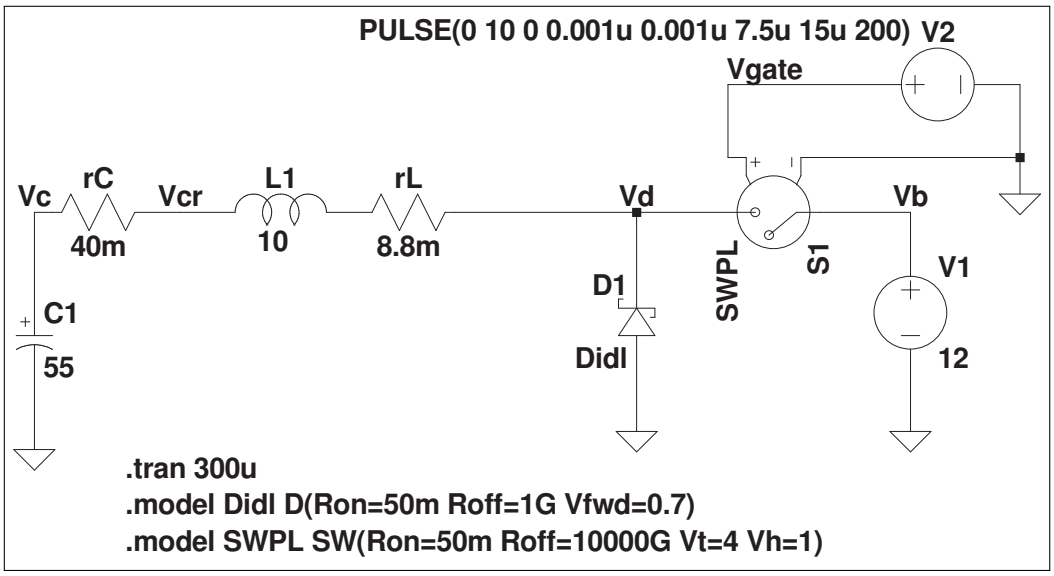

Figure E.1: LTSpice diagram of SMPS showing how the components are connected

Note: Series/parallel switching is not implemented in the Spice simulation. The Spice net-list associated with this diagram is,

```
1  * Spice Net-List
2  V1 Vb 0 24
3  D1 0 Vd Didl
4  L1 Vcr N001 10µ Rser=0
5  C1 Vc 0 55 Rser=0 Lser=0 Rpar=0
6  V2 Vgate 0 PULSE(0 10 0 0.001u 0.001u 7.5u 15u 200)
7  rC Vcr Vc 40m
8  rL Vd N001 8.8m
9  S1 Vb Vd Vgate 0 SWPL
10 .model D D
11 .lib C:\Program Files\LTC\LTspiceIV\lib\cmp\standard.dio
12 .tran 300u
13 .model Didl D(Ron=50m Roff=1G Vfwd=0.7)
14 .model SWPL SW(Ron=50m Roff=10000G Vt=4 Vh=1)
15 .backanno
16 .end
```

E.2 Matlab

The following MATLAB code shows how all the variables and matrices for the simulation are initialised.

```
%% Simulate buck stage of bidirectional converter first-order model
% initialise all vectors and component values
m = 10^-3;
u = m*m;
nano = u*m;
Tspan = 0.3*m;
stps=100;
dt = 15*u;
Ts = dt;
tspan = [0: dt: Tspan];
Vc = [0];
Ic = [0];
Vl = [0];
time = [0];
Pin = [0];
El = [0];
Prl = [0];
Pd = [0];
Prd = [0];
Ec = [0];
Prc = [0];
PswS = [0];
PswDyn = [0];

L = 10*u;
rL = 8.8*m;
C = 0;
C1 = 27.5;
C2 = 27.5;
rC1 = 40*m;
rC2 = 40*m;
rC = 0;
rDS = 50*m;
rD = 50*m;
vb = 12;
vd = 0.7;
vthres = 4;
ton = 13*10^-9;
toff = 293*10^-9;
Ib = 4;
i1 = 0;
i2 = 0;
Icav = 0;
stage = 0; %0 is series, 2 is parallel, 3 is finished
t01 = 0;
t12 = 0;
t23 = 0;
```

Before starting the simulation we need to determine whether or not the parallel only case is being simulated or the series/parallel switching is being simulated. If we are in `stage==0` (series configuration) then the ESR's of each capacitor is summed (`rC1+rC2`) to give `rC`. The capacitances are also summed to give the total pack capacitance.

```
%% Simulate buck stage of bidirectional converter first-order model
% determine whether or not starting in series config or parallel config
if stage==0,
    rC=rC1+rC2;
    C = (C1*C2)/(C1+C2);
end
if stage==2,
    C=C1+C2;
    rC=(rC1*rC2)/(rC1+rC2);
end
```

The simulation code now loops until we reach `stage=3` where $v_c > 10$ V indicating that the supercapacitor bank is fully charged in parallel configuration.

```
%% Simulate buck stage of bidirectional converter first-order model
% simulate power-supply till capacitor bank is in parallel config and Vc>10V
while 1,
    % calculate and limit the duty-cycle between 0 and 80%
    Dtemp = Ib/Ic(end);
    if (Dtemp>0.80),
        D = 0.80;
    elseif (Dtemp<0),
        D = 0;
    else
        D = Dtemp;
    end
    % determine which stage we are operating in
    if (Vc(end)>10) && (stage==2),
        break
    end
    if (Vc(end)>vb-1.5) && (stage==0),
        t01=time(end);
        Vc(end) = Vc(end)/2;
        C=C1+C2;
        rC=(rC1*rC2)/(rC1+rC2);
        stage = 2;
    end

    i=i1;
    T=time(end);
    while time(end)<T+D*Ts-Ts*m,

        Pin = [Pin, i*vb+vb*i*(ton+toff)/(2*Ts)];
        El = [El, 0.5*L*i^2];
        Prl = [Prl, rL*i^2];
        Pd = [Pd, 0];
        Prd = [Prd, 0];
        Prc = [Prc, rC*i^2];
        PswS = [PswS, rDS*i^2];
        PswDyn = [PswDyn, vb*i*(ton+toff)/(2*Ts)];

        R = rL+rC+rDS;%
        vstep = vb - Vc(end)  - R*i + L*i;

        % switch closed
        t = Ts/stps;
        a = R/(2*L); B = 0; c = 1; w = sqrt(-a^2);
        i = vstep/L*exp(-a*t)*(B*cos(w*t) + (c-a*B)/w*sin(w*t)) + i;

        % switch open
```

```
47          vctemp = Vc(end) + 1/C*(Ic(end)+i)/2*t; %improves accuracy
48          Ic = [Ic, i, i];
49          Vc = [Vc, vctemp, vctemp];
50          time = [time, time(end) + t, time(end) + t];
51
52          Pin = [Pin, i*vb+vb*i*(ton+toff)/(2*Ts)];
53          El = [El, 0.5*L*i^2];
54          Prl = [Prl, rL*i^2];
55          Pd = [Pd, 0];
56          Prd = [Prd, 0];
57          Ec = [Ec, 0.5*C*vctemp^2, 0.5*C*vctemp^2];
58          Prc = [Prc, rC*i^2];
59          PswS = [PswS, rDS*i^2];
60          PswDyn = [PswDyn, vb*i*(ton+toff)/(2*Ts)];
61      end
62      i2=i;
63
64      T=time(end);
65      while time(end)<T+(1-D)*Ts-Ts*m,
66
67          Pin = [Pin, 0+vb*i*(ton+toff)/(2*Ts)];
68          El = [El, 0.5*L*i^2];
69          Prl = [Prl, rL*i^2];
70          Pd = [Pd, vd*i];
71          Prd = [Prd, rD*i^2];
72          Prc = [Prc, rC*i^2];
73          PswS = [PswS, 0];
74          PswDyn = [PswDyn, vb*i*(ton+toff)/(2*Ts)];
75
76          R = rL+rC+rD;
77          vstep = -(vd) - Vc(end) - (R)*i + L*i;
78          t = Ts/stps;
79          a = R/(2*L); B = 0; c = 1; w = sqrt(-a^2);
80          i = i + vstep/L*exp(-a*t)*(B*cos(w*t) + (c-a*B)/w*sin(w*t));
81
82          if (i<0),%dcm
83              ccm = 0;
84              d = -Ic(end)*t/(i-Ic(end));
85              Icav = Ic(end)/2*abs(d);
86              time=[time, time(end)+abs(d)];
87              i = 0;
88              Ic = [Ic, i];
89              Vc = [Vc, Vc(end) + 1/C*Icav*t];
90
91              Pin = [Pin, 0+vb*i*(ton+toff)/(2*Ts)];
92              El = [El, 0.5*L*i^2];
93              Prl = [Prl, rL*i^2];
94              Pd = [Pd, vd*i];
95              Prd = [Prd, rD*i^2];
96              Ec = [Ec, 0.5*C*Vc(end)^2];
97              Prc = [Prc, rC*i^2];
98              PswS = [PswS, 0];
99              PswDyn = [PswDyn, vb*i*(ton+toff)/(2*Ts)];
100
101             Ic = [Ic, i];
102             Vc = [Vc, Vc(end)];
103
104              Ec = [Ec, 0.5*C*Vc(end)^2];
105
106             time = [time, time(end-1)+t];
107         else %ccm
108             ccm = 1;
```

```
109             Icav = (Ic(end)+i)/2;
110             Ic = [Ic, i, i];
111             Vc = [Vc, Vc(end) + 1/C*Icav*t, Vc(end) + 1/C*Icav*t];
112 
113             Pin = [Pin, 0+vb*i*(ton+toff)/(2*Ts)];
114             El = [El, 0.5*L*i^2];
115             Prl = [Prl, rL*i^2];
116             Pd = [Pd, vd*i];
117             Prd = [Prd, rD*i^2];
118             Ec = [Ec, 0.5*C*Vc(end)^2, 0.5*C*Vc(end)^2];
119             Prc = [Prc, rC*i^2];
120             PswS = [PswS, 0];
121             PswDyn = [PswDyn, vb*i*(ton+toff)/(2*Ts)];
122 
123             time = [time, time(end)+t, time(end)+t];
124         end
125     end
126     i1=i;
127 
128     Pin(end)= 0;
129     PswS(end) = 0;
130 
131 end
132 
133 Ein = abs(integrate(time, Pin));
134 Erl = abs(integrate(time, Prl));
135 Ed = abs(integrate(time, Pd));
136 Erd = abs(integrate(time, Prd));
137 Erc = abs(integrate(time, Prc));
138 EswS = abs(integrate(time, PswS));
139 EswDyn = abs(integrate(time, PswDyn));
140 
141 Ewaste = El'+Erl'+Ed'+Erd'+Erc'+EswS'+EswDyn';
142 
143 Error = Ein'-(Ec'+Ewaste);
144 n = (Ein(end)-Ewaste(end))/Ein(end)*100
```

References

[1] V. H. Johnson and A. A. Pesaran, "Temperature-dependent battery models for high-power lithium-ion batteries," *Electric Vehicle Symposium*, vol. 17, pp. 1–17, January 2001.

[2] P. Leijen and J. Scott, "Failure analysis of some Toyota Prius battery packs and potential for recovery," *SAE Technical Paper 2013-01-2561*, 2013.

[3] M. Eshani, Y. Gao, and A. Emadi, "Modern electric, hybrid electric and fuel cell vehicles," *CRC Press*, p. 534, September 2010.

[4] G. L. Plett, "Recursive approximate weighted total least squares estimation of battery cell total capacity," *Journal of Power Sources*, vol. 196, pp. 2319–2331, February 2011.

[5] H. Li, C. Liao, and L. Wang, "Research on state-of-charge estimation of battery pack used on hybrid electric vehicle," *Power and Energy Engineering Conference*, pp. 1–4, March 2009.

[6] W. Guoliang, L. Rengui, Z. Chunbo, and C. Chan, "State of charge estimation for NiMH battery based on electromotive force method," *IEEE Conference on Vehicle Power and Propulsion*, pp. 1–5, September 2008.

[7] K. Bundy, M. Karlsson, G. Lindbergh, and A. Lundqvist, "An electrochemical impedance spectroscopy method for prediction of the state of charge of a nickel-metal hydride battery at open circuit and during discharge," *Journal of Power Sources*, vol. 72, no. 2, pp. 118–125, 1998.

[8] I. Buchmann, *Batteries in a Portable World.* Cadex Electronics Inc., second ed., 2001.

[9] L. Zhang, "AC impedance studies on sealed nickel metal hydride batteries over cycle life in analog and digital operations," *Electrochimica Acta*, vol. 43, pp. 3333–3342, July 1998.

[10] P. Leijen, "Off-line NiMH battery state of charge and state of health measurement," 2011.

[11] W. K. Hu, M. M. Geng, X. P. Gao, T. Burchardt, Z. X. Gong, D. Noreus, and N. K. Nakstad, "Effect of long-term overcharge and operated temperature on performance of rechargeable NiMH cells," *Journal of Power Sources*, vol. 159, no. 2, pp. 1478–1483, 2006.

[12] J. Cao and A. Emadi, "Batteries need electronics," *IEEE Industrial Electronics*, vol. 5, pp. 27–35, March 2011.

[13] H. Leijen, *Hybrid Diagnostics (EMS1-4)*. AECS Ltd, 2012.

[14] Toyota, *Toyota Prius Workshop manual*, 2001.

[15] O. Barbarisi, R. Canaletti, L. Glielmo, M. Gosso, and F. Vasca, "State of charge estimator for NiMH batteries," *IEEE Conference on Decision and Control*, vol. 2, pp. 1739–1744, December 2002.

[16] N. Kulatatna, *Power Electronics Design Handbook*. Newnes, 1998.

[17] A. Ledovskikh, E. Verbitskiy, A. Ayeb, and P. H. L. Notten, "Modelling of rechargeable NiMH batteries," *Journal of Alloys and Compounds*, vol. 356-357, pp. 742–745, August 2002.

[18] A. J. Salkind, C. Fennie, P. Singh, T. Atwater, and D. E. Reisner, "Determination of state-of-charge and state-of-health of batteries by fuzzy logic methodology," *Journal of Power Sources*, vol. 80, pp. 293 – 300, July 1999.

[19] A. Eddahech, O. Briat, N. Bertrand, J.-Y. Deletage, and J.-M. Vinassa, "Behavior and state-of-health monitoring of Li-ion batteries using impedance spectroscopy and recurrent neural networks," *International Journal of Electrical Power & Energy Systems*, vol. 42, pp. 487 – 494, November 2012.

[20] N. A. Windarko and J. Choi, "Hysteresis modeling for estimation of state-of-charge in NiMH battery based on improved Takacs model," *Telecommunications Energy Conference*, pp. 598–603, October 2009.

[21] J. Banerjee, J. McPhee, P. Goossens, T.-S. Dao, and H.-D. Ahn, "Physics-based models, sensitivity analysis, and optimization of automotive batteries," *SAE International Journal Passenger Cars Electronic Electrical Systems*, vol. 7, 2014.

[22] M. Shahriari and M. Farrokhi, "Online state-of-health estimation of VRLA batteries using state of charge," *IEEE Transactions on Industrial Electronics*, vol. 60, pp. 191 – 202, January 2013.

[23] H.-T. Lin, T.-J. Liang, and S.-M. Chen, "Estimation of battery state of health using probabilistic neural network," *IEEE Transactions on Industrial Informatics*, vol. 9, pp. 679 – 685, May 2013.

[24] J. Kin and B. H. Cho, "State-of-charge estimation and state-of-health prediction of a Li-ion degraded battery based on an EKF combined with a per-unit system," *IEEE Transactions on Vehicular Technology*, vol. 60, pp. 4249 – 4260, November 2011.

[25] P. Bauerlein, C. Antonius, J. Loffler, and J. Kumpers, "Progress in high-power nickel-metal hydride batteries," *Journal of Power Sources*, vol. 176, no. 2, pp. 547–554, 2008.

[26] F. Huet, "A review of impedance measurements for determination of the state-of-charge or state-of-health of secondary batteries," *Journal of Power Sources*, vol. 70, pp. 59 – 69, January 1998.

[27] N. Kong Soon, M. Chin-Sien, C. Yi-Ping, and H. Yao-Ching, "Enhanced coulomb counting method for estimating state-of-charge and state-of-health of lithium-ion batteries," *Applied Energy*, vol. 86, pp. 1506 – 1511, September 2009.

[28] J. Remmlinger, M. Buchholz, M. Meiler, P. Bernreuter, and K. Dietmayer, "State-of-health monitoring of lithium-ion batteries in electric vehicles by on-board internal resistance estimation," *Journal of Power Sources*, vol. 196, pp. 5357 – 5363, June 2011.

[29] M. Thele, O. Bohlen, D. U. Sauer, and E. Karden, "Development of a voltage-behavior model for NiMH batteries using an impedance-based modeling concept," *Journal of Power Sources*, vol. 175, pp. 635–643, January 2008.

[30] A. Szumanowski and Y. Chang, "Battery management system based on battery nonlinear dynamics modeling," *IEEE Transactions on Vehicular Technology*, vol. 57, no. 3, pp. 1425–1432, 2008.

[31] B. S. Bhangu, P. Bentley, D. A. Stone, and C. M. Bingham, "Nonlinear observers for predicting State-of-Charge and State-of-Health of lead-acid batteries for hybrid-electric vehicles," *IEEE Transactions on Vehicular Technology*, vol. 54, pp. 783–794, May 2005.

[32] M. Maja, C. Orecchia, M. Strano, P. Tosco, and M. Vanni, "Effect of structure of the electrical performance of gas diffusion electrodes for metal air batteries," *Electrochimica Acta*, vol. 46, no. 23, pp. 423 – 432, 2000.

[33] A. Jossen, "Fundamentals of battery dynamics," *Journal of Power Sources*, vol. 154, no. 2, pp. 530–538, 2006.

[34] K. Miyamoto, H. Ichimura, T. Wagner, M. J. Schning, and T. Yoshinobu, "Chemical imaging of the concentration profile of ion diffusion in a microfluidic channel," *Sensors and Actuators B: Chemical*, vol. 189, no. 0, pp. 240 – 245, 2013. Selected Papers from the 26th European Conference on Solid-State Transducers.

[35] A. Fick, "On liquid diffusion," *Journal of Membrane Science*, vol. 100, no. 1, pp. 33 – 38, 1995. The early history of membrane science selected papers celebrating vol. 100.

[36] P. Grathwohl, *Diffusion in Natural Porous Media: Contaminant Transport, Sorption/Desorption and Dissolution Kinetics*. Kluwer international series: Topics in environmental fluid mechanics, Springer US, 1998.

[37] E. D. Palmes and R. H. Lindenboom, "Ohm's law, Fick's law, and diffusion samplers for gases," *Analytical Chemistry*, vol. 51, no. 14, pp. 2400–2401, 1979.

[38] M. Greenleaf, H. Li, and J. Zheng, "Modeling of Li_xFePO_4 cathode li-ion batteries using linear electrical circuit model," *Sustainable Energy, IEEE Transactions on*, vol. 4, pp. 1065–1070, Oct 2013.

[39] E. Karden, S. Buller, and R. W. D. Doncker, "A method for measurement and interpretation of impedance spectra for industrial batteries," *Journal of Power Sources*, vol. 85, no. 1, pp. 72 – 78, 2000.

[40] E. Kuhn, C. Forgez, P. Lagonotte, and G. Friedrich, "Modelling NiMH battery using Cauer and Foster structures," *Journal of Power Sources*, vol. 158, no. 2, pp. 1490 – 1497, 2006.

[41] D. Linden and T. B. Reddy, *Handbook of Batteries*. McGraw-Hill, third ed., 1995.

[42] P. E. Pascoe and A. H. Anbuky, "Standby power system VRLA battery reserve life estimation scheme," *IEEE Transactions on Energy Conversion*, vol. 20, pp. 887 – 895, December 2005.

[43] K. Kutluay, Y. Cadirci, Y. S. Ozkazanc, and I. Cadirci, "A new online state-of-charge estimation and monitoring system for sealed lead-acid batteries in telecommunication power supplies," *IEEE Transactions on Industrial Electronics*, vol. 52, pp. 1315 – 1327, October 2005.

[44] M. Chen and G. Rincon-Mora, "Accurate electrical battery model capable of predicting runtime and I-V performance," *IEEE Transactions on Energy Conversion*, vol. 21, no. 2, pp. 504–511, 2006.

[45] W. Renhart, C. Magele, and B. Schweighofer, "FEM-based thermal analysis of NiMH batteries for hybrid vehicles," *IEEE Transactions on Magnetics*, vol. 44, no. 6, pp. 802–805, 2008.

[46] S. J. Moura, J. L. Stein, and H. K. Fathy, "Battery-health conscious power management in plug-in hybrid electric vehicles via electrochemical modeling and stochastic control," *IEEE Transactions on Control Systems Technology*, vol. 21, pp. 679 – 694, May 2013.

[47] B. Schweighofer, K. M. Raab, and G. Brasseur, "Modeling of high power automotive batteries by the use of an automated test system," *IEEE Transactions on Instrumentation and Measurement*, vol. 52, pp. 1087–1091, 2003.

[48] M. Verbrugge and E. Tate, "Adaptive state of charge algorithm for nickel metal hydride batteries including hysteresis phenomena," *Journal of Power Sources*, vol. 126, pp. 236–249, February 2004.

[49] L. Serrao, Z. Chehab, Y. Guezennee, and G. Rizzoni, "An aging model of Ni-MH batteries for hybrid electric vehicles," *IEEE Conference on Vehicle Power and Propulsion*, 2005.

[50] J. Takacs, "A phenomenological mathematical model of hysteresis," *International Journal for Computation and Mathematics in Electrical and Electronic Engineering*, vol. 20, no. 4, pp. 1002–1014, 2001.

[51] L. Gao, S. Liu, and R. A. Dougal, "Dynamic lithium-ion battery model for system simulation," *IEEE Transactions on Components and Packaging Technologies*, vol. 25, pp. 495–505, 2002.

[52] H. He, R. Xiong, H. Guo, and S. Li, "Comparison study on the battery models used for the energy management of batteries in electric vehicles," *Energy Conversion and Management*, vol. 64, pp. 113 – 121, 2012. IREC 2011, The International Renewable Energy Congress.

[53] A. Tenno, R. Tenno, and T. Suntio, "Battery impedance characterization through inspection of discharge curve and testing with short pulses," *Journal of Power Sources*, vol. 158, no. 2, pp. 1029 – 1033, 2006.

[54] J. Li and M. S. Mazzola, "Accurate battery pack modeling for automotive applications," *Journal of Power Sources*, vol. 237, pp. 215 – 228, 2013.

[55] T. Hu and H. Jung, "Simple algorithms for determining parameters of circuit models for charging/discharging batteries," *Journal of Power Sources*, vol. 233, pp. 14–22, 2013.

[56] M. Gholizadeh and F. R. Salmasi, "Estimation of state of charge, unknown nonlinearities, and state of health of a lithium-ion battery based on a comprehensive unobservable model," *IEEE Transactions on Industrial Electronics*, vol. 61, pp. 1335 – 1344, March 2014.

[57] C. R. Gould, C. M. Bingham, D. A. Stone, and P. Bentley, "New battery model and state-of-health determination through subspace parameter estimation and state-observer techniques," *IEEE Transactions on Vehicular Technology*, vol. 58, pp. 3905 – 3916, October 2009.

[58] S. Ebbesen, P. Elbert, and L. Guzzella, "Battery state-of-health perceptive energy management for hybrid electric vehicles," *IEEE Transactions on Vehicular Technology*, vol. 61, pp. 2893 – 2900, September 2012.

[59] I. Bloom, B. Cole, J. Sohn, S. Jones, E. Polzin, V. Battaglia, G. Henriksen, C. Motloch, R. Richardson, T. Unkelhaeuser, D. Ingersoll, and H. Case, "An accelerated calendar and cycle life study of Li-ion cells," *Journal of Power Sources*, vol. 101, no. 2, pp. 238 – 247, 2001.

[60] J. Wang, P. Liu, J. Hicks-Garner, E. Sherman, S. Soukiazian, M. Verbrugge, H. Tataria, J. Musser, and P. Finamore, "Cycle-life model for graphite-LiFePO4 cells," *Journal of Power Sources*, vol. 196, no. 8, pp. 3942 – 3948, 2011.

[61] S. Buller, M. Thele, R. W. A. A. De Doncker, and E. Karden, "Impedance-based simulation models of supercapacitors and li-ion batteries for power electronic applications," *IEEE Transactions on Industry Applications*, vol. 41, pp. 742 – 747, May/June 2005.

[62] D. Andre, A. Nuhic, T. Soczka-Guth, and D. Sauer, "Comparative study of a structured neural network and an extended Kalman filter for state of health determination of lithium-ion batteries in hybrid electric vehicles," *Engineering Applications of Artificial Intelligence*, vol. 26, no. 3, pp. 951–961, 2013.

[63] O. Barbarisi, F. Vasca, and L. Glielmo, "State of charge Kalman filter estimator for automotive batteries," *Control Engineering Practice*, vol. 14, no. 3, pp. 267–275, 2006.

[64] W. L. Burgess, "Valve regulated lead acid battery float service life estimation using a Kalman filter," *Journal of Power Sources*, vol. 191, no. 1, pp. 16 – 21, 2009.

[65] J. Han, D. Kim, and M. Sunwoo, "State-of-charge estimation of lead-acid batteries using an adaptive extended Kalman filter," *Journal of Power Sources*, vol. 188, no. 2, pp. 606

– 612, 2009.

[66] Y. Hu and S. Yurkovich, "Battery cell state-of-charge estimation using linear parameter varying system techniques," *Journal of Power Sources*, vol. 198, pp. 338 – 350, 2012.

[67] R. H. Milocco and B. E. Castro, "State of charge estimation in NiMH rechargeable batteries," *Journal of Power Sources*, vol. 194, no. 1, pp. 558–567, 2009.

[68] G. L. Plett, "Sigma-point Kalman filtering for battery management systems of LiPB-based HEV battery packs: Part 1: Introduction and state estimation," *Journal of Power Sources*, vol. 161, no. 2, pp. 1356 – 1368, 2006.

[69] D. V. Prokhorov, "Toyota prius HEV neurocontrol and diagnostics," *Neural Networks*, vol. 21, pp. 458 – 465, 2008.

[70] S. Sepasi, R. Ghorbani, and B. Y. Liaw, "Improved extended Kalman filter for state of charge estimation of battery pack," *Journal of Power Sources*, vol. 255, pp. 368 – 376, 2014.

[71] A. Vasebi, S. Bathaee, and M. Partovibakhsh, "Predicting state-of-charge of lead-acid batteries for hybrid electric vehicles by extended Kalman filter," *Energy Conversion and Management*, vol. 49, no. 1, pp. 75 – 82, 2008.

[72] A. Vasebi, M. Partovibakhsh, and S. M. T. Bathaee, "A novel combined battery model for state-of-charge estimation in lead-acid batteries based on extended Kalman filter for hybrid electric vehicle applications," *Journal of Power Sources*, vol. 174, no. 1, pp. 30 – 40, 2007.

[73] R. Xiong, X. Gong, C. C. Mi, and F. Sun, "A robust state-of-charge estimator for multiple types of lithium-ion batteries using adaptive extended Kalman filter," *Journal of Power Sources*, vol. 243, pp. 805 – 816, 2013.

[74] A. H. Anbuky, P. Hunter, T. Johnson, and D. Lim, "Vrla battery intelligent node," in *Telecommunications Energy Conference, 2002. INTELEC. 24th Annual International*, pp. 169–175, 2002.

[75] N. Mohan, T. M. Undeland, and W. P. Robbins, *Power Electronics Converters, Applications, and Design*. John Wiley & Sons, Inc., 1989.

[76] P. Kurzweil, "Capacitors electrochemical double-layer capacitors," *Encyclopedia of Electrochemical Power Sources*, pp. 607–633, 2009.

[77] E. H. E. Brouji, O. Briat, J.-M. Vinassa, N. Bertrand, and E. Woirgard, "Impact of calendar life and cycling ageing on supercapacitor performance," *IEEE Transactions on Vehicular Technology*, vol. 58, pp. 3917 – 3929, October 2009.

[78] P. Sharma and T. Bhatti, "A review on electrochemical double-layer capacitors," *Energy Conversion and Management*, vol. 51, pp. 2901–2912, December 2010.

[79] A. Burke, "Ultracapacitors: why, how, and where is the technology," *Journal of Power Sources*, vol. 91, pp. 37 – 50, 2000.

[80] H. Liu, Z. Wang, J. Cheng, and D. Maly, "Improvement on the cold cranking capacity of commercial vehicle by using supercapacitor and lead-acid battery hybrid," *IEEE Transactions on Vehicular Technology*, vol. 58, pp. 1097 – 1105, March 2009.

[81] Maxwell, "datasheet_k2_series," 2012.

[82] H. Gualous, D. Bouquain, A. Berthon, and J. Kauffmann, "Experimental study of supercapacitor serial resistance and capacitance variations with temperature," *Journal of Power Sources*, vol. 123, pp. 86–93, September 2003.

[83] W. Li, G. Joós, and J. Bélanger, "Real-time simulation of a wind turbine generator coupled with a battery supercapacitor energy storage system," *IEEE Transactions on Industrial Electronics*, vol. 57, pp. 1137 – 1145, April 2010.

[84] L. Zubieta and R. Bonert, "Characterization of double-layer capacitors for power electronics applications," *IEEE Transactions on Industry Applications*, vol. 36, pp. 199 – 205, January/February 2000.

[85] T. Funaki and T. Hikihara, "Characterization and modeling of the voltage dependency of capacitance and impedance frequency characteristics of packed EDLCs," *IEEE Transactions on Power Electronics*, vol. 23, pp. 1518 – 1525, May 2008.

[86] S.-H. Kim, W. Choi, K.-B. Lee, and S. Choi, "Advanced dynamic simulation of supercapacitors considering parameter variation and self-discharge," *IEEE Transactions on Power Electronics*, vol. 26, pp. 3377 – 3385, November 2011.

[87] F. I. Simjee and P. H. Chou, "Efficient charging of supercapacitors for extended lifetime of wireless sensor nodes," *IEEE Transactions on Power Electronics*, vol. 23, pp. 1526 – 1536, May 2008.

[88] R. L. Spyker and R. M. Nelms, "Classical equivalent circuit parameters for a double-layer capacitor," *IEEE Transactions on Aerospace and Electronic Systems*, vol. 36, pp. 829 –

836, July 2000.

[89] H. Yang and Y. Zhang, "Analysis of supercapacitor energy loss for power management in environmentally powered wireless sensor nodes," *IEEE Transactions on Power Electronics*, vol. 28, pp. 5391 – 5403, November 2013.

[90] A. Xu, S. Xie, and X. Liu, "Dynamic voltage equalization for series-connected ultracapacitors in EV/HEV applications," *IEEE Transactions on Vehicular Technology*, vol. 58, pp. 3981 – 3987, October 2009.

[91] Y. Cheng, "Assessments of energy capacity and energy losses of supercapacitors in fast charging–discharging cycles," *IEEE Transactions on Energy Conversion*, vol. 25, pp. 253 – 261, March 2010.

[92] D. Simon, *Optimal State Estimation: Kalman, H Infinity, and Nonlinear Approaches*. Wiley-Interscience, 2006.

[93] T. Hu, B. Zanchi, and J. Zhao, "Simple analytical method for determining parameters of discharging batteries," *IEEE Transactions on Energy Conversion*, vol. 26, no. 3, pp. 787–798, 2011.

[94] A. Barré, B. Deguilhem, S. Grolleau, M. Gérard, F. Suard, and D. Riu, "A review on lithium-ion battery ageing mechanisms and estimations for automotive applications," *Journal of Power Sources*, vol. 241, pp. 680 – 689, 2013.

[95] S. M. Rezvanizaniani, Z. Liu, Y. Chen, and J. Lee, "Review and recent advances in battery health monitoring and prognostics technologies for electric vehicle (EV) safety and mobility," *Journal of Power Sources*, vol. 256, pp. 110–124, 2014.

[96] W. Waag, C. Fleischer, and D. U. Sauer, "Critical review of the methods for monitoring of lithium-ion batteries in electric and hybrid vehicles," *Journal of Power Sources*, vol. 258, pp. 321–339, 2014.

[97] Y. Zheng, L. Lu, X. Han, J. Li, and M. Ouyang, "LiFePO4 battery pack capacity estimation for electric vehicles based on charging cell voltage curve transformation," *Journal of Power Sources*, vol. 226, pp. 33–41, 2013.

[98] Y. Hu, S. Yurkovich, Y. Guezennec, and B. J. Yurkovich, "Electro-thermal battery model identification for automotive applications," *Journal of Power Sources*, vol. 196, no. 1, pp. 449–457, 2011.

[99] P. Leijen and N. Kularatna, "Developing a monitoring system for Toyota Prius battery-packs for longer term performance issues," *IEEE International Symposium on Industrial Electronics (ISIE)*, pp. 1–6, 2013.

[100] P. Ramadass, B. Haran, R. White, and B. N. Popov, "Mathematical modeling of the capacity fade of Li-ion cells," *Journal of Power Sources*, vol. 123, no. 2, pp. 230 – 240, 2003.

[101] P. Krüsemann, A. Mank, A. Belfadhel-Ayeb, and P. Notten, "Low volume sampling device for mass spectrometry analysis of gas formation in nickel-metalhydride (NiMH) batteries," *Analytica Chimica Acta*, vol. 566, no. 2, pp. 238–245, 2006.

[102] Linear Technology, "High side micropower MOSFET driver," 1992.

[103] Microchip, "Low-power linear active thermistor ICs," 6 August 2006.

[104] Allegro MicroSystems, Inc., "Hall effect linear current sensor with overcurrent fault output for 100 V isolation applications," 2008-2012.

[105] N. Gardner, *PIC C An introduction to programming the Mircochip PIC in C*. Character Press Limited, 1998.

[106] D. Bell and M. Parr, *C# for Students*. Addison-Wesley, 2004.